**Politecnico di Milano**
**Energy Department**
**Doctoral Programme in Materials Engineering**

---

# Development of Novel, Advanced Molybdenum-based Composites for High Energy Physics Applications

Doctoral Dissertation of:
**Nicola Mariani**

Supervisor:
**Ing. Alessandro Bertarelli (CERN)**

Tutor:
**Prof. Marco Beghi (Politecnico di Milano)**

The Chair of the Doctoral Program:
**Prof. Chiara Castiglioni (Politecnico di Milano)**

Cycle XXVI - 2014

Supervisor:

**Ing. Alessandro Bertarelli (CERN)**

Tutor:

**Prof. Marco Beghi (Politecnico di Milano)**

The Chair of the Doctoral Program:

**Prof. Chiara Castiglioni (Politecnico di Milano)**

To Valentina, my family and my friends...

# Acknowledgements

I would like to acknowledge all the people who contributed to this extraordinary project, but of course they are so many that I here there will be only a very short selection.

First of all a special thank must be given to Alessandro Bertarelli (CERN EN/MME), who supervised this work with incredible energy and tons of ideas giving the right fuel for exploring new, unknown territories. The second most important person who contributed to this work is Stefano Bizzaro from BrevettiBizz: he not only provided an invaluable experience on materials and production techniques, but also helped me to grow and understand the world surrounding us from all the possible perspectives, thus allowing the realization of my projects. Afterwards, I want to give another special thank to Prof. Marco Beghi, who assisted me in my personal and university path since many many years, always believing in me and giving his extraordinary support.

Then the other members of the Project Engineering section: Alessandro Dallocchio, Federico Carra, Luca Gentini, Benoit Riffaud, Didier Steyaert and Marc Timmins, Marco Garlasch, Edyta Krzyzak, Guillaume Maitrejean, Elena Quaranta and many other students who did a part of the road with us: we shared this years at CERN and during all this time I knew I could count on their help and their friendship, so I want to thank them once more for everything and I wish them all the best!

Following I would like to thank all the colleagues from the MME group, too many to be cited here, and the people working with us on the EuCard activities, with a special mention for Lorenzo Peroni and Martina Scapin of Politecnico di Torino, Michael Kitzmantel and Erich Neubauer of RHP Technology, and Alexander Ryazanov of NRC-Kurchatov Institute.

Finally, my last big thank goes to my girlfriend Valentina, my family and my friends who bear me during this long and difficult years: I know it has been hard for you too but I love you all!

# Abstract

Newly introduced particle accelerators such as the Large Hadron Collider (LHC) of CERN (Geneva, CH) exhibit a huge increase in the energy stored inside the accelerated beam with respect to previous machines, bringing to the need of more efficient, reliable and robust Collimation Systems to properly clean the beam from outgoing particles and protect the rest of the accelerator in case of accidental beam impacts on sensitive and expensive components such as superconducting magnets or particle detectors.

The research on new materials for Beam Intercepting Devices (BID) is therefore receiving strong interest at CERN and in the rest of the particle accelerators community with the aim to improve the cleaning efficiency and the robustness of BID. In that framework the aim of the present PhD work is to develop, characterize and produce new composite materials to be used in LHC Collimators active part (socalled Jaw) that must satisfy multiple requirements in terms of: density and average atomic number (Cleaning Efficiency), electrical conductivity (RadioFrequency Impedance), mechanical strength at high strain rates (Impact Resistance), thermal conductivity and thermal expansion (Thermal Stability). In addition, since the material will be heavily irradiated during its life cycle, it must not contain elements that create dangerous isotopes and must be able to withstand high cumulated doses before to lose its properties by radiation induced degradation.

The thesis work has been divided into two main multidisciplinary axes that are strongly interconnected between each other: the novel composites R&D and their characterization in standard conditions and second the experimental testing of proposed materials against a real proton beam impact, supported by realtime measurements and postimpact analysis.

The first part included a preliminary study of present solutions and available composites, the characterization of already developed materials like Copper Diamond (CuCD, developed by RHP Technology, Seibersdorf, AT), and finally the research, development and characterization of new Molybdenum based composites.

CuCD is a metal matrix composite produced by Rapid Hot Pressing (RHP) of Copper, Boron and diamond powders especially developed for thermal management applications. The combination of the good physical properties of diamonds (high thermal conductivity, low thermal expansion and density) with the electrical conductivity of Copper give rise to a material having a thermal conductivity $\approx$ 25% higher than Copper OFE with a thermal expansion coefficient at RT of only 7 $ppm/K$. Unfortunately, the intrinsic brittleness of such material combined with its thermal instability at higher temperatures are limiting the material appealing, so that a second R&D program has been established to overcome such limitations by exploring alternative composite families with higher thermal stability at high Temperature.

The R&D of Molybdenum-based composites has been carried out in collaboration with the private company BrevettiBizz (Verona, IT) between 2011 and 2013, and has been managed by the student who provided proposals for compositions and production cycles, microstructural, thermal and mechanical characterization and interpretation of results. The supporting thermo-mechanical characterization has been made under standard conditions using ad-hoc experimental apparatus that in certain cases has been designed and produced inside CERN EN/MME with the contribution of the student, like the thermal conductivity and thermal conductance measuring apparatus described in the thesis work. Molybdenum has been chosen as the main element because of its extraordinary mechanical properties combined with very high Thermal Stability and a good chemical affinity with carbon materials like diamond and graphite. The most important milestones in the materials R&D presented in the thesis work are Molybdenum - Copper - Diamond (MoCuCD), Molybdenum Carbide - Graphite (MoGR) and

Molybdenum Carbide - Graphite - Carbon Fibers (MoGRCF).

- MoCuCD has been a great improvement of CuCD from the mechanical point of view (thanks to the formation of Molybdenum carbides at the interface between diamonds and Molybdenum) but the presence of Copper used to fill the interstitials is still limiting its resistance to high Temperatures;
- MoGR relies on the high temperature reaction between Molybdenum and graphite to promote the complete transformation of Molybdenum in refractory carbide $Mo_2C$. One peculiarity of $Mo_2C$ is its metal like electrical conductivity that results in a conductive MoGR composite. In addition MoGR is completely refractory ($T_M$ >2500$^oC$) and has a very high Thermal Stability, but does not shine for physical and mechanical properties;
- MoGRCF, finally, includes the refractory behaviour of MoGR while enhancing its thermal and physical properties by the addition of Carbon Fibers. The material is then sintered in liquid phase to melt and squeeze the $Mo_2C$ phase and let it fill the interstitials between Fibers. The result is an outstanding material with a thermal conductivity in excess of 700 $W/mK$ and a density of only $2.8g/cm^3$.

The second part of the thesis is the final testing of proposed materials against a direct beam impact to compare the different collimator materials in a reallife accidental situation. Preliminary hydrodynamic FEM analysis of the beam impact have been performed to predict the damage entity on standard collimator related materials. The simulations have been carried out using the commercial code Autodyn involving nonlinear materials models like Equations Of State and complex strength and failure models. The simulations allowed to predict (for known materials) the physical effective damage on the materials impacted by the proton beams and to properly tune the design of the samples and the sample holder in order to obtain measurable parameters with the proposed experimental apparatus. The experiment, id. $HRMT-14$, took place into the HiRadMat facility at CERN

(High Radiation to Materials) during SeptemberOctober 2012, entailing the controlled impact on 6 different Collimator materials with increasing proton beam intensities of the Super Proton Synchrotron particles accelerator of CERN (operating at 440 GeV). The energy of the impacts was enough to observe the samples explosion by high speed video camera (during the high intensity shots) and the observation of macroscopic damage on impacted samples.

Finally, the proposed comparison of the different materials will be the background for the final choice of the LHC Collimator materials to be taken in next years at CERN.

Keywords: Beam Intercepting Devices (BID); LHC Collimators; Carbon Fiber Carbon (CFC); Inermet180; Molybdenum; Glidcop; metal-diamond composites; Copper-Diamond (CuCD); metal carbide graphite composites; metal carbide carbon fibers reinforced composites; Molybdenum-Copper-Diamond (MoCuCD); Molybdenum Carbide-Graphite composite (MoGR); Molybdenum Carbide-Graphite-Carbon Fibers composite (MoGRCF); Rapid Hot Pressing (RHP); Liquid Phase Sintering (LPS); HiRadMat; proton beam impacts; hydrodynamic simulations; Autodyn.

# Contents

# List of Figures

# List of Tables

# 1

# Thesis Structure

This Chapter describes the structure of the thesis which is organized as follows: context and motivations of the work, analysis of present solutions, development of novel materials and testing under extreme conditions entailed by highly energetic beam impacts.

Motivations, context and main scientific contributions of the work are summarized in Chapter 2.

Chapter 3 includes a brief introduction to the Large Hadron Collider (LHC) and to its unique Collimation System: this part will allow to understand the special requirements of materials for Beam Intercepting Devices (BID), object of the present R&D program.

Chapter 4 presents the state of the art of LHC Collimators materials in order to define a proper basis for the novel materials R&D.

Chapters 5 and 6 describes the analytical methods used for predicting materials properties as well as the experimental tools applied to materials characterization.

Chapter 7 describes the characterization performed on CuCD, the first composite material proposed as solution for future Hi-Lumi LHC Collimators.

Chapter 8 presents the R&D of Molybdenum - Copper - Diamond (MoCuCD) that is the first material developed during the present thesis work. This Chapter includes a first part on the innovations introduced in production procedures (powder selection and cleaning, coatings, production cycle improvements) followed by the characterization of the two best performing MoCuCD materials obtained.

Similarly Chapters 9 and 10 illustrate the main steps of the R&D on Molybdenum Carbide - Graphite (MoGR) and Molybdenum Carbide - Graphite - Carbon Fibers

(MoGRCF) respectively.

Finally, Chapter 11 describes the robustness tests performed on developed materials, including advanced numerical simulations of high energy beam impacts. The experimental activity included the active participation to a first-of-its-kind experiment carried out in 2012 entailing the direct impact of energetic particle beams on the materials presented in this work.

Chapter 12 summarizes the results obtained with the newly introduced materials and proposes a future outlook.

# 2

# Thesis Motivations

In this Chapter the motivations and the context of the thesis work are presented and discussed.

## 2.1 Aim of the Thesis

This thesis aims at identifying and characterize new composite materials for Beam Intercepting Devices (BID) that could be used to produce the jaws of future High Luminosity LHC Collimators. As will be explained in details in Chapter 3 the jaws of LHC Collimators are closely interacting with the incredibly energetic LHC beam. That makes LHC Collimators one of the most challenging equipment from thermo-mechanics and material science point of view. Innovative results obtained in this thesis can be of high interest for a large palette different applications, such as aero-spatial components, nuclear plants, high temperature furnaces, electronics,

## 2.2 Context

The thesis context is the upcoming upgrade of the LHC (the High Luminosity LHC) that will bring the machine beyond the limits of the presently used Collimator materials (see Chapter 4), pushing for new efforts in the research on novel advanced composites for BID.

The research has been funded by the European Coordination for Accelerator Research & Development Project (EuCARD) Working Package 8.3, titled "Materials and thermal shock waves" (8)) with the aim at developing and characterize materials for

particle accelerators Collimators: the R&D activity involved several institutes including CERN, AIT (Austrian Institute of Technology), Politecnico di Torino, GSI (Helmholtz Centre for Heavy Ion Research), NRC- Kurchatov Institute, EPFL (Ecole Polytechnique Federale de Lausanne).

## 2.3 Overview of PhD activities

The thesis started with the study of currently used Collimators materials and the characterization of the composites developed by partner institutes during the past EuCard WP8 activities (Copper - Diamond, CuCD, see Chapter 7).

The performed analysis of the material behaviour with respect to the BID application enlighten how the used materials would intrinsically limit the machine in its ultimate configuration, increasing the appealing of new composite materials as CuCD. However, since the characterization of CuCD proved that the material is not completely fulfilling all the requirements imposed for Hi-Lumi LHC Collimators (see Chapter 7), the research moved to the identification of other possible composite materials having improved behaviour with respect to the BID application. So the following part of the thesis entailed the development of a large number of novel Mo-based composites, the most important being listed below:

- Molybdenum - Copper - Diamond (MoCuCD, see Chapter 8);
- Molybdenum Carbide - Graphite (MoGR, see Chapter 9);
- Molybdenum Carbide - Graphite - Carbon Fiber (MoGRCF, see Chapter 10).

All produced materials have been characterized at CERN (and in other cited partner institutes) in terms of thermal and mechanical properties in order to determine the following steps of the R&D campaign. The conclusion of this work, lasted three years, is MoGRCF: the produced composite exhibits in fact outstanding thermal and physical properties thanks to the innovative composition and to the improved production process, thus being a very good candidate for future Hi-Lumi LHC Collimators.

However the BID requirements include the resistance, in the worst accidental scenario, against high energy beam impacts: this potentially catastrophic phenomena cannot been handled with standard tools and requires on one side complex numerical simulations to predict the damage and on the other challenging experiments to

validate the proposed models under the extreme conditions encountered during the impacts. The numerical tool used for the impact simulation is the hydrodynamic code Autodyn coupled with the Smooth Particle Hydrodynamics algorithm, which allows to follow the evolution of the fragments ejected by the target during the beam impact. The simulations however require scarcely available materials models, excluding the prediction of damage on new materials.

For that reason, and to validate the models on known materials, a first-of-its-kind experiment has then been setup at CERN HiRadMat (High Radiation to Materials) facility, allowing the controlled impact of highly energetic proton beams on materials samples. The experiment was a complete success allowing for the first time in the best of our knowledge the direct observation of the material samples explosion during a beam impact, thus allowing for a comparison of the behaviour of different materials that is of valuable interest for future researches on BID materials. The main contributions given to the experiment were the design of samples via hydrodynamic simulations, the development of a high speed, radiation hard video camera acquisition system and the novel composites samples production.

The results of the beam impact residual damage coupled with the benchmark of the proposed materials in the steady state conditions will then allow for the identification of the future LHC Collimator materials.

# 3

# Introduction to LHC Collimators

## 3.1 The Large Hadron Collider (LHC)

The exploration and understanding of the world surrounding us is a natural and ancient instinct of human kind, and many progresses have been done since the first men looked at the stars wondering how they could shine...

The particle physics born in the early XX century aims to understand the intimate structure of matter: how the elementary particles behave and combine together, how is made their internal structure and, last but not least, how they have been created. These studies involve the investigation of particles that are infinitely small and cannot be detected by human senses, leading to the need of more and more accurate and sophisticated instruments for the observation.

In that framework we can consider the particle accelerators as the main tool for modern particle physicists: these machines are to accelerate charged particles (usually protons, but also electrons and heavier ions) up to relativistic energies that are well beyond the standard energies experienced on earth, permitting the observation of otherwise inaccessible physical phenomena, such as the formation of non-stable systems like subatomic particles and anti-matter.

The last step in the world's particle accelerators evolution is CERNs Large Hadron Collider (LHC, Geneva, Switzerland) (9), that has become on November 2009 the worlds highest energy particle accelerator, reaching the energy of 1.18 TeV in each beam and overcoming the maximum energy of previous biggest particle accelerator, the Tevatron (Batavia, US). The beam energy value alone is not sufficient to describe the huge

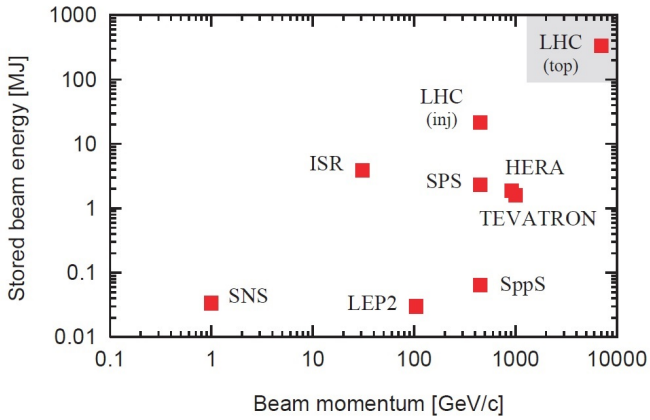


**Figure 3.1:** Stored beam energy versus beam momentum for past, present and future Particles Accelerators

destructive power of the travelling proton beams because it's dependent of the number of particles in transit along the ring: for the LHC the nominal total stored energy per beam is 362 MJ, that is enough to melt 500 Kg of Copper and is orders of magnitude higher than any other older particle accelerator, as shown in Figure 3.1. (10)

The LHC machine upgrade program schematically presented in Figure 3.2 shows how the machine operated safely at the energy of $4TeV$ per beam in 2012 reaching up to the 75% of the nominal luminosity: the various improvements foreseen during the Long Shutdown 1 (LS1) will permit to reach the nominal energy of 7 TeV per beam at the nominal luminosity in 2017, while the final LHC configuration (the so-called High Luminosity LHC, Hi-Lumi LHC) will be reached only in 2020 after major upgrades to the superconducting magnets and to the protection system. (1).

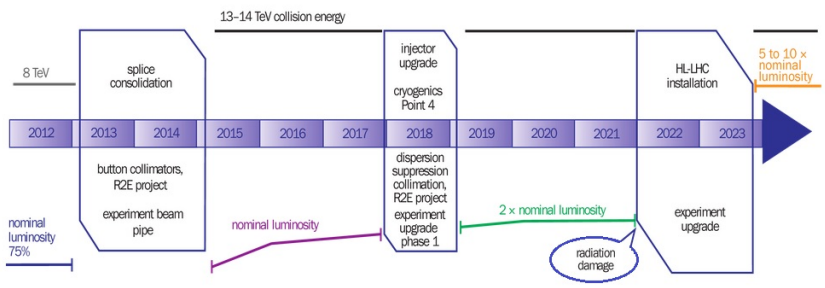


**Figure 3.2:** High Luminosity LHC Upgrade Plan (1)

It is therefore clear how great are the technological challenges that CERN engineers and scientists have to tackle during the LHC design, construction and operation: LHC components are going close to the XX century technology limit so that CERN is continuously investing on the development of new materials, methods and physical models in order to fulfil the LHC design requirements.

## 3.2 LHC Layout & Experiments

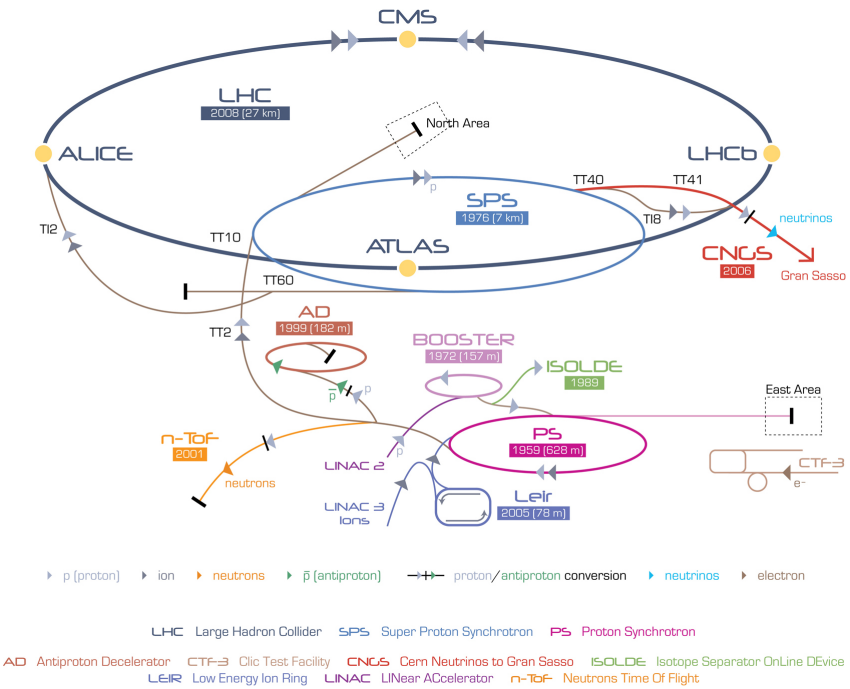


**Figure 3.3:** CERN accelerator complex in Meyrin, CH.

The LHC is the last accelerating ring of the CERN particle accelerator complex shown in Figure 3.3; the underground tunnel circumference is $26.659km$ and its average depth is 100m below the ground, the ring being placed in the France region just beside the Swiss-France border close to Meyrin (CH). The LHC beam lines accommodate two counter rotating proton or Lead ion beams (beam 1 clockwise, beam 2 counter-clockwise) that are injected in the two insertion areas, located in the points IR2 (beam 1) and IR8(beam 2) shown in Figure 3.4. The particles enter in the LHC from the Super Proton Synchrotron (SPS) with a nominal energy of $450GeV$ and are then accelerated

up to the nominal top energy (see Table 3.1) by the Radio-Frequency (RF) cavities located in IR4. The two beams will then be brought into collision at the four interaction points (IPs in Figure 3.4) where the main experiments are placed: ATLAS (IP1) (11), ALICE (IP2) (12), CMS (IP5) (13) and LHCb (IP8) (14). In normal conditions the beams will collide for several hours of beam lifetime and at the end of this period, or in case of a failure detection, the beams will be aborted by the dump system located in IR6.

**Table 3.1:** LHC beam parameters for proton operations.

| **Parameter** | **Unit** | **Injection** | **Collision** |
|---|---|---|---|
| Energy | $[GeV]$ | 450 | 7000 |
| Relativistic $\gamma$ | $[-]$ | 479.6 | 7461 |
| N. of particles per bunch | $[-]$ | $1.15 * 10^{11}$ | $1.15 * 10^{11}$ |
| N. of bunches per beam | $[-]$ | 2808 | 2808 |
| Stored Energy per beam | [MJ] | 23.3 | 362 |
| Bunch spacing | [ns] | 25 | 25 |
| Revolution Frequency | [kHz] | 11.245 | 11.245 |
| Peak Luminosity in IP1 and IP5 | $[cm^{-2}s^{-1}]$ | $[-]$ | $10^{34}$ |

Table 3.1 lists few beam parameters of interest for this work in the case of nominal machine operation with protons. The LHC is designed to reach a peak luminosity of $10^{34}cm^2s^1$ in ATLAS and CMS; these are multi-purpose detectors dedicated to investigation of the broadest range of physics possible and to the Higg's Boson discovery. LHCb is a low luminosity ($L = 10^{32}cm^2s^1$) specialized detector with the main objective of explaining the asymmetry between matter and antimatter in the universe by studying the beauty quark physics. Two further experiments, TOTEM (15) and LHCf (16) are also installed upstream and downstream of the high luminosity IPs (IP5 and IP1 respectively), they have been devised to detect particles coming out from the experiments with small deviation angles in order to measure the elastic scattering cross section. Finally, ALICE is dedicated to the studies of the quark-gluon plasma generated by Lead ion collisions. The various experiments requirements have been taken into account in the LHC Collimation system layout, that is presented in next chapter.

The LHC hardware (not taking into account the experiments facilities) can be divided in 5 categories:

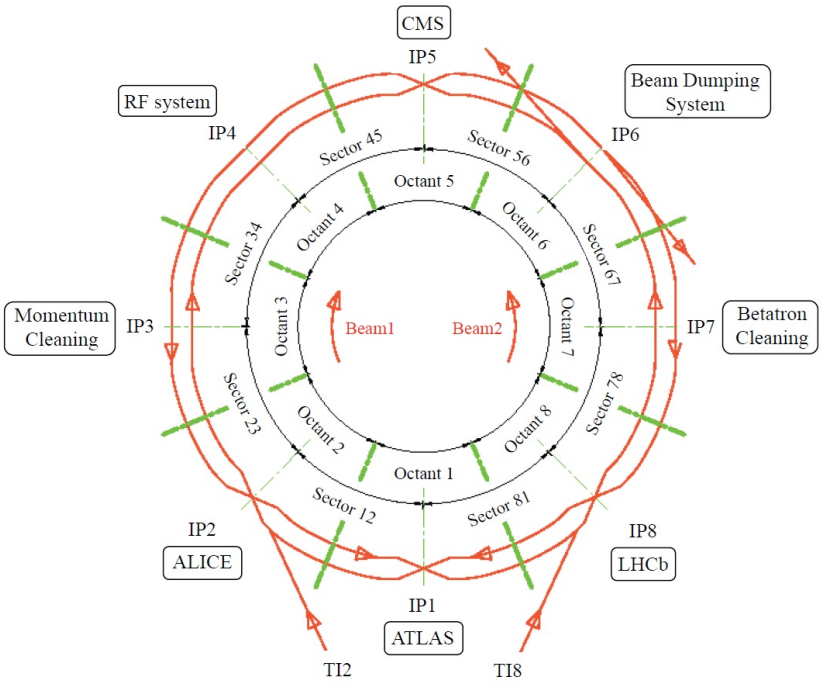


**Figure 3.4:** LHC Rings Design: Experiments, Cleaning, Accelerating and Dump Systems locations.

- Superconducting magnets
- Radio Frequency Accelerating Cavities
- Collimation system
- Beam Lines
- Control equipment (Beam Loss Monitors, Wire Scanners, Vacuum gauges)
- Support equipment for Ultra High Vacuum and Cryogenics (pumps, cryostats)

The most sensitive equipment from the beam losses point of view are the superconducting magnets, that are responsible for bending and focusing the beams. In the LHC tunnel 1232 main dipoles, 386 main quadrupole plus more than 4000 correctors are operated at cryogenic temperatures of 1.8 K and 4.5 K. The actual superconducting magnets, based on Nb superconducting wires, are capable to generate a magnetic field of $8.33T$ along their length of 14.3 m (in the case of the main dipoles). Note that in

each magnet unit there are two opposite magnets for the two opposite beams. The new version of superconducting magnets will use a more performing $Nb_3Sn$ superconducting materials that will allow to reach $\approx 11T$ requiring smaller magnet spires length.

The superconducting magnets are sensitive against any heating generated by the beam or other sources because they will lose their super-conductivity provoking an cascade temperature increase that will not allow the passage of the nominal current coming from the power source, leading to catastrophic failure of the entire magnet unit and of the supporting equipment (power lines, cryostats, ecc). The effects of local heat increase in magnets have unfortunately already been observed during the accident occurred in 2008, where a welded connection was not properly transferring the current from one unit to the other provoking the failure of the magnet and a prolonged machine stop. After that experience many improvements have been implemented to avoid any other accident on magnets and high energetic power sources.

The studies on the heat deposition on magnets and equipment due to beam losses have shown how the unique solution to increase safely the machine performance was to establish a powerful and reliable protection system, composed by remotely controlled Collimators, that has to withstand directly the most energetic particle beam created by the human kind while protecting the rest of the machine even during severe accidents.(17)

It is therefore clear the importance of the development and design of the LHC Collimation system in order to handle the enormous amount of energy concentrated in the LHC beams.

## 3.3 LHC Collimation System

The active collimation system of the LHC (18) is a unique of its kind complex protection and cleaning system especially developed to handle the enormous amount of energy stored in LHC beams: it consists of more than 100 collimation units (or Collimators) placed at specific positions all over the LHC ring, as shown in Figure 3.5.

The Collimation system is not a static infrastructure of the LHC machine but instead is continuously tuned and modified to better accomplish its tasks by the addition of features to existing designs or by major design and materials modification.

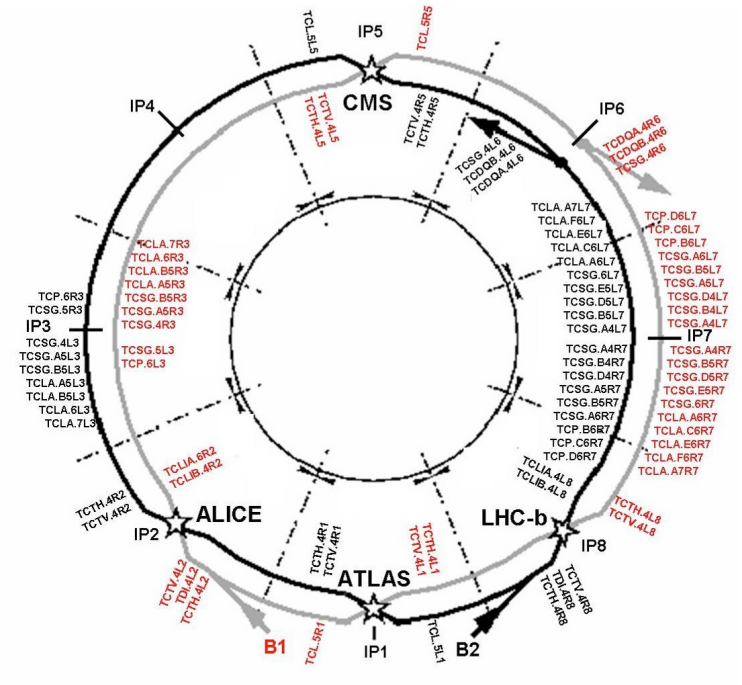


**Figure 3.5:** Summary and position of existing Collimators over the LHC ring.

Actually there are three main families installed, labelled TCP, TCS and TCT, where the T is "target", C is "Collimator" and P, S and T are Primary, Secondary and Tertiary respectively, as will be explained in the following paragraphs. Actually installed Collimators were also commonly identified as Phase I in many presentations and papers, however this notation is no more valid and we will refer to each collimator type with its specific nomenclature. Examples of collimators actually under preparation are the new TCTP (Tertiary) featuring the Beam Position Monitors (BPMs) and the TCSM prototype (Secondary) still under development.

### 3.3.1 Beam Cleaning

During normal operations the collimators are to intercept the unavoidable halo of particles that tend to escape from the beam correct trajectory (Beam Cleaning): those particles are highly energetic and is of paramount importance to avoid them hitting delicate equipment such like superconducting magnets and particles detectors because they could provoke magnets quenches as stated in various previous works (19) (20)

The collimation mechanism itself relies on two parallel jaws that define a slit for the

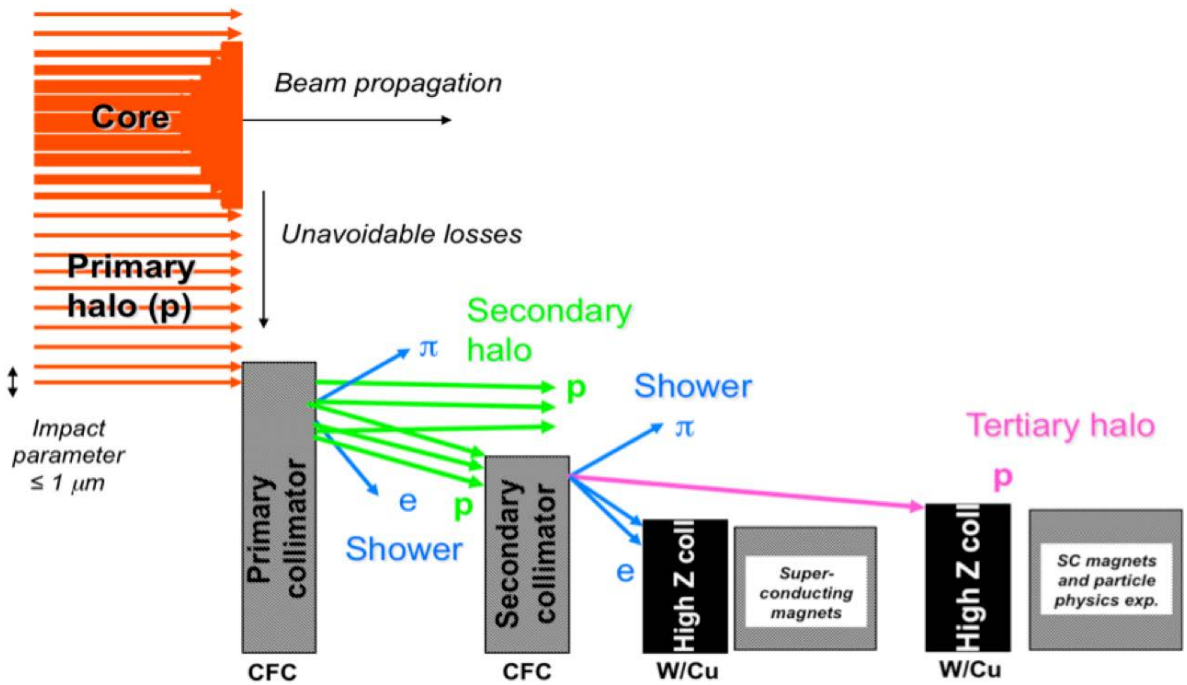


**Figure 3.6:** Schematics of LHC Multi-stage Collimation system

beam, with different collimators having different orientations to cover the whole beam halo circumference. The beam halo is therefore intercepted by the Collimators jaw and only the central part of the beam prosecutes without being perturbed. Secondary particles showers are also produced during the interaction between the highly energetic beam and the collimator jaws, in order to clean the residual showers a multi-stage system has been implemented as shown in Figure 3.6. The multi-stage cleaning system relies on dynamic movement of the collimators jaws to assure always a cascade between Primaries (the only ones really touching the beam), Secondaries and Tertiaries, avoiding concentrated energy absorption that might overcome the Collimators cooling capabilities. Furthermore, different materials are used in a strategic positions to take advantage of their different stopping powers.

### 3.3.2 Machine Protection

The second and most critical assignment of the Collimation System is the machine protection in case of accidental beam orbit errors: if an entire LHC bunch directly impacts onto a target, the whole energy of the bunch is deposited into a relatively small region

of the target itself. As we already touched on, the energy stored is really enormous and is potentially destructive for the large majority of materials and structures. In the case of LHC Collimators, the risks are to damage the cooling water pipes (with water leak inside the cryogenic vacuum of LHC Beam Line) and to eject melted and vaporized materials inside the LHC Beam line. A further catastrophic scenario is the melting and bonding of the collimator's jaws that would not allow the passage of the beam until the collimator's removal. In all those cases the consequences on the entire LHC machine operations will be catastrophic, forcing to a complete stop of the machine, the collimator substitution and the reconditioning of the entire interested LHC Beam Line sector. The expected maximum beam impact scenario has been initially calculated to be about 20 bunches (21). The beam impact scenario has then been modified in last years following the evolution of the LHC beam optics and Collimators operations: first, the value was reduced to about 8 bunches impinging in the same position and perfectly parallel to the jaw, this modification is due to a substantial improvement in the dump re-trigger time that reduces the number of bunches that impact on the collimator before the activation of counter measures. This configuration has been extensively used to evaluate the beam impact resistance of Tertiary Collimators (22). More recent studies carried out at CERN explored the effect of the impinging angle of the beam with respect to the collimator jaw in the case of Tertiary Collimators (23), showing that the previous scenario was largely conservative. A more detailed discussion about the effects of direct beam impacts parameters will be presented in Chapter 11. The LHC Collimation system has been therefore developed to protect the machine in case of accidental beam orbit errors, the collimator being the first, expendable device that the beam sees in accidental scenario. In the next Paragraphs the basic physical principles of the beam-target interaction will be discussed to produce a more accurate view of the entire phenomena and introduce the requirements of the LHC Collimation system.

### 3.3.3 Beam Matter Interaction Principles

As we stated the two main functions of the collimation system are the beam cleaning and the machine protection: both are based on the physical interaction between the energetic proton beams and a solid target, the first being a continuous interaction between the beam external tail and the second being an instantaneous, highly energetic impact of the whole proton beam on the target itself. From the physical point of view,

the interaction between the proton beam and the solid target gives rise to a myriad of different phenomena, that we can briefly summarize in few elementary categories:

- Proton-Electrons interaction: electrons and photons emission;
- Proton-Nucleus interaction: isotopes formation, elementary particles emission, kinetic energy transfer, atomic spallation (24);
- Electron-Electron and Nucleus-Nucleus: thermal energy transfer (thermalization) from energetic atoms inside the target to adjacent atoms.

Those interactions can be predicted relying on a CERN developed Monte-Carlo software (FLUKA, (25)): the software implements the statistical models of all the possible particles interactions to produce the history of the single particle in terms of internal energy, velocity, trajectory and nuclear modifications. The solution of the single particle path represents of course only one of the possible solutions of the problem, so the simulation is repeated for another particle, that will have a different history, and so on until a statistically acceptable distribution has been obtained (i.e. repeating the process does not vary the energy distribution profile normalized to particle number).

Another important effect of continuous interaction with the beam external halo (Beam Cleaning) is the formation of defects, isotopes, fundamental particles trapped in the lattice, ecc, that will modify the thermal, mechanical and electrical properties of the target material, until it might no more be able to fulfil its fundamental assignments, fortunately usually after some years of continuous irradiation.

The long time needed to intimately modify the material's structure is due to the fact that the beam contains a relatively small number of protons: only 1.5 $10^{11}$ protonsbunch, for a maximum amount of 2800 bunches. So one bunch corresponds to a mass of $\approx 10^{-12}g$, therefore the number of electrons emitted, the number of isotopes created and defects formed by spallation are very low compared to the number of atoms inside the impacted target volume in the case of a single beam-target impact, which volume extension is various $cm^3$. However, during the direct impact the target interacts with the beam core that is by far more energetic than the beam external halo: in that case the amount of the kinetic energy transferred to the target leads to a very sharp and concentrated internal energy profile inside the target. The deposited energy

might be enough to locally melt the target material and generate a compressive shock-wave inside the target itself. This situation is very dangerous and has been extensively studied during the present thesis work, see Chapter 11.

The collimation system main constraints have been extensively discussed in past works (26) and have been constantly updated in the following years when new studies and information become available. The historical design constraints presented in cited works have been defined for protons operation, however similar constraints can be applied to ions operations too.

### 3.3.4 LHC Collimators Requirements

Apart from the two main functions of the Collimation system there are other requirements that must be fulfilled:

- Radio Frequency Impedance: collimators can produce significant transverse resistive impedance due to the small gaps between the collimators jaw, leading to high beam perturbations that don't allow to fulfil the LHC nominal beam parameters. The perturbations are due to electron clouds formed by the beam electro magnetic field along the Collimators surfaces that interact with the following incoming particles. The charge evacuation is difficult in non conductive materials like CFC, (see next paragraph 4.1.1) and is actually limiting the LHC from reaching its nominal energy.

  This effects are being carefully studied by CERN RF Group through advanced analytical and numerical methods, methods that are beyond the scope of the present thesis and will not be extensively discussed: it is sufficient to mention that RF experts pointed the importance of replacing Secondary Collimators in CFC with Secondary Collimators having conductive jaw materials. Further studies also suggested that the introduction of a thin layer of conductive material on top of the Collimator's jaw might be sufficient to accommodate the dispersed RF currents providing the requested RF Impedance reduction, at least when dealing with high frequencies (stable beam operations).

- Vacuum: the collimators are to operate inside the Ultra High Vacuum (UHV) of the LHC beam lines and therefore they must be bakeable (i.e. capable to

sustain a thermal cycle at $300^oC$ for several days) and their outgassing rates must remain acceptable to sustain the LHC beam line UHV. For example, for a graphite collimator this imposes special heat treatments (up to $1000^oC$ for several hours), and careful out baking. In addition, during operations the maximum jaw temperature must be kept below $50^oC$ by collimator cooling to avoid increases in the degassing rate. Specific tests are carried out by the CERN Vacuum Group on every new Collimator material and tank assembly to validate the device with respect to LHC beam line vacuum requirements.

- Dimensional Stability: The gap between the collimators jaws is a crucial parameter for the beam cleaning and the beam stability, therefore is of paramount importance to have perfectly flat and parallel jaw surfaces having the correct gap and inclination. The tolerance defined for the collimators jaws are: jaw surface flatness ($40\mu m$), reproducibility of jaw settings ($20\mu m$), step size in jaw movements ($10\mu m$, $15\mu rad$) and knowledge in collimator gap $< 50\mu m$. Summarizing, the collimator's jaws must have a surface flatness below $40\mu m$ over 1 m length of the collimator jaw during operations, requiring, in addition to fine machining and metrological control of pieces, the careful containment of the jaw thermal expansion due to the beam losses.

- Reliability and maintenance: the lost protons will activate the installations in the cleaning insertions leading to maximal dose rates of up to several $mSv/h$ at direct accessible hot-spots to the tunnel line. The collimator jaws may reach higher values. The expected dose rates depend strongly on the collimation layout, the materials chosen, the cooling time as well as the exact location in the insertion. However, human interventions such as maintenance nearby highly activated installations must be restricted to the absolute minimum, hence collimators and belonging equipment must be designed for maximum reliability and fastest maintenance or removal operations. This includes the choice of materials that must not lose quickly their properties by radiation induced degradation.

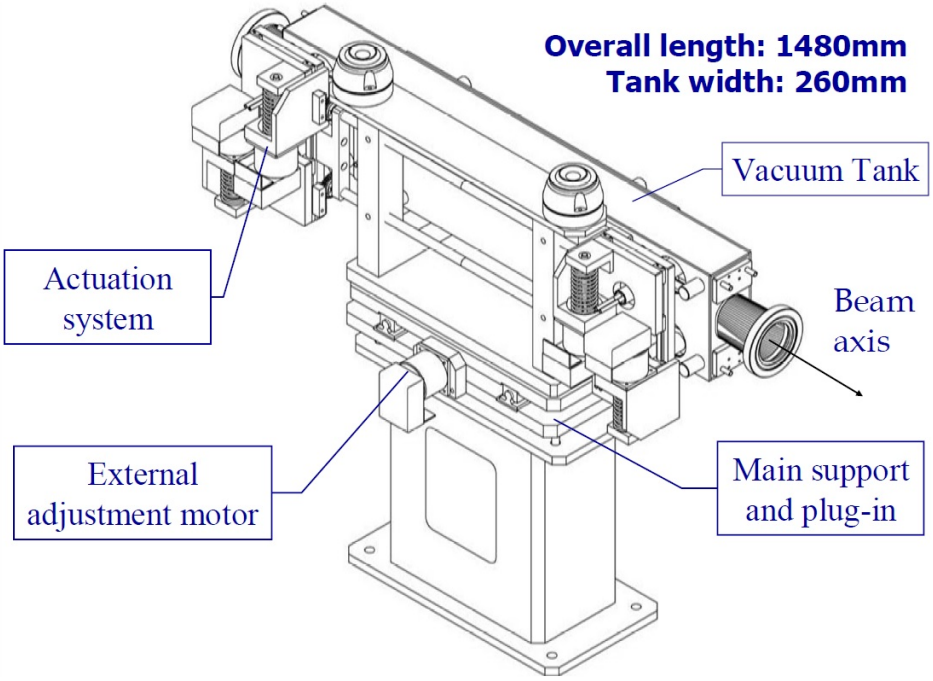


**Figure 3.7:** Structure of a Primary LHC Collimator.

## 3.4 Overview of LHC Collimators Design

### 3.4.1 Present LHC Collimators design

The already installed LHC Collimators, as shown in Figure 3.7 (6), are made up of a support on which the vacuum tank (containing the beam slit) and the actuation mechanism are positioned thanks to a plug-in system; particle beam enters longitudinally into the vacuum tank through the connections at the extremities (see Figure 3.7 ). It's worth noting that the collimator operates on one beam line only, therefore to collimate the opposite beam a second collimator has to be placed.

Inside the vacuum tank there are the two collimation jaw assemblies, core of the system, these are the components having direct interaction with particle beams (see Figure 3.8. In nominal working condition particle beam grazes jaw assemblies with its external halo; actuation system assure the alignment of the jaws with an high precision. Figure 3.8 shows more in detail how the jaw assemblies are supported at the extremities by two shafts that transmit the movement given by the actuation system.

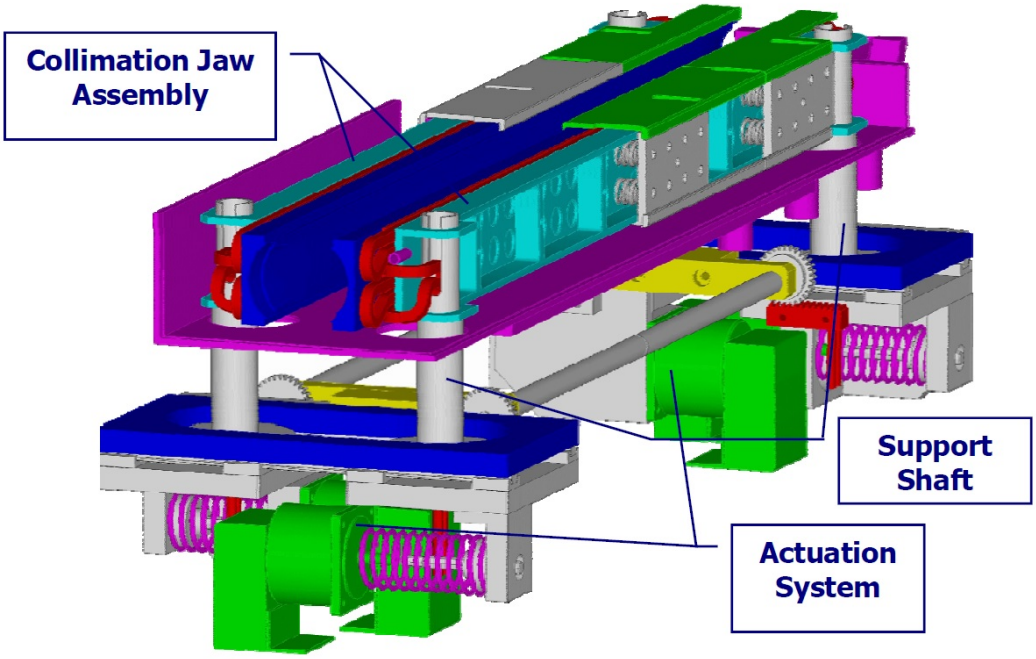


**Figure 3.8:** Schematics of the internal structure of the Collimator.

### 3.4.2 Future HL-LHC Collimators

The design of the next generation of collimators needed for the High Luminosity LHC Upgrade started in 2008 with the aim to overcome the major limitations of actual Secondary Collimators: RF impedance and limited Cleaning Efficiency. The main design baselines of the next generation of collimators as defined in preliminary design phase (27) are listed below:

- Supporting structure compatible with installed Collimators allowing rapid installation in the pre-existing tunnel infrastructures with minimal personnel intervention. The design of the support remains very similar to Figure 3.7.
- Modular design of the jaw assembly to allow the use of alternative materials for the jaw. The material must however be brazable to the Copper cooling circuit and respect all the requirements stated in Paragraph 3.3.
- Back-stiffener concept to allow maximum geometrical stability (improves collimator efficiency): this is obtained by geometrical optimization and by the usage of very stiff Molybdenum bars, as shown in Figure 3.9.

- Optimized internal cooling circuit to absorb higher heat-loads. The brazed cooling circuit is more efficient than the previous TCS and TCP design (cooling pipes in Cu-Ni alloy pushed on the jaw by springs), see Figure 3.9.
- Integrated Beam position Monitors (BPMs) to minimize set-up time, as already done in new TCTP collimators, see Figure 3.9.

The first prototype actually under assembly features a Glidcop (Alumina Strengthened Copper) jaw designed to have dense jaw material with optimal electrical conductivity. However, Copper's high density leads to a more localized energy deposition accompanied by large deformations (due to its high CTE), so to help keep geometrical stability the jaw has been divided in three blocks, each one having its apposite cooling circuit and embedded in a INOX and Molybdenum structure (called Stiffener).

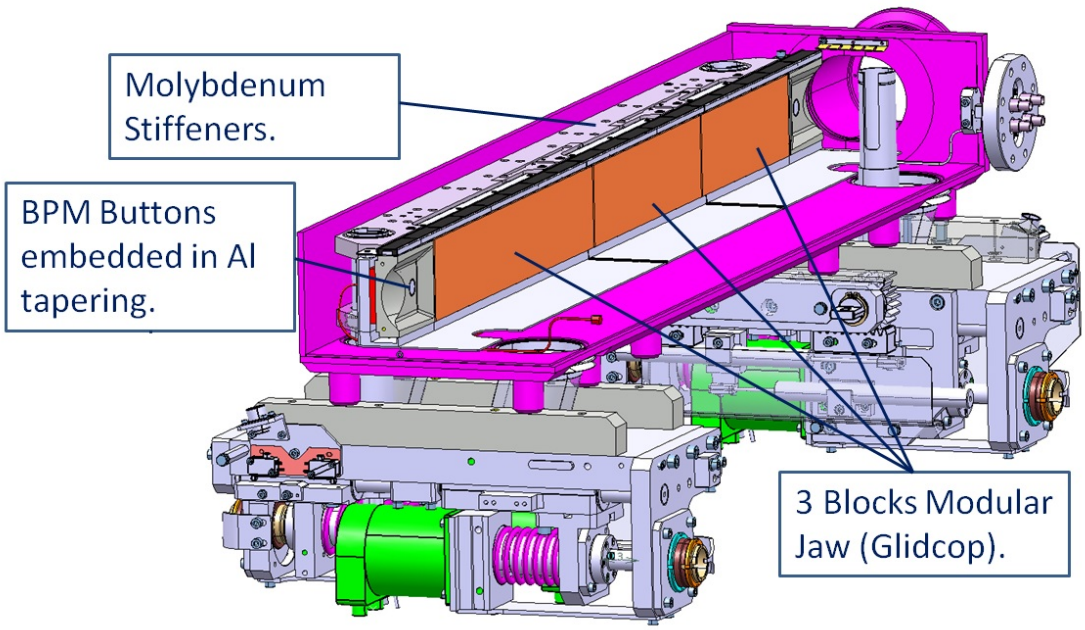


**Figure 3.9:** Details of the single jaw inside the tank with specific improvements with respect to present Collimators.

To not being limited by the heat transfer through the beam pipe-jaw interface the cooling circuit has been obtained machining a Copper piece and brazing it directly to the Glidcop jaw on one side and to the INOX support on the other. The brazing

assures the best thermal continuity but doing so the brazed joint separates the water of cooling circuit from the UHV of the LHC beam line: all brazing must be carefully controlled to assure the absence of leakages through ad-hoc Helium leakage tests and Ultra sounds controls of pieces.

# 4

# State of the Art of LHC Collimator Materials

In this paragraph, thermo-physical and mechanical properties of materials presently used for the BID of interest for this thesis (LHC Collimators) are discussed, giving a motivation for the choice of each material (28) and introducing the Figure of Merit (FoM) used to benchmark existing and new solutions.

## 4.1 Survey of LHC Collimators Materials

As explained in previous Chapter the most critical component of the whole collimator is the jaw (see Figure 3.9), that is the only part having direct interaction with the high energy beams, thus being submitted to intense thermal loads both in nominal working conditions as well as in case of accident scenario. Of course all other components are subjected to showers and nuclear activation but their requirements are less strict than the jaw and are therefore not treated in present work: the only exception being Molybdenum, which is presently used as Jaw Stiffener material in the TCSM prototype but not as Jaw material. The reasons for including Mo in this treatment are first its usage as basis for the new MoCuCD, MoGR and MoGRCF composites (presented in Chapters 8, 9 and 10), and second because its higher robustness with respect to Tungsten Heavy Alloys, observed in the HiRadMat experiment results in Chapter 11, increased its appealing as Jaw material for Tertiary Collimators.

Summarizing, the materials are:

- Carbon Fiber Carbon (CFC) composite;
- Graphite
- Tungsten Heavy Alloy (Inermet180)
- Dispersion Strengthened Copper (Glidcop AL-15)
- Molybdenum

### 4.1.1 Carbon Fibres Carbon composites

Carbon Fibre Carbon composite (CFC) is made by Carbon Fibres embedded into a graphitic matrix, giving a very light carbon materials that has outstanding mechanical and thermal properties with respect to pure graphite. It has been developed initially for Formula 1 cars brake discs, and is actually widely used in sports cars and other special equipment such as high-performance tennis rackets. Regarding the collimators application, it has been chosen for the Primary and Secondary LHC Collimators because of its good resistance to high thermal shocks and for its low coefficient of thermal expansion that ensure a high geometrical stability, as required by the design specifications discussed in the Paragraph 3.3.

The CFC used for collimators is a commercial material labelled AC-150K: it is a 2D composite with short Carbon Fibres in a graphite matrix, the Carbon Fibres being randomly disposed to create a layer in the yz plane; several layers are bundled over the thickness in the x directions. In this way it is possible to obtain an orthotropic material with equal properties in the layer plane yz and a different behaviour in the x direction transversal to the layers (see Figure 4.1). However, the bars used for the LHC Collimators have been also extruded to increase the final density, giving a different Flexural Strength between the two planar directions, as confirmed by the measurements of Flexural Strength made at CERN Mechanical Laboratory (29) presented, together with the other thermo-physical and mechanical properties of CFC (7), in Table 4.1 [1].

[1] Values measured using the equipment described in Paragraph 6.4.1 along the three directions of the CFC bar: $R_{Fl,x}$ has not been reported because it was below the measuring range of the equipment.

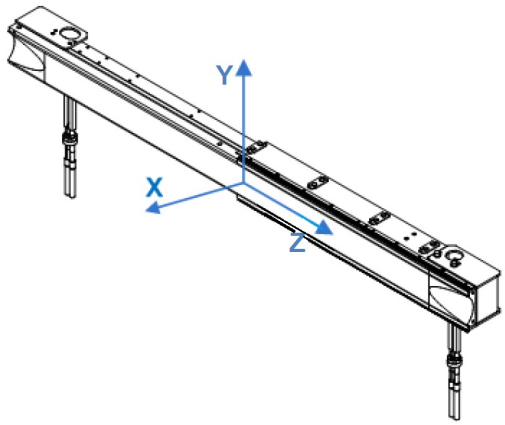


**Figure 4.1:** Orientation of Carbon Fibre Carbon Composite with respect to Jaw Assembly.

**Table 4.1:** Carbon Fibre Carbon Composite $AC-150K$ properties along the three principal directions in Figure 4.1 (6) (7).

| **Property** | **Unit** | **Values** | | |
|---|---|---|---|---|
| Density | $[g/cm^3]$ | 1.656 | 1.656 | 1.656 |
| Specific Heat | $[J/KgK]$ | 780 | 780 | 780 |
| Young Modulus | $[GPa]$ | $E_{xx} = 5$ | $E_{yy} = 77$ | $E_{zz} = 77$ |
| Shear Modulus | $[GPa]$ | $G_{xy} = 2.98$ | $G_{xz} = 2.98$ | $G_{yz} = 33$ |
| Poisson's Ratio | $[-]$ | $\nu_{xy} = 0.158$ | $\nu_{xz} = 0.165$ | $\nu_{yz} = 0.165$ |
| Flexural Strength | $[MPa]$ | $R_{Fl,x} = [-]$ | $R_{Fl,y} = 106.0$ | $R_{Fl,z} = 155.9$ |
| Coefficient of Thermal Expansion | $[10^{-6}K^{-1}]$ | $\alpha_x = 8.75$ | $\alpha_y = -1.55$ | $\alpha_z = -1.55$ |
| Thermal Conductivity | $[W/mK]$ | $k_x = 68$ | $k_y = 218$ | $k_z = 218$ |

### 4.1.2 Graphite

Polycrystalline extruded Graphite is the second carbon material actually used for Primary Collimators Jaws: the commercial name of the material, proposed as die for continuous casting of metals, is Graphite R4550 produced by SGL CARBON GmbH, (30), whose properties are reported in Tables 4.2 and 9.1. The values have been measured at CERN during 2006 (7). The material is obtained by extrusion of graphite powders and sequential thermal treatment to promote graphitization and enhance thermal and mechanical properties (31): a more detailed description of graphite production, structure and properties will be presented in Paragraph 9.1.2 along with the R&D of graphite reinforced Molybdenum Carbide composite.

Analysing the values of Table 9.1 it is clear as polycrystalline graphite has overall lower properties with respect to CFC, however its low density combined with the low CTE give anyway to the material a very good robustness, as confirmed by the value of TSNI in Table 4.2 presented in next Chapter. For those reasons CFC has been preferred to Graphite R4550 as Primary Collimator jaw material.

### 4.1.3 Tungsten Heavy Alloys

Inermet180 is the commercial name of the Tungsten Heavy Alloy (Plansee, (32)) used for Tertiary Collimators Jaws. The material exhibits good thermal and mechanical properties combined with a high density and average Z number: for those reasons it is actually used as particles absorbers to stop the last shower of particles before sensitive equipment.

The thermal, mechanical and physical properties of Inermet 180 measured at CERN EN/MME and at AIT (Austrian Institute of Technology) are listed in Table 4.2, the values beiing at Room Temperature (RT). The evolution of the thermal properties as a function of the Temperature are shown in Figure 4.3.

The material is obtained by liquid phase sintering of W, Cu and Ni powders in the nominal composition of $95\%_w\ W$, $3.5\%_w\ Ni$ and $1.5\%_w\ Cu$: the big W grains, approximately 100 $\mu m$, are surrounded by the Ni-Cu phase that melts at $1400°C$ and infiltrates the voids between adjacent W particles, providing the necessary thermal and electrical continuity to the material.

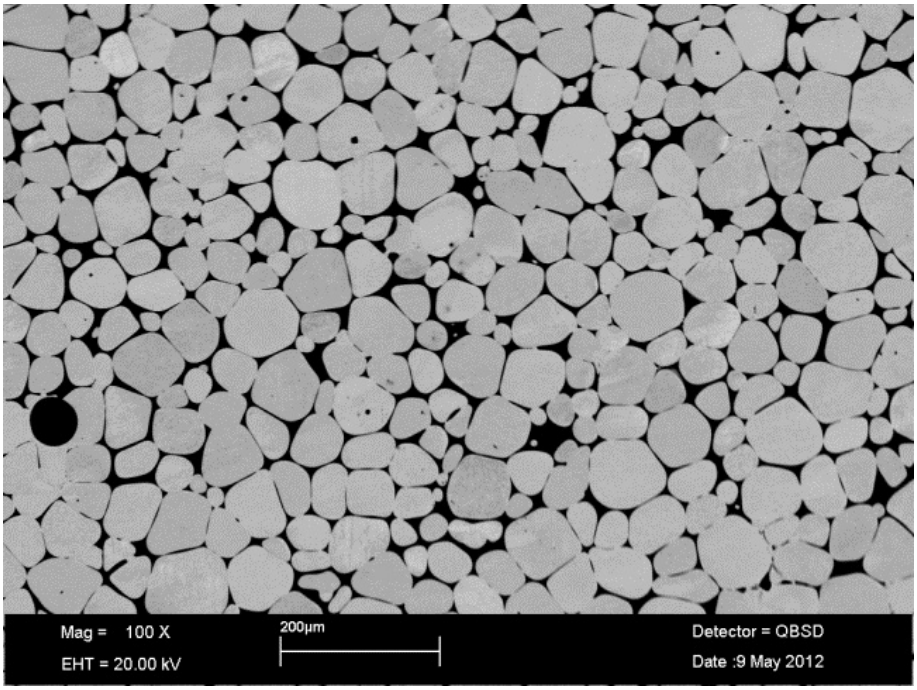


**Figure 4.2:** QBSD image at low magnification of Inermet180 microstructure. The Tungsten grains are clear while the Ni-Cu phase appears black.

In addition, the presence of Ni increases locally the diffusion of W atoms through the grain borders providing a partial adhesion of the W particles itself giving mechanical strength to the composite (33),(34).

Those effects have been confirmed by the SEM analysis carried out at CERN (Figure 4.2) and by the thermal characterization carried out at AIT presented in Figure 4.3.

### 4.1.4 Dispersion Strengthened Copper

Glidcop $AL-15$ is the commercial name of the Alumina Strengthened Copper Alloy produced by SCM Metals that is one of the candidates for the Secondary Collimators jaws. The peculiarity of the material is that, unlike the large majority of Copper alloys, it is obtained by powder metallurgy (35) instead of casting or electrolytic methods: the process starts from a pre-alloyed powder of Cu having small concentration of Al ($\%_w$ $Al = 0.15\%$, corresponding to $\approx 0.23\%_w$ of $Al_2O_3$), mixed with fine Copper Oxide powder that solid state react with Al to form a fine dispersion of nano-metric alumina particles inside Cu grains, as shown in Figure 4.4.

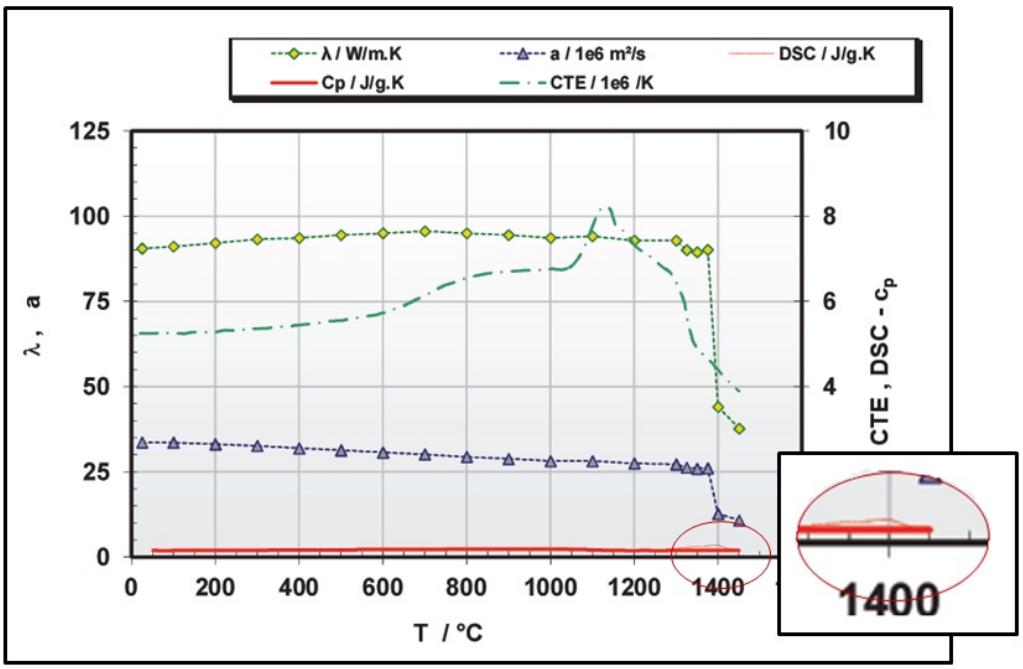


**Figure 4.3:** Thermal properties of Inermet 180 as a function of the temperature. The magnified zone indicates the melting of the Ni-Cu phase in the Differential Scanning Calorimetry (DSC) plot.

The material is then compacted and cold worked by extrusion to reduce Cu grain size in order to enhance the elastic limit: the alumina particles block the movement of dislocations and avoid the grain growth at high temperatures, permitting to maintain high mechanical properties at high temperatures while keeping thermo-physical properties very close to the ones of pure Copper (36).

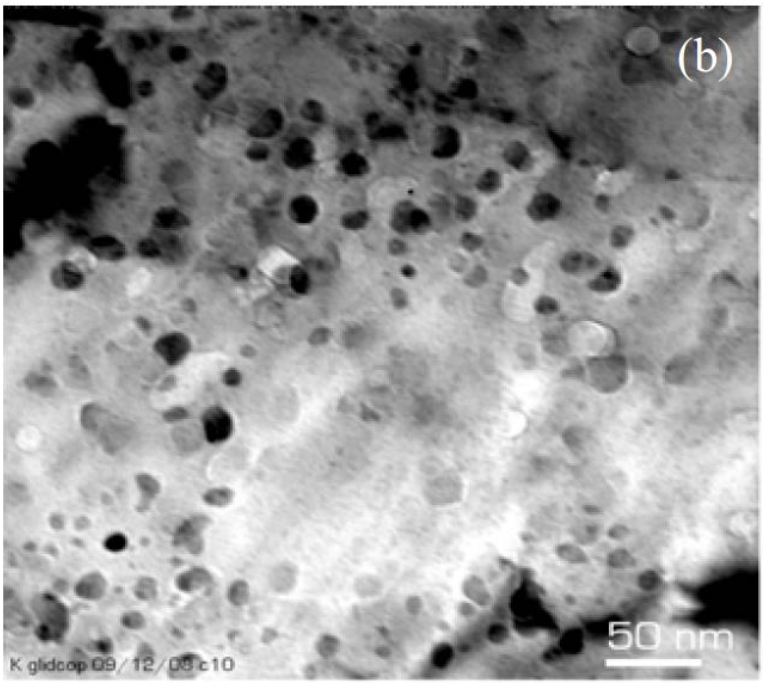


**Figure 4.4:** Transmission Electron Microscopy of Glidcop $AL-15$: the very small and uniformly dispersed alumina particles are clearly visible.

Glidcop has been initially chosen as jaw material for Hi-Lumi LHC Collimators, however its density has been determined to be too high for secondary Collimators and new composite materials have been indicated as more promising jaw material (37).

Glidcop remains a top choice for supporting the jaw active material because of its capability to maintain high Yielding Strength even after the brazing process at $780^oC$, assuring a good thermal dissipation of the heat generated on the jaw.

### 4.1.5 Molybdenum

Molybdenum deserves a description even if it is not used for the Collimators jaws because of two main reasons: it is already used for the Jaw stiffeners of the newly in-

troduced Collimators design and is one of the main components of the newly introduced composites that will be described in the present thesis work.

The Mo used for LHC Collimators stiffeners is commercially pure, cold worked Mo produced by Plansee: the material is obtained by sintering of pure Mo powder at high temperature (over $2000^oC$), and sub-sequential cold working up to 50% reduction in thickness.

The microstructure is made by elongated Mo grains with few small inclusions (mostly $Mo_2C$) that are finely dispersed inside the Mo matrix, see Figure 4.5. This situation permits to obtain a very high elongation to fracture in the cold working direction with a completely ductile behaviour, while maintaining adequate properties in the transversal direction.

As made for Inermet180, Molybdenum has been characterized at CERN in terms of thermal, physical and mechanical properties in order to confirm the suppliers material's datasheet (32).

Molybdenum is used as Stiffener in Hi-Lumi LHC Collimators because of its high mechanical properties and high thermal stability, but recent results enlighten the possibility to use it as alternative to Inermet180 in Tertiary Collimators. The summary of Mo properties at RT are reported in Table 4.2 in next Chapter.

## 4.2 BID Materials Figures of Merit

The present Paragraph explain the different parameters (or Figures of Merit, FoM) used to benchmark BID materials. The FoM have been developed for the specific case of LHC Collimators but are of course valid for any BID.

In fact BID materials are to combine peculiar properties in order to interact with the incoming particle beam (in the following, beam) without being damaged, because as mentioned in Paragraph 3.3.3 during the beam matter interaction there are a large number of different physical phenomena that must be understood and quantified in order to benchmark the materials.

In order to classify and rank relevant materials against the key requirements summarized in previous paragraphs, five main FoM were identified and used for new materials benchmarking (38): those FoM cannot cover all the aspects discussed in the aforemen-

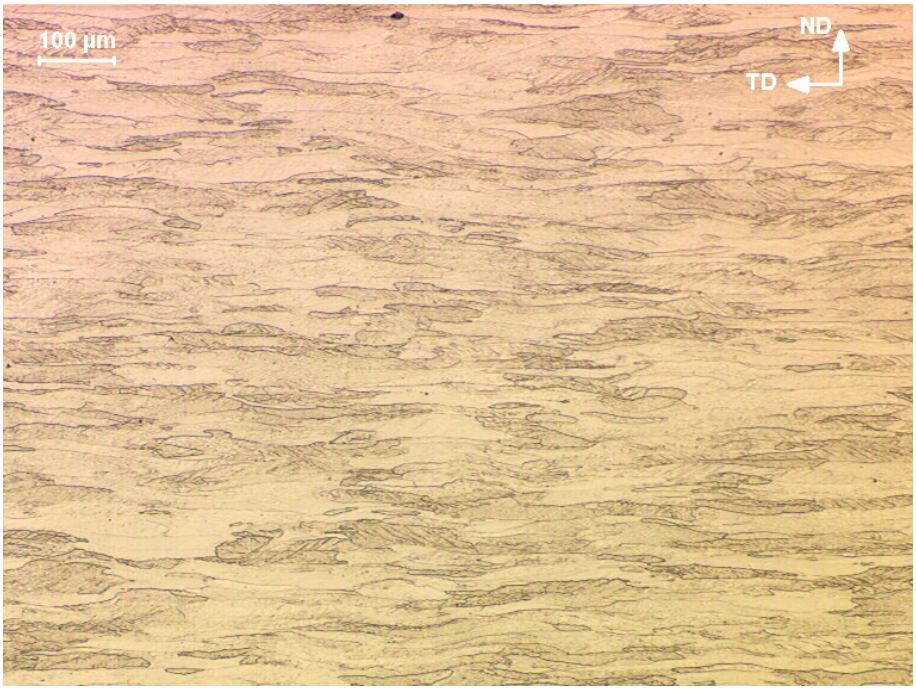


**Figure 4.5:** Optical Microscopy of Molybdenum microstructure: the grains are elongated and there are no visible pores and inclusions.

tioned LHC Collimators design constraints, but are to give a valuable indication of the materials behaviour for the more general BID application.

The definition of the FoM have been modified during the years adding the density in the Steady-state Stability Normalized Index, while some values already reported in previously cited works (38) have been substituted with new, more reliable measurements, like the ultimate strength of CFC that has been recently measured at CERN with the flexural test fixture, see Paragraph 4.1.1 and 6.4.1).

In the case of anisotropic materials, like the orthotropic CFC shown in Table 4.1, there is a significant reduction of thermal and mechanical properties along the transversal direction. In order to give a more realistic representation of the material behaviour the value of CTE used for calculating the Steady-state Stability Normalized Index (SSNI) and the Transient Thermal Shock Normalized Index (TSNI) is a ROM between the three principal directions.

- Density $\rho$ (and Atomic Number Z). It provides a rough indication of the material cleaning efficiency as discussed in Paragraph 3.3. The higher the density (and

atomic number) the better the cleaning efficiency but also the more concentrated energy deposition with the consequences described in Chapter 11. This value depends strongly on the Collimator's family, being as low as possible for Primaries ($< 2\ g/cm^3$), intermediate for Secondaries ( $2.5\ < \rho\ < 5.5\ g/cm^3$), and sufficiently high for Tertiaries ($> 10\ g/cm^3$).

- Electrical conductivity. This parameter is not mandatory for BID in general but is of paramount importance for LHC Collimators and therefore has been included in the FoM. For LHC Collimators the electrical conductivity has to be maximized in order to limit RF impedance, as discussed in paragraph 3.3.4 . However, recent calculations performed at CERN RF Group showed that is not necessary to have a very good conductor as jaw material, if it is coated with a sufficiently thick conductive support that accommodates the RF electromagnetic field.

- Steady-state Stability Normalized Index (SSNI). This parameter, defined as $k/\alpha\rho$ (where k: Thermal Conductivity, $\alpha$: Coefficient of Thermal Expansion, $\rho$: Density), expresses an indication of the ability of the material to maintain the geometrical stability of the jaw when submitted to steady-state losses. Density has been added to the formulation to express the effect of the more localized and concentrated energy deposition in dense matter.

- Transient Thermal Shock Normalized Index (TSNI). Parameter defined as $R(1-\nu)c_p/E\alpha$ (where R: ultimate tensile strength, $\nu$ Poissons ratio, $c_p$ specific heat, E Youngs Modulus). TSNI is correlated to the highest absorption rate of impacting particles before the onset of mechanical damage. It's worth to mention that dynamic failures require specific materials models to be correctly analysed: those tools, together with their experimental validation, will be presented in Chapter 11.

- Melting Temperature $T_m$. It provides an indication of the maximum temperature the material can achieve before being permanently damaged by melting. Note that for composite materials (or pseudo alloys like Inermet180) this number is always referred to the lower melting phase: for Inermet180 $T_m \approx 1400°C$, even if the $95\%_w$ of the material is composed by Tungsten which melts at $3400°C$.

This assumption might seem drastic but has been confirmed experimentally by the post impact damage on Inermet180 samples, as shown in Chapter 11.

## 4.3 Benchmarking of present Collimator materials

The presently used Collimator materials have been studied and their FoM have been evaluated to give an overview of their effectiveness as BID materials. In the case of orthotropic materials, like CFC, the values reported of $k$, $CTE$, Tensile Strength and Poisson's Ratio are a ROM calculation over the three principal directions reported in Table 4.1 in order to give a simplified indication of the behaviour all over the three dimensions.

**Table 4.2:** Physical and mechanical properties and Figures of Merit of Carbon Fibre Carbon Composite (CFC), Graphite R4550, Inermet 180, Glidcop and Molybdenum. Values of $k$, $CTE$, Tensile Strength and Poisson's Ratio are a ROM calculation for CFC are obtained by a ROM calculation over all the three principal directions.

| **Property** | **Unit** | **CFC** | **R4550** | **Inermet180** | **Glidcop** | **Mo** |
|---|---|---|---|---|---|---|
| Density | $[g/cm^3]$ | 1.65 | 1.83 | 18 | 8.93 | 10.22 |
| Atomic Number (Z) | $[-]$ | 6 | 6 | 70.83 | 29 | 42 |
| Radiation Length $\chi_0$ | $[cm]$ | 12.25 | 12.25 | 0.35 | 1.47 | 0.98 |
| Melting Temperature | $[°C]$ | 3650 | 3650 | 1400 | 1083 | 2623 |
| Thermal Conductivity | $[W/mK]$ | 168 | 100 | 90.5 | 365 | 138 |
| CTE | $[10^{-6}K^{-1}]$ | 1.88 | 4.29 | 5.25 | 16.6 | 5 |
| Specific Heat | $[J/KgK]$ | 780 | 780 | 150 | 391 | 251 |
| Young's Modulus | $[GPa]$ | 53 | 11.5 | 360 | 130 | 330 |
| Tensile Strength | $[MPa]$ | 87 | 40 | 660 | 413 | 660 |
| Poisson's Ratio | $[-]$ | 0.16 | 0.15 | 0.29 | 0.33 | 0.36 |
| SSNI | $[Wm^2/g]$ | 54.1 | 12.7 | 0.96 | 2.5 | 2.7 |
| TSNI | $[J/g]$ | 570.8 | 537.5 | 37.4 | 50.1 | 64.7 |
| Electrical Conductivity | $[MS/m]$ | 0.14 | 0.077 | 8.6 | 53.8 | 19.2 |

Table 4.2 indicates the values of all the Figures of Merit for the aforementioned materials (CFC, Graphite R4550, Inermet180, Molybdenum and Glidcop): comparing the TSNI of CFC and Graphite R4550 with those of metallic materials it is clear how it is not possible for a metallic material to reach the robustness (TSNI) of CFC,

at least along the Longitudinal direction. The reasons are the very low density and CTE of Graphite that give to the material a superb thermal shock resistance, but the low density also limits the cleaning efficiency in steady state conditions and the low electrical conductivity leads to high RF Impedance. This material remains the best choice for Primary Collimators but is limiting the machine when used in Secondary Collimators. The material initially proposed for the Secondary Collimator Prototype TCSM, Glidcop, has optimal electrical properties but is now considered too dense to act as a Secondary Collimator: the energy deposition is way more concentrated with respect to CFC (see the radiation length values in table 4.2) and the material expansion becomes more important, as discussed in previous Chapter. This effect reflects itself in TSNI parameter, that is one order of magnitude lower than for CFC.

A single material that maximizes all the FoM at the same time does not exist: in fact there is the need for ceramics typical properties (low density, low CTE, high melting point and Thermal Stability) and for metals common properties (electrical conductivity, mechanical strength). The only way to overcome such limitations is to develop ad-hoc composites that are to combine the good qualities of metals and ceramics in a single form.

# 5

# Analytical Modelling of Composite Materials Properties

In this chapter the main mathematical and experimental tools used for the thesis work are presented and discussed.

The study of new materials is always delicate because there are not well established standards to guide the characterization work and the results interpretation, therefore many different techniques were used to have the maximum amount of information. Many assumptions made in the preliminary phase of the material design have then been validated or rejected by the following experimental results, leading to a dynamically evolving and not always linear material's R&D roadmap.

## 5.1 Introduction to Composite Materials

There are infinite numbers of composite materials that use different matrix constituents, different reinforcement materials having different shapes (39); a general and not exhaustive list of the different composite materials categories is:

- Polymer matrix composites (PMC)
- Metal matrix composites (MMC)
- Ceramic matrix composites (CMC)

The more used composites are PMC due to their light weight and the low cost of both raw materials and production cycle, they can be filled with any kind of reinforcement. As stated in Chapter 3.3 it is not possible to use highly degassing materials (such as polymers) in the LHC Beam Vacuum environment, therefore this class of material has not been studied in the present work.

MMC (40) are more difficult to produce and the raw materials are usually more expensive than for PMC: while in PMC the matrix phase is usually initially in the liquid form so that it infiltrates the voids between reinforcement particles or fibres and only after it solidifies or react becoming solid, for metallic matrix composites it is often more difficult to melt the metallic matrix (apart from very low melting metals such as Aluminium) due to technological limits of used furnaces and equipment. In that case the material compaction has to rely entirely on solid state diffusion (Solid State Sintering, SSS) that is a slower and more delicate process than Liquid Phase Sintering (LPS). However, such composites keep many important features of metallic materials, such like high thermal conductivity, low thermal expansion, high melting point (depending on the matrix phase), high stiffness, electrical conductivity and, to a certain extent, ductility. This family of composite materials has been extensively studied for thermal management applications where specific thermal expansions are needed, for example to match the Silicon thermal expansion in computer microelectronics (41).

A third process to produce MMC is composed by prior compaction of dry reinforcement followed by infiltration by the liquid matrix: this process is called Liquid Infiltration, and can be done only when dealing with highly fluid liquid metals having a relatively low melting point. The drawbacks of this process are the difficulties in obtaining a pore free and homogeneous material and the limited dimensions of produced pieces.

Finally, CMC are more expensive (and technological challenging) materials that use a ceramic phase as matrix and, usually, a second ceramic phase as reinforcement. With commercially available technologies this kind of composites can only be produced by Solid State Sintering because the temperatures needed to melt ceramics (usually beyond $2000^oC$) exceed the application range of the large majority of furnace materials. Ceramic matrices give to the composite the highest hardness and chemical stability, combined with a high melting temperature and thermal stability. Cons are their high

brittleness and their very low electrical conductivity: for those reasons the main application of CMC are cutting tools, where the CMC are used as small inserts screwed or bonded to a metallic support. CMC might be the best option for the LHC Collimators application if the ceramic matrix is capable to conduct current, that is the case of Molybdenum Carbide used in the newly developed materials (see Chapter 9).

The reinforcements might in principle be of any kind of material, the most commonly used reinforcements being ceramics in forms of particles or fibres due to their high stiffness, strength and lightness. The fibres might be short, long or continuous, the two more widely used being glass fibres and carbon fibres (as used in present work).

The parameters needed to correctly define a composite material are:

- Quantity of reinforcement (usually expressed in Volume percentage $\%_v$ or Volume fraction $f_V$);
- Shape and dimensions of reinforcement;
- Relative orientation of reinforcement (for non-spherical particles only) usually defined with respect to production geometry (for example in pressed materials the orientation is referred to the direction normal to pressing direction);
- Quality of the matrix-reinforcement interface: a chemical bonded interface gives usually higher adhesion (and higher final properties of the composite) with respect to non chemical interfaces. Bonding elements might be added to the composite especially to provide a chemical bond (Si addition to Al-Graphite composite to form SiC at the interface (42)).
- Internal Structure of reinforcements: in certain cases the reinforcements might have a fair complex internal structure, or they might have been coated to create an intermediate reaction layer to assure a chemical bond or a better space filling.
- Porosity: all composite materials made by powder blending have a certain amount of residual voids. The amount of pores has obviously to be minimized in order to achieve the best final properties, apart from the case of foam materials where the porosity is a key feature of the material.

With the knowledge of all the reinforcement's parameters and of the constituent's properties it is possible to estimate the final properties of composite materials by adequate analytical methods under precise assumptions (43). The approximations usually proceed from ideal conditions, i.e. optimal boundary, ideal reinforcement distribution (very small number of contacts of the reinforcements among themselves) and no influence of the reinforcement on the matrix (independent behaviour).

However, in reality a strong interaction arises between the components involved, so that these models can only indicate the potential of a material and provide design guidelines during materials development. In the following various models having increased complexity are presented to allow the estimation of the properties of interest for LHC Collimators Materials.

## 5.2 Physical Properties

The first and most important physical property of a composite material is its density ($\rho$, $[g/cm^3]$), followed by the atomic number ($Z$, a-dimensional) and by the radiation length ($\chi_0$, $[cm]$), that defines the ability of the material of stopping incoming particles (inversely proportional to $\rho$ and $Z$). A fourth physical property of interest is the specific heat ($c_p$, $[J/KgK]$) that due to its strong connection with the thermal properties of the materials have been described in Paragraph 5.4.

All this properties are mass only dependant, so we can assume that each constituent will give a contribution proportional to its volume fraction: this simple model is the well-known Rule Of Mixture Model (ROM) that weighted means the properties ($P_i$) of the single components (m: matrix and r: reinforcement, in the case of a two components material) to obtain the property of the composite ($P_{ROM}$):

$$P_{ROM} = f_{v,m} * P_m + f_{v,r} * P_r \tag{5.1}$$

where $P$ is $\rho$, $Z$, $\chi_0$ or $c_p$.

### 5.2.1 Electrical Properties

The electrical properties (i.e. the electrical conductivity $\sigma$ in $[MS/m]$) of composite materials depend on the nature of the constituents: usually in MMC the matrix is conductive while the reinforcement is a ceramic insulator (diamonds, SiC, $Al_2O_3$, ecc)

or a low conductor like graphite or carbon fibres; the situation in CMC is different because the matrix is usually not conductive and the final conductivity relies on the conductivity of the reinforcement (if any).

In the situation of insulating particles embedded into a conductive matrix, the ROM model would tend to overestimate the effective conductivity because of the hypothesis of independent behaviour of matrix and reinforcement that is not true because the current flow is limited by the effective geometry of the conductive phase. An empirical model that expresses the electrical conductivity as a power function of the reinforcement volume fraction has been obtained at EPFL for diamond reinforced MMC based on very good metallic conductors (Cu, Ag, Al) (44):

$$\sigma_c = \sigma_m * f_{v,m}^{1.57} \tag{5.2}$$

On the other hand in CMC the absence of an isotropic conductive phase (like in MMC) hampers the usage of already presented simple models such as 5.1 and 5.2. For that reason we considered in first approximation the ROM model and the MMC empirical model as upper and lower limit of the CMC conductivity. A more detailed description of the electrical conductivity of Carbon Fibres reinforced composites will be given in Chapter 10.

## 5.3 Mechanical Properties

In order to conveniently define the mechanical properties of a composite material, it is better to separate the elastic behaviour (that can be predicted with relatively good accuracy) and the non-elastic behaviour comprehending plasticity and fracture, which are governed by the defects statistics and have a more complex mathematical treatment that not always leads to acceptable results.

The entire elastic tensor (45) of a homogeneous, continuous and isotropic solid body can be expressed by the linear combinations of two independent constants, that usually are the Young's Modulus (E, in [GPa]) and the Poisson's ratio ($\nu$, a-dimensional and valid between 0 and 0.5) or the Young's Modulus E and the Shear Modulus (G, in [GPa]).

The isotropy hypothesis is valid for all composite materials that do not exhibit a preferential orientation of the reinforcement: in our case it applies only to CuCD and MoCuCD.

In all other studied materials the relative orientation of the matrix and the reinforcement brings to an orthotropic material having different properties between the Hot-Pressing direction and the plane normal to the pressing direction, like for CFC (see Paragraph 4.1.1), or for MoGR and MoGRCF, where the recrystallization of graphite plays an important role in the material anisotropy (see Chapter 9). For those materials 5 independent elastic constants are needed to precisely define the entire elastic tensor.

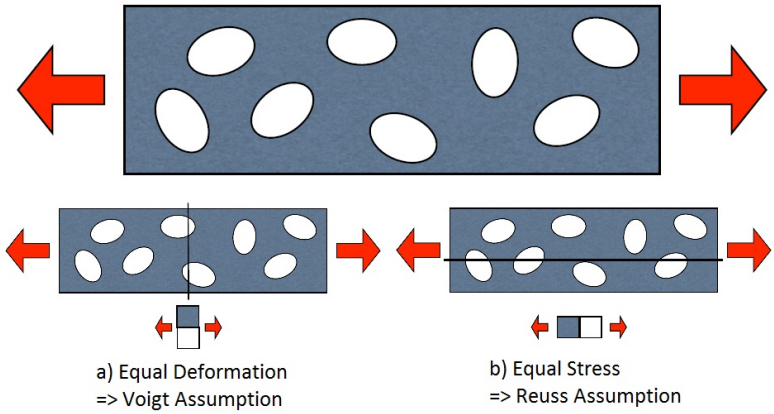


**Figure 5.1:** Schematics of Voigt (Equal Strain) and Reuss (Equal Stress) assumptions for particulate reinforced composite.

Looking at the reinforcement distribution of Figure 5.1 we can immediately define two limit cases: if we consider the a) case, in which the body has been ideally cut perpendicularly to the load application, to conserve the continuity of matter the deformations of the two phases must coincide in every point (assumption of Voigt), while if we consider the b) case to assure the force balance the stresses on the two phases must coincide. The mathematical treatment is very simple and is not worth reporting here, summarizing we can express the Young's Modulus in two ways:

$$E_V = f_{v,m} * E_m + f_{v,r} * E_r \tag{5.3}$$

$$E_R = (f_{v,m}/E_m + f_{v,r}/E_r)^{-1} \tag{5.4}$$

that can be considered respectively as the upper and lower limit of the isotropic composite, as shown in Figure 5.2. The third line is the Hill model that simply makes an average between the Voigt and the Reuss models.

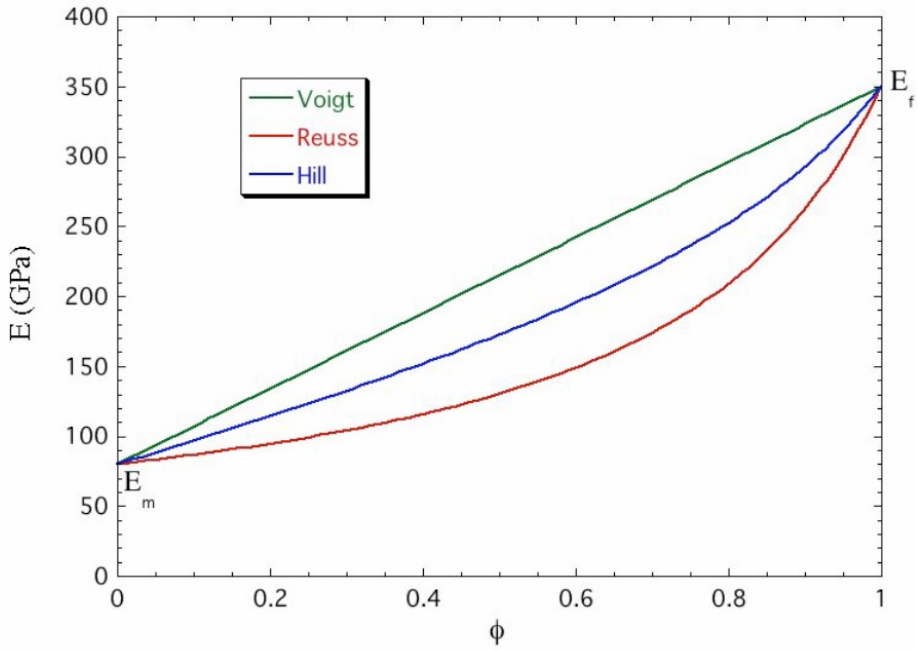


**Figure 5.2:** Comparison of Voigt, Reuss and Hill models for Al-SiC composite as a function of the SiC fraction ($\theta$).

Analogous calculations can be done with the Shear Modulus $G_i$ to obtain the second independent variable needed to define the entire stress tensor.

### 5.3.1 Elastic Constants of Orthotropic Materials

The precise definition of the entire elastic tensor of an orthotropic material requires the identification of 5 independent variables ($C11$, $C12$, $C13$, $C33$, $C44$) as extensively discussed in past master thesis work (46); the material is assumed having a layered geometry oriented as presented in Figure 5.3.

The model proposed reconstructs the composite materials elastic constants starting from the isotropic constants of the single components by imposing opportune boundary conditions. Once obtained the elastic constants it is possible to calculate the Young's Modulus and the Shear Modulus along any direction.

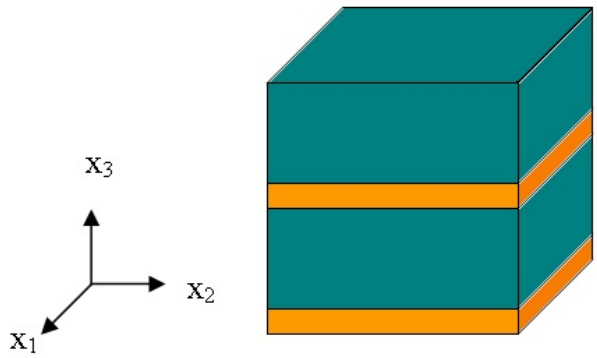


**Figure 5.3:** Axis Definition for an orthotropic materials, here simplified as a layered structure.

Model Hypothesis:

- Homogeneous, isotropic layers having same known $E_i$ and $G_i$, that allow calculation of $C11$ and $C44_i$ constants by the following equations:

$$C11_i = \frac{E_i * (1 - \nu)}{(1 + \nu) * (1 - 2\nu)} \tag{5.5}$$

$$C44_i \equiv G_i \tag{5.6}$$

- Perfect, planar interfaces without phase mixing;

Boundary Conditions:

- $C11_c$: Reuss combination of $C11_i$ (to assure stress continuity);
- $C44_c$: Reuss combination of $C44_i$ (to assure stress continuity);
- $C13_c$: Voigt combination of $C44_i$ (to assure strain continuity);
- $C33_c$: Voigt combination of $C11_i$ (to assure strain continuity).
- $C12_c$: Arbitrarily assumed $\equiv$ to $C44_c$ (46),

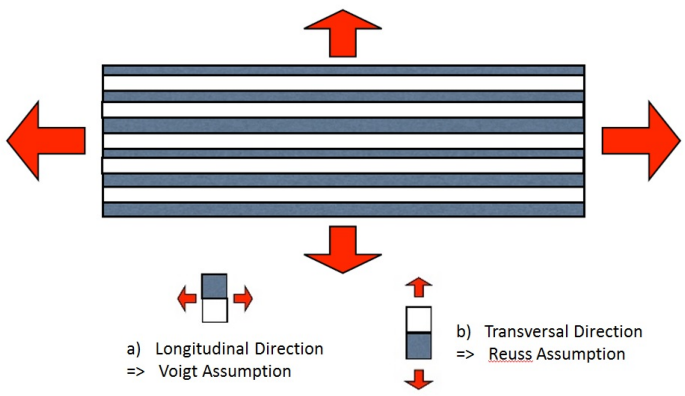


**Figure 5.4:** Schematic representation of the Voigt and Reuss Models applied to Orthotropic materials.

Using the composite elastic constants calculated by we can define the Elastic Modulus along fibres direction (in our case is the plane normal to the pressure application) and in the normal direction as longitudinal ($E_L$) and transversal ($E_T$) Modulus as expressed in equations 5.7 and 5.8 below.

$$E_L = \frac{C33 * (C11^2 - C44^2) + 2 * C13^2 * (C44 - C11)}{C11 * C33 - C13^2} \tag{5.7}$$

$$E_T = \frac{C33 * (C11 - C44) - 2 * C13^2}{C11 + C44} \tag{5.8}$$

In the present work, which is a preliminary $R\&D$ investigation, we can rely on the Elastic Modulus evaluation along the two principal direction to compare (in first approximation) the behaviour of the newly introduced orthotropic composites.

### 5.3.2 Strength and Failure of Composite Materials

As anticipated the prediction of the composite material strength and failure is not trivial and relies strongly on the relative properties between the constituents.

The materials of interest for LHC Collimators are mainly MMC reinforced with diamonds (CuCD and MoCuCD) and CMC reinforced with fibres and graphite (MoGR and MoGRCF), so we can expect to have always a brittle behaviour with limited plasticity, in the first case because the content of diamonds is so high that it does not

allow Cu to plastically deform, in the second case because the ceramic constituents don't allow plastic deformation by dislocation movement.

It is well known that for brittle materials the fracture appears always on a "critical defect", where the critical defect is a defect that provokes a tri-axial stress intensification high enough to overcome locally the material's resistance (47). In MMC the tri-axial stress intensification is also enhanced by the presence of particle clusters formed by a non homogeneous particle distribution in the material (48) that must therefore been kept under control to avoid drastic reductions in mechanical properties. In addition, as stated in the introduction of this Chapter, our composites obtained by SSS have always a certain amount of closed porosity that acts mechanically as a defect distribution.

The only way to correctly treat the effect of porosity is by using statistical means such as the Johnson-Holmquist Model (49) for brittle materials adding the effect of the limited inter-facial strength. The model can be implemented in hydrodynamic codes such as Autodyn or LS-Dyna (50) as shown in Chapter 11 in the case of the Johnson-Cook model implementation for Inermet180.

Since these models are all based on a llarge amount of experimental tests it has not been possible to apply them to the composites of interest, therefore in the present work the strength of the composites is only qualitatively estimated by evaluating the porosity content of the composite: the more porous the composite material the lower the strength.

## 5.4 Thermal Properties

The thermal properties we are interested in are: thermal conductivity (k, $[W/mK]$), coefficient of thermal expansion (CTE, also expressed as $\alpha$, $[K10^{-1}]$), and (volumetric) specific heat ($c_p$, $[J/KgK]$).

### 5.4.1 Thermal Conductivity

The thermal conductivity $k$ expresses the ratio between the amount of heat that passes through a solid body and the temperature difference at the body's extremities: this is a transport property that depends strongly on the heat transfer mechanism, that is only phononic for ceramics (absence of free electrons) and phononic and electronic

for metals. The composite final properties are a combination of the two mechanisms balanced by the reinforcement-matrix bond.

Furthermore, since it is a transport property the relative reinforcement orientation with respect to the thermal flux direction plays an important role, as is the case for MoGRCF.

For isotropic composite materials the parameters that play a role in establishing the thermal transport inside the microstructure are:

- Shape of the particles,
- Dimensions of the particles,
- Volume fraction of particles,
- Thermal conductance of the interface (or thermal resistance).

In the case of orthotropic materials having non spherical particles with a preferential orientation (like MoGRCF) we have also to consider the:

- Distribution of fibres orientation

When using the ROM model we assume to have a perfect interface between the two phases (which transmits without resistance the heat) and we disregard the effect of diamond particle size, shape and orientation.

Those effects are important in the real particle reinforced composites because the interface is not perfect and acts as a thermal resistance: since reducing the particles dimensions increases the surface/volume ratio, and therefore the total thermal resistance along the material, using smaller particles results in lower values of thermal conductivity.

Let's take as example the simple system Cu-diamond of CuCD, well studied in past works (51): the low wetting and the low chemical affinity of the diamond surfaces with Cu results in a weak inter-facial bonding, that reflects itself in a lower value of measured thermal conductivity with respect to the ROM estimation, that is mathematically expressed as a thermal resistance at the interface. If we assume a simple model made of sphere particles homogeneously distributed in a continuous matrix with ideal heat transfer at the interface, we can calculate an effective thermal conductivity

of the composite by using the original theory of Maxwell (52): this method tends to overestimate the effective thermal conductivity because disregards the effect of the reinforcement size and of the interfacial thermal resistance. To overcome this limitations an improvement of Maxwell's model has been proposed by Hasselmann and Johnson (53) and is reported in equation 5.9:

$$k_c = k_m * \left( \frac{2\left(\frac{k_r}{k_m} - \frac{k_r}{a*h_c} - 1\right) * f_{v,r} + \frac{k_r}{k_m} + 2 * \frac{k_r}{a*h_c} + 2}{\left(1 - \frac{k_r}{k_m} + \frac{k_r}{a*h_c}\right) * f_{v,r} + \frac{k_r}{k_m} + 2 * \frac{k_r}{a*h_c} + 2} \right) \tag{5.9}$$

where:

$k_{c,r,m}$ = Thermal conductivity of composite, reinforcement and matrix respectively $[W/mK]$, $\%_{v,r}$ = Volume percentage of reinforcement, $a$ = Reinforcement spherical particles Diameter $[m]$, $h_c$ = Thermal conductance at the interface $[W/m^2K]$.

The main issue with the Hasselmann and Johnson model is that the value of thermal conductance $h_c$ depends strongly on the reinforcement - matrix interface (that also depends on the production process) and is not known for the large majority of applications: the model however permits to evaluate the thermal conductance by measuring the thermal conductivity of the composite. Using this method Yoshima and Morigami found a conductance value between Boron-doped Copper and Diamonds of $2.97*10^7 W/m^2K$ (51). It is worth noting that the thermal conductance at the diamond metal interface is the bottleneck of diamond metal matrix composites and that huge efforts are made to improve the interfacial heat exchange by adding carbide forming elements that provide a local chemical bond between the phases (54) (44).

The relatively simple mathematical treatment of the spheres reinforced composites thermal conductivity presented in last Paragraph is unfortunately not valid in the more general case of ellipsoidal particles having a preferential orientation, like in the case of MoGR composites or MoGRCF Composites. In order to handle such materials a more general approach, the so-called Kapitza Model, has been used instead of Maxwell model: the interfacial thermal resistance is now thought as the limiting case of heat transport across bulk phase separated by a thin, poorly conducting interphase region, the thermal conductance effect being represented by the thickness of the poorly conducting phase (defined as $\alpha_k$, the Kapitza radius) (55). Using this assumption is it possible to express the effective thermal conductivity of a known particulate reinforced material along every direction taking into account the ellipsoids relative direction distribution: while

the detailed mathematical treatment is omitted for simplicity and can be found in the literature (55), the results for the various composites calculated following the formulas given by Nana and Birringer will be presented in the chapters dedicated to the new materials R&D.

### 5.4.2 Coefficient of Thermal Expansion

Analytical expressions for describing the CTE of composites materials have been proposed by many authors: Turner (56) first established the fundamental bonding between the thermal expansion and the elastic properties of the different phases by taking into account the Bulk Modules $K_i$ of both matrix and reinforcement, as shown in Equation 5.10.

$$\alpha_c = \frac{\alpha_m * K_m * f_{v,m} + \alpha_r * K_r * f_{v,r}}{K_m * f_{v,m} + K_r * f_{v,r}} \tag{5.10}$$

The proposed Turner model is based on the hypothesis of ideal, perfectly bonded interfaces that transmit the strains and the stresses through the constituents; following works from Kerner (57) improved Turner's model by taking into account also the Shear Modulus when calculating the thermally induced stress distribution around the inclusions.

In addition to the Kerner model, that is the most suitable for metal-diamond materials and has been used in the present work, many different formulations have been proposed in last years to better describe specific composite materials families: here we present the formulation given in the most recent bibliography by Hsieh and Tuan (58).

$$\alpha_c = \alpha_m * f_{v,m} + \alpha_r * f_{v,r} + f_{v,m} * f_{v,r} * (\alpha_r - \alpha_m) * \frac{K_r - K_m}{\alpha_m * f_{v,m} + \alpha_r * f_{v,r} + 3 * K_m * K_r/(4 * G_m)} \tag{5.11}$$

### 5.4.3 Specific Heat

Since it is a mass only dependant property, the specific heat $c_p$ is correctly predicted by the ROM Model of equation 5.1.

# 6

# Composite Materials Characterization Techniques

In this Chapter the tools used to measure the materials properties are explained with the aim to provide a systematic approach to new materials characterization. The measurements are divided in non-destructive and destructive tests, the first being performed with as received plates while the second being performed after the plate cutting and the sample preparation. Unfortunately diamond based material samples cannot be machined by standard cutting tools but have to be prepared relying on the water jet cutting technique only, giving some limitations in samples shape and dimensions, as will be presented in Chapter 8.

## 6.1 Preliminary Non-destructive Analysis

### 6.1.1 Density

The first (and probably the most important) property to be verified on a newly produced composite sample is its density ($\rho, [g/cm^3]$), the measurement being made using an Archimedes principle balance: the sample is weighted both dry and while being submerged in water, by the difference between the dry and the submerged weight it is possible to calculate the specific weight, or density, of the sample.

We can define the samples compaction rate ($\rho/\rho_{th}$) from the ratio between the measured density $\rho$ and the theoretical density $\rho_{th}$ (calculated using 5.1): this value expresses the effectiveness of the sintering process and is a good indicator of the final

properties of the composites, especially when dealing with transport properties (electrical and thermal conductivity). Note that this method will not take into account the effect of the open superficial porosity due to water penetration from the surface. The Archimedes balance used in BrevettiBizz to measure the effective density of produced composites is shown in Figure 6.1 (59).

**Figure 6.1:** Achimedes balance used in BrevettiBizz to measure the composites density.

### 6.1.2 Electrical Conductivity

The second non-destructive analysis made on newly produced composite plates is the mapping of the superficial electrical conductivity ($\sigma, [MS/m]$): in addition to the average $\sigma$ (and its standard deviation) the mapping will give valuable information about the homogeneity of the produced composite plate. As explained in previous Chapter these materials are produced by powder blending and sintering, so there is always an intrinsic risk of powder segregation during the powder handling (for example when placing the blended powder in the graphite moulds) due to the significant difference in density, shape and dimension of the constituents.

Various techniques have been developed in BrevettiBizz to minimize the powder segregation and assure the best homogeneity of the produced composites, two examples are the powder blending made in various steps (adding small amounts of powders each step) and the powder insertion in the mould made relying on vibrating plates. However, changing the materials composition and/or the shape of the mould might have detrimental effects on the final material homogeneity, that have to be verified on

each newly produced composite plate. On top of that, variations of the temperature distribution during sintering might lead to density or composition non homogeneities in the plate even if starting with perfectly distributed powders, as will be explained for MoGRCF composites in Chapter 10

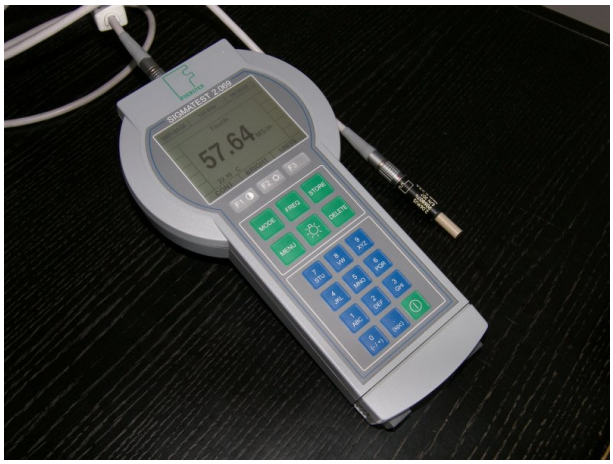


**Figure 6.2:** Foerster Sigmatest 2.069 used for mapping the superficial electrical conductivity. The used sensor is 6 mm diameter and the effective analysed area per measure point is about 8 mm in diameter.

The analysis have been performed using a Foerster Sigmatest 2.069 apparatus (60) (shown in Figure 6.2): it measures the superficial electrical conductivity by evaluating the variations induced by the body on the emitted RF electromagnetic field. The higher the frequency, the lower the effective penetration depth of the signal, thus changing the frequency allows to evaluate the electrical conductivity at different depths inside the sample. In addition, the electrical conductivity of the sample influences the penetration depth too, so it is possible to verify the investigated thickness by an empiric formula provided by the machine manufacturer. Finally, the instrument sensor is approximately 6 mm in diameter, while the effective investigated area is approximately 25% larger so each measured point has to be spaced by at least 10 mm to have meaningful measurements.

## 6.2 Samples Preparation

After the preliminary non destructive analysis the composite plate has to be cut to obtain the samples needed for the following analysis: while in diamond based composites

it is practically mandatory to use the water-jet technique (due to the diamond hardness) on soft, graphite based composites it is possible to use precision cutting machines to obtain the samples.


**Figure 6.3:** Samples of MoCuCD (8) cut by water jet: the cutting cone, the cut surface roughness and the cutting end residuals are clearly visible.

The water jet technique has also some drawbacks, the first being the cutting cone effect that leaves trapezoidal section samples, and the second being a pronounced roughness of the cut surfaces, that can be only partially removed by sand paper, and the third being a residual left by the cut endings (that is kept on non functional surfaces). If parallel surfaces have to be obtained, for example for CTE measurements, the samples can be milled by diamond tools taking care of avoiding samples overheating, like shown in Figure 6.4 for CTE samples.

It is also convenient to identify the spatial origin of each sample to verify materials non homogeneities (as already discussed) and reconstruct a map of materials properties and sample's orientations, like shown in Figure 6.5. Unfortunately, during water jet cutting it is normal that the samples detach and fall inside the water bath, so it is not possible to assign to each sample its correct position in the original plate.

**Figure 6.4:** Thermal conductivity (diameter 10 mm H4 mm), thermal expansion (16x4x4 mm) and specific heat (diameter 3 mm H1 mm) samples of MoCuCD.

After cutting and polishing, the samples have to be cleaned by ultrasound in alcohol, carefully dried and stocked. For SEM samples (see section 6.3.1 below) it is also mandatory to perform a degassing cycle inside desiccators to reduce the sample degassing inside the SEM vacuum chamber. Finally, the samples should always satisfy the dimensional tolerances foreseen in international standards for the specific tests.

## 6.3 Microstructural Analysis

The analysis and interpretation of the materials internal structure is of paramount importance for understanding the composite materials behaviour and improving its production process, therefore all composite materials of interest have been observed using optical microscopy, Scanning Electron Microscopy (SEM) and X-Rays Diffraction to characterize in the most exhaustive ways their internal structure.

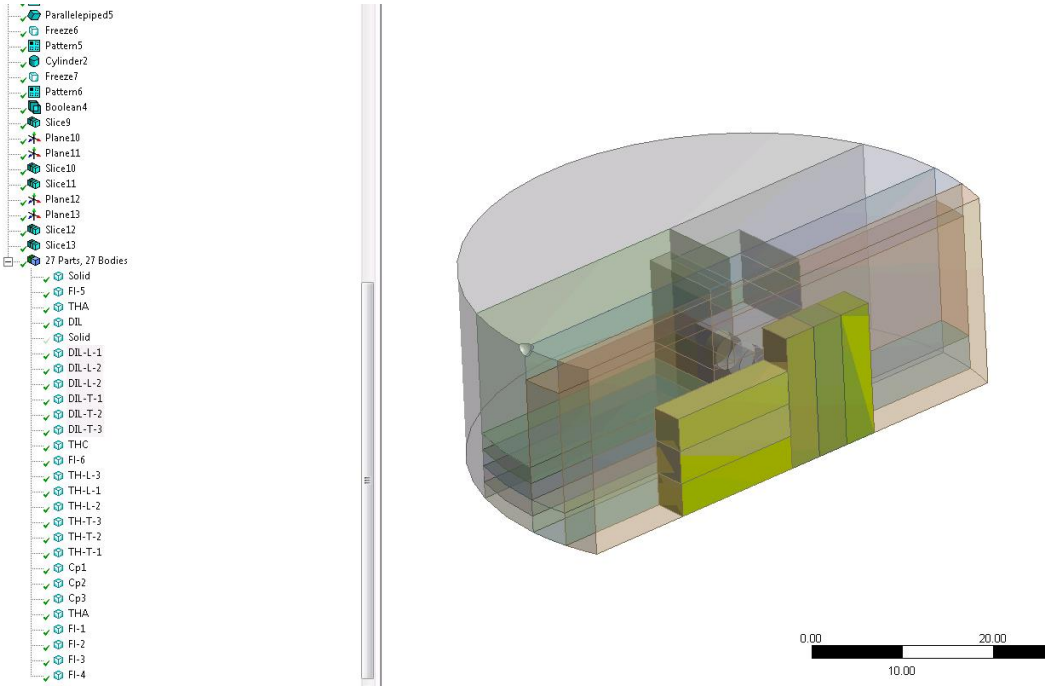


**Figure 6.5:** 3D representation of samples positions (and orientations) for MoGRCF plate cut by precision cutting machine.

### 6.3.1 Imaging through Optical and SE Microscopy

The real composite materials behaviour, as explained in previous Chapter, is strongly influenced by the presence of interfaces between phases and by the presence of defects such as macro-cavities and porosity. In addition the shape, dimensions and crystallographic orientation of the phases contribute to the final properties of the material so that it is of paramount importance to properly characterize the materials microstructure.

The two imaging techniques used in the present work are the Optical Microscopy (OM) and the Scansion Electron Microscopy (SEM).

In OM a focused light beam is reflected by the sample surface (that has to be planar, disposed perpendicularly to the beam and polished) and is then transmitted to an ocular or a video camera for the computer acquisition. The technique requires planar and polished surfaces in order to properly reflect the incoming light, and the sample's surfaces has to be etched (slightly corroded with acids) to reveal the grain boundaries (and the presence of constituents) that will appear black because the light

will not be transmitted by the eroded grain boundary area.

On the other hand in SEM the probe is an electron beam focused on the sample and the image is reconstructed point by point by acquiring the electrons emitted by the scanned surface. The two techniques are very similar in concept (both analyse a sample surface giving an image at the chosen magnification) but SEM has many advantages with respect to OM, not only in terms of image quality (higher effective resolution and depth of field) but also because it can give additional information about the chemistry (by Back Scattered Electrons Imaging and Energy Dispersion Spectroscopy, EDS) and the crystallographic orientation (by Electron Back Scatter Diffraction, EBSD) of the present phases.

The SEM technique has then been extensively used on all composites materials to verify:

- Fracture Surface Analysis:
  - fracture surface aspect,
  - fracture position and type (inter-phase or intra-phase),
- Material microstructure at different magnifications:
  - dimensions, shape and orientation of phases,
  - aspect and chemical nature of interfaces,
  - spatial distribution and relative orientation of reinforcement,
  - verification of materials homogeneity in different positions,
- Material Compaction:
  - position, dimensions and orientation of cavities ($> 1\mu m$) and pores ($< 1\mu m$),
  - position, dimensions and orientation of micro-cracks,
- Chemical Composition:
  - EDS analysis on large areas (to verify nominal composition),
  - punctual EDS analysis on impurities or secondary phases,

The results obtained by the different techniques will be presented in next Chapters 8, 9 and 10 together with a discussion of the SEM parameters used to investigate the different aspects of the composites listed above.

### 6.3.2 X-Rays Diffraction

X-Rays Diffraction is a technique based on the Bragg's interaction between collimated X-rays (having a precise wavelength when impacting the sample) and the sample crystallographic planes: the interaction, expressed by Bragg's law 6.1, gives rise to different peaks in the spectrum at precise angles. By the peak's position we can then calculate the inter planar distance of the sample crystal by inverting 6.1 .

$$n\lambda = 2dsin(\theta) \tag{6.1}$$

where: n = integer; $\lambda$ = X-ray wavelength; d = distance between two adjacent crystallographic planes; $\theta$ = angle of incoming X-Rays beam.

The technique is traditionally used on powders to have a statistical distribution of each crystallographic plane orientation and observe all crystallographic directions in the same spectrum, however it is also possible to investigate a bulk sample with known composition to verify the relative orientations of the phases with respect to the X-rays incoming beam. This particular technique has been extensively used to verify the relative orientation of the recrystallized graphite grains inside the MoGR and MoGRCF composites instead of the EBSD technique: in fact the X-Rays Diffraction gives less information about the crystal orientation with respect to EBSD, however the back scattered pattern image coming from graphite was too weak to be treated by the software and was not giving reasonable results. Therefore the EBSD technique cannot be applied to graphite based materials, as will be presented in Chapter 10.

## 6.4 Mechanical Characterization

The material's mechanical properties of interest for Beam Intercepting Devices are the Young's Modulus, the Ultimate Strength (or the Yield Strength for ductile materials) and the Poisson's ratio, of course for anisotropic materials these properties have to be evaluated along all the principal directions of the material in order to obtain the parameters stated in previous Paragraph 5.3.1.

The common test capable to obtain all the mechanical parameters is the Tensile test, however all studied composites were brittle with practical absence of plastic deformation so the trials to make a Tensile test resulted in samples braking on the holders or in too

small values of stresses and deformations to have a meaningful measurement. Only few measurements made at high temperature, with the sample heated by induction spires, were successful. For all those reasons the composites have been tested by Flexural Tests according to the ASTM Standard C 1161 - 02c (61) using appositely developed fully articulated fixtures like the one presented in Figure 6.6.

The fixtures, made in Stainless Steel with bearings in hardened steel, respect all the requirements for a Fully Articulated 4 point Fixture stated in ASTM C 1161 - 02c standard. The fixtures have been produced in three dimensions to test different samples dimensions and materials and have been also provided to other institutes involved in the Collimation Materials characterization inside EuCARD and US-LARP activities.

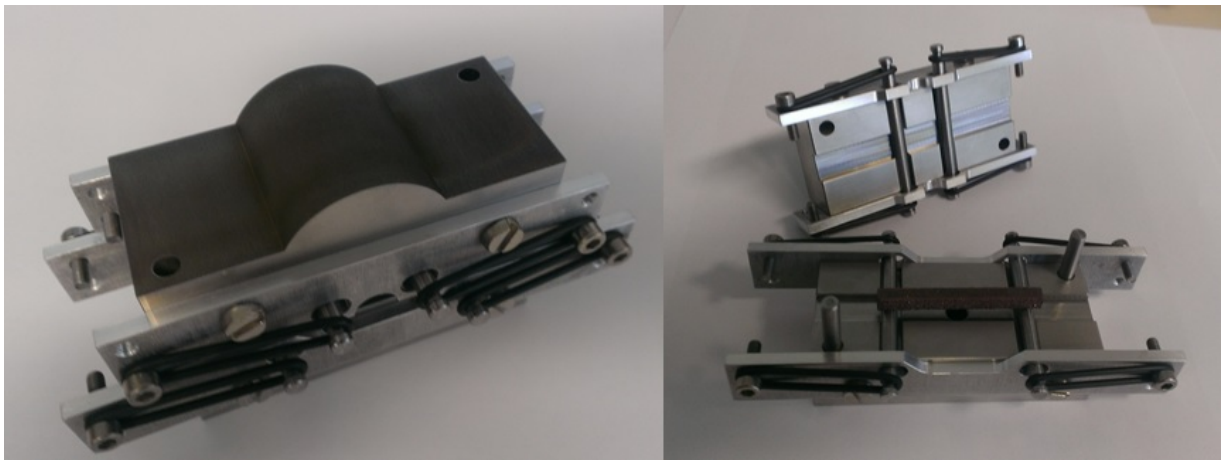

**Figure 6.6:** Flexural Fixture developed and produced at CERN EN/MME to test advanced composites.

The dimensions of the Fixture, identified by the Support Span (L, [mm]) are listed below together with the dimensions of the samples: the samples have not the standard dimensions foreseen in ASTM c1161 standard because of the difficulties in machining metal-diamond composites that fixed the thickness at 4 mm, the other dimensions being proportional to the proposed ones. Afterwards it was reasonable to keep the same dimensions on machinable metal carbide graphite composites in order to have the best possible comparison.

- Large samples 60x5.5x4 mm (Fixture with L=50 mm)
- Medium Samples 40.9x4x4 mm (Fixture with L=35 mm)

- Small samples 25x2x1.5 mm (Fixture with L=20 mm)

### 6.4.1 Ultimate Strength

The formula used for the evaluation of the maximum stress generated in the sample during a flexural test given by ASTM C1161 Standard is:

$$\sigma_{Fl} = \frac{3 * L * F}{4 * w * h^2} \tag{6.2}$$

where: $\sigma_{Fl}([MPa])$= Maximum Tensile (and Compressive) Flexural Stress; $L([mm])$= Loading Span; $F([N])$= Applied Force; $w([mm])$= Sample width; $h([mm])$= Sample height.

For brittle materials we can assume that the ultimate flexural strength ($R_{Fl}$) corresponds to the maximum value of force applied to the sample and we can disregard the effects of plasticity and necking. The corresponding ultimate tensile strength ($R$), measured by the tensile test, is lower and we have found empirically that for brittle composites we can assume $R \approx 2/3 R_{Fl}$.

To measure $R_{Fl}$ it is suggested to use large samples to investigate the largest possible portion of material in order to avoid the dimensional effects of the internal structure: both the large grain size of the phases and the presence of cavities and pores lead to the need of testing a representative portion of material. The ASTM Standard in fact requires a large number of tests to have a statistically representative result ($\geq 10$), however the relatively small dimension of the composite plates leads to a limited number of Flexural samples per produced plate, typically from 4 to 6 samples per plate: it is therefore very important to obtain a narrow distribution of results from the limited number of tests available. Since in brittle materials the ultimate strength is given by the stresses intensification around the most critical defect, and that the defects are statistically distributed in the material volume, the best way to have a narrow distribution of results (with a limited number of tests) is to have in each sample the same defects distribution. In the case of 4-point Flexural Tests the volume subjected to the maximum Stress is approximately 1/3 of the total, so the volume explored during the analysis in a 60x5.5x4 mm sample is $440mm^3$, large enough to be statistically representative of the material and to assure a good reproducibility of the results. Recent tests with the smaller Fixture (L=20 mm, explored volume $30mm^3$) confirmed that

using small samples of composite leads to a very broad distribution of the results, even if the average value is close to the big samples measurements.

### 6.4.2 Elastic properties

The flexural tests itself don't allow a direct evaluation of the elastic deformation of the samples, while it will give only the vertical displacement ($\delta z$) of the central part of the sample: the initial slope of the plot $\sigma_{Fl} = \sigma_{Fl}(\delta z)$ represents the flexural modulus of the material and is generally different than the Young's Modulus measured by a tensile test; in addition the flexural modulus cannot be directly used in engineering calculations.

However we can obtain correct measurements of the Young's Modulus by flexural tests applying a strain gauge to the lower face of the samples (the face subject to tension) in order to measure the real deformation ($\epsilon$) of the most loaded face and obtain the real Young's Modulus simply by:

$$E = \delta\sigma/\delta\epsilon \tag{6.3}$$

while in the first elastic part of plot. The technique has been validated by tests on reference materials (Mo and Cu-OFE) and gives values with a reasonable ($\leq 10\%$) error, at least for the preliminary characterization that is required during the R&D phase.

## 6.5 Thermal Characterization

### 6.5.1 Thermal Conductivity

The thermal conductivity ($k$) is defined as:

$$k = \rho * c_p * \alpha \tag{6.4}$$

where $\rho$ is density $[Kg/m^3]$, $c_p$ is the specific heat $[J/KgK]$ and $\alpha$ is the thermal diffusivity $[m^2/s]$.

The thermal conductivity can be therefore evaluated both relying on a direct measurement of $k$ (in the case of steady state thermal flux) or by a measurement of the

diffusivity in a transient thermal test (complemented by specific heat and density measurements).

The first method has been implemented at CERN by the development and production of an ad-hoc thermal test bench that relies on the generation of a stationary heat flux passing in series through reference pieces and the sample itself, the temperature distribution along the reference pieces and the sample being measured by thermal probes. The heat flux is then evaluated by measuring the $\delta T_{ref}$ along a known section ($A_{ref}$) of the reference piece (having a known $k_{ref}$) by:

$$Q = k_{ref} * A_{ref} * \frac{\delta T_{ref}}{\delta x_{ref}} \tag{6.5}$$

and finally the Thermal Conductivity of the sample $k$ is easily determined knowing the heat flux and the geometry of the sample by inverting the equation 6.5.

This method is based on the ASTM E1225 - 09 Standard (Test Method for Thermal Conductivity of Solids by Means of the Guarded-Comparative-Longitudinal Heat Flow Technique) and gives a direct, density and specific heat independent, measurement of the final thermal conductivity of the material along the heat flux direction. There are many examples of applications of this method to the evaluation of the thermal resistance at the interface between two solids ((62), (63)) or applied to the evaluation of the thermal conductivity of graphite materials ((64), (65).

As stated in cited articles there are many technological issues to be kept under control in order to obtain an accurate and reproducible measurements, a brief list of issues accompanied by the implemented solutions is the following:

- Thermal resistance at the interface sample-references: high thermal resistance reduces the heat transfer along the sample reducing the measured $\delta T$ and, in the assumption of equal thermal probe error, the measurement's accuracy.
  - Usage of thermal paste to assure a good thermal conductance ($\geq 10W/mK$) across interfaces.
- Heat Losses by convection and radiation: heat lost by convection and radiation will reduce the validity of equation 6.5 leading to increasing measurement errors.

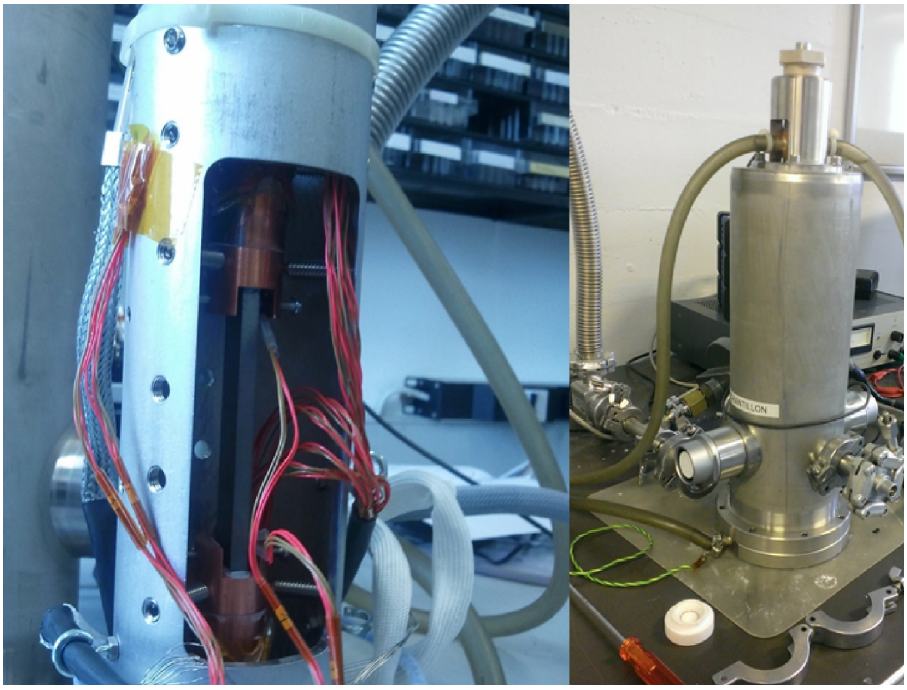

**Figure 6.7:** Left: internal view of the developed thermal test bench, showing the INOX shield (that accommodates also the cables and the screws to fix the sample inside) and the instrumented sample. Right: closed set-up showing the cooling circuits on top and on the bottom, the top screw to adjust the pressure on the sample and the external connections for the thermal probes.

  - Convection losses are reduced placing the setup inside a tight tank (shown in the right picture of Figure 6.7) kept under vacuum with a primary rotary vane pump.
  - Radiation losses are reduced by placing an internal shield of INOX between the sample (shown in the left picture of Figure 6.7) and reference pieces and the external vacuum tank, in order to reflect back to the centre the outgoing radiation.

- Errors in measurement of temperature distribution along the sample and the reference blocks.
  - Usage of redundant measuring points on the reference pieces to statistically reduce the error.

- Non homogeneous heat flux distribution across the sample and reference section that lead to incorrect measurement of the heat flux itself.
  - Usage of samples having exactly same cylindrical section as the reference pieces, possible for metals but not for composites.
  - Usage of sample holders in Cu-OFE to pass from the cylindrical section of the reference pieces to the rectangular section of the sample, see Figure 6.8.
  - Appropriate design of the joint between the heating and cooling elements and the reference pieces to have a regular transition across the joint and obtain a constant Heat Flow across the instrumented section of the reference pieces.

The preliminary analysis on known materials confirmed the validity of the setup, that measures from few $W/mK$ (AISI 304L Stainless Steel) to hundreds of $W/mK$ (Al and Copper OFE) with a constant overestimation of around 10% of the real value.

Note that the sample temperature vary from $\approx 10°C$ up to $\approx 50°C$ so the measurement reflects the properties of the material in that range, and due to the design of the instrument, it is not possible to measure the Thermal Conductivity at different temperatures.

The thermal test bench alone cannot measure over the temperature range of interest due to its intrinsic limitations, however by providing a fast and reliable measurement

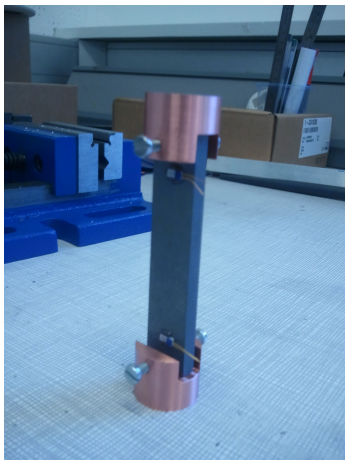

**Figure 6.8:** Molybdenum Graphite instrumented sample to be used in the thermal test bench. The sample is attached by screws to the two Cu-OFE sample holders, the screw tips being sharpened to reduce heat flow through the screws.

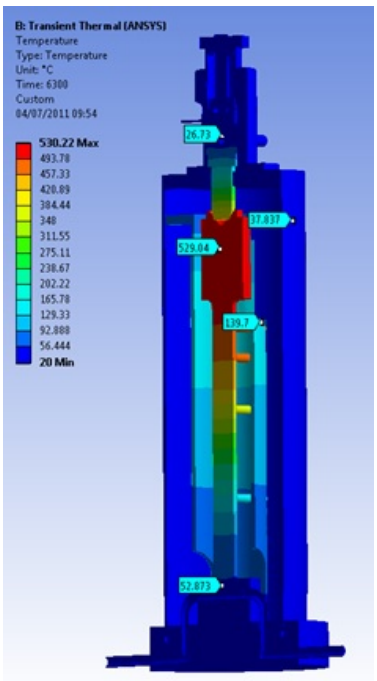


**Figure 6.9:** FEM simulation performed to validate the Thermal Test Bench. The effects of radiation between all surfaces, convection with the ambient and with the cooling water together with the thermal resistance at the interfaces have all been taken into account. The analysis has been carried out using Ansys Transient Thermal module.

of the material properties close to RT it allowed a quick comparison of produced composites that was crucial to tune the production cycle and the composition of the new materials in the phases of the materials R&D.

When a promising material was identified then its temperature dependant thermal properties have been measured by the laser flash technique, that measures the thermal diffusivity of the sample at different temperatures by depositing energy on the sample with a laser and measuring the time evolution of the temperature. The thermal diffusivity is then estimated by solving the heat's equation.

Since the technique has not been used directly during the work it will not be extensively cover here, further details can be found in the experimental apparatus producer website (Netszsch, (66)). The machine used for the Collimator materials tests is a Netzsch LFA 427 analyser capable to measure the thermal diffusivity up to $1600^oC$ ((67), typically with an error lower than 2%. The measurement is qualified by the ASTM E 1461-01 Standard (standard test method for thermal diffusivity by laser flash).

To obtain the thermal conductivity the diffusivity measure has then been integrated with the CTE measurement made with the dilatometer (see next paragraph 6.5.2), the density measurement with Archimedes balance (see paragraph 6.1.1, and the specific heat measurement made with the Differential Scansion Calorimeter (DSC, see paragraph 6.5.3 to obtain all the temperature dependant parameters involved in equation 6.4.

### 6.5.2 Coefficient of Thermal Expansion

The CTE (expressed in $[K^{-1}]$) is defined as the relative variation of the body dimensions divided by the temperature variation:

$$\alpha = \frac{dL(T)}{L_0} * \frac{1}{dT} \tag{6.6}$$

The most widely used dilatometer type is based on the push rod system in which an alumina bar is kept in contact with the sample, whose expansion during controlled heating is measured with high precision to obtain the relative expansion for the given temperature variation. Since the values of $\delta L$ are very small the measurement must take into account the apparatus deformations and the whole instrument has to be precisely calibrated to give reliable results. As for the laser flash measurements of

thermal diffusivity the CTE measurements have been carried out in the AIT Energy Department in Wien, the instrument used being a Netzsch DIL 402C dilatometer (68).

### 6.5.3 Specific Heat

The Specific Heat (expressed in $[J/KgK]$) is defined as the energy needed to increase the temperature of a finite mass of material. It is usually measured by placing the sample in a heating chamber together with a known reference sample, both being heated up while measuring the temperature on the samples surfaces. The heat passing to the sample is assumed to be equal to the heat passing through the reference, that can be calculated by using equation 6.7.

$$\Delta Q = c_p * m * \Delta T \tag{6.7}$$

Once known the heat it is straight forward to calculate the $c_p$ of the sample by reverting equation 6.7

The instrument used in AIT is a Netzsch DSC 404C equipped with a furnace capable to reach $1600 \circ C$ (69) with a typical error of 1%.

# 7

# Copper - Diamond (CuCD) Composites

In present Chapter the characterization of CuCD, carried out at CERN inside the EuCard WP8 activities, will be presented as already mentioned in Chapter 2.

The Chapter is so summarized:

- Introduction to diamond-reinforced MMC;
- Diamond properties;
- Diamond degradation during processing;
- CuCD characterization.

## 7.1 Introduction to diamond-reinforced MMC

Copper Diamond is part of the Diamond reinforced MMC (see Paragraph 5.1) developed for special thermal management applications that were extensively studied in recent years, in spite of the high cost of raw material and production cycle, because of the unique combination of thermal and physical properties such as low Density, high Thermal Conductivity and low CTE. As shown in Figure 7.1 they are particularly appealing for the LHC Collimator application because they maximize both the SSNI and TSNI indexes while having high Electrical Conductivity and matching Density.

Many works can be found in literature about the production and the characterization of CuCD different composites, few examples are CuCD materials with tailored

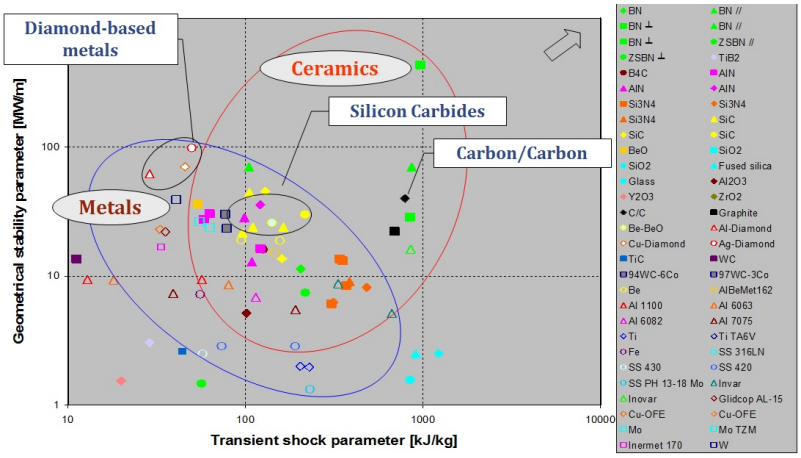


**Figure 7.1:** Figures of Merit SSNI and TSNI for different materials of interest.

CTE for electronics applications (70) are more sophisticated CuCD substrates produced by shock wave consolidation (71). Future promising applications are microprocessors cooling elements or heat exchangers in solar cells.

Other similar materials characterized during the thesis work are Silver - Diamond (AgCD), that can be seen in Figure 7.2, and Aluminium - Diamond (AlCD), both produced by Prof. L. Weber at EPFL (44) using the liquid infiltration technique. They aim to combine the properties of diamonds (hardness, low density, high thermal conductivity, high Young's Modulus) with the good properties of the respective metal, usually mechanical strength and electrical conductivity.

AgCD is obtained by infiltration of pressed natural diamonds by molten Ag-Si eutectic alloy. The SiC particles formed during the process, clearly visible in Figure 7.2 provide a very high bonding between the two phases leading to exceptional mechanical properties, with measured flexural strength above $500MPa$. However, the low melting temperature of the eutectic limits the range of use of such material for BID application and the material was not further studied.

In that case the use of liquid infiltration helps in filling the empty spaces between diamonds assuring a good compaction rate, however the usage of liquid infiltration is limited to metallic matrices with low melting temperatures because of the diamond degradation that starts already at temperatures below $1000^oC$ (72), (73); the details of the phenomena are explained in Paragraph 7.1.2. For all those reasons CuCD is usually produced with Solid State Sintering (SSS) at the lowest Temperature as possible.

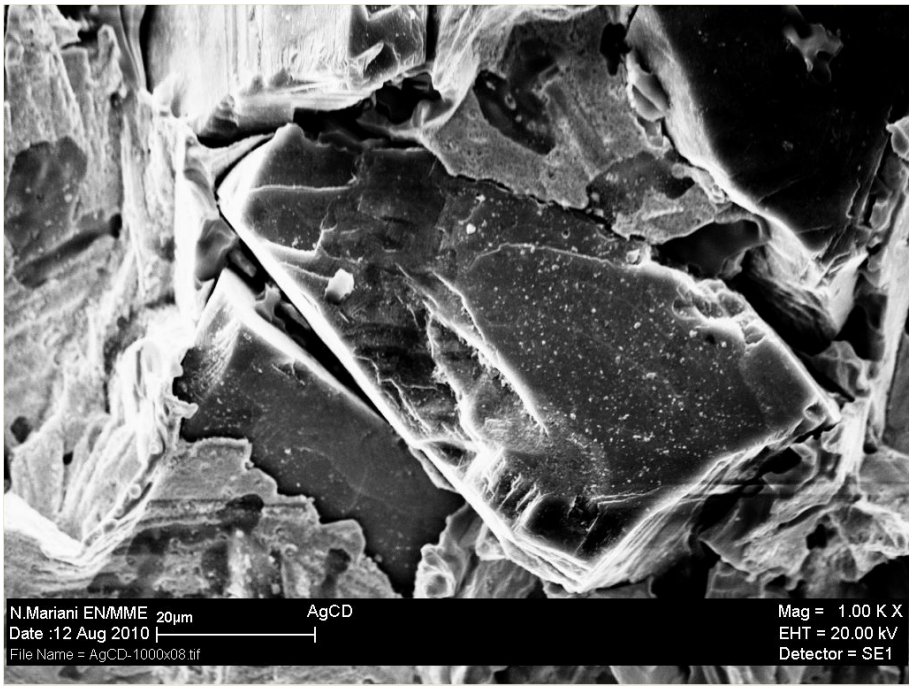


**Figure 7.2:** SE Image at medium magnification of fracture surface of AgCD sample produced at EPFL.

### 7.1.1 Diamond Properties

Diamond is a ceramic material made by $sp^3$-bonded carbon atoms arranged in a deformed cubic lattice that exhibits extraordinary physical and mechanical properties due to the very high strength and directionality of its covalent bonds (74).

The diamond natural structure is obtained by the compression of carbon at very high pressures (4.5 up to 6 $GPa$) and at relatively low temperatures between 900 and 1300$^oC$. On the earth the only place where this conditions are met is the lithospheric mantle below stable continents, however natural diamonds can also be found on meteorite crash sites (75). It is worth mentioning that the main part of the natural diamond obtained by mines is in the form of fine powder (or lime) of small raw particles that are then milled to collect the different mesh sizes to be used in industry and jewellery.

The natural diamonds appear like stones, the surfaces are rough and have irregular shape, with sharp edges and indented surfaces, as shown in Figure 7.3.

In order to artificially form the diamond structure it is necessary to apply both high pressure and temperature to graphite doped with metallic fine powder: the metallic

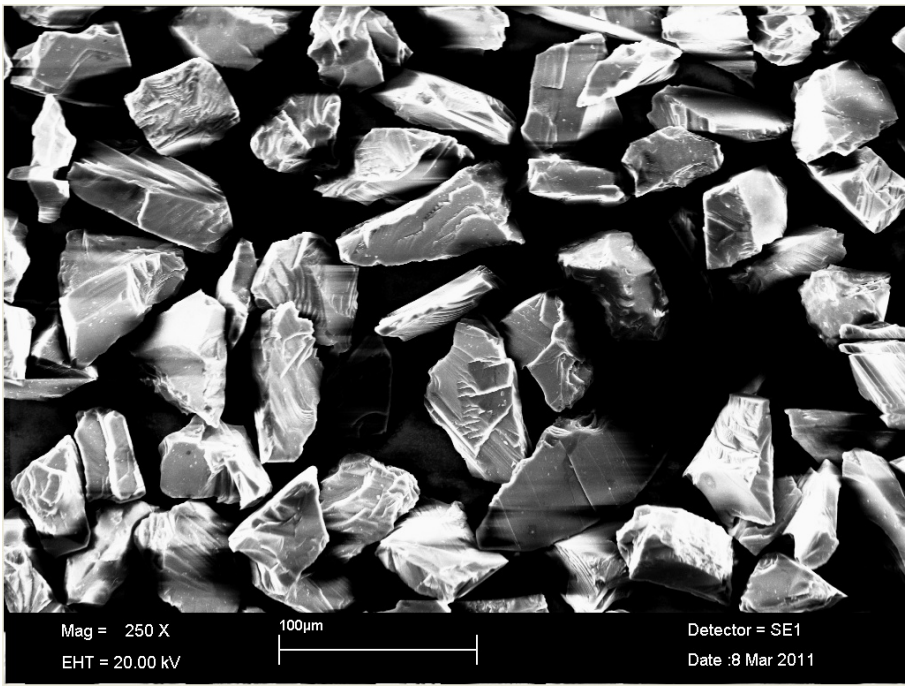


**Figure 7.3:** SE Image at medium magnification of natural diamond powder used in BrevettiBizz for the production of MoCuCD composites. The cleavage fracture formed during the milling are clearly visible.

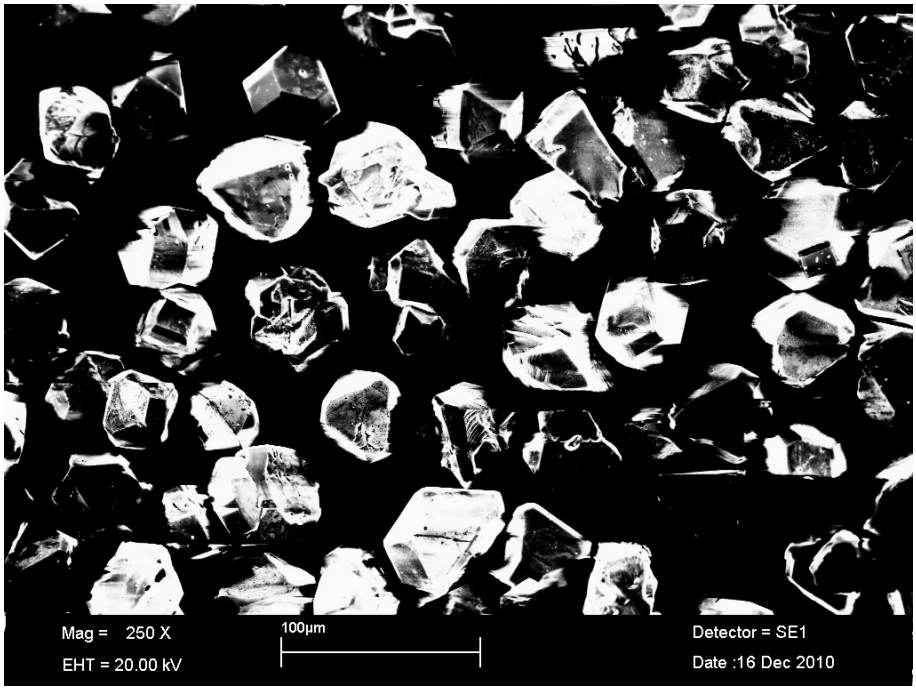


**Figure 7.4:** SE Image at medium magnification of synthetic diamond powder used in BrevettiBizz for the production of MoCuCD composites.

atoms act as growing seeds for the diamond structure allowing the production of significantly big diamond in a reasonable time, that could not been achieved by relying only on the physical means (temperature and pressure). Of course the presence of metallic atoms in the diamond core has detrimental effects on the diamond properties because it introduces defects in the practically perfect diamond lattice; for that reasons synthetic diamonds have usually lower hardness with respect to natural diamonds and are therefore considered of lower quality for standard grinding applications. However synthetic diamonds have the advantages of a very regular shape with smoother surfaces due to the absence of mechanic grinding, as can be seen in Figure 7.4.

Both diamond types have been characterized and used for the production of MoCuCD composites, the results are shown in Chapter 8.

### 7.1.2 Diamond Degradation

As introduced, the main challenge in diamond based composites production is to reduce diamond graphitization during sintering: diamond graphitization will reduce signifi-

cantly both mechanical and thermal properties of the composite, because the graphite formed at the interface between the diamonds and the metallic matrix is brittle and has a very low thermal conductivity, therefore it will act as a barrier for thermal diffusion across the interfaces. A very important point to have in mind is that $sp^3$ carbon (diamond) is meta-stable in standard conditions (RT, 1 Atm) and tends to return to $sp^2$ carbon (graphite) if energy is given to the system according to the carbon phase diagram reported in Figure 7.5 (76) (77); however, the kinetic of the process at RT is so low that we will not observe diamond graphitization even for very long times. Pressure can be given to the system to counteract this phenomena but unfortunately the pressure needed to avoid graphitization is too high to be practically achieved (78).

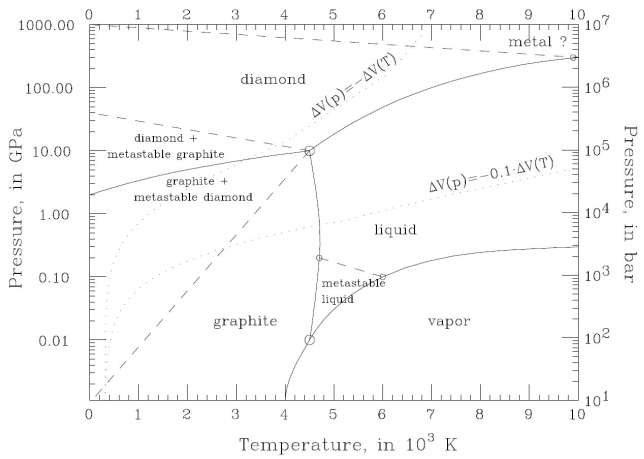


**Figure 7.5:** Phase diagram of carbon.

From a physical point of view diamond graphitization can be divided into two different physical phenomena, both activated by temperature: superficial graphitization and bulk graphitization (74)

#### 7.1.2.1 Superficial Graphitization

If a diamond is heated under normal atmosphere ($\approx$ 21% Oxygen), its surface will start to react with Oxygen even at low temperatures ($500 - 600^0 C$) forming $sp^2$ carbon atoms with $C = O$ bonding on the diamond surface. The process is exothermic and will lead to total diamond graphitization starting from the surface. If there is some water in the atmosphere, there will be also the formation of $COOH$ and $COH$ groups (79). The main way to reduce superficial graphitization is to reduce the oxygen content on

diamond surface: the use of high vacuum and hydrogen rich atmosphere during sintering process helps to contain graphitization taking away some of the oxygen present both on diamonds and on metallic powders (as in Mo and Cu powder always remain some oxygen due to unavoidable exposure to atmosphere), but oxygen cannot be completely removed. Increasing the temperature will increase the kinetic of superficial graphitization process with the results reported in Figure 7.6.

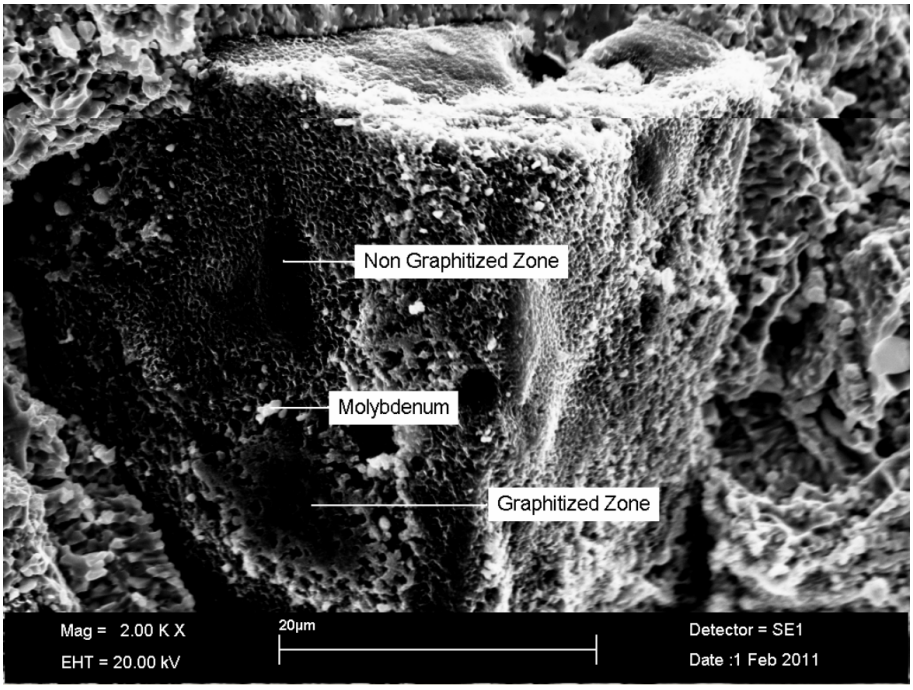


**Figure 7.6:** Aspect of graphitized diamond surface

#### 7.1.2.2 Bulk Graphitization

In addition to superficial graphitization, when the temperature reaches $1700 - 1800^oC$, $sp^3$ carbon will start to degrade to $sp^2$ carbon even inside diamond bulk: this mechanism is not yet completely understood, but it seems to be related to impurities inside diamond lattice which act as catalysts for diamond transformation. This suggestion is confirmed by the fact that synthetic diamonds are more susceptible to bulk graphitization than natural diamonds: synthetic diamonds are produced using metallic seeds as starting points for diamond lattice growth, therefore they have a preferential starting point for diamond bulk graphitization that is absent in natural diamonds. We must re-

mark that, in addition to growing seed, every kind of diamond (even the most pure and expensive one) has some impurities inside the lattice, so its not possible to completely avoid bulk graphitization by using high purity natural diamonds.

## 7.2 CuCD for BID

Concerning the use of CuCD as BID material, the interest in joining Cu and diamond is mainly to optimize their behaviour as thermal management materials as discussed in Chapter 2. Always in mentioned chapter is reported the description of the tools used to benchmark BID materials (the Figures of Merit).

The values obtained for CuCD are presented in Table 4.2 and Figure 7.1 with respect to Glidcop (introduced in section 4.1.4): the density reduction allows for a smoother energy deposition profile that results in high beam impact strength, as confirmed by the HiRadMat HRMT-14 experiment (see Chapter 11), while the smaller CTE increases the thermal stability during steady state operations as required by the LHC Collimators dimensional tolerances (see Paragraph 3.3); even more important the high electrical conductivity assures a very low RF Impedance at high frequencies as requested by the LHC operations. The drawbacks are the lower mechanical strength, the completely brittle behaviour and the higher Young's Modulus, that are reducing the TSNI (lower robustness). Another concern regards the effective radiation hardness of such material that is actually practically completely unexplored by the scientific community and requires special studies, as described in Paragraph 7.2.2.2.

The comparison between the properties predicted by the analytical means presented in Chapter 5 is presented in table 7.1, using the ROM model 5.1 for the density and the specific heat, the Hasselmann and Jonson model for the thermal conductivity (using 5.9 with $h_c = 2.97x10^7\ W/m^2K$ and $a = 200\mu m$), the Turner model for CTE and the empirical formula 5.2 for the electrical conductivity. The reference values for Cu and diamond are listed as well.

RHP Technology produced many sample plates with dimensions up to 200x80x4 mm to be used for characterization in EuCard partner institutes such as NRC - Kurchatov Institute, GSI and of course CERN. Another characterization program is ongoing in collaboration with Brookhaven National Laboratories inside the U.S. LHC Accelerator Research Program (LARP) collaboration activities. The characterization campaign has

**Table 7.1:** Comparison between predicted and measured properties for CuCD at RT. Density and Specific Heat evaluated by ROM model 5.1, CTE by Kerner model 5.11, k by Hasselmann and Johnson model 5.9 and E is conservatively assuming the Reuss assumption 5.4.

| Property | Unit | Estimation | Measured | Variation % |
|---|---|---|---|---|
| $\rho$ | $[g/cm^3]$ | 5.61 | 5.33 | 95.0% |
| CTE | $[10^{-6}K^{-1}]$ | 6.25 | 7.8 | 124.8% |
| k | $[W/m/K]$ | 615 | 490 | 79.7% |
| $\sigma$ | $[MS/m]$ | 13.7 | 12.6 | 92.0% |
| E | $[GPa]$ | 230 | 240 | 104.3% |
| $R_{Fl}$ | $[Mpa]$ | $[-]$ | 120 | $[-]$ |

been performed to obtain a comprehensive picture of the effective material behaviour inside the LHC in view of the choice for new Hi-Lumi LHC collimators; the work includes a mechanical, physical, thermal and electrical characterization followed by an extensive study on the effects of radiations on such properties (80).

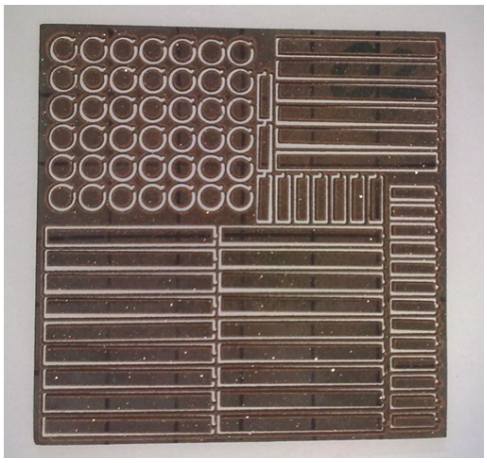

**Figure 7.7:** CuCD plate produced in RHP Technology in 2010 after water jet cutting.

Finally it is worth mentioning that diamond based materials cannot be machined with standard means so the final shape must be obtained directly from the mould and that to obtain a specific roughness it is necessary to leave a Cu layer on the materials plates that can be machined afterwards. However it must be said that this technique did not well adapt to cylindrical samples used in the HiRadMat HRMT-14 experiment,

leaving samples with large diamond contamination on the lateral surfaces that had to be machined by special diamond tools afterwards to match the dimensional specifications: the machining had to be done dry to avoid contamination and slowly to avoid samples overheating, so the Copper layer technique will be only used on parallelepiped shaped samples in the future.

### 7.2.1 CuCD Production

The material tested at CERN has been produced in RHP Technology headquarters in Seibersdorf (Austria) in 2010 (81): the plate final dimensions were 150x150x4 mm, the details about the production cycle are listed below.

- Composition of starting powder: $60\%_V$ diamond powder (of them the 90% is a 70/80 mesh (corresponding to $\approx 100\mu m$), the remaining 10% is finer 325-400 mesh) $1\%_V$ of Boron powder and $39\%_V$ of Cu Powder.
- RHP main parameters: heating and cooling rate about $50K/min$, maximum temperature $1020^oC$ for 30 minutes, constant applied pressure $30MPa$, vacuum atmosphere $10^{-4}$ $mbar$ with reducing atmosphere.
- Heat treatment: to relieve the stresses inside the copper matrix the plates have been heated to $250^oC$ for 30 minutes after Hot Pressing.

### 7.2.2 CuCD Characterization

#### 7.2.2.1 Microstructural Analysis

The composition chosen by RHP technology reflects many empirical principles that can be found in the experience of the experts of composites: the content of diamond is kept at $60\%_V$ because higher content would not allow the compaction of the material due to the interference between hard diamonds; the diamond content itself is divided in a large and small particles with ratio 9/1 to let the small diamonds fill the interstitials between the large ones (see Figure 7.9, and the thermal cycle is kept as low as possible to avoid superficial diamond degradation (as shown in Figure 7.10, see following section 7.1.2 allowing anyway to reach the 95% of compaction with respect to nominal density.

One of the main obstacles in obtaining tough CuCD composites is the low affinity between the two components that does not lead to good intimate bonding across the

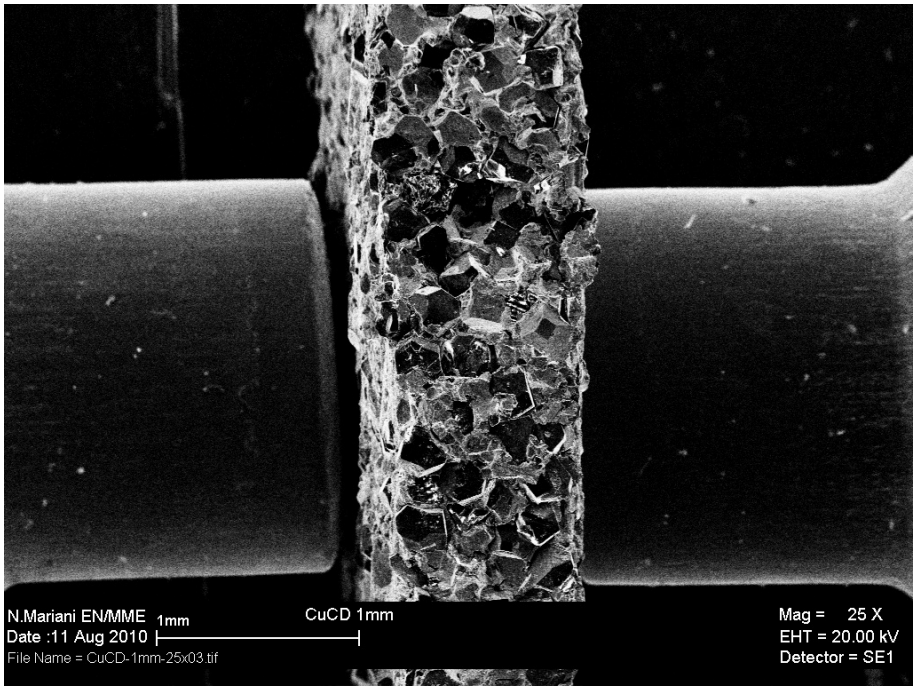


**Figure 7.8:** SE Image: Fracture surface of CuCD sample embedded inside the sample holder observed at SEM.

interfaces. The absence of a strong bonding is confirmed also by the aspect of the fracture surface shown in Figure 7.10: the fracture passed preferentially across the brittle interfaces and there are no visible signs of plastic deformation of the Copper matrix.

This non ideal condition is limiting not only the strength (as discussed in section 5.3.2) but also the thermal conductivity that might drastically reduce when the two phases start to detach, for example after several thermal expansions and contractions, thus limiting the usage as heat exchanger.

RHP overcome at least partially the issue by adding a strong carbide former (Boron) that is also soluble inside the Copper matrix: it can be observed in the SEM Figures 7.11 and 7.12 that many Boron particles close to the diamonds surfaces form a stable carbide layer on the diamond surface and dissolve on the other side inside the Cu matrix, giving an intrinsic mechanical bonding to the material, $\approx 120MPa$ of flexural strength and $70MPa$ of tensile strength.

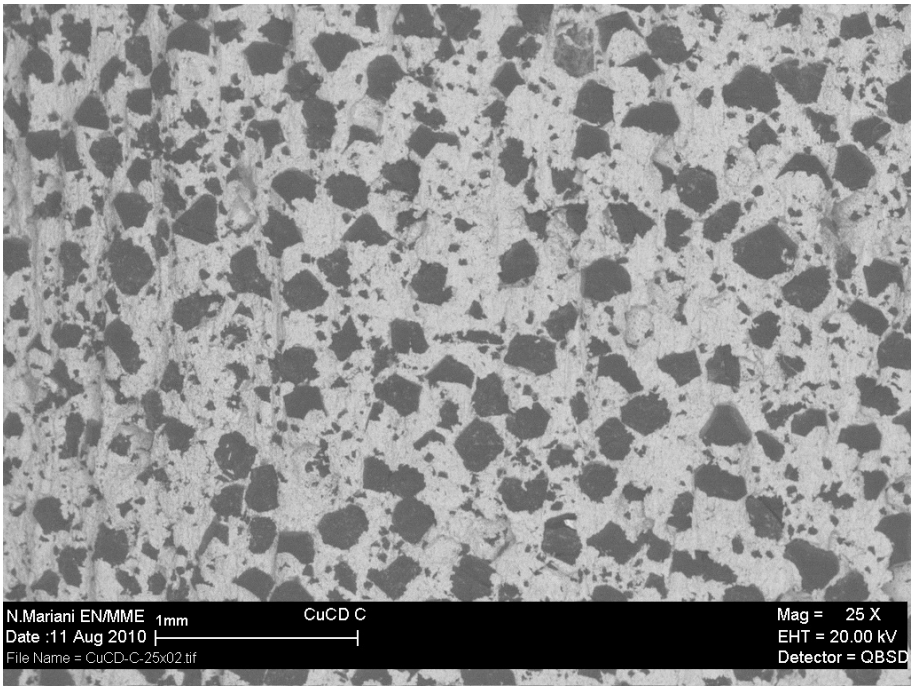


**Figure 7.9:** QBSD Image: Low magnification SEM Observation at CERN of the fracture surface of CuCD. The distribution of diamonds (dark grey) in the bulk material and the two dimensions of the diamonds are clearly visible.

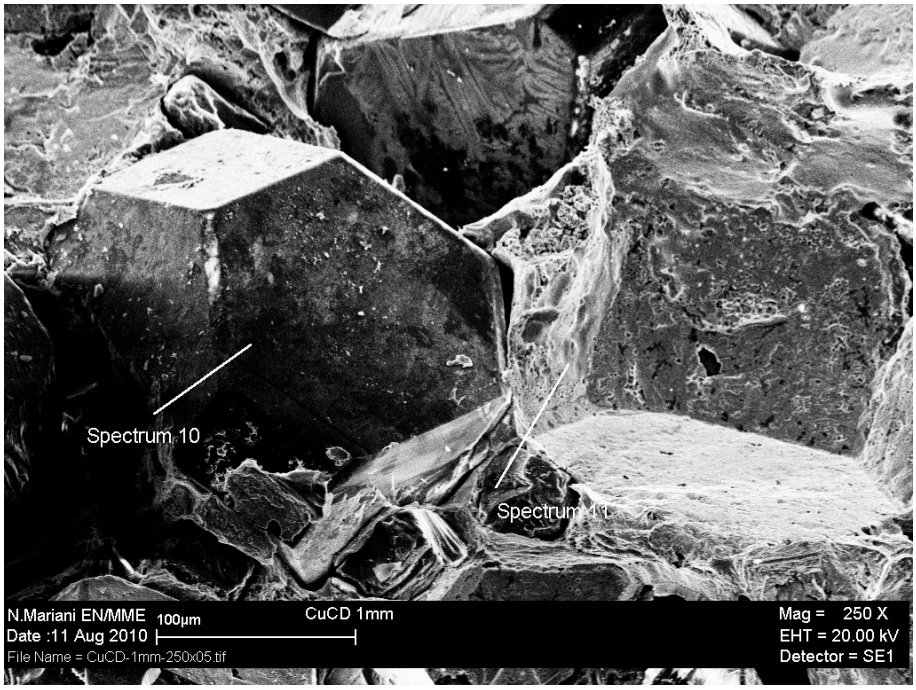


**Figure 7.10:** SE Image: Medium magnification SEM Observation at CERN of the fracture surface of CuCD. The Cu matrix detached on one diamond while remained attached to the adjacent one, confirming the low adhesion between the phases. The surface of the diamond on the left appears smooth and with signs of visible graphitization as expected by the low temperature cycle.

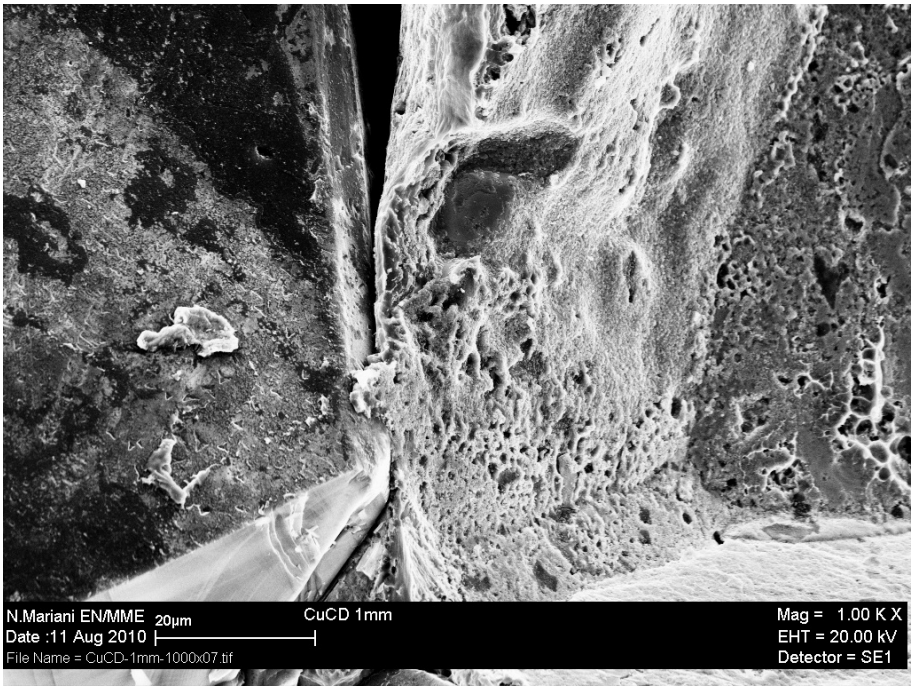


**Figure 7.11:** SE Image: High magnification SEM Observation at CERN of the fracture surface of CuCD. The small particles attached to the diamonds are Boron carbides formed during the process, as the larger particle attached at the bottom of the diamond.

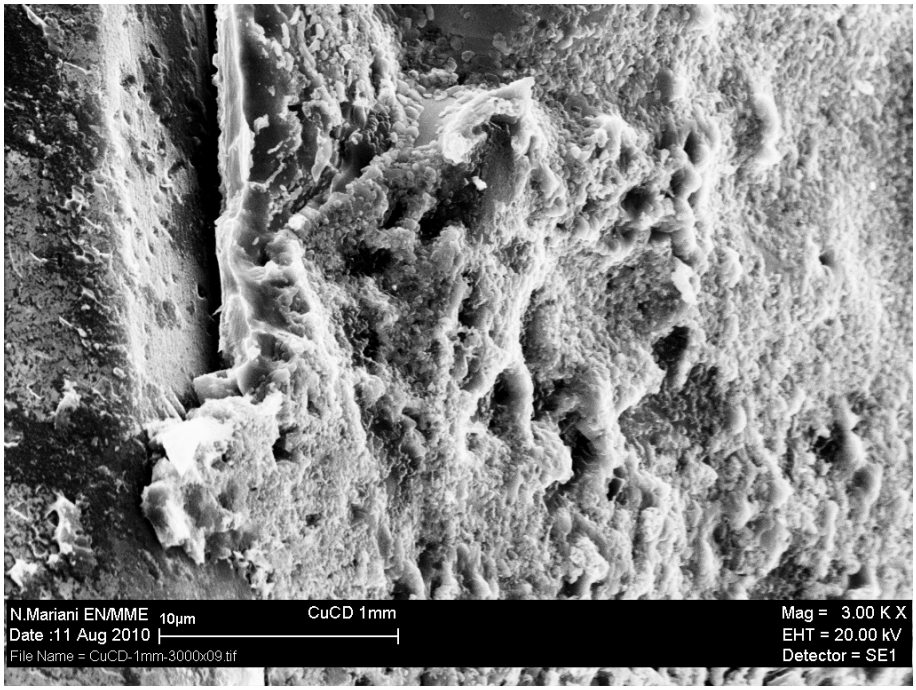


**Figure 7.12:** SE Image: High magnification SEM Observation at CERN of the fracture surface of CuCD. High magnification of the Boron carbide particle.

#### 7.2.2.2 CuCD Radiation Hardness

Two main studies are ongoing to assess the degradation of CuCD after prolonged exposure to highly energetic protons fluencies: the first program started in 2010 at NRC-Kurchatov Institute (Moscow, Ru) (2) using 30 MeV protons while the second program started in 2013 at BNL (New York, US) (82): both focus on the measurement of key mechanical and thermal properties before and after different radiation doses to assess the properties reduction as a function of the dose received.

The experimental work at NRC Kurchatov Institute on CuCD is now concluded and the results will be published soon, here we will just introduce few results of interest; on the other hand the studies at BNL suffered from technical problems with the failure of a vacuum capsule inside the irradiation facility that provoked the delay of the activities until 2014 (83) and will therefore not been mentioned here.

The studies at NRC Kurchatov Institute were composed by a first theoretical part to assess the different doses received by the two components of the composite, followed by the characterization of pristine materials samples, the irradiation of another set of

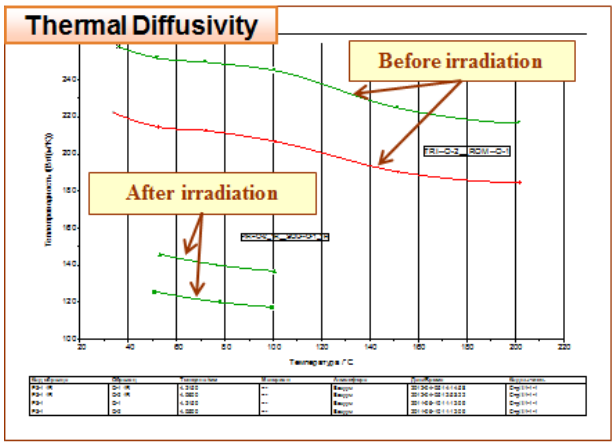


**Figure 7.13:** Thermal Diffusivity reduction after exposure to $10^{17}$ protons at 30 MeV. Source (2).

samples and its characterization.

The theoretical investigation of the dpa level shows different irradiation profiles for the Cu and the diamond phases, with higher dpa in Cu, see Figure 7.14; however the defects can recombine more easily in Cu at the irradiation temperature of $100^oC$ while are blocked inside the covalent diamond structure, leading to a more pronounced degradation of the diamond properties in the long period. A brief summary of the obtained results presented by Prof. Ryazanov of NRC-Kurchatov Institute is reported in Table 7.2 below.

**Table 7.2:** CuCD properties variation after irradiation of $10^{17}$ protons at 30 MeV in NRC-KI.

| Property | Unit | Reference | After Irradiation | Variation % |
|---|---|---|---|---|
| CTE | $[10^{-6}K^{-1}]$ | 7.80 | 8.30 | 6.4% |
| k | $[W/mK]$ | 490 | 330 | -43.1% |
| $\sigma$ | $[MS/m]$ | 12.6 | 9.80 | -22.2% |
| E | $[GPa]$ | 240 | 330 | 37.5% |

The most significant result obtained by the characterization at NRC Kurchatov Institute is the large reduction in thermal conductivity after even low doses of 30 MeV protons, as shown in Figure 7.13 courtesy of A. Ryazanov. The other modifications observed in the material are an increase in the Young's Modulus (as expected by the

increase of defects in the Cu matrix), together with a pronounced embrittlement. The electrical conductivity and the CTE however did not change with respect to pristine situation: the first because the defects in the Cu phase were not enough to reduce significantly its excellent electrical conductivity (there is anyway a very slight reduction), the second because the effects of the volume increase (swelling) of the Cu phase were in a certain way compensated by the increase in Young's Modulus that helped in keeping low CTE values even after $10^{17}$ protons. A summary of the variations is reported in Table 7.2.

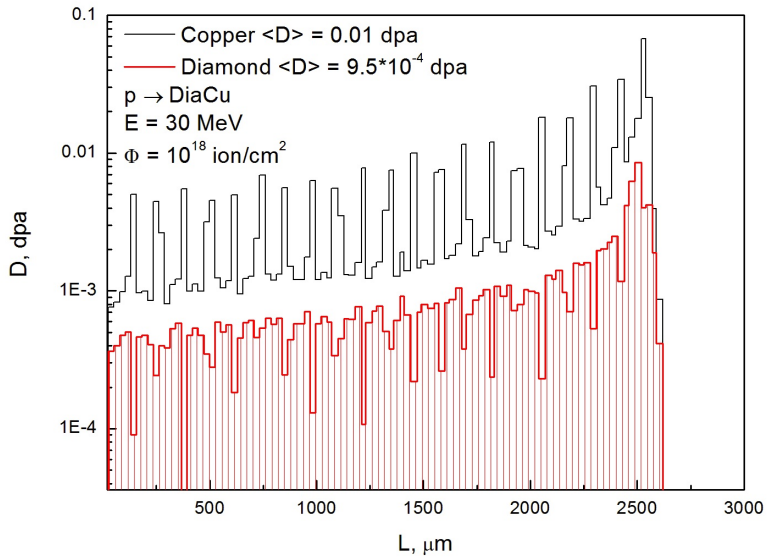


**Figure 7.14:** Dpa distribution along the two phases in the case of alternate layers of Cu and diamond (respectively 65 and 130 $\mu m$ thick). The higher density of Cu leads to a much higher dpa level with respect to the diamond phase.

The studies to correlate the dpa level at different energies are still ongoing and should provide an indication of the life expectancy of CuCD while irradiated by the H-Lumi LHC beam.

## 7.3 Conclusions on CuCD

CuCD is without any doubt a very interesting material for the next generation of LHC Collimators and more in general for any BID where very high thermal dissipation is needed. Its low density (which is crucial for BID to smooth the energy absorption) gives them high appealing also for new heat exchangers in high-end electronics, a field where mobility is becoming more and more researched. The extensive characterization work performed in the present thesis confirms the validity of the choice and the effectiveness of the R&D work carried out in RHP technology. The few disadvantages found in CuCD are the difficulties in the production, the high brittleness and the detrimental effect of radiations on the thermal transport. On the other hand its tailored density allows for an optimal (and smooth) beam cleaning. Table 7.3 compares the values obtained for both CuCD and Glidcop giving a more general view of the improvements with respect to the BID application: the relatively low value of TSNI is due to the limited mechanical properties of CuCD at RT, however the material showed a good robustness in the beam impact tests (see Chapter 11 thanks to its very low density which smoothed the energy deposition over a large volume of material.

**Table 7.3:** CuCD material properties compared to Glidcop AL-15. The properties have been measured on the material produced by RHP Technology at CERN and Kurchatov Institute (2).

| **Material** | **Unit** | **Glidcop** | **CuCD** |
|---|---|---|---|
| Density | $[g/cm^3]$ | 8.93 | 5.4 |
| Atomic Number (Z) | $[-]$ | 29 | 11.4 |
| Melting Temperature | $[^oC]$ | 1083 | 1083 |
| Thermal Conductivity | $[W/mK]$ | 365 | 490 |
| CTE | $[10^{-6}K^{-1}]$ | 16.6 | 7.8 |
| $C_p$ | $[J/kGK]$ | 391 | 420 |
| E | $[GPa]$ | 130 | 220 |
| Tensile Strength | $[MPa]$ | 413 | 70 |
| Poisson's Ratio | $[-]$ | 0.33 | 0.22 |
| $\sigma$ | $[MS/m]$ | 53.8 | 12.6 |
| Radiation Length $\chi_0$ | $[cm]$ | 1.47 | 4.78 |
| SSNI | $[kWm^2/kg]$ | 2.5 | 11.6 |
| TSNI | $[kJ/kg]$ | 50.1 | 13.4 |

# 8

# Molybdenum - Copper - Diamond (MoCuCD) Composites

Present Chapter reports the R&D work and the results obtained in the first development of advanced Molybdenum-based composites, MoCuCD.

As anticipated in Chapter 2 CuCD did not completely satisfy the key requirements for LHC Collimators materials (identified in Paragraph 4.2) therefore the research on novel materials moved on establishing a new R&D program on Metal-Diamond composites, taking advantage of the large experience previously acquired with CuCD adding Molybdenum as third element.

## 8.1 MoCuCD for BID

Aim of the R&D was to obtain a material having lower CTE and higher strength (to increase both the SSNI and the TSNI indexes) with respect to Glidcop and CuCD: with this objective in mind the choice for the third component fall naturally on Mo (Paragraph 4.1.5), a material that has been already used for LHC Collimators due to its excellent mechanical and electrical properties combined to adequate thermal conductivity and high thermal stability at high temperature, as shown in Table 4.2.

More important, Mo is a strong carbide former that easily reacts with carbon above $400^oC$ (84): as for Boron in CuCD the carbides formed on the diamond surface are responsible for the final mechanical strength of the composite. Finally, the Mo addition should also help to compensate the high Cu CTE especially at high temperature.

# 8. MOLYBDENUM - COPPER - DIAMOND (MOCUCD) COMPOSITES

After evaluating possible partners for the new R&D program CERN established a collaboration with BrevettiBizz, a small dynamic Italian company having valuable experience in metal diamond composites (59). Following a preliminary introduction meeting BrevettiBizz provided a first example of MoCuCD material (85) produced by Rapid Hot Pressing technique (RHP) like for CuCD: the first attempt proposed by BrevettiBizz in August 2010 can be seen in Figure 8.1, showing high porosity and diamonds graphitization. Furthermore, the diamonds are not homogeneously distributed inside the matrix, resulting in poor compaction and low properties. This considerations however leave space for large improvements in such kind of composites, as shown in following Paragraphs.

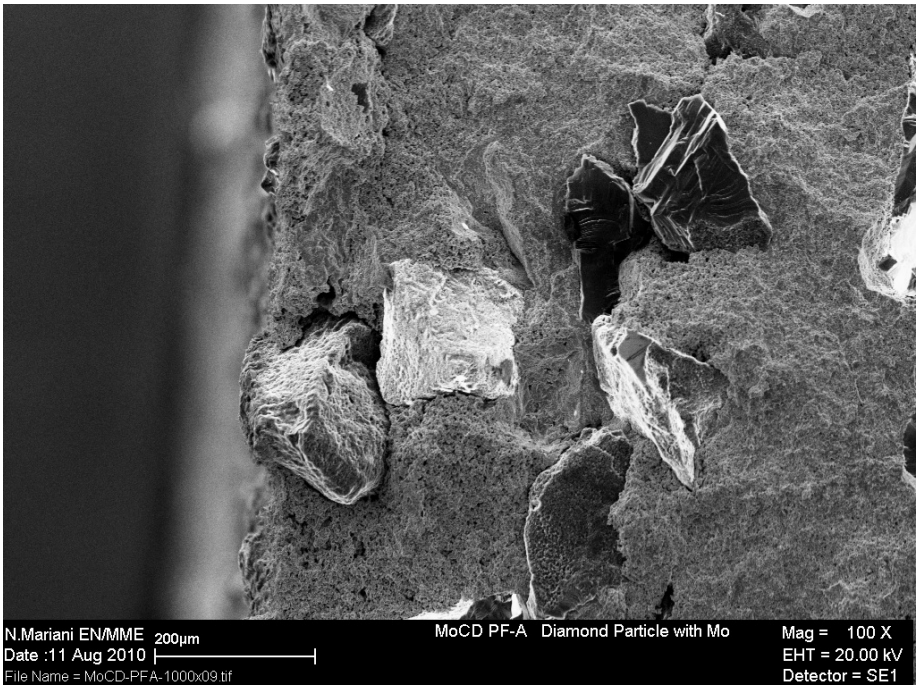


**Figure 8.1:** SE Image at low magnification of the first MoCuCD. The matrix appears porous and the natural diamonds are graphitized. The plate's composition is: $60\%_V$ 45 $\mu m$ Mo, $30\%_V$ 174 $\mu m$ synthetic diamonds, $10\%_V$ 45 $\mu m$ Cu and has been sintered under primary vacuum for 180 min at $1020^oC$.

The works prosecuted for more than one year exploring many possible additions and thermal cycles to maximize the material's properties while avoiding diamond degradation at high temperature, as explained in Paragraph 7.1.2, until the optimal production cycle and composition have been identified and deeply characterized. The summary

of the most important innovations is presented in the following Section, followed by the development and characterization of Cu coated diamonds and finally by the results obtained with the most important milestones in the materials R&D:

- MoCuCD Production R&D Key points
- MoCuCD with Cu coated diamonds
- MoCuCD final material with tailored composition and improved production cycle

## 8.2 MoCuCD Production

The observation of the first material proposed by BrevettiBizz reported in Figure 8.1 allowed to establish few key points for the MoCuCD composite production.

The diamond degradation is clearly visible in Figure 8.1 by the grey colour and the roughness of the diamonds surfaces. Graphite is forming on diamonds surfaces even at the relatively low Temperature of production of the plate $MoCuCD_A$ and is hampering the formation of the proper $Mo_2C$ interface between diamonds and Mo particles. Starting from the assumptions stated in Paragraph 7.1.2 several adjustments have been made to the production cycle, to the raw material and to the material composition as reported in the following.

### 8.2.1 Production Cycle Improvements

The first parameter to operate with when trying to reduce reinforcement degradation is the sintering time.

The sintering of pure Mo requires very high temperatures ($>2/3\ T_m$, $\approx 1750^oC$) and sintering times: from the example in Figure 8.2 (86), using $4\mu m$ Mo powder, to obtain a compaction rate around 90% is sufficient 1 hour at $1750^oC$, while at $1400^oC$ more than 10 hours would be necessary(87), (86).

It is also clear that it will not possible to sinter properly Mo particles without damaging the diamonds surfaces, so the compaction process has to rely on the solid state diffusion of the Cu phase inside the interstitials between the diamond and Mo particles, as happens in CuCD, or by melting of the Cu phase and internal liquid infiltration as finally done with MoCuCD.

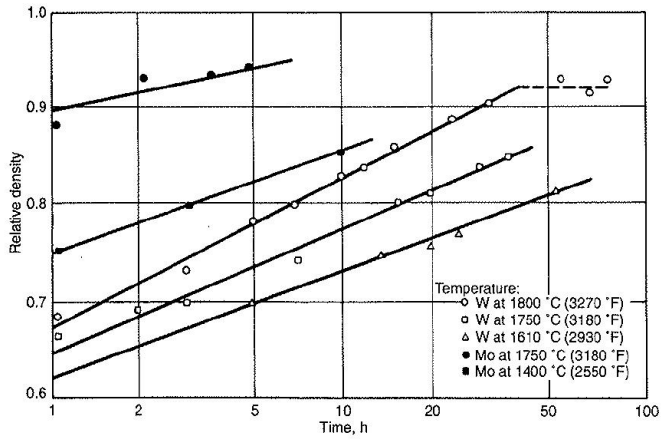


**Figure 8.2:** Effect of temperature and time on the relative density of sintered $4\mu m$ W and Mo powders.

Many other important factors contribute to the compaction time, such as powder dimension (smaller powder leaves smaller voids and sub sequential higher density, and also a smaller grain in final Mo structure), powder superficial reactivity (fresh, non oxidized surfaces diffuse atoms faster), powder shape (spheres pack differently from lamellas and from fibers), and powder chemical purity (carbon and oxygen will have a detrimental effect on Mo sintering), (88).

Obviously, also the the heating and cooling ramps will give their contribution to the final diamond degradation, therefore it is mandatory to limit to the ramps to the minimum duration technologically achievable.

Another point to keep in mind is that reducing the sintering time the importance of the heating and cooling ramps increases and so will their contribution to the final degree of diamond graphitization. BrevettiBizz continuously improved the power capabilities of the RHP machine during the entire R&D program so the improvements have been added stepped in time, the heating rate passed from few $K/min$ up to $\approx 1K/s$, drastically reducing the ramp duration and the final diamond degradation.

### 8.2.2 Oxygen content reduction

Even with the usage of the purest available Cu powder (Electrolytic Cu powder, (36), there will always be a residual oxygen content on the powder surface due to the powder production and to the unavoidable exposure to atmosphere. Removing the natural

**Figure 8.3:** Ad hoc powder cleaning system developed at BrevettiBizz.

oxygen layer on powders helps the diffusion across grains of Cu and Mo and the adhesion of Mo to diamonds, resulting in a more compact material.

The powder cleaning can be performed or during the raw powder preparation or during the RHP process when the powders are inserted in the mould, as already made in RHP Technology for CuCD, see Paragraph 7.2.1; both methods use as reducing element a gas made of hydrogen and nitrogen ($3 - 5\% H_2$, higher values would lead to explosion risks at the process temperature) that has to flow through the powder reacting with oxygen and allowing the evacuation of the formed water molecules.

In order to maximize the effectiveness of the process an ad hoc powder cleaning system (Figure fig:powdercleaning) have been developed where the powders are kept in suspension by the flowing $H_2 - N_2$ gas at $600^oC$ inside a quartz pipe. The higher particle surface exposure together with the constant and tailored Temperature allow a more proper and homogeneous powder cleaning than with the cleaning inside the mould. The combination of both methods gave optimal results concerning the reduction of diamond degradation.

### 8.2.3 Choice of Diamond Type

As stated in Paragraph 7.1.2 there are many different types of diamond powder, mainly divided in natural diamonds and synthetic diamonds. The first have higher chemical purity that should avoid the internal bulk graphitization and therefore are often considered as more resistant to diamond degradation. However this phenomena appears at

very high temperature ($> 700^oC$) and it will not observed in MoCuCD plates sintered below $1200^oC$ so higher purity of natural diamonds is not helping in reducing graphitization. On the other hand the superficial graphitization depends on the content of defects and of the reactivity of the diamond surface, and in that case synthetic diamonds are significantly better due to the very smooth and regular surfaces compared to the indented cleavage fracture surfaces of natural diamonds (see Figures 7.4 and 7.3 for the surface comparison) that offer a large number of nucleation points for the graphitization process. For that reason, and after few experimental tests with natural diamonds, synthetic diamonds have been chosen for the final MoCuCD material.

### 8.2.4 Particles Coatings

To reduce the diamond degradation the protective coatings (made to avoid the presence of oxygen at the surface that catalyses the graphitization process) have been studied and applied to MoCuCD during the present thesis work.

Generally, powders are coated for two main reasons: to promote a favourable reaction between non affine elements (active coatings) or to protect the reinforcement from contamination or other degradations that can occur during the cycle (protective coatings). In both cases the coating should be as thin as possible (down to few atomic layers), have homogeneous thickness, be chemically pure and dense. In addition for protective coatings it is important to cover homogeneously all the particle surface avoiding the Oxygen penetration during the production cycle.

Apart from this two kind of coatings, that can be considered as chemically acting coatings, there is a third way coatings might help the sintering process of the material: thick coatings. As we have already pointed out in many occasions the reinforcement must be homogeneously dispersed in the matrix to obtain the maximum of properties because adjacent particles leave voids and large matrix volumes without reinforcement (that will not sinter as supposed to), leading to low thermal and mechanical properties. Of course since the powder mixing cannot be perfect there will always be such kind of non homogeneities in sintered composites leaving adjacent diamonds, so here it comes the idea of transferring the Cu content of the material from the raw Cu powder directly to the diamonds surfaces before the mixing: during the cold mixing the thick coatings assure always a Cu layer of few $\mu m$s between adjacent diamonds resulting in much more compacted materials with respect to analogous non coated composites.

In the case of diamonds this coatings have to be obtained relying on electro-Less methods (89) due to the dielectric nature of the particles; furthermore the low chemical affinity between diamonds and Cu forces to insert an intermediate element that assures the chemical bonding, such as titanium. The result is that such coatings tends to detach from the powder and to give rise to chemical contamination of the final material, as will be shown in details in Paragraph 8.2.5.

### 8.2.5 Copper Coated Diamonds

The Cu coated diamonds (in the following CucCD, see Picture 8.4) used to produce MoCuCD in BrevettiBizz have been extensively studied with SEM and EDS during the thesis to investigate the nature of the coating and to explain the non linear results obtained with the composites produced.

The coating process that has been declared by the supplier is the following: first a very thin deposition of palladium ($\approx\ 1nm$), followed by Cu deposition for $23\mu m$, depending on the position on the diamond surface. The Pd function is to create a chemical affinity between the diamond surface and Cu as anticipated in previous Paragraph.

However during the SEM analysis made on the composite fracture surface at CERN it was not possible to identify the Pd signal by EDS, while we found high concentrations of Ti, P and Ni located near the diamond surface. Ni is usually added in order to increase the deposition rate of Cu, while Ti provides good mechanical bonding between Cu and diamond surfaces (Ti is one of the strongest carbide former). P is present due to its presence in the Ni bath.

All those elements (apart from Pd) have detrimental effects on Cu thermal and electrical conductivity and are usually strictly controlled in Cu metallurgy (36).

#### 8.2.5.1 Sample Preparation and SEM Imaging

In order to check the presence and the position of Ti, Ni and P, a metallographic section of the coating has been analysed at SEM and EDS: the CucCD have been embedded in a conductive metallographic sample (polymer resin with Copper particle addiction, especially used for SEM analysis), that has been polished in order to take away only the coating on one diamond edge, leaving a polished, skewed section of the coating on the side of the diamond, see the scheme in Figure 8.4.

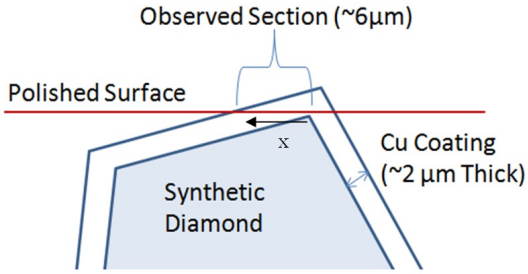


**Figure 8.4:** Scheme of observed section.

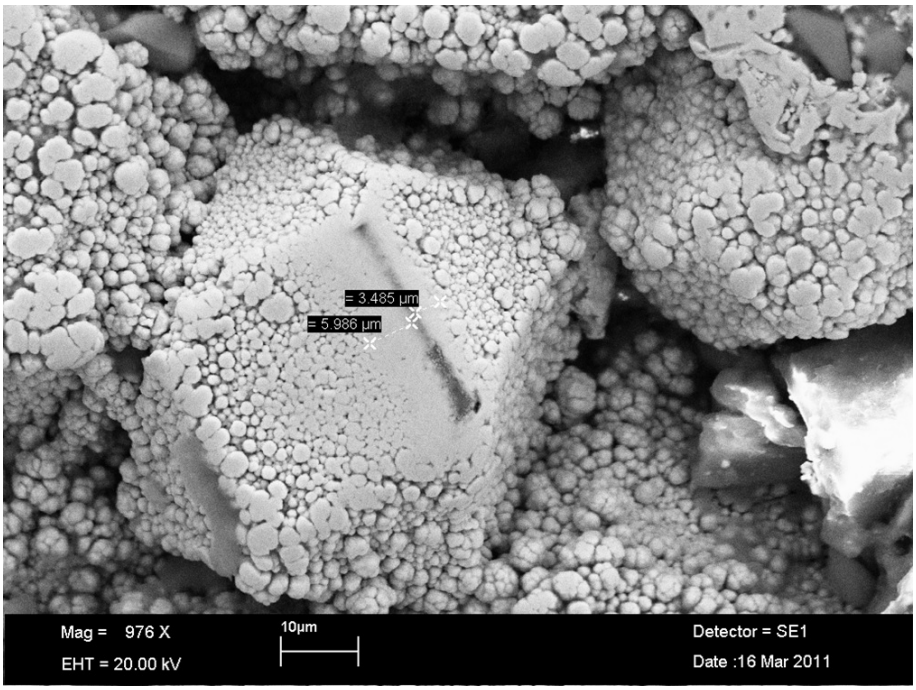


**Figure 8.5:** QBSD Image at intermediate magnification of the observed diamond particle embedded into the polymeric resin sample.The regular shape of the diamond can be clearly seen, together with the regularity of the observed section.

The experimental apparatus used in the present investigation is the SEM Leo 430i coupled with EDS ISIS Software for spectrum analysis; the used filament voltage was 15 kV, a good compromise between analysed area ($\approx$ $2\mu m$) and received signal: the skewed section was necessary to obtain a good spatial resolution between the spectrums, which have been taken along the x direction with intervals of 0.5 $\mu m$.

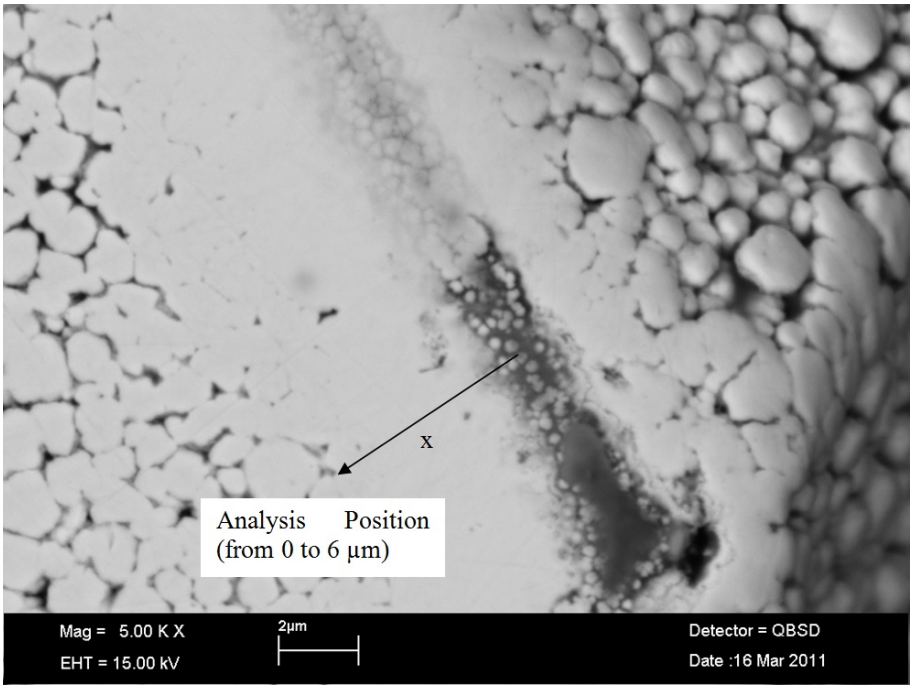


**Figure 8.6:** QBSD Image at high magnification of the analysed surface: the arrow indicates the location of the EDS spectrums, starting from the diamond edge up to the end of the coating section ($6\mu m$).

#### 8.2.5.2 EDS Analysis

To show the evolution of the impurity content the most representative spectrums (taken at 0, 1.5, 3 and 4.5 $\mu m$ along the x direction in Figure 8.6) are reported below: note that the spectrum at 4.5 $\mu m$ (Figure 8.10) is equivalent to the following ones and to the ones taken on the coating surface.

The spectrum taken in position $x = 0$ in Figure 8.7 shows a strong C signal (transmitted through the thin Ti and Cu-Ni layer that remained attached to the diamond surface) together with strong O and Ti peaks. The Cu, Ni and P peaks are also present,

while the Pd peak has not been detected, probably due to the very limited Pd content not detectable by EDS method.

Prosecuting along the thickness at 1.5 $\mu m$ (Figure 8.8 the C, Ti and O peak decrease (as expected) while the P and Ni signals increase significantly; prosecuting along the thickness at 3 $\mu m$ (Figure 8.9 the Ti and O signal totally disappear and also the P signal is strongly decreased.

Finally the spectrum at 4.5 $\mu m$ (Figure 8.10) reports the composition on the coating surfaces.

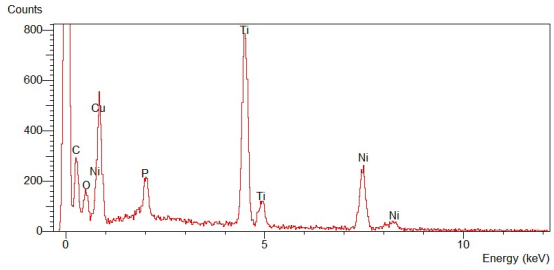


**Figure 8.7:** EDS Spectrum in position $x = 0$ $\mu m$: Presence of C, O, Ti, P, Cu and Ni.

## 8.3 MoCuCD Characterization

As anticipated the following Paragraphs contain the characterization results of the two most important diamond based composites developed during the thesis work: Molybdenum - Copper Diamond with and without Copper coated Diamonds (respectively MoCucCD and MoCuCD).

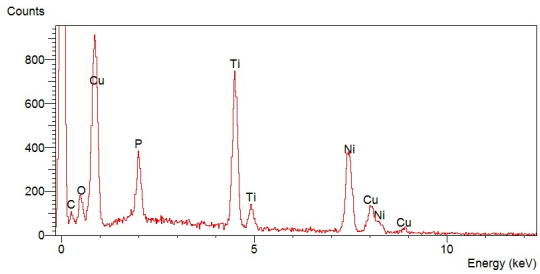


**Figure 8.8:** EDS Spectrum in position $x = 1.5$ $\mu m$: Cu, Ni and P peaks are becoming higher, C peak is reducing while Ti and O peak remain constant.

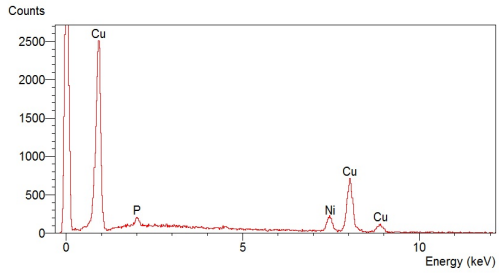


**Figure 8.9:** EDS Spectrum in position $x = 3\ \mu m$: O, C and Ti peaks are not visible, also the P and Ni peaks are reduced.

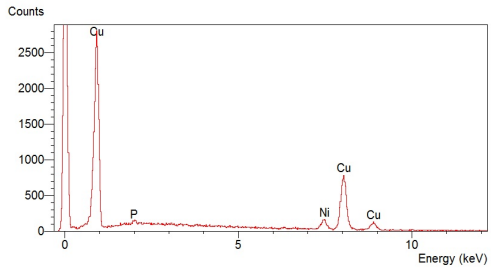


**Figure 8.10:** EDS Spectrum in position $x = 4.5\ \mu m$: presence of Cu and Ni only. P peak is indicated only to show that its signal is negligible on the coating surfaces and therefore cannot be detected on powder during the standard analysis.

### 8.3.1 MoCuCD with Copper Coated Diamonds (MoCucCD)

#### 8.3.1.1 Composition

MoCucCD has been produced with the following parameters:

- Composition of starting powder: 42.72$\%_V$ Cu coated 45 $\mu m$ diamond powder, 50$\%_V$ of 5 $\mu m$ Mo powder and 8.28$\%_V$ of 45 $\mu m$ Cu Powder. The raw powder composition has been calculated taking into account the Cu content on the diamond surfaces to obtain a final composition of $\approx$ 33$\%_V$ diamond, 17$\%_V$ Cu and 50$\%_V$ Mo.
- RHP main parameters: graphite moulds and electrodes, sintering temperature 1200$^oC$ for 30 minutes, constant applied pressure 30$MPa$, vacuum at $10^{-4}mbar$ with reducing atmosphere 97$\%N_2 - 3\%H_2$.
- Produced plates dimensions: diameter 90 mm thickness 4 mm.
- Samples production: water jet cutting followed by manual grinding on diamond tools. Microstructures are all made from fresh fracture surfaces.

The plate production cycle includes all the innovations listed in previous Paragraphs: powder cleaning before mixing, reducing atmosphere and the liquid phase infiltration from molten Cu phase. From the point of view of the composition it is important to remark the passage to smaller 5 $\mu m$ Mo particles instead of previous 45 $\mu m$ powder: the small Mo particles tend to infiltrate the small interstitials increasing the compaction.

#### 8.3.1.2 Microstructural Analysis

A fresh fracture surface of the MoCucCD plate has been observed by SEM and EDS: the pictures are shown below.

#### 8.3.1.3 MoCucCD results

The results of performed analysis in Table 8.1 are reported in a similar way to CuCD comparing the predicted properties to the measured one using the analytical means and the experimental techniques described in Chapter 5.

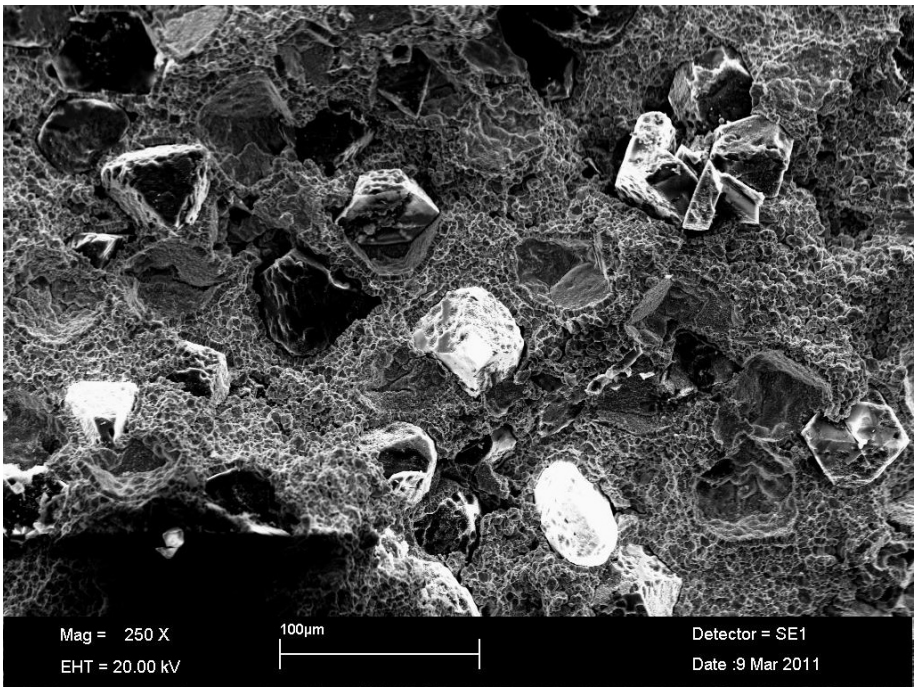


**Figure 8.11:** SE Image at low magnification of MoCucCD. The metallic phase is formed by small Mo particles embedded in Cu, while the diamonds showed some graphitization. The fracture passed preferentially along the diamond-matrix interfaces (absence of broken diamonds).

**Table 8.1:** Predicted and measured properties for MoCucCD at RT. Density and specific heat evaluated by ROM model 5.1, CTE by Kerner model 5.11, k by Hasselmann and Johnson model 5.9 and E is conservatively assuming the Reuss assumption 5.4.

| **Property** | **Unit** | **Estimation** | **Measured** | **Var.** % |
|---|---|---|---|---|
| $\rho$ | $[g/cm^3]$ | 7.79 | 7.15 | 91.8% |
| $\alpha$ | $[10^{-6}K^{-1}]$ | 5.00 | 7.00 | 140.0% |
| $k$ | $[W/m/K]$ | 397.46 | 100.00 | 25.1% |
| $\sigma$ | $[MS/m]$ | 12.67 | 7.10 | 56.0% |
| $E$ | $[GPa]$ | 487.00 | 260.00 | 53.4% |
| $R_{Fl}$ | $[Mpa]$ | $[-]$ | 408 | $[-]$ |

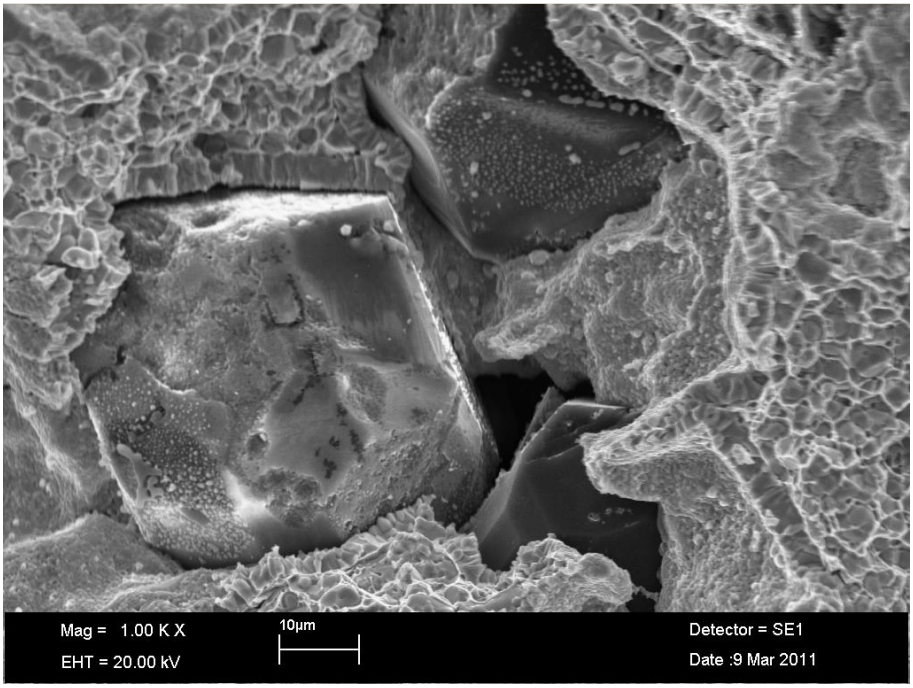


**Figure 8.12:** SE Image at intermediate magnification of MoCucCD. Aspect of a partially graphitized diamond (on the left) and of the surrounding Mo-Cu matrix. The diamonds have plenty of small titanium carbide particles attached due to the reaction between titanium oxide and diamond surfaces.

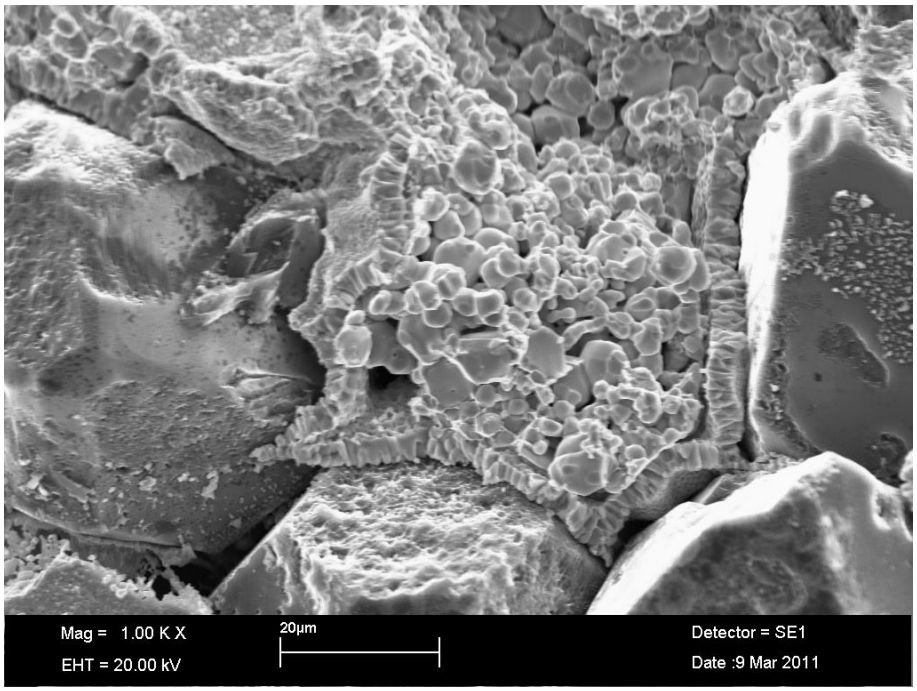


**Figure 8.13:** SE Image at intermediate magnification of MoCucCD: aspect of Mo-Cu matrix. In the spaces between the diamonds the Mo particles are not well compacted and the structure appears porous. Near the diamond surfaces there is a continuous Mo layer formed by small particles all oriented perpendicularly with respect to the diamond surfaces: the formation of this layer could be related to the presence of the Cu coating which encapsulate the Mo particles during heating (when Cu starts to become very soft). The matrix is still porous because there is not enough Cu to infiltrate completely the voids between Mo particles.

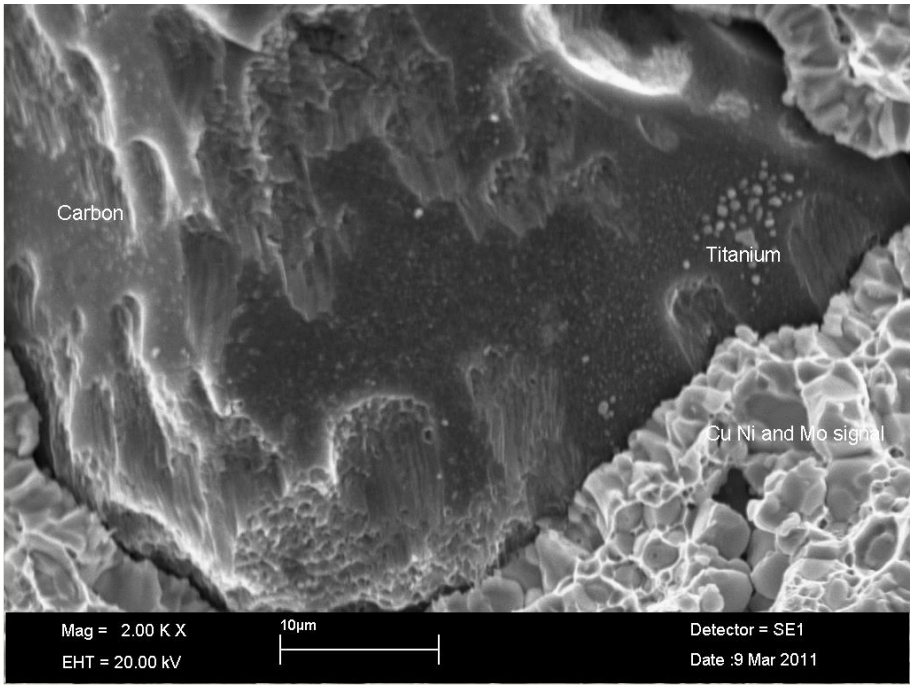


**Figure 8.14:** SE Image at high magnification of MoCucCD: particular of the diamond surface. The diamond graphitization leaded to the formation of holes on the diamond surface where graphite detached. In some area of the diamond there are also the small titanium carbides, while in the matrix near the diamonds we have the presence of Ni (which was present in the Cu coating).

#### 8.3.1.4 Conclusions on MoCucCD

The Cu coating made on the synthetic diamonds has been deeply analysed together with the results obtained with a MoCuCD composite produced. In particular the presence of Nickel and Phosphorous, added to increase the deposition rate, had detrimental effect on Cu thermal and electrical properties as shown by the very low obtained values compared to the expected one (respectively 25.16% and 56.04% of theoretical values).

On the other hand the effect of the first titanium oxide layer is to provide a better mechanical adhesion between the metallic matrix and the diamonds, by the formation of titanium carbides at the diamond surface: the result is an extraordinary flexural strength for such kind of composites.

The drawback is the presence of O close to diamond surfaces (and not removable by powder cleaning methods) that catalysts the superficial graphitization which further reduces the final thermal and electrical properties.

For all those reasons the use of Cu coated diamonds have been avoided in following composites, that instead rely on a deep powder cleaning and to a liquid phase infiltration to obtain a compacted and not graphitized MoCuCD composite.

### 8.3.2 MoCuCD

#### 8.3.2.1 Composition

The final composition of MoCuCD has been modified with respect to MoCucCD increasing the content of synthetic diamonds and Cu to help the space filling:

- Composition of starting powder: $40\%_V$ 45 $\mu m$ synthetic diamond powder, $35\%_V$ of 5 $\mu m$ Mo powder and $25\%_V$ of 45 $\mu m$ Cu Powder.

- RHP main parameters: graphite moulds and electrodes, sintering temperature $1200^oC$ for 30 minutes, constant applied pressure $30MPa$, vacuum at $10^{-4}mbar$ with reducing atmosphere $97\%N_2 - 3\%H_2$.

- Produced plates dimensions: the first test plate ($MoCuCD - 1$) has been made with standard moulds (Diameter 90 mm Thickness 4 mm), then 5 plates $200x80x4$ mm (id. $MoCuCD - P - L_i$ with $i = 1, 5$) have been produced to perform the final material characterization presented in this Chapter.

- Samples production: water jet cutting followed by manual grinding on diamond tools. Microstructures are all made from fresh fracture surfaces.

The production cycle is virtually identical to previous MoCucCD apart from the raw material's and the powder mixing procedure: in order to reproduce the benefit effects of the thick Cu coating (absence of interstitials between Diamonds) the powder mixing has made in sequential steps mixing first hydrogen cleaned diamonds and Mo particles adding Cu only during the last step. The high chemical affinity (enhanced by the powder cleaning at $600^oC$ that leaves very reactive surfaces) between Mo and diamond helps in keeping the metallic particles close to the diamonds surfaces even after the powder insertion in the mould. The result is an optimal starting powder spatial distribution that allows:

- Optimal formation of $Mo_2C$ carbide at the interface
- Filling of the interstitials between diamonds
- Surrounding of diamonds by Mo particles like in plate MoCucCD (see Figure 8.13)
- Matrix filling by molten Cu due to sponge effect

As in previous Chapter we will first see the materials micro structures, followed by the characterization results and by the conclusions on MoCuCD R&D program.

#### 8.3.2.2 Microstructural Analysis

The microstructure of plates $MoCuCD-P-L_i$ have been deeply analysed discovering a situation very similar to previous $MoCucCD$ plate, as explained in following pictures 8.15, 8.16, 8.17 and 8.18.

#### 8.3.2.3 Mechanical Characterization

The mechanical characterization has been started at CERN by flexural tests and then prosecuted at the Dynamic Laboratory of Politecnico di Torino with quasi-static and dynamic compressive tests and temperature dependent tensile tests.

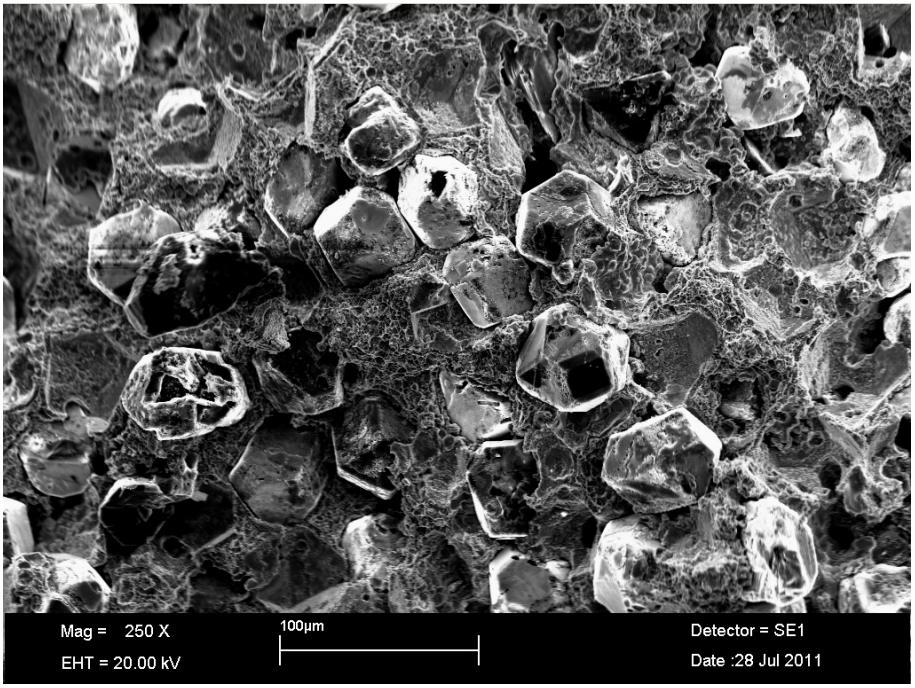


**Figure 8.15:** SE Image at low magnification of MoCuCD-P-L1 fracture surface. The fracture passes as in previous composites preferentially along the diamond matrix interface. The majority of Diamonds are well spaced but there is the presence of empty interstitials between Diamonds.

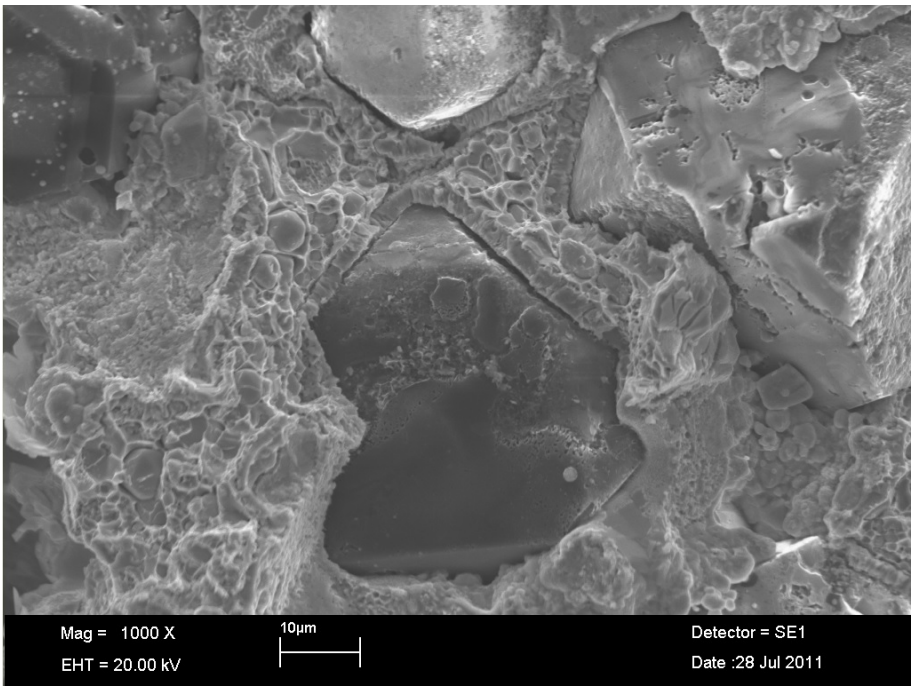


**Figure 8.16:** SE Image at high magnification of MoCuCD-P-L1 fracture surface. The diamond surface is still covered by $Mo_2C$ and appears only slightly graphitized. The Mo distribution along the diamond surface is still present thanks to the new powder mixing method. The matrix looks dense with Cu infiltrating deeply the porous Mo matrix.

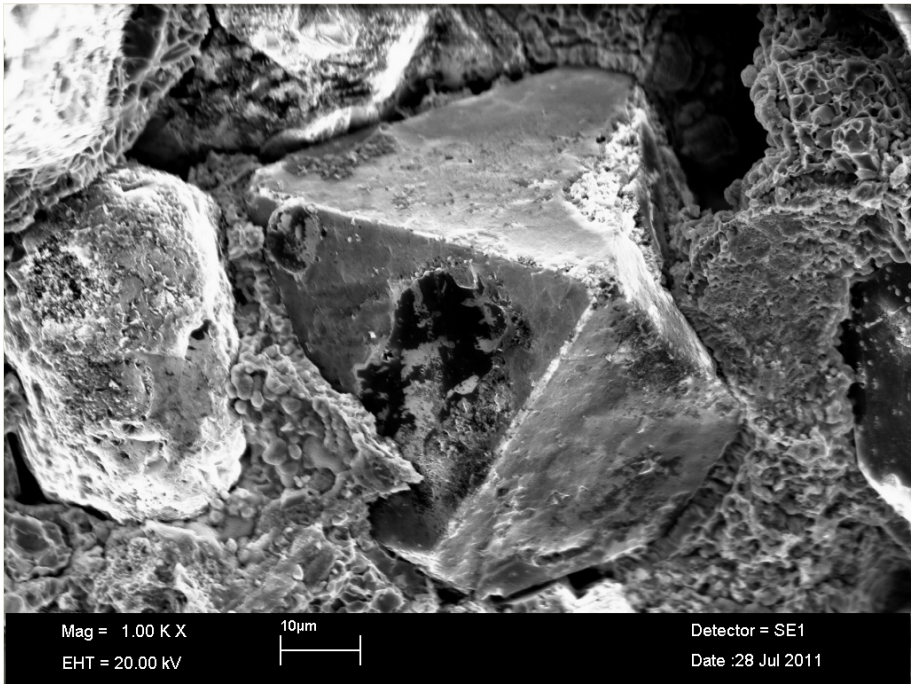


**Figure 8.17:** SE Image at high magnification of MoCuCD-P-L1 fracture surface. Detail of diamond superficial aspect, thanks to charging effect if the diamond surface is rough (due to graphitization or bonded particles) it will appear brighter as the upper right edge of the diamond.

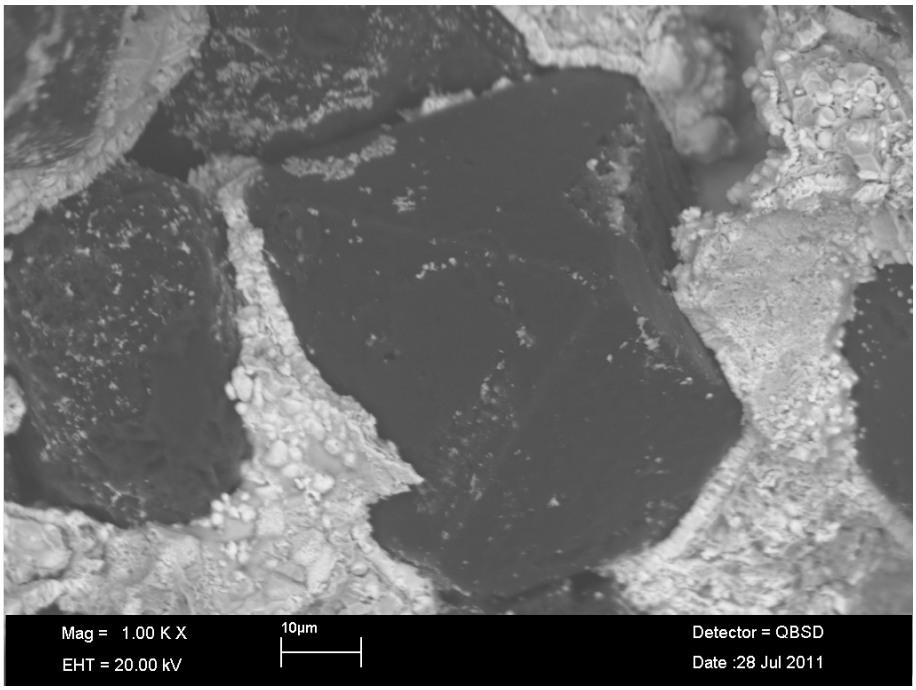


**Figure 8.18:** QBSD Image at high magnification of MoCuCD-P-L1 fracture surface in the exact same position of Figure 8.17. The QBSD technique allows to distinguish between $Mo_2C$ carbides attached to diamond surface and graphite thanks to their density contrast (lighter materials are darker), as the case of the upper right diamond edge that in fact is covered by formed $Mo_2C$, while the other regions without grey in QBSD Image are effectively graphitized areas.

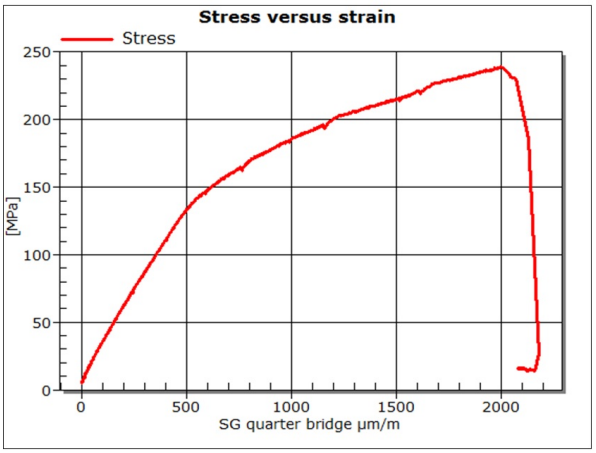


**Figure 8.19:** Flexural test results for MoCuCD.

The flexural Tests have been performed using Strain Gauges glued to the samples to measure also the real elongation of the stretched side of the samples, allowing the evaluation of the Young's Modulus $E$.

The results are reported in Figure 8.19, the measured average Youngs Modulus and Elongation to fracture being respectively $260GPa$ and 0.21% while the Ultimate Flexural Strength $R_{Fl}$ is $\approx 240MPa$. The fracture is completely brittle without visible plasticity of the metallic matrix as shown in the Fracture Surface Microscopy.

The Quasi-Static Tests (c1 and c2 in Figure 8.20) show yielding around $700MPa$ followed by stress reduction until 0.15% of Strain, and then the increases again until fracture. The explanation for the behaviour is related to the intrinsic microstructure of the material: after the first elastic part, there is a very small plastic deformation of the metallic matrix, which continues until the Diamonds starts to touch each other; in this moment the material retrieves some strength until fractures (orientated along radial direction) are forming on the external surface, causing the failure of the samples with a Stress around $750 - 780MPa$.

Looking at the dynamic tests (h2 and h3 in Figure 8.20) we can see an analogue plot, that has a much higher Yielding Stress ($\approx 1100MPa$) together with the same sub sequential reduction due to matrix deformation; in dynamic conditions the matrix has less time to deform and form the superficial cracks so that the Failure appears over $1500MPa$. The failure appears more like a total disaggregation of the samples instead of crack formation like in quasi-static case, but the mechanism has not been yet fully eviscerated.

Finally, the two tests reported in Figure 8.21 have been made in quasi-static conditions at RT and at $600^oC$; the heating has been made by an induction spire located in the loaded zone of the sample, the measurement of deformation has been made by extensometers and the temperature has been measured by a $PT - 100$ sensor glued on the sample surface. The curve at RT shows a Youngs Modulus around $270 - 275$ GPa (in good agreement with the flexural tests) and an ultimate strength around $140MPa$. The plasticity is negligible ($< 0.002\%$). The curve at $600^oC$ shows a much lower ultimate strength ($\approx 65MPa$) and Youngs Modulus ($\approx 40 - 50GPa$) together with a slightly higher elongation to fracture ($\approx 0.005\%$).

It is worth noting that during the heating on air of the samples above $600^oC$ Mo react with the water present in the atmosphere forming complex hydrated Mo oxides

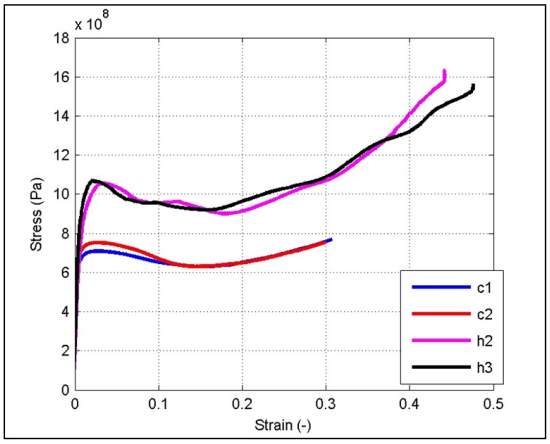


**Figure 8.20:** Compressive Tests performed at Politecnico di Torino. c1 and c2 are the curves obtained by quasi-static tests, while h2 and h3 are obtained by Hopkinson Bar Tests (strain rate $\approx 1000s^{-1}$).

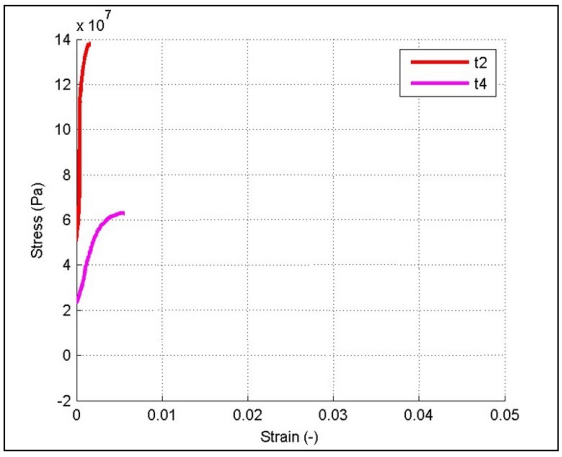


**Figure 8.21:** Tensile Tests performed at Room Temperature (t2) and at $600^oC$ (t4) on MoCuCD.

(formerly known as Molybdenum Blue).

#### 8.3.2.4 Thermal Characterization

After the preliminary estimation of the thermal conductivity using CERN's thermal test bench on the sample obtained from the diameter 90 mm test plate, the final thermal characterization of MoCuCD has been carried out at AIT by Dr. W. Hohenauer using samples obtained from the $MoCuCD - P - L_i$ plates. The values reported are the combination of three different samples obtained from the same plate.

The characterization techniques and instruments are the same used by Dr. Hohenauer for Inermet180 thermal characterization:

- Specific heat by Dynamic Scansion Calorimeter (DSC Netzsch 404 coupled to a precision balance Sartorius ME235P) from RT to $900^oC$
- Thermal expansion coefficient by push rod dilatometer (Netzsch $Dil - 402$) from RT to $900^oC$
- Thermal diffusivity by Laser Flash (LFA Netzsch 427) from RT to $900^oC$
- Thermal conductivity is then evaluated by using equation 6.4

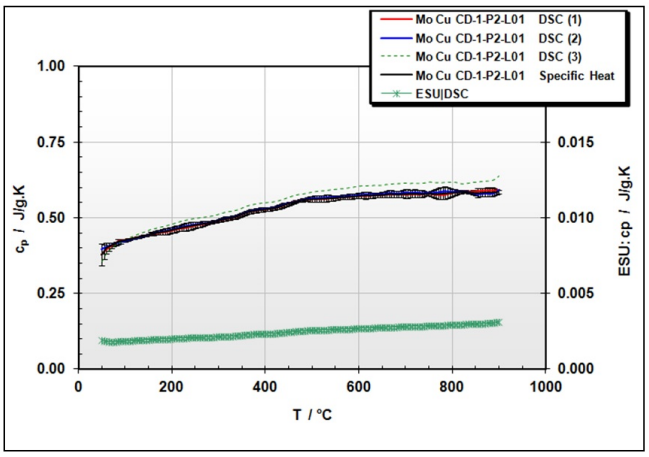


**Figure 8.22:** Plot of specific heat of MoCuCD as a function of the temperature. The $c_p$ confirms the good thermal stability of MoCuCD at least in vacuum environment.

The specific heat plot in Figure 8.22 shows that the specific heat increases linearly from 360 $J/KgK$ at RT to $590 - 640$ $J/KgK$ at $500^oC$, after it remains constant

up to $900^oC$. Note that there is no phase change or chemical reaction taking place during the heating: since the measurements have been performed under controlled Ar atmosphere, we can exclude the presence of unwanted reactions inside the material in the LHC Collimator operational conditions (UHV).

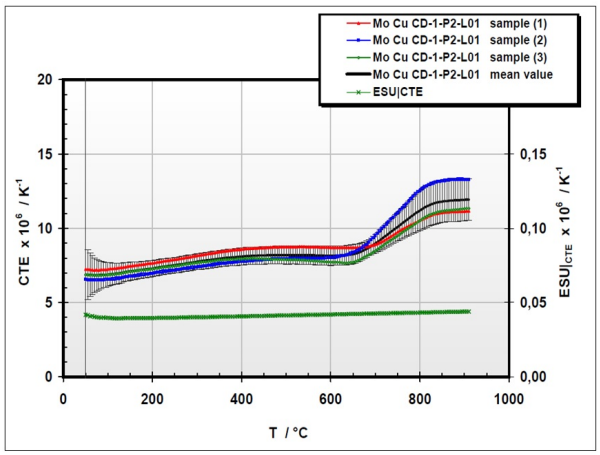


**Figure 8.23:** Plot of CTE of MoCuCD as a function of the temperature. The CTE shows a large instability at $700^oC$ that is related to Cu expansion.

As can be seen in Figure 8.24, the thermal conductivity starts from $\approx 160W/mK$ at RT and then decreases slowly to $\approx 115W/mK$ at $900^oC$. The discontinuity observed at $700^oC$ is not an experimental error since it is confirmed also by the CTE measurement in Figure 8.23: the CTE in fact starts from 7 $10^{-6}K^{-1}$ at RT and increases regularly up to 8 $10^{-6}K^{-1}$ at $400^oC$ remaining then constant up to $650^oC$; at that moment the stress generated by the blocked thermal expansion of Cu overcomes the bonding force of the net made by Mo and diamonds and the material starts to expand significantly reaching $\approx 12$ $10^{-6}K^{-1}$ at $800^oC$. After it remains constant.

#### 8.3.2.5 Electrical Characterization

The electrical conductivity has been measured at CERN using the SigmaTest 2.067 measuring device presented in Paragraph 6.1.2. The working frequency as been fixed to $60kHz$, that corresponds to a penetration depth of the measure around $0.5mm$. The first cylindrical plate $MoCuCD-1$ has been measured in nine positions on both sides in order to check eventual non homogeneities of the superficial conductivity, while the other 5 plates $MoCuCD-P-L_i$ have been measured in 40 positions for each side,

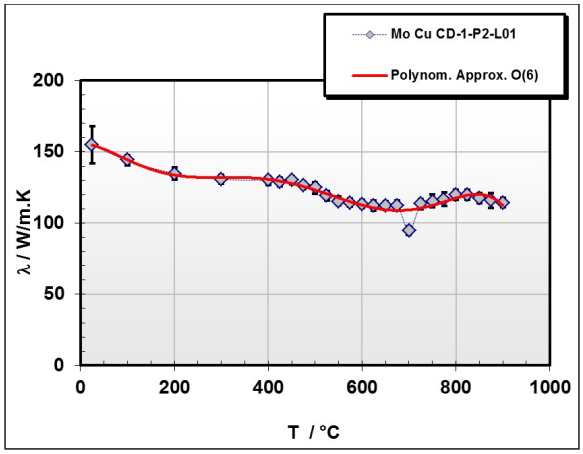


**Figure 8.24:** Plot of thermal conductivity of MoCuCD as a function of the temperature. The large instability at $700^oC$ is always present on different samples and is observed at every thermal cycle.

each position representing an area of $4cm^2$: the measurements permits to identify local variations in Copper superficial content, as shown in Figure 8.25 below.

#### 8.3.2.6 MoCuCD Results

As for the other materials the final properties of MoCuCD are compared in Table 8.2 to the predicted ones in order to evaluate the effectiveness of the material's R&D.

**Table 8.2:** Predicted and measured properties of MoCuCD at RT. Density and specific heat evaluated by ROM model 5.1, CTE by Kerner model 5.11, k by Hasselmann and Johnson model 5.9 and E is conservatively using the Reuss assumption 5.4.

| Property | Unit | Estimation | Measured | Var. % |
|---|---|---|---|---|
| $\rho$ | $[g/cm^3]$ | 7.22 | 6.9 | 95.6% |
| $\alpha$ | $[10^{-6}K^{-1}]$ | 5.38 | 7.00 | 130.0% |
| k | $[W/mK]$ | 422 | 155 | 36.7% |
| $\sigma$ | $[MS/m]$ | 15.62 | 10.00 | 64.0% |
| E | $[GPa]$ | 487 | 260 | 53.4% |
| $R_{Fl}$ | $[Mpa]$ | $[-]$ | 240 | $[-]$ |

- Increase in thermal conductivity allows to overcome pure Mo value, however the thermal barrier due to unavoidable graphitization of diamonds hampers an

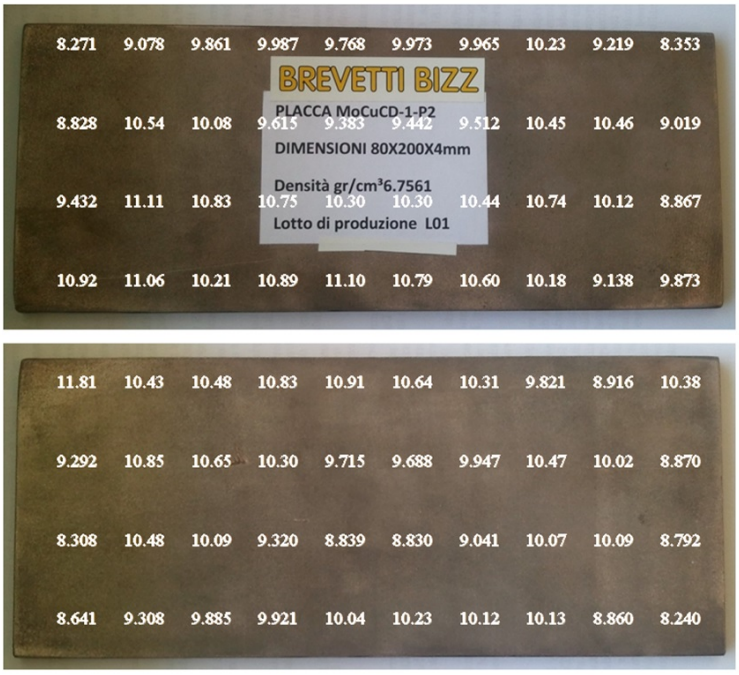


**Figure 8.25:** Aspect of large 200x80x4 mm MoCuCD-1P2-L01 plate plus Electrical Conductivity measurements. Values in MS/m.

optimal heat transfer across the interfaces not allowing to take advantage of the excellent heat transfer of the Diamond Phase.

- Increase in electrical conductivity thanks to a high purity of the raw material. In addition the electrical conductivity maps confirm the good homogeneity of the produced plates. The electrical conductivity is less conditioned by the diamond graphitization so the final value is closer to the predicted one.
- The Young's Modulus is influenced by the interface made by $Mo_2C$ and graphite that contribute to reduce the final value with respect to the predictions.
- The presence of significant quantity of Cu results in high CTE values above $700^oC$ that will reduce the material thermal stability at high temperatures.

## 8.4 Conclusions on MoCuCD

The R&D Program on MoCuCD brought after approximately one year of experimental activity to a suitable material for BID devices: the composite MoCuCD has good com-

paction, good thermal conductivity and adequate mechanical properties. In addition the electrical conductivity is good for a Mo composite having the 40% in volume of diamonds. The values of the properties together with the FoM estimations are reported in Table 8.3 below.

**Table 8.3:** Final properties and Figures of Merit for MoCuCD compared to CuCD and MoCucCD. Values with * for MoCucCD have been assumed, in absence of apposite tests, to be equal to MoCuCD ones.

| **Material** | **Unit** | **CuCD** | **MoCuCD** | **MoCucCD** |
|---|---|---|---|---|
| Density | $[g/cm^3]$ | 5.4 | 6.9 | 7.15 |
| Atomic Number (Z) | $[-]$ | 11.4 | 17.4 | 20.2 |
| Melting Temperature | $[^oC]$ | 1083 | 1083 | 1083 |
| Thermal Conductivity | $[W/mK]$ | 490 | 155 | 100 |
| CTE | $[10^{-6}K^{-1}]$ | 7.8 | 7 | 7* |
| Specific Heat | $[J/kGK]$ | 420 | 360 | 360* |
| Young's Modulus | $[GPa]$ | 220 | 260 | 260* |
| Tensile Strength | $[MPa]$ | 70 | 140 | 250 |
| Poisson's Ratio | $[-]$ | 0.22 | 0.3 | 0.3* |
| Electrical Conductivity | $[MS/m]$ | 12.6 | 10 | 7.1 |
| Radiation Length $\chi_0$ | $[cm]$ | 4.78 | 2.82 | 2.82* |
| SSNI | $[kWm^2/kg]$ | 11.6 | 3.2 | 2.0 |
| TSNI | $[kJ/kg]$ | 13.4 | 19.4 | 34.6 |

The proposed material has however some intrinsic limits that will play an important role in the final material choice:

- Brittle behaviour with limited tensile strength;
- Moderately high CTE, with a drastic increase around $700^oC$.
- Sufficient but not enthusiastic thermal conductivity (only few % higher than pure Mo), due to residual diamond graphitization.
- The density of $\approx$ 7 $g/cm^3$ is probably too high for the use in secondary Collimators, as discussed in Chapter 11.

# 8. MOLYBDENUM - COPPER - DIAMOND (MOCUCD) COMPOSITES

For all those reasons the research moved to the next family of composites, Molybdenum carbide - Graphite (MoGR), in order to overcome the two limitations of Cu content and diamond degradation.

# 9

# Molybdenum Carbide - Graphite (MoGR) Composites

Present Chapter introduces the molybdenum carbide-based composite developed during the thesis work. The Chapter starts as usual with an introduction about the properties of the constituents (graphite and $Mo_2C$), passing then to the innovations implemented and to the results obtained.

## 9.1 Introduction to carbide-reinforced CMC

Starting from the idea that to better match the requirements for Hi-Lumi LHC Collimators it is necessary to reduce the CTE and the density of the composite with respect to MoCuCD while increasing its resistance to high temperatures, we did two assumptions:

- no more presence of high CTE and low melting phases (Cu);
- use of graphite flakes instead of diamonds.

The first assumption permits us to have a material that is made only by high melting points components, giving the maximum as possible of thermal stability and high melting temperature.

The second assumption is more drastic and relies on the following considerations:

- Graphite is lighter than diamonds;

- Graphite is already the most stable form of carbon, while Diamond is metastable and degrades when heated;
- Graphite is strongly anisotropic and shows exceptional properties along the $< 1000 >$ direction of the crystallographic lattice, while has poor properties on the other direction. If properly oriented the graphite grains will give exceptional properties in the planar direction, which is the most important for the collimators strength;
- Graphite is much cheaper than diamonds and permits to increase the number of tests with the same budget.

Concerning the carbide phase, the choice fall on molybdenum carbide because is one of the most promising refractory carbide in terms of thermal stability at high temperatures: Mo is added in the form of pure metallic powder that, at the temperatures needed for the process, completely react with graphite forming hexagonal molybdenum carbide $Mo_2C$, as described in Paragraph 9.3.1. The material has been however commonly called Molybdenum Graphite (in the following MoGR) instead of Molybdenum Carbide - Graphite for simplicity.

### 9.1.1 Previous R&D on Metal Carbide - Graphite Composites

The first investigations on the feasibility of composite materials made by refractory metal carbides and graphite were made in the early 60s at IITRI by Y. Harada and G.A. Rubin (90). The work of Harada focused on the graphitization and sub sequential reaction of calcined petroleum coke with metallic powder of various carbide forming metals: the Hot Pressing process have been made at very high temperatures ($2800^oC$ and $3000^oC$ for MoGR composites) resulting in the complete melting of metal carbide phase which is then squeezed out of the composite by the applied pressure, leaving a composite material having a volume fraction of carbide somewhere between 5 and 10%. The process permitted to obtain good mechanical and electrical properties but is intrinsically limited by the petroleum coke reaction mechanism: during the hot pressing a non quantifiable amount of $Mo_2C$ flows out from the mould giving rise to non-homogeneities in the material microstructure and to difficulties in the production of a material with a precise and reproducible composition. A second problem of petroleum

coke is the formation of volatile organic compounds during heating. In fact, many trials have been made in the past to increase the resistance of the metal carbide graphite composites, focusing mainly on the reduction of porosity due to the volatile element formation: John and Jenkins (91) proposed in the 80s a technique for the hot-working of many metal carbide - graphite composites, obtaining a significant reduction in porosity. However, even if they started from a mixture of pure metallic (or metal carbide) powder and graphite, there was the melting and the squeezing of the liquid metal carbide during the process. To overcome these limitations and to have the complete freedom in the choice of the material composition, we explored a different way to produce the composite that does not involve organic precursors or liquid phase formation: the solid state reaction between pure graphite flakes and Mo powder at temperatures lower than the melting point of $Mo_2C$. The possibility to change the composition without limitations due to the process is crucial for the tailoring of the composite density that will allow us to match the optimal beam cleaning of the collimation system during LHC operations.

### 9.1.2 Graphite Properties

Graphite is a ceramic material composed by an allotropic form of carbon consisting in loosely packed layers of hexagonally arranged $sp^2$ carbon atoms (graphene layers), that can be found naturally on earth or produced artificially by carbonization and graphitization of an organic precursors. In this electronic configuration there is one remaining $\pi$-orbital electron for each carbon atom. In the case of the hexagonal graphite cell these electrons form a large delocalized high electron probability region commonly called benzene ring (see Figure 9.1).

The delocalized electrons assure an excellent heat and electrical transport along the planar direction, while the covalent $sp^2$ bonds oriented at $120^o$ give very high stiffness.

Graphite is then composed by a multiple packing of graphene layers bonded by weak Van der Waals forces, with the packing structure represented in Figure 9.2 (31): the graphene layers are free to slide on top of each other giving to graphite a very low friction coefficient that is of valuable interest for many applications where dry lubrication is needed (an example are the rings of the shaft in LHC Primary Collimators). The graphene planes are usually identified by the crystallographic plane $\{0001\}$ while the directions along the plane are all the $< 1000 >$.

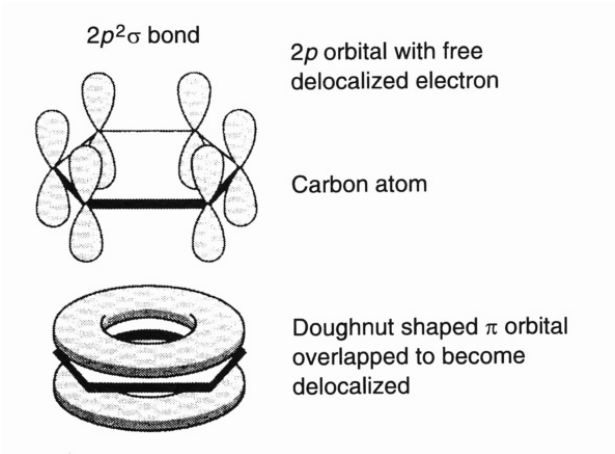


**Figure 9.1:** Schematics of the electron delocalization in graphite single molecule. For extended foils of graphene the delocalized region can be considered as continuous all over the plane.

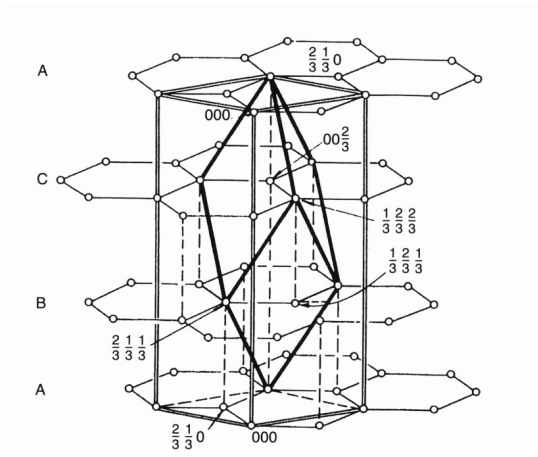


**Figure 9.2:** Scheme of the graphite cell.

Since the $sp^2$ carbon form is stable at standard Temperature and Pressure Graphite is the most common form of carbon on earth (see the Carbon phase diagram shown in Figure 7.5 in Chapter 7).

Graphite is present in a wide variety of forms giving rise to a certain incertitude on its properties definition: ideally perfectly crystalline graphite (like the one used in the present work) has a brilliant silver like aspect and exhibits excellent thermal and mechanical properties along its planar direction, whereas polycrystalline graphite appears dark grey and has very low thermal and mechanical properties. Probably the most commonly used form of graphite in industry is extruded polycrystalline graphite, which shows anisotropic properties with elongated grains along the axis that increase the degree of crystal orientation in the material.

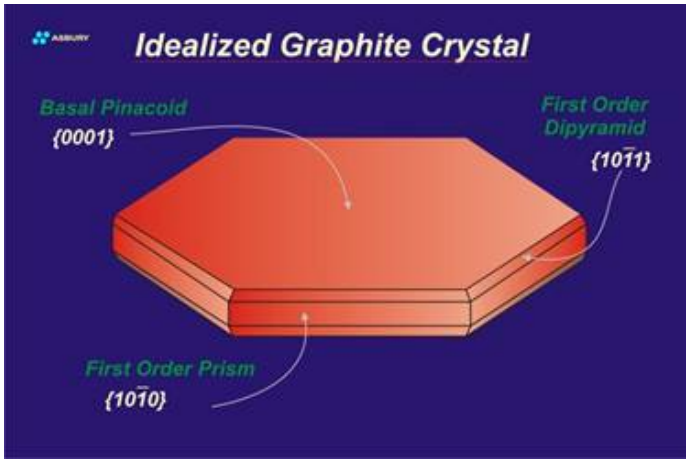


**Figure 9.3:** Idealized Graphite Crystal structure. Source Asbury Graphite website (3)

It is difficult to give precise values for the ideal single graphite crystal properties (see Figure 9.3 (3)) since such material does not exist in real world and the properties given in this work are either calculated or based on measurements of graphite crystals that approach the ideal crystal structure (92). A brief list of relevant properties for the single graphite crystal at RT is given in table 9.1 for the ideal graphite crystal compared to the polycrystalline pyrolytic graphite R4550. Note that all the properties measured on MoGR materials produced are evaluated along the planar direction, that as we will see in the X-Rays Diffraction results (9.4.2 ) corresponds roughly to the {0001} plane of graphite crystals.

**Table 9.1:** Properties of ideal graphite crystal compared to pyrolitic Graphite $R4550$ used for LHC Collimators.

| Material | Unit | Graphite R4550 | Ideal Graphite Crystal | |
|---|---|---|---|---|
| | | | 0001 Plane | $10\bar{1}0$ plane |
| Density | $[g/cm^3]$ | 1830 | 2.2625 | 2.2625 |
| Atomic Number (Z) | $[-]$ | 6 | 6 | 6 |
| Melting Temperature | $[^oC]$ | 3650 | 3650 | 3650 |
| Thermal Conductivity | $[W/mK]$ | 100 | 4180 | 2 |
| CTE | $[10^{-6}K^{-1}]$ | 4 | 25 | -0.5 |
| Specific Heat | $[J/kGK]$ | 710 | 710 | 710 |
| Elastic Constants | $[GPa]$ | $E = 11.5$ | $C11 = 1060$ | $C44 = 4$ |
| Tensile Strength | $[MPa]$ | 40 | [-] | [-] |
| Electrical Conductivity | $[MS/m]$ | 0.077 | 0.2 | $3.30 * 10^{-4}$ |

The exceptional properties of the single crystal are of course impossible to be reproduced into a massive material but are a very good starting point for the novel materials $R\&D$. It is worth mentioning that graphite burns in oxygen-rich atmosphere already at $400^oC$ therefore its usage as refractory element is limited to vacuum or inert environments.

The graphite powder that used for MoGR production is the Asbury 3260 spheroidal graphite flakes: this graphite powder exhibits the highest chemical purity and degree of graphitization of lamellar graphite flakes with small dimensions ($45\mu m$) and a regular round shape that helps the compaction of the powder and reduces the final anisotropy of the composite. See Figure 9.4 for the SEM image.The two main advantages of spheroidal graphite particles are:

- good mixing of raw powders, resulting in higher compaction of final composite.
- lower dimensions and possibility to select a chosen powder size by riddling the powders.

It is important to point out that the spheroidal graphite particles will recrystallize during the process giving rise to an anisotropic structure even if they were not oriented during the powder deposition inside the mould: on the other hand the use of spheroidal graphite helps in having a fine $3 - D$ distribution of graphite in the final composite.

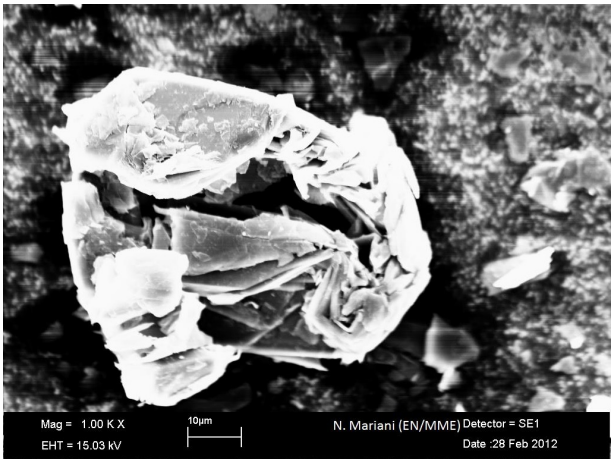


**Figure 9.4:** SE Image at high magnification of Asbury 3260 Graphite flake.

### 9.1.3 Molybdenum Carbide Properties

Refractory metal carbides such as hexagonal $Mo_2C$ have been studied in the last years because of their exceptionally high maximum operating temperature, for example $Mo_2C$ melts slightly above $2500^oC$ and maintains adequate properties up to $2000^oC$. The phase diagram of the system Molybdenum - Carbon is reported in Figure 9.5 (93) while a brief list of properties taken from literature (94) is reported in table 9.2.

**Table 9.2:** Physical and mechanical properties of hexagonal $Mo_2C$.

| **Material** | **Unit** | $Mo_2C$ |
|---|---|---|
| Density | $[g/cm^3]$ | 9.06 |
| Atomic Number (Z) | $[-]$ | 18 |
| Melting Temperature | $[^oC]$ | 2505 |
| Thermal Conductivity | $[W/mK]$ | 21.5 |
| CTE | $[10^{-6}K^{-1}]$ | 7.9 |
| Specific Heat | $[J/kGK]$ | 148 |
| Young's Modulus | $[GPa]$ | 347 |
| Poisson's Ratio | $[-]$ | 0.234 |
| Electrical Conductivity | $[MS/m]$ | 1.4 |

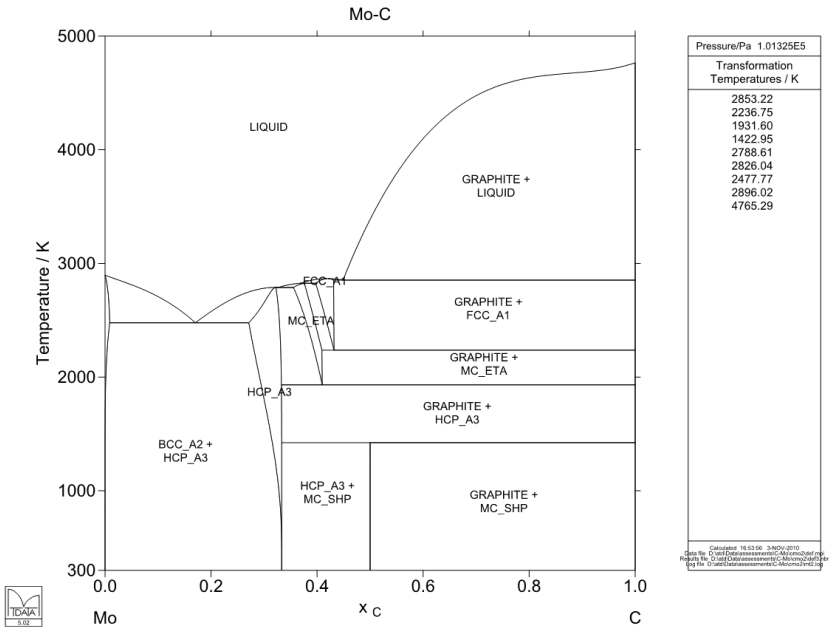


**Figure 9.5:** Calculated phase diagram of the Molybdenum - Carbon system.

## 9.2 MoGR for LHC Collimators

## 9.3 MoGR Production

### 9.3.1 Molybdenum Carbide formation reaction

Mo and graphite are chemically affine to each other; when fine powders of metallic Mo and Graphite are heated up over $1000^oC$ they immediately form hexagonal $Mo_2C$: the reaction is controlled by the atomic diffusion of Carbon atoms inside the Mo bcc lattice interstitials. When the amount of carbon reaches the $33\%_{at}$ a new structure of hexagonal $Mo_2C$ starts to growth from the interface between Mo and graphite and prosecutes the transformation of the entire Mo grain (84).

$$2Mo \ + \ C \leftrightarrow Mo_2C \tag{9.1}$$

The reaction prosecutes by the diffusion of C inside $Mo_2C$ and the formation of MoC carbide: MoC can have a good effect on the mechanical properties if we manage to finely disperse it inside the $Mo_2C$ matrix, otherwise the presence of MoC at grain boundaries

or in acicular form inside the grains can reduce significantly the final strength of the composite. For that reason we need to find the good combination of temperature and sintering time to obtain a fine dispersion of MoC inside the $Mo_2C$ grains. Finally, since the entire process is diffusion controlled, we can play with the powder dimensions to increase or reduce the reaction kinetic maintaining constant the sintering parameters.

### 9.3.2 Sintering Aids in High Temperature sintering

The diffusion activated reaction occurring during the sintering of MoGR is a slow process that requires time and energy to be accomplished. Fortunately, the diffusive physical process can be enhanced by adding some activator element in the starting powder: many studies have been done on Mo (and W) activation sintering (95) showing that the addition of small amounts of other metals on Mo particles surfaces will enhance the diffusion between adjacent Mo grains, resulting in faster compaction of the particles. For Mo the main activator element is Pd, followed by Ni, Rh, Co, Pt, Au and Fe.

In literature works, the effect of having atomic mono layers of activator on W and Mo particles has been investigated, and two different mechanism have been presented: the model of Brophy, Hayden and Wulff (95) foresees that the diffusion of Mo is enhanced in the activator phase, so that Mo diffuses preferentially inside the activator layer instead than diffusing trough the interface between adjacent Mo particles, therefore the bonding will be assured by connecting the surfaces of Mo adjacent particles; the second model from Toth and Lockington, always presented in the paper of Corti, on the other hand foresees that Mo dissolves at the interface Mo-Activator, forming an intermediate layer with mixed composition that interacts with the intermediate layer of the adjacent particle forming a Mo-Activator bonding zone. The two models are represented in the Figure 9.6 for the system W-Ni.

The most suitable elements for Mo activation are Pd and Ni (96): the effect of Pd is higher than the one of Ni, but the first choice in terms of availability and costs would be Ni, because Pd has a much higher price. Unfortunately, Ni addition has a detrimental effect on Mo mechanical properties and has therefore been rejected (97). In fact Ni is not soluble in Mo lattice at low temperatures, and during cooling there will be the segregation of $\delta$ Ni-Mo inter metallic phase at grain boundaries, which is brittle and has a low melting point ($1360^oC$) (98). Pd, on the other hand, is soluble in

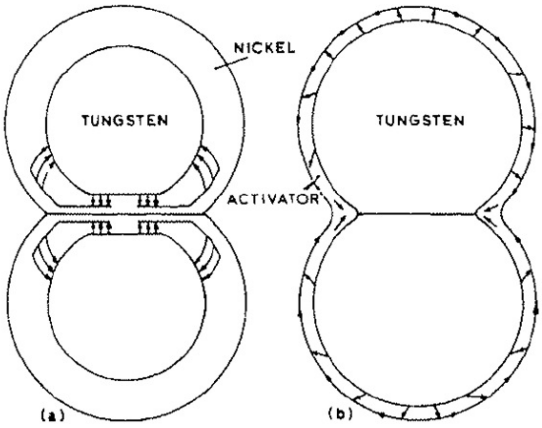


**Figure 9.6:** a) Model of Brophy, Hayden and Wulff; b) Model of Toth and Lockington for Ni assisted W sintering. The mechanism is the same for Mo.

Mo up to $3\%_w$ at RT (98), therefore will not form the brittle inter granular compound. For this reason Pd has been chosen as sintering activator in the present study.

Pd powder ($0.25 - 0.55\mu m$) has been added to the Mo powder in amount of $0.8\%_w$. The powders will be mixed together before to start the sintering process in multiple steps to assure the best homogenization as possible. This situation will be different from the one described in the already mentioned works (95) because he coated W and Mo powder with a very thin and regular layer of activator elements instead of adding pure powders of activator to the mixture.

### 9.3.3 Production cycle improvements

All tests plates of MoGR have been produced at BrevettiBizz using the modified RHP machine shown in Figure 9.7: the machine is able to reach very high heating rates (in the order of $1K/s$) while maintaining hydrogen rich atmosphere inside the sintering chamber to reduce the oxygen content, that can reduce significantly the diffusion at grain boundaries as previously discussed.

A complex cooling circuit has been implemented by S. Bizzaro to keep the temperatures of the external part of the machine at RT when having $1700^oC$ inside the sintering chamber: the combination of very high temperatures, hydrogen rich atmosphere and very high heating rates permits to control with high precision the sintering process

**Figure 9.7:** Hot Pressing Machine used for MoGR production at BrevettiBizz.

limiting the detrimental effects of heating and cooling ramps. In addition the powders are always cleaned under hydrogen atmosphere to reduce the natural superficial oxygen absorption like for MoCuCD (see paragraph 8.2) inside the machine especially developed by BrevettiBizz shown in Figure 8.3.

The main innovation of the proposed production technique is the use of high purity graphite flakes as carbon source. The other additions are pure Mo powder (a combination of $5\mu m$ and $45\mu m$ Mo particles shown in Figure 9.8 and Figure 9.9 respectively) and very fine Pd powder (as explained in paragraph 9.3.2).

The absence of the pyrolysis reaction of the calcined petroleum coke avoids the formation of volatile molecules and reduces the amount of impurities in the final composite, resulting in dense, pure structures. In addition graphite flakes have a very high degree of densification, which permits to obtain a fully dense graphite phase even sintering at temperatures below $2000^oC$. A complete characterization of the starting powders has been performed at CERN (see Paragraph 9.1.2 in order to check the effective powder size, shape, chemical purity and the presence of inclusions for all used powder. Graphite flakes are obtained by high temperature processing of natural graphite and are supposed to be made by close packed layers of $sp^2$ carbon along the planar direction.

### 9.3.4 MoGR R&D

The R&D program on MoGR had a first preliminary part where we focused on testing many different graphite types and different temperatures (from $1400^oC$ up to $1800^oC$)

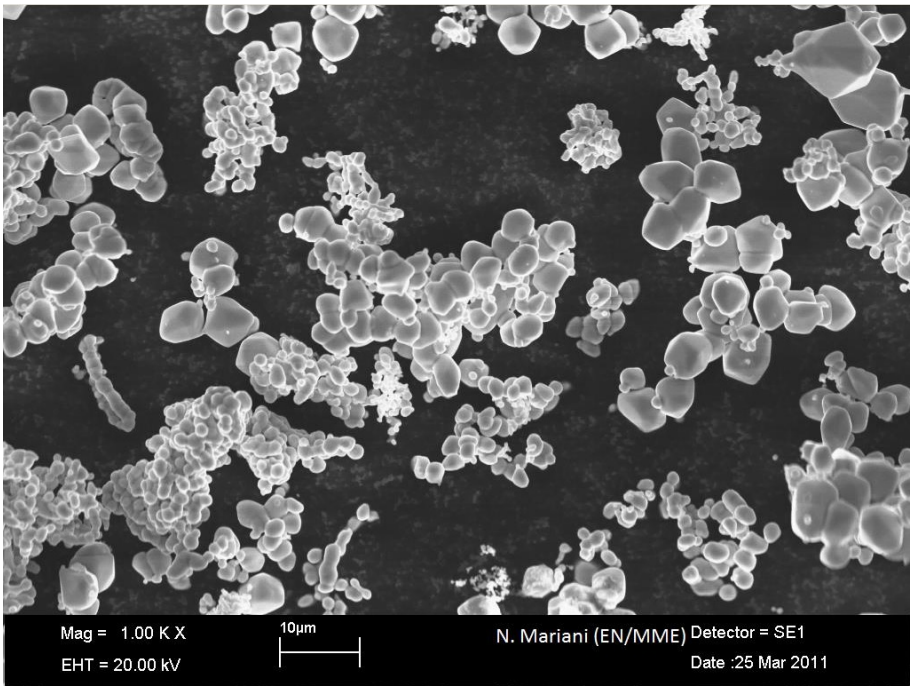


**Figure 9.8:** SE Image: High magnification SEM Observation at CERN of the $5\mu m$ Molybdenum powder used for MoGR production.

with a large scan. This preliminary part allowed to choose the most promising graphite type (spheroidal flakes of Asbury 3260 graphite) and to reduce significantly the temperature interval of interest (from $1600^oC$ up to $1750^oC$). For all plates we kept a constant $60\%_V$ of graphite in order to have a final density of $\approx 5.6g/cm^3$, which represents a good compromise in terms of energy absorption between CFC and pure metallic solution and is very close to the density of CuCD.

After having fixed the region of interest we started to deeply analyse the effect of 4 main parameters independently (sintering pressure, temperature and time and graphite particles dimensions) in order to find the best combination of production parameters.

The final MoGR material composition and production cycle parameters are reported below.

- Composition of starting powder: $40\%_V$ Mo (divided in 90% 45 $\mu m$ powder and 10% 5 $\mu m$ powder) having the $0.8\%_w$ of Pd (see Figure 9.10), the rest being Asbury 3260 Graphite Selected $<45\mu m$ (see Figure 9.4).

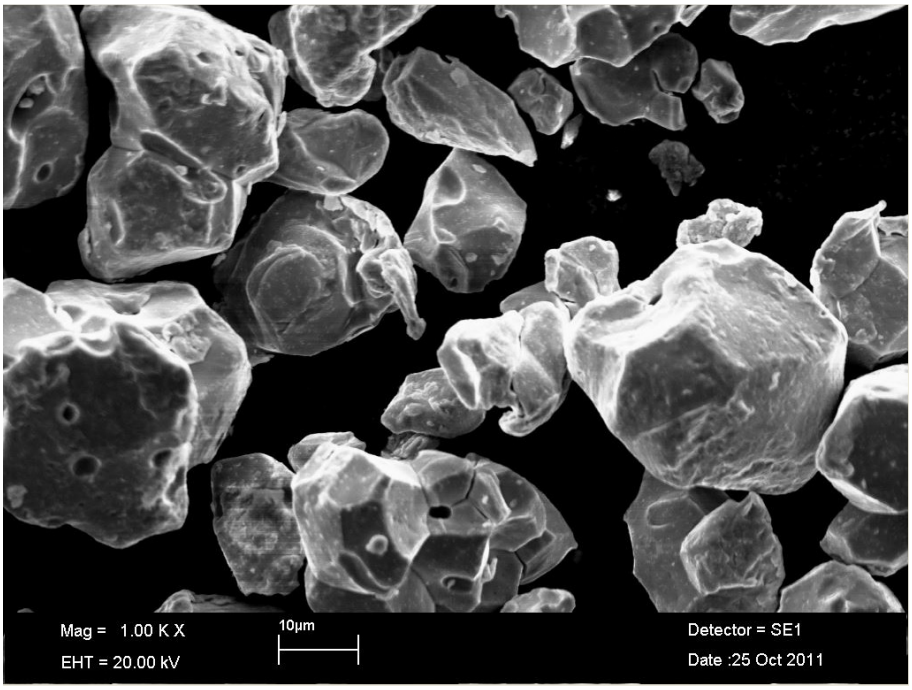


**Figure 9.9:** SE Image: High magnification SEM Observation at CERN of the $45\mu m$ Molybdenum powder used for MoGR production.

- Rapid Hot Pressing main parameters: Graphite moulds and electrodes, sintering temperature $1700^oC$ for 10 minutes, constant applied pressure $45MPa$, vacuum atmosphere $10^-4mbar$ with reducing atmosphere $97\%N_2 - 3\%H_2$.
- Produced plates dimensions: 70x55 mm having rounded edges with R=5 mm.

The obtained plate has been cut by water jet to obtain the samples for the mechanical and thermal characterization at CERN (always carried out along the longitudinal direction of the plates) and for the microstructural analysis by SEM, EDS and X-ray diffraction. The results being reported in the following section.

## 9.4 MoGR Characterization

All the produced plates have been then tested at BrevettiBizz and CERN in order to classify them in terms of density, flexural mechanical strength, electrical conductivity (by RF impedance measurements ), and thermal conductivity using the apparatus presented in Paragraph 6. Further analysis by X-Rays, optical and SE microscopy

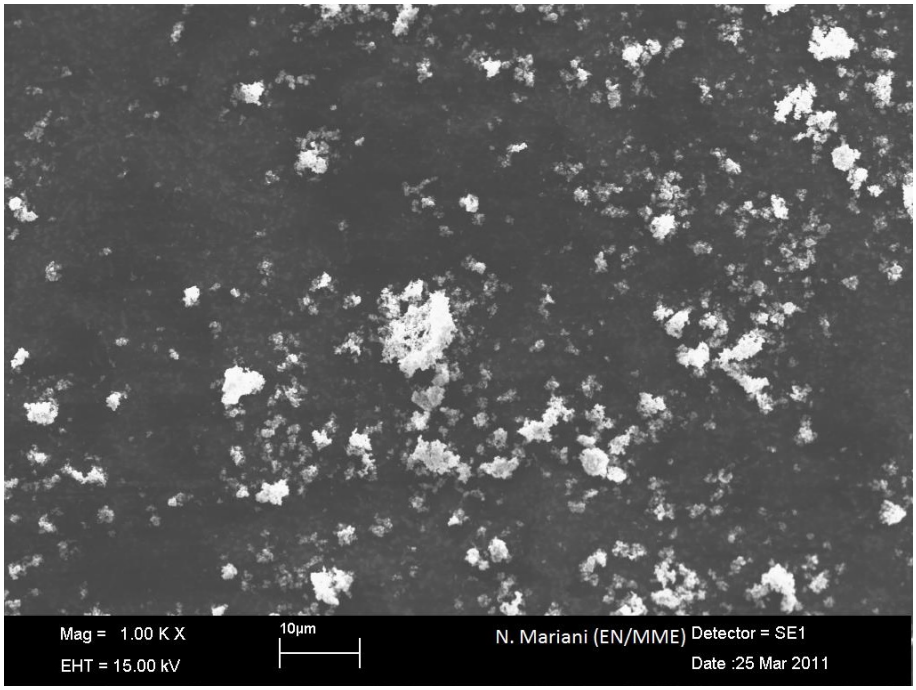


**Figure 9.10:** SE Image: High magnification SEM Observation at CERN of the $0.25 - 0.55\mu m$ Palladium powder used for MoGR production.

permitted an interpretation of the obtained results. Finally we want to point out that during the sintering process there is a significant recrystallization of graphite grains that orient themselves parallel to the plate: the final material is therefore anisotropic and has different properties between the longitudinal and the transversal direction with respect to parallel surfaces of the composite plate, as confirmed by X-Ray analysis.

The characterization results of the most promising MoGR material is reported in next paragraphs.

### 9.4.1 Microstructural Analysis

The SEM images of MoGR were always taken on the transversal cross section of the analysed sample, which has been polished by 1200 mesh sand paper followed by diamond paste down to 1/4 $\mu m$, then cleaned in alcohol with ultra sounds and degassed. The microstructure appearance along the longitudinal direction is very similar to the transversal one, thanks to the use of spheroidal graphite that does not lead to high preferential orientation of the particles. However, the lattices of recrystallized graphite

grains and of the newly formed $Mo_2C$ grains are heavily oriented due to the application of unidirectional pressure during the sintering process.

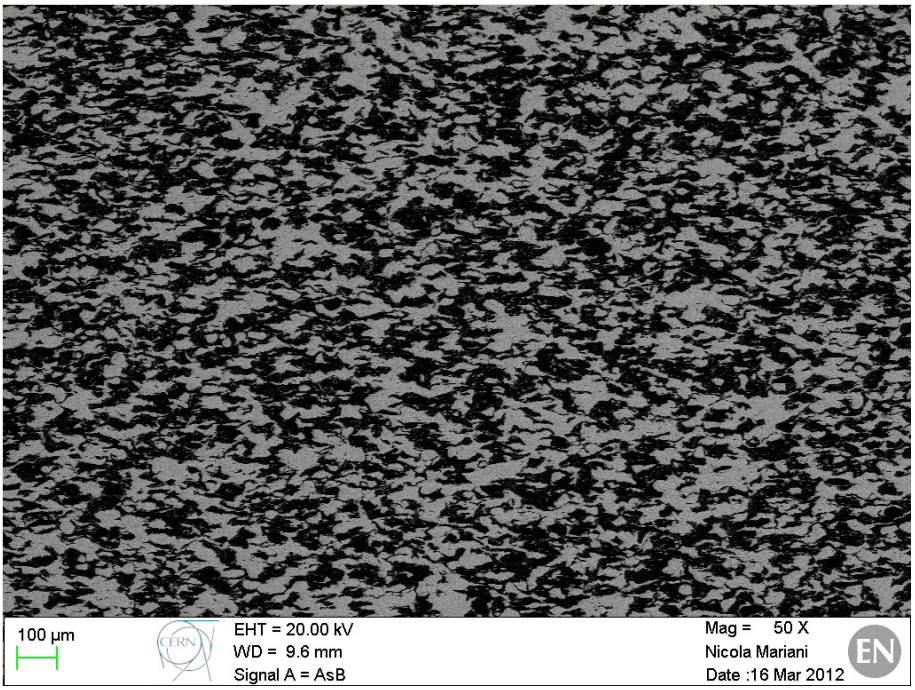


**Figure 9.11:** QBSD Image at low magnification of MoGR (transversal direction) made using fine selected Asbury3260 graphite. The clear (heavier) phase is $Mo_2C$ formed during the solid state reaction. The grains are mostly regular with the presence of some macro-grains formed by the coalescence of adjacent grains.

As shown in Figure 9.11 the material appears homogeneous, with a regular distribution of graphite grains surrounded by partially interconnected $Mo_2C$ grains having irregular shapes. The dimensions of the $Mo_2C$ grains are significantly greater than the initial Mo particles, suggesting a massive coalescence of the grains that brings to the interconnected structure. The interconnection between $Mo_2C$ grains are the responsible for the final mechanical strength of the material and for the good electrical conductivity, that could not be achieved if the conductive $Mo_2C$ grains were separated.

The BSE image of Figure 9.12 gives a closer view to the $Mo_2C$ grains shape and internal structure: the grains are made by several initial carbide grains that grow consuming the embedded graphite particles, leaving small acicular graphite inclusions inside the newly formed grains.

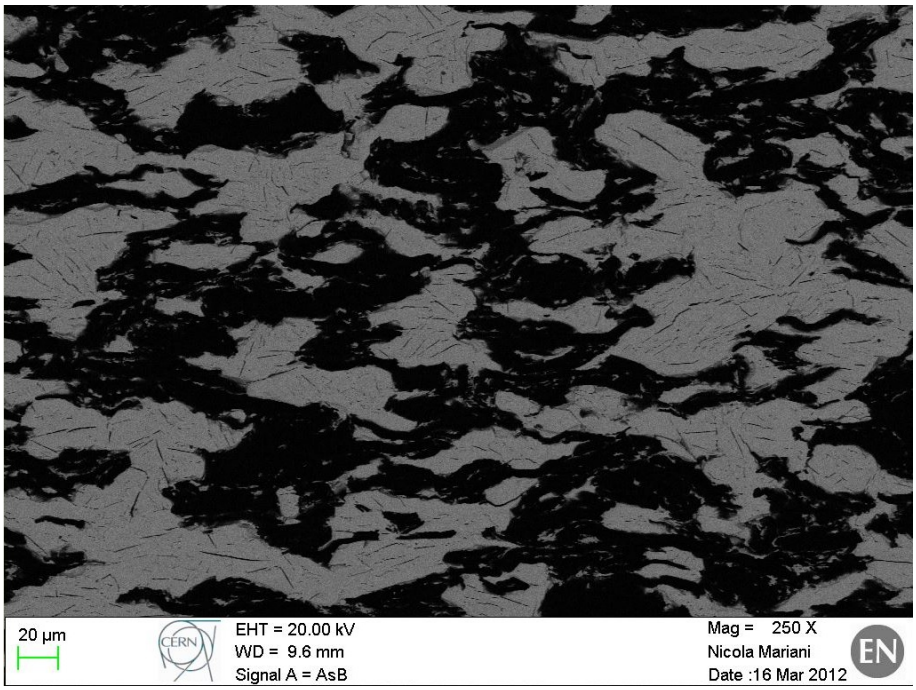


**Figure 9.12:** QBSD Image at intermediate magnification of MoGR (transversal direction) made using fine selected Asbury3260 graphite. Aspect of recrystallized $Mo_2C$ grains and of the internal acicular inclusions. There are also many small $Mo_2C$ grains embedded inside the graphite phase, due to the presence of the small $5\mu m$ Mo particles.

The QBSD Images allowed to clearly see the carbide grains enhancing the contrast and removing the charge effect on the $Mo_2C$ grains (since surrounding graphite is not conductive): however, Figure 9.13 has been obtained using the "InLens" Secondary Electron Detector of the Sigma Zeiss SEM in order to verify also the internal structure and porosity of the graphite phase. Graphite appears generally compacted, with the presence of porosity mainly at the interface between two graphite grains, as shown in Figure 9.13 on the left. There are also many small $Mo_2C$ particles remained embedded between graphite grains. The interface between the two parts of the big carbide grain in the middle of the image confirms the origin of the acicular inclusions.

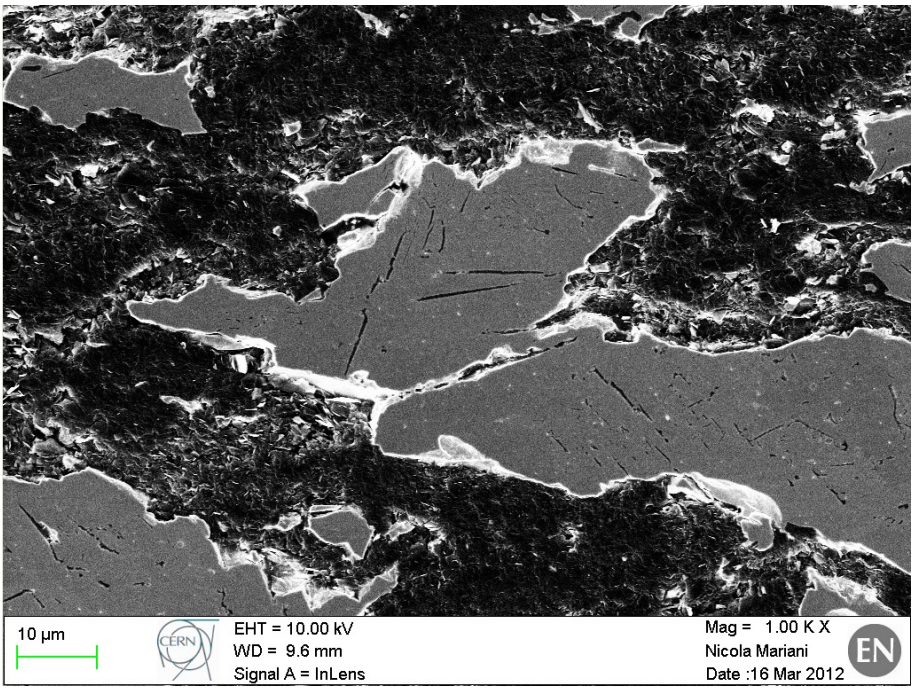


**Figure 9.13:** SE Image at high magnification of MoGR (transversal direction) made using fine selected Asbury3260 graphite.

### 9.4.2 Graphite Orientation

The orientation of the graphite lattice has been verified by X-Rays analysis (see Paragraph 6.3.2) carried out placing the sample on both longitudinal and transversal orientation. The comparison for MoGR is reported in Figure 9.14, where the red curve represents the spectrum acquired in transversal direction while the black curve the

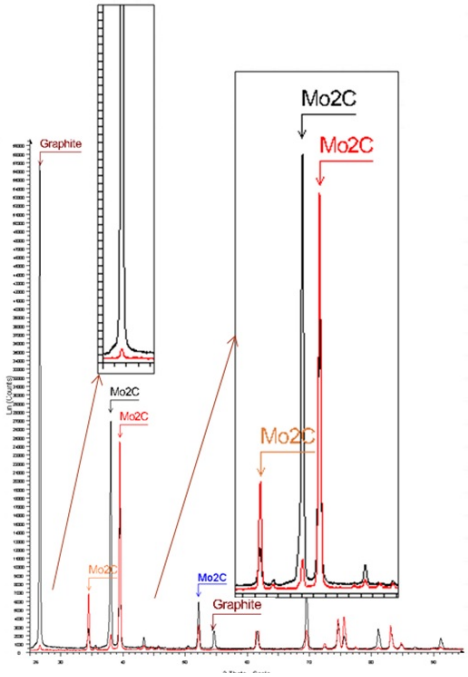


**Figure 9.14:** MoGR 24-C X-Ray analysis in Longitudinal (Black) and Transversal (Red) direction.

longitudinal one.

The first graphite peak at $25^o$ is the $< 1000 >$ peak of graphite lattice: we can clearly see that the peak is predominant in the case of longitudinal orientation while disappears in the transversal orientation, meaning a nearly perfect recrystallization of graphite grains. Also $Mo_2C$ orients itself during the process along the Longitudinal Direction, but in a less pronounced way with respect to Graphite.

## 9.5 Conclusions on MoGR

In this section the final results of the MoGR R&D program are discussed and compared with the analytical estimations and with the other proposed materials. As already introduced at the beginning of the present Chapter the results obtained with MoGR were not satisfactory and the R&D program moved to the development of Carbon Fiber reinforced MoGR (MoGRCF), so the final MoGR material has not been extensively characterized as for CuCD and MoCuCD and only the results of BrevettiBizz

and CERN measurements (density, electrical conductivity, thermal conductivity and flexural strength all at RT) are available.

The remaining properties have been only analytically evaluated under the assumptions discussed below.

### 9.5.1 MoGR Properties estimation

Given the anisotropy of MoGR and MoGRCF the treatment is more complex than with previously discussed isotropic materials so an entire Paragraph has been devoted to the discussion about MoGR properties estimation.

The major differences between the previous estimations of the expected properties composites and the ones for anisotropic materials, such as for MoGR and MoGRCF, are listed below.

- Density and specific heat: the stoichiometry of the solid state reaction 9.1 and the density differences between Mo and $Mo_2C$ have to be taken into account to obtain the final volumetric fractions of the two components $Mo_2C$ and graphite in order to use equation 5.1 to evaluate $\rho$ and $c_p$. The hypotheses are that all Mo reacts with graphite forming $Mo_2C$ leaving the graphite in excess in the form of completely compacted graphite ($\rho = 2.25 g/cm^3$);

- Thermal conductivity: the thermal conductivity of orthotropic materials has been evaluated by the Kapitza model as already discussed in Paragraph 5.4.1. However the uncertainty in the effective thermal conductivity of the partially graphitized graphite grains (stage N.3 in Figure 10.2 in next Chapter) hampers a reliable evaluation of MoGR thermal conductivity. On the other hand in the case of MoGRCF the calculation has been performed assigning arbitrary to the entire graphitic phase (graphite grains + Carbon Fibers) the properties of the Carbon Fibers: this choice is based on the fact that at MoGRCF sintering temperature the graphite grains should recrystallize completely and directionally reaching the stage N.4 structure which is close to the one of CF recrystallized at similar temperatures.

- Young's Modulus: the Young's Modulus along the two principal directions $E_L$ and $E_T$ has been evaluated using the equations reported in Paragraph 5.3.1 using

the elastic constants of pyrolytic Graphite R4550; however as already introduced since graphite elastic constants have a large dispersion depending on the internal structure of the grains this assumption is arbitrary.

- CTE: the correct evaluation of the CTE along the two principal directions should take into account the anisotropy of the graphite phase for both the thermal and the mechanical point of view, since the thermally induced stresses around one particle depend on the relative orientation of all surrounding grains that contribute non linearly to the final thermal expansion. An analytical method has still not been implemented and in present work we will simply use the conservative Turner model in the assumption of isotropic material. A possible solution still not implemented could be to reproduce the thermal expansion of a significant volume of the bi-phase material with coupled thermo-mechanical Finite Element Method (FEM) simulations and then transpose the results to the equivalent homogeneous material.

- Ultimate Strength: the ultimate strength has been conservatively assumed $\approx$ 2/3 of measured $R_{Fl}$.

### 9.5.2 Final Results of MoGR R&D

During the $R\&D$ program carried out at CERN in collaboration with BrevettiBizz many efforts have been done to obtain a Molybdenum Carbide Graphite material with the production of a huge amount of experimental data that allowed to choose the best production cycle and composition for Molybdenum Carbide - Graphite composites realized by RHP of powders in solid state.

The obtained material has a good combination of thermal and mechanical properties like can be seen in table 9.3, however the comparison with the other candidates, namely CuCD and MoCuCD, shows that the only advantage of MoGR is it's higher thermal stability at high temperature.

The R&D on MoGR has been therefore suspended without completing the detailed characterization made for CuCD and MoCuCD.

The work prosecuted with the introduction in MoGR of a second reinforcement (Carbon Fibers) and with a higher sintering temperature in order to achieve higher thermal properties while reducing density and CTE.

**Table 9.3:** Final properties and Figures of Merit for MoGR compared to CuCD and MoCuCD. Values with * are estimations based on the considerations reported in 9.5.1 .

| **Material** | **Unit** | **CuCD** | **MoCuCD** | **MoGR** |
|---|---|---|---|---|
| Density | $[g/cm^3]$ | 5.4 | 6.9 | 5.3 |
| Atomic Number (Z) | $[-]$ | 11.4 | 17.4 | 15.9 |
| Melting Temperature | $[^oC]$ | 1083 | 1083 | 2505 |
| Thermal Conductivity | $[W/mK]$ | 490 | 155 | 135 |
| CTE | $[10^{-6}K^{-1}]$ | 7.8 | 7 | 7.59* |
| Specific Heat | $[J/kgK]$ | 420 | 360 | 261 |
| Young's Modulus | $[GPa]$ | 220 | 260 | 179.25* |
| Tensile Strength | $[MPa]$ | 70 | 140 | 95.7 |
| Poisson's Ratio | $[-]$ | 0.22 | 0.3 | 0.19* |
| Electrical Conductivity | $[MS/m]$ | 12.6 | 10 | 1 |
| Radiation Length $\chi_0$ | $[cm]$ | 4.78 | 2.82 | 4.99 |
| SSNI | $[kWm^2/kg]$ | 11.6 | 3.2 | 3.4 |
| TSNI | $[kJ/kg]$ | 13.4 | 19.4 | 14.9 |

# 10

# Molybdenum Carbide Graphite Carbon Fiber (MoGRCF) Composites

Present Chapter presents the R&D and the results obtained with the the addition of Carbon Fibers (CF) to the already developed MoGR material.

Instead of previous Chapters, where there was a first introduction to the new constituent, followed by the developed innovations and by the obtained results, in this case the innovations and the results have been split into two distinct sections, each one having the same internal logical order as in previous Chapters. This is due to the fact that the R&D spaced between two very different parts that are conceptually separated, the Solid State Sintering (SSS) and the Liquid Phase Sintering (LPS), that require specific treatments.

## 10.1 Introduction to Carbon Fiber-reinforced CMC

As already anticipated the relatively low results obtained with MoGR leaded to the research of possible additions to improve its thermal properties without sacrificing the optimal thermal stability at high temperatures of $Mo_2C$ and graphite by adding other low melting elements. In the Chapter the structures and properties of CF will be presented, followed by the description of the R&D work carried out at CERN and BrevettiBizz and by the characterization of the obtained material.

The graphitization stages reported in Figure 10.2 suggest that in MoGR we were not perfectly aligning the graphene layers obtaining an internal structure of graphite grains similar to stage number 3 in the picture, where the graphene layers are woven like. In this case the graphene macro-molecular delocalized $\pi$-orbital is deformed with respect to the molecular planar direction. The graphitization process prosecutes with the formation of completely planar graphene layers, that instead give properties close to the ideal graphene layer already discussed in previous Chapter. The temperature needed to form perfectly planar graphene layers is indicatively higher than $2100^oC$ so the MoGRCF R&D program starts with the production of MoGRCF plates at $2200^oC$, where all the components are still in solid phase. Further improvement has been the increase in Temperature up to the melting of $Mo_2C$ at $2505^oC$ to take advantage of LPS and obtain a fully dense material.

The production of MoGRCF involved not only a huge research and characterization work but also an important upgrade of the RHP machine made in BrevettiBizz to reach safely the temperatures needed to sinter MoGRCF. This improvements have been implemented stepped with time, giving rise to two parts of the R&D program, the SSS of MoGRCF and the LPS of MoGRCF, which are presented in next Paragraphs.

The R&D started in the middle of 2012 and is still ongoing with the aim to reproduce the optimal results obtained on test plates (70x55x4 mm or Diameter 90 mm Thickness 4 mm) on big massive pieces having suitable dimensions for the LHC Collimators (140x40x22 mm). The main issues that have been encountered switching from thin to thick plates are differences in the spatial distribution of the fibers inside the mould and in pressure and temperature spatial distribution during the process that lead to less homogeneous, less oriented and less compacted material (lower final properties).

## 10.2 Carbon Fibers Properties

After diamond and graphite, already introduced in Paragraphs 7.1.1 and 9.1.2, the remaining carbon materials are Carbon Fibers (CF), carbon nanotubes, graphene foils and fullerenes (92); between all of them only CF can practically be used for producing massive composite pieces at a reasonable cost (31). CF have exceptional physical and mechanical properties and have been widely used for producing composites; however some intrinsic limits of graphite based materials (low oxidation resistance, low hardness,

difficulty to machine pieces together with need to use dry powder aspirators) limited their expansion and are actually mostly used for particular applications such as aero spatial and sport industry, in addition of course to the very specific BID application object of the present work.

Carbonization of fiber was first applied by Edison in his process of obtaining incandescent filaments about a century ago and is now an essential process in the CF production. CF are unique materials and have a wide variety of applications, especially high performance CF gained in the last 30 years considerable attention and are now widely used as a reinforcing component of the advanced composite materials for specific applications where very low density has to be combined with high elastic properties or high thermal dissipation. These applications of CFCs are based on the high strength, high modulus and high heat transport of the fibers, which are attributable to the structure of highly oriented hexagonal carbon-carbon networks, similar to that of single crystal graphite.

Since the thermal conductivity takes advantage too from the high orientation of the graphene layers (see Paragraph 9.1.2) CF can be of invaluable interest for thermal management composites such as the CFC already used in Primary LHC Collimators jaws (see Paragraph 4.1.1).

However the intrinsic porosity of CFC (due to the absence of filling elements) does not allow to take fully advantage of the CF high transport properties: in CFC the matrix is obtained by vapour infiltration and deposition of carbon, while in MoGRCF the use of LPS process allows the full compaction of the interstitials between CF by the molten phase, giving exceptional thermal properties at the cost of higher density if compared to CFC.

A comparison of some different types of CF precursor is described in the next Paragraph together with the obtained properties. The main emphasis of this section will be on mesophase pitch-based CF that have been used for the production of MoGRCF.

### 10.2.1 Comparison of Carbon Fibers

In order to obtain CF with desirable properties, a wide variety of organic materials have been investigated for their use as precursors during the past decades. Mainly rayon, polyacrylonitrile (PAN), and carbonaceous pitch have been used in the industry as the precursors for CF giving different final properties and unique advantages.

Some indicative properties of CF provided in literature (99) are shown in Table 10.1 for PAN based fibers produced by Toray (T800 and M50) and for mesophase pitch based fibers produced by Union Carbide (P25 and P120); as can be clearly seen different production process parameters can give very different properties depending on the achieved graphitization ratio, therefore it is necessary to always identify the commercial name of the fiber and verify its properties and structure.

The literature value are then compared, always in Table 10.1, to Granoc $XN-100-03Z$ and to Cytek DKD ThermoGraph CF used in the production of MoGRCF (data provided by Nippon Graphite Fiber Corporation (100) and Cytec (101)). These newly introduced advanced mesophase pitch fibers have been especially developed to optimize the thermal conductivity along the fiber axis by allowing a even more complete graphitization of their structure.

There are other older methods to produce CF such as rayon (Union Carbide) and mesophase pitch but they are significantly more expensive than the other two methods so actually PAN and mesophase pitch are the preferentially employed precursors for carbon fibres. Especially, mesophase pitch is expected to have better characteristics as the precursor of CF than PAN because of its higher "graphitizing" characteristics.

**Table 10.1:** Comparison of properties of different PAN- and mesophase pitch- based CF

| **Fiber Type** | **Unit** | **PAN** | | **Mesophase Pitch** | | | |
|---|---|---|---|---|---|---|---|
| Commercial name | | T800 | M50 | P25 | P120 | XN-100-03Z | Cytek DKD |
| Density | $[g/cm^3]$ | 1.8 | 1.91 | 1.9 | 2.18 | 2.22 | 2.15-2.20 |
| Thermal Conductivity | $[W/mK]$ | [–] | [–] | [–] | [–] | 900 | 400-650 |
| Young's Modulus | $[GPa]$ | 290 | 490 | 160 | 830 | 1000 | 1380 |
| Tensile Strength | $[MPa]$ | 5600 | 2400 | 1400 | 2200 | [–] | 690-830 |
| Elongation | [%] | 1.9 | 0.4 | 0.9 | 0.3 | [–] | [–] |
| Electrical Conductivity | $[MS/m]$ | 0.077 | 0.14 | 0.077 | 0.45 | 0.67 | 0.33 |

In case of mesophase pitch-based CF, tensile modulus in excess of 1000 GPa can be attained, which is practically equivalent to the theoretical value for the ideal graphite crystal along {0001} planes reported in Table 9.1. The electrical conductivity is another parameter that increases together with the regularity of the graphene planes, giving to pitch based fibers a quasi-metallic electrical conductivity.

This result is achieved by the very high chemical purity of the obtained fiber and by the high precision of the graphene structure.

As both the elastic and transport properties of the graphene layers (Young's Modulus, thermal and electrical conductivity) depend strongly on the defects density along the graphene planes the thermal conductivity at RT of such fibers can reach up to 900 W/mK while the estimated thermal Conductivity along the fiber radial direction is few W/mK.

In contrast, the maximum value of the modulus attained for PAN-based fibers is considered to be about 500 GPa. Figure 10.1 shows the tensile properties of manufactured PAN- and mesophase pitch-based CF.

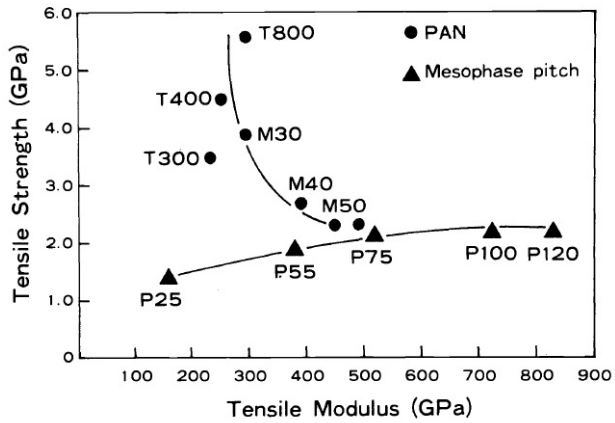


**Figure 10.1:** Mechnical Properties comparison between PAN- and mesophase pitch-based fibers (produced respectively by Toray Ind., Torayca and by Union Carbide, Thornel)

### 10.2.2 Production techniques

Most organic materials can be carbonized on heat treatment at a high temperature above $700 - 800^oC$ under inert atmosphere. Graphitizable carbons exhibit the characteristic of structural conversion on heat treatment passing through several stages as shown in the plot of Figure 10.2, by which the hexagonal carbon-carbon networks are highly oriented in the three-dimensional order. Mesophase pitch is known as one of the most typical graphitizable carbonaceous materials.

The processes of mesophase pitch- and PAN-based CF are shown in Fig. 10.3. Both processes after the initial molten pitch spinning (made inside an extruder, see

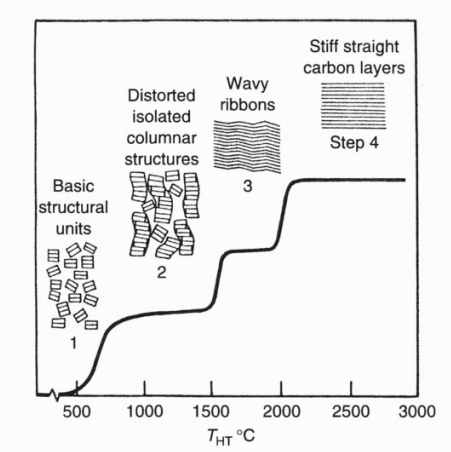


**Figure 10.2:** Graphitization stages in graphitizable carbon as a function of the heat treatment temperature ($T_{HT}$), source Goma et Oberlin (4)

Figure 10.4) are essentially the same: the material is first oxidized (under active oxygen rich atmosphere), then carbonized (under reducing atmosphere) and finally graphitized (under vacuum). However, the oxidation in each process has a different purpose: for mesophase pitch is to cross-link molecules to the extent of making it stronger by introducing oxygen, while the oxidation of PAN brings about a ring formation of PAN chain molecules.

From the chemical point of view pitch (a distillation residue of petroleum) is a complex mixture of thousands of aromatic hydrocarbons having $3 - 8$ fused ring systems and an average molecular weight of $300 - 400\ g/mol$. Isotropic pitch is first subjected to polymerization and condensation to obtain mesophase anisotropic pitch: the pitch passes through many different stages of the mesophase formation (102) until the formation of a structure in which fused aromatic rings networks are stacked together by aromatic like $\pi$ - electrons.

Thanks to the particular disposition of the aromatic rings it is possible to grow fibers having precise and regular graphene planes along the fiber axis during the following carbonization and graphitization, with precise layers disposition depending on the mesophase production parameters as shown in next Paragraph.

After oxidation the pitch is carbonized under vacuum to remove the superficial $OH$ and $COOH$ groups and obtain a pure CF: en example of used equipment is reported in Figure 10.5. A similar furnace is then used for the last heat treatment in vacuum at

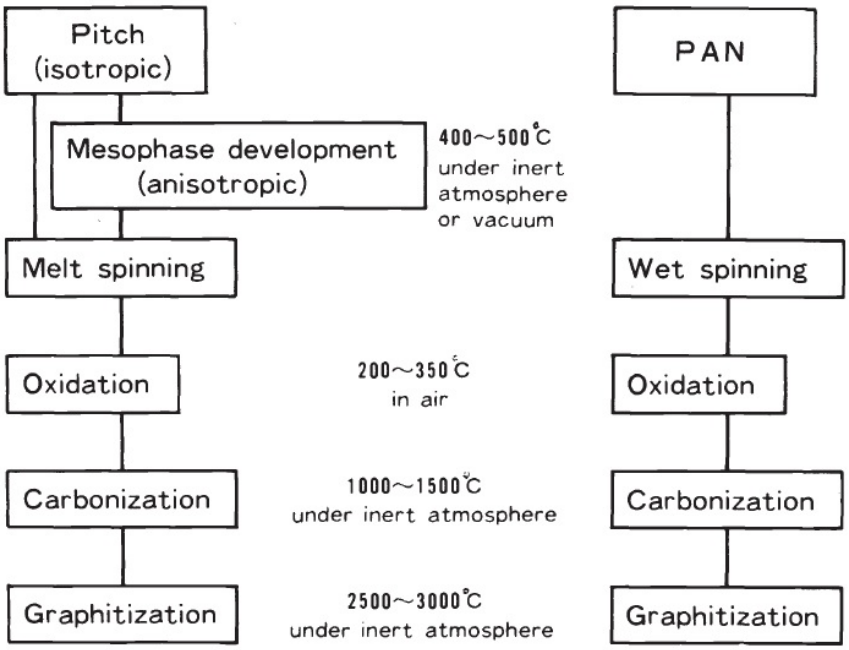


**Figure 10.3:** Comparison of the different production cycles for PAN- and pitch-based CF.

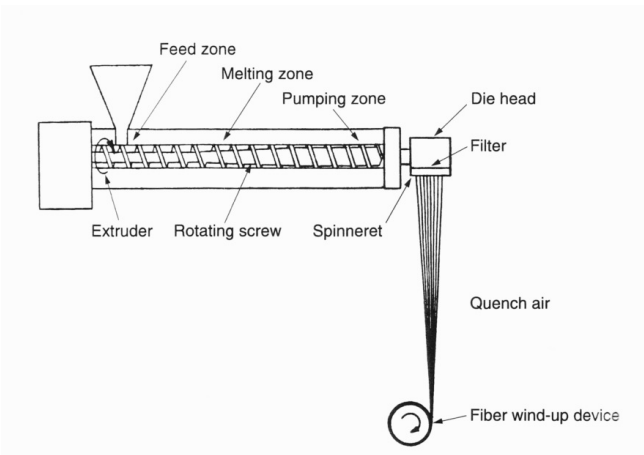


**Figure 10.4:** Schematics of a common extruder used for the melt spinning of mesophase pitch (5).

very high temperature to promote the fibers graphitization.

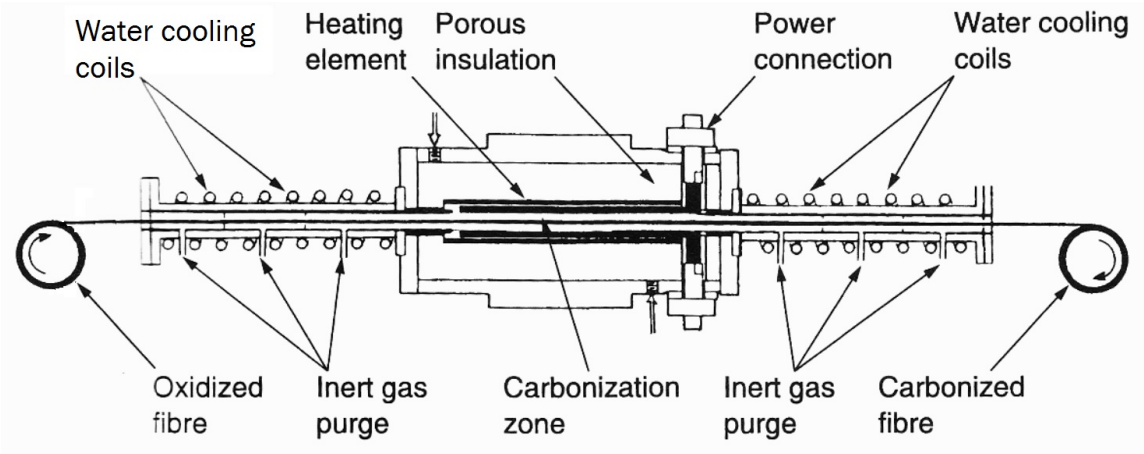


**Figure 10.5:** Schematics of an hairpin element furnace used to carbonize mesophase pitch fibers.

### 10.2.3 Structure of Carbon Fibers

The internal structure of CF has been already deeply analysed in the past, in particular it has been found that mesophase pitch based CF can have one of the following different transverse structures: radial, onion-skin, random arrangements and of course intermediate structures of these three categories (103).

Figure 10.6 shows the obtained structure of the fiber as a function of the pitch viscosity and of the melt spinning temperature during the mesophase development, while Figure 10.8 shows the internal structure of a mesophase pitch CF characterized at CERN.

Pitch based CF will contain internal packing defects that remain from the mesophase pitch structure and will affect their final properties: a description of the most common mesophase pitch configurations have been made by Zimmer et al. and is reported in Figure 10.7 (104).

It is also worth noting that CF are usually chopped or milled to achieve the desired average fibers length. These operations break the fibers leaving small fiber fragments that remain attached to the fibers surface by electrostatic forces. Of course the amount of fragments is higher in milled fibers than in chopped fibers. The presence of small fragments is however not negative into a material having also a graphite phase because

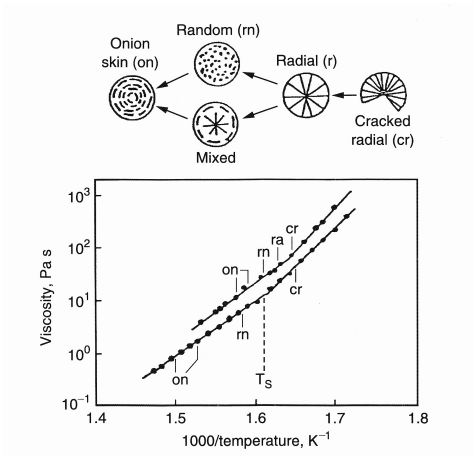


**Figure 10.6:** Fiber structure as a function of the the melt spinning parameters.

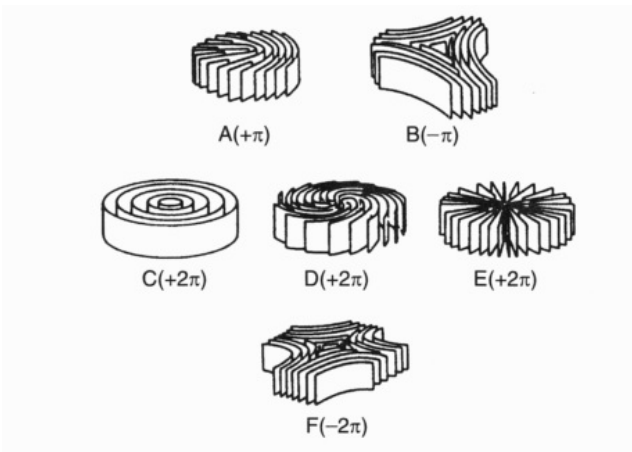


**Figure 10.7:** Possible inernal sttructures of mesophase pitch precursors.

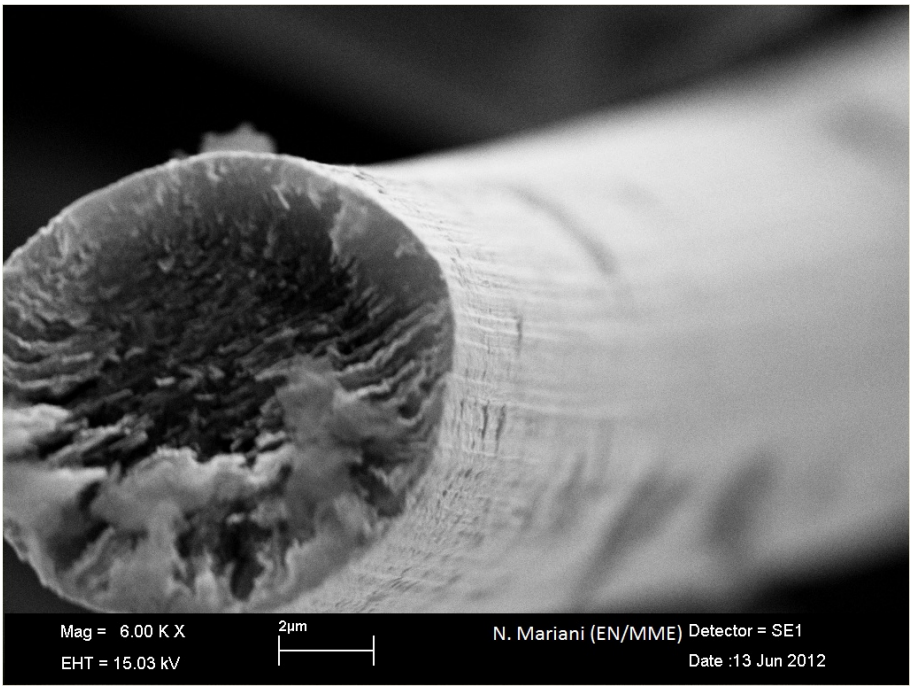


**Figure 10.8:** Internal Structure of pitch based CF used for MoGRCF production. The internal structure is made by radially oriented graphene planes.

the fiber fragments have a much higher compaction with respect to the graphite flakes helping in achieving denser composites with the same cycle.

The milled or chopped fibers will always have a broad distribution of lengths because of the intrinsic difficulties in selecting the fibers lengths, so every fiber supply have been observed at SEM and optical microscope to verify (visually) the fibers length distribution.

Another issue when dealing with long fibers is their tendency to form macroaggregates bonded along the fibers length by Van der Waals forces: these aggregates can be macroscopic like shown in Figures 10.10 and 10.9 and unfortunately are not removed by the standard powder mixing made before the sintering process. For that reason the long CF Granoc $XN-100-03Z$ have been softly separated by mixing them inside a mechanical blender. The beneficial effect of avoiding macro-aggregates (together with the presence of fragments, already fully dense graphite particles) overcomes the fibers length reduction giving higher properties and homogeneity to the obtained composites.

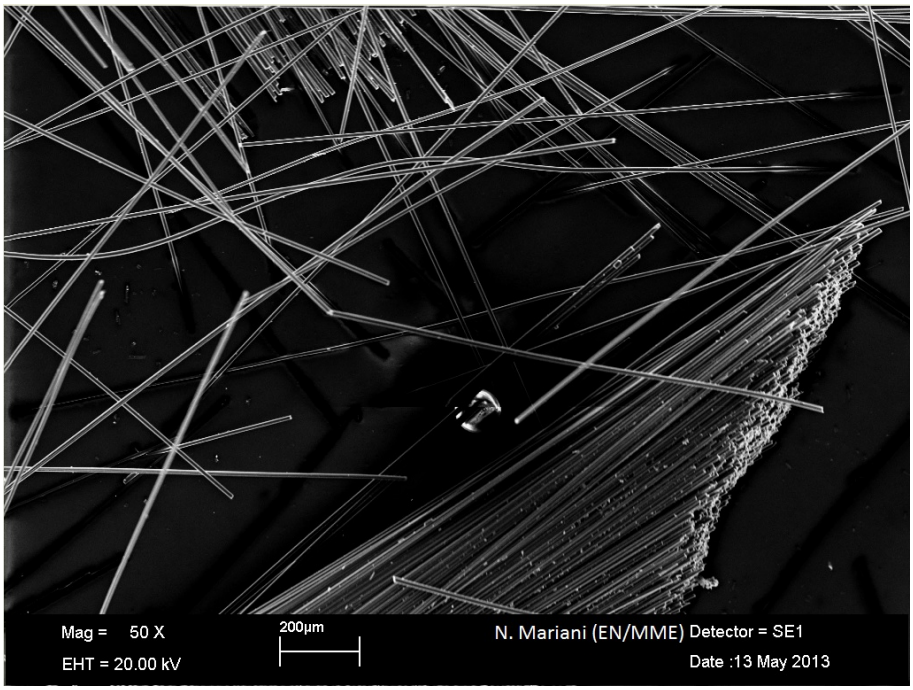


**Figure 10.9:** Granoc XN-100-03Z 3 mm long CF. Presence of macroaggregates of packed fibers with dimensions up to few mm in diameter.

**Figure 10.10:** Aspect of Granoc XN-100-03Z CF. The macroaggregates are clearly visible.

## 10.3 MoGRCF Production and Characterization

### 10.3.1 Solid Phase Sintering of MoGRCF

The brief summary of the first batch of 5 plates produced in solid state at $2200^oC$ is reported in table 10.2: all plates have been produced with the same raw material (based on the results obtained from MoGR) and production cycle:

- Composition
  - Molybdenum: content fixed to $20\%_V$ for all plates of 5 $\mu m$ Mo powder (see Figure 9.8;
  - Graphite: Not Selected Asbury 3260 (see Figure 9.4);
  - Short CF: Cytec ThermalGraph DKD - nominal length 250 $\mu m$ (see Figure 10.8);
  - Long CF: NGF Granoc $XN-100-03Z$ - nominal length 3 $mm$ (see Figure 10.9).
  - All powders have been cleaned with hydrogen before mixing using the equipment described in Paragraph 8.2.
  - Theoretical density after solid state reaction (see Paragraphs 5.2 and 9.5.1): $\rho_{th} = 3.91\ g7cm^3$.
- Process Parameters
  - Temperature: $2200^oC$ measured by a high temperature pyrometer pointed on the graphite mould;
  - Atmosphere: vacuum $10^{-4}mbar$ with reducing atmosphere $97\%N_2 - 3\%H_2$ as for MoCuCD and MoGR;
  - Pressure: three steps application of pressure during the process as a function of the temperature, last step being 30 MPa.
  - Moulds and Electrodes: rectangular mould in pyrolytic graphite (plates dimensions 70x55x4 mm with rounded edges $R = 5\ mm$), cylindrical electrodes in pyrolytic graphite;
  - Cooling system: increased refrigerator cooling power to 60 KW.

Three different total amount of CF contents have been chosen, 20%, 40% and 60%, which are extremely high for a standard fiber reinforced CMC and will usually lead to undesirable high content of porosity. Many authors report maximum values of fiber content around the 25% (31) in the case of metallic matrix solid state sintering, that can increase up to 30% if switching to liquid state infiltrating processes.

However in the case of MoGRCF the composition of the MoGR matrix have been tailored to maximize the space filling: first the use of Not Selected Asbury graphite, which has proven to have a high content of very fine, dense and pure graphite particles, allows to obtain a relatively high compaction rate of 94% with the $20\%_V$ of fibers, that decreases down to $\approx 90\%$ in the case of the $60\%_V$ of Fibers. It must also be said that at $2200^oC$ the diffusion controlled reaction between Mo and C is extremely fast allowing to form relatively large $Mo_2C$ grains that incorporate the small graphite grains, as shown in Figure 10.11. In this case the usage of Pd as a sintering activator, discussed in Paragraph 9.3.2, is no more necessary and has been abandoned reducing the cost of the material.

**Table 10.2:** Summary of the first batch of MoGRCF plates produced in solid state during 2012 at BrevettiBizz. *The value is measured in the centre of the plate.

| Plate Id. | GR | Short CF | Long CF | $\rho$ | $\rho/\rho_0$ | $\sigma$ | $k$ | $R_{Fl}$ |
|---|---|---|---|---|---|---|---|---|
| Unit | $\%_V$ | $\%_V$ | $\%_V$ | $[g/cm^3]$ | % | $[MS/m]$ | $[W/mK]$ | $[MPa]$ |
| $N.1$ | 60 | 20 | 0 | 3.68 | 94.1% | 0.61 | 240 | 59 |
| $N.2$ | 40 | 40 | 0 | 3.65 | 93.3% | 0.41 | 200 | 45 |
| $N.3$ | 40 | 20 | 20 | 3.65 | 93.3% | 0.98* | 315 | 53 |
| $N.4$ | 20 | 30 | 30 | 3.53 | 90.2% | 0.3 | 200 | 37 |
| $N.4Bis$ | 20 | 30 | 30 Blended | 3.73 | 95.3% | 0.42 | 205 | 77.5 |

The most representative microstructures of the first 5 plates are reported in the next Paragraph together with a brief discussion of the different aspects already mentioned.

#### 10.3.1.1 Solid State MoGRCF Characterization

As already mentioned MoGR itself shows a large anisotropy between the longitudinal (perpendicular to applied pressure) and transversal (parallel to applied pressure) direction of the produced plates, so in the case of MoGRCF the anisotropy is enhanced

by the presence of the CF that tend to dispose themselves along the longitudinal direction. The fiber disposition is however not regular due to the fiber-fiber interference during the powder deposition that leaves large macrocavities, as expected by the high fiber content. The SEM images are always taken on the longitudinal or transversal cross section of the analysed sample, which has been polished by 1200 mesh sand paper followed by diamond paste down to 1/4 $\mu m$, then cleaned in alcohol with ultra sounds and degassed.

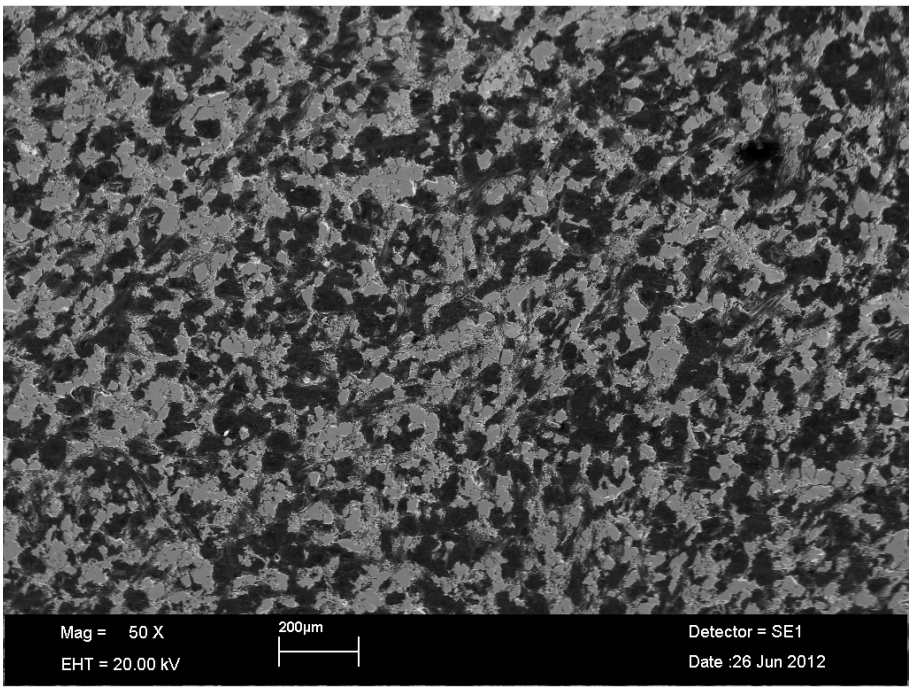


**Figure 10.11:** SE image at low magnification of MoGRCF-1 plate (longitudinal cross section) sintered at $2200^oC$ with the $20\%_V$ of short fibers. $Mo_2C$ diffused more than in previous MoGR plates sintered at $1700^oC$ forming large, porous grains up to few hundreds of $\mu ms$. the planar orientation of the fibers is also visible where the graphite matrix detached during the polishing and ultra sound cleaning.

#### 10.3.1.2 Conclusions on Solid State MoGRCF

From the test plates reported in Table 10.2 and the microstructural observations in previous Paragraph it is possible to start to compare few parameters:

- Effect of higher sintering temperature;

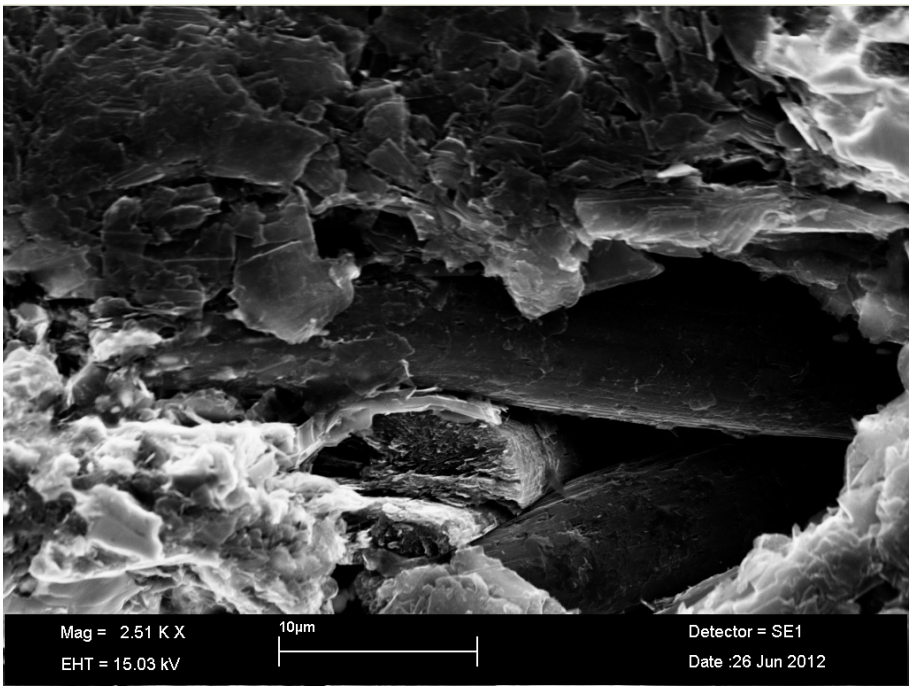


**Figure 10.12:** SE image at high magnification of MoGRCF-1 plate (transversal cross section) sintered at $2200^oC$ with the $20\%_V$ of short fibers. Particular of a macro cavity formed by the intersection of 3 (visible) fibers that was not filled by graphite or $Mo_2C$.

- Effect of short fiber quantity from 20 to $40\%_V$ (between plates N.1 and N.2) and of total fiber content from $40\%_V$ to $60\%_V$ (between plates N.3 and N.4);
- Effect of using only short fibers or a combination of 50% Long and 50% short fibers (plates N.2 and N.3);
- Effect of fiber blending to separate the macroaggregates (plates N.4 and $N.4bis$).

First of all, as expected by previous considerations about the new temperature of $2200^oC$ in MoGRCF the graphite phase recrystallizes encapsulating the CF and the $Mo_2C$ particles and giving a dense and continuous graphitic matrix, as can be seen in Figures 10.14, 10.15 taken in the periphery of plate N.3.

The effect of the fiber content is related to the difficult fiber packing inside the Fiber reinforced material instead of the Asbury 3260 Spherical Flakes of graphite, that lead to lower compaction (and lower properties) in plate N.2 with respect to plate N.1 (see Table 10.2) and plate N.4 with respect to N.3, as clearly shown in Figures 10.16

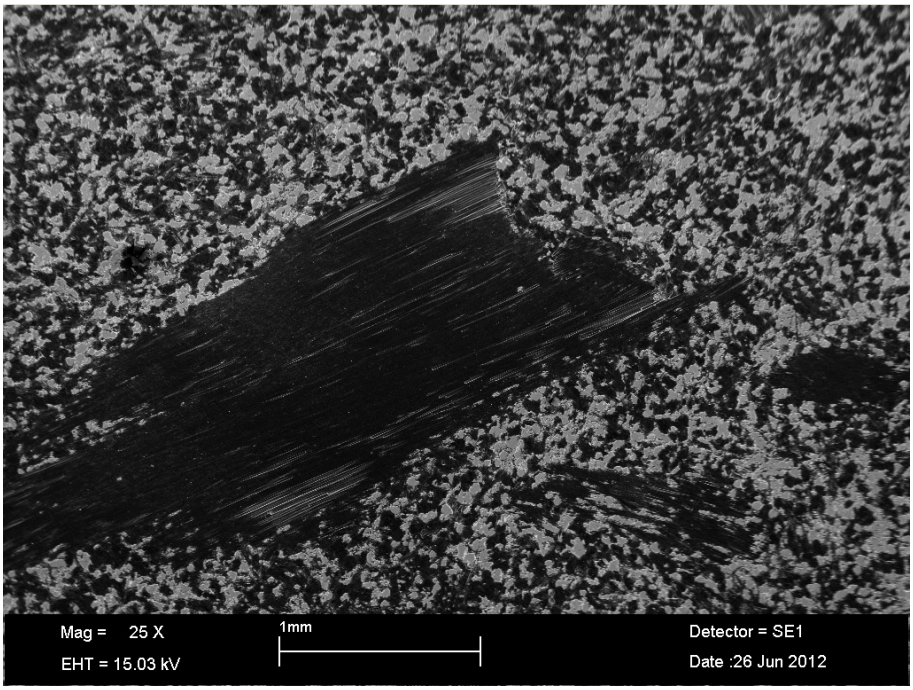


**Figure 10.13:** SE image at low magnification of MoGRCF-3 plate (longitudinal cross section) sintered at $2200^oC$ with the $20\%_V$ of short fibers and the $20\%_V$ of long fibers. Aspect of one macro aggregate of long CF remained trapped inside the structure.

and 10.14 respectively. However also in plate N.1 there are large macrocavities in the regions of fiber-fiber interference, like the one showed in Figure 10.12. The only way to completely remove such cavities is to fill them with liquid since pores larger than $2\mu m$ will not fill themselves by the solid state sintering diffusion process.

The third effect is more difficult to define because the introduction of the macroaggregates of Granoc Fibers leaded to a non homogeneous plate with higher compaction (confirmed also by the electrical conductivity measurements) in the centre of the plate. This effect has been deeply analysed finding that there have been a partial melting in the middle of the plate of the matrix phase due to very high thermal gradients during the production. However this effect has been observed only in plate N.3 inside the first batch of material, probably because of the very anisotropic behaviour of the CF macroaggregates (see Figure 10.9 and 10.13) that reduced the powder electrical conductivity along the transverse direction, increasing the ohmic heat generation inside the mould.

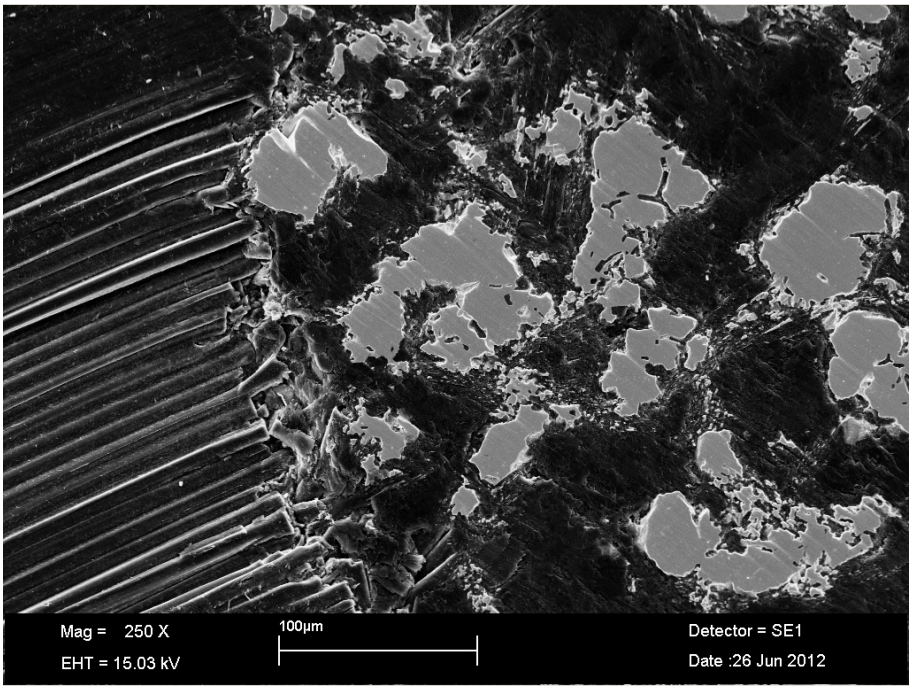


**Figure 10.14:** SE image at intermediate magnification of MoGRCF-3 plate (longitudinal cross section) sintered at $2200^oC$ with the $20\%_V$ of short fibers and the $20\%_V$ of long fibers. The interface between the fiber macro aggregate and the matrix is poorly filled, while the MoGR matrix looks denser than in previous MoGRCF-1 plate thanks to the local higher Mo content.

It must be said that at this temperature the only suitable measuring device is a pyrometer operating through a window and pointed to the outside of the graphite mould: the measured temperature is therefore always related to the incertitude of the effective temperature distribution inside the plate with respect to the temperature of the external face of the mould. However for sake of simplicity the plates will be identified only by the nominal temperature measured by the pyrometer.

Finally, the powder blending explained in Paragraph 10.2.3 allowed to achieve much better mechanical properties and to increase the fibers content up to the $60\% : V$ while obtaining anyway a very good compaction and a good phase distribution homogeneity in plate MoGRCF-4Bis as shown in Figure 10.17, thanks to the fibers separation and to the presence of the sub micro-metric fibers fragments that help in filling the interstitials.

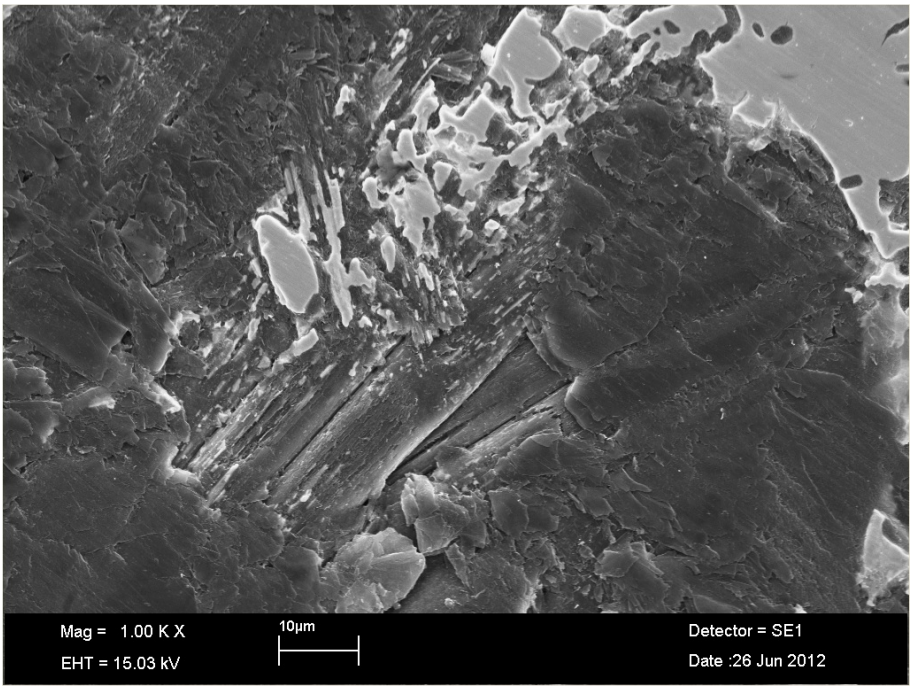


**Figure 10.15:** SE image at high magnification of MoGRCF-3 plate (longitudinal cross section) sintered at $2200^oC$ with the $20\%_V$ of short fibers and the $20\%_V$ of long fibers. The CF and the graphite matrix tend to sinter together encapsulating the finely dispersed small $Mo_2C$ particles.

### 10.3.2 Liquid Phase MoGRCF

The next milestone in MoGRCF R&D is made by a combination of the two best results of the first batch of plates, Plates N.3 and N.4: the idea is to take advantage of the fiber blending used in Plate N.4-Bis and to replicate the fruitful local increase in temperature observed in plate N.3. The obtained plate (id. Plate N.10) has a even more pronounced difference between its central melted part and the not-melted periphery, as verified with SEM analysis, electrical conductivity mapping and Local thermal conductivity measurements presented in following Paragraphs. As already introduced in paragraph 5.1 the use of LPS will allow for a better space filling inside the material paying the cost in a more pronounced non homogeneity of the produced plates. In addition, the presence of molten carbides will allow for a higher mobility of graphite thus increasing the graphite recrystallization (105).

- Composition of MoGRCF-10: $20\%_V$ 5 $\mu m$ Mo, $40\%_V$ 45 $\mu m$ Asbury3260 graphite,,

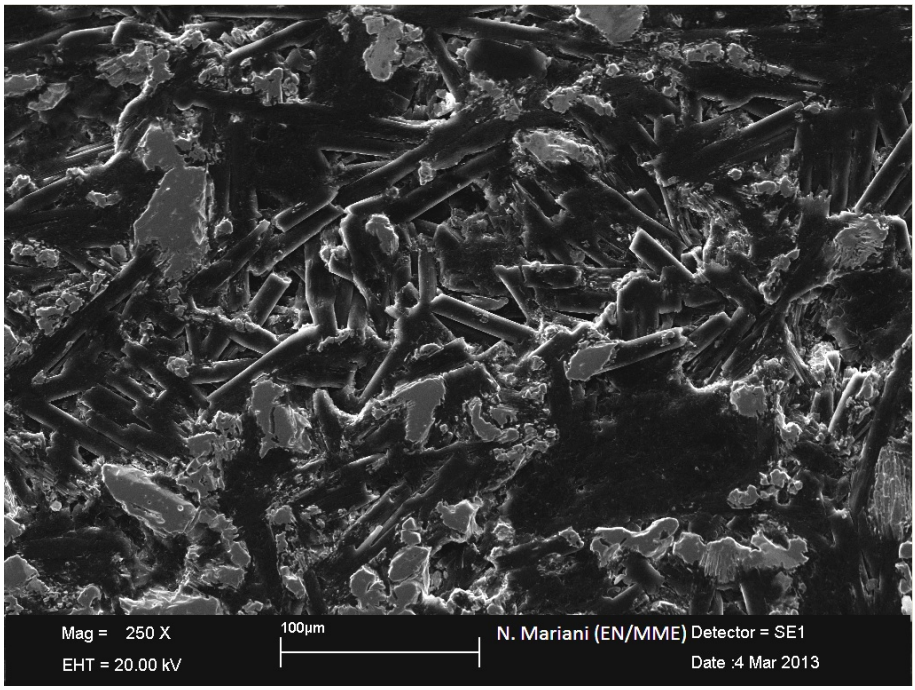


**Figure 10.16:** SE image at intermediate magnification of MoGRCF-4 plate (longitudinal cross section) sintered at $2200^oC$ with the $30\%_V$ of short fibers and the $30\%_V$ of long fibers. The fibres formed an opened net that hampered the space filling by the MoGR matrix, leaving a very porous material.

$20\%_V$ short CF, $20\%_V$ blended long CF ($\rho_{th} = 3.91\ g/cm^3$);

- Cycle: exactly analogous as previous plates.
- Mould: cylindrical mould diameter 90 mm thickness 4 mm.

In order to reduce the non-homogeneity in temperature distribution the moulds returned to cylindrical shape instead of rectangular: in this way it is possible to properly observe the radial variations in chemical composition (by EDS analysis on representative areas see 6.3.1) and electrical conductivity (by local SigmaTest measurements with low frequency, see Paragraph 6.1.2) without geometrical induced perturbations.

#### 10.3.2.1 Liquid Phase MoGRCF Characterization

The results of aforementioned tests on Plate N.10 are shown in the plot of Figure 10.18: the plate centre has a significantly reduced molybdenum carbide content and a higher electrical conductivity with respect to to the plate periphery.

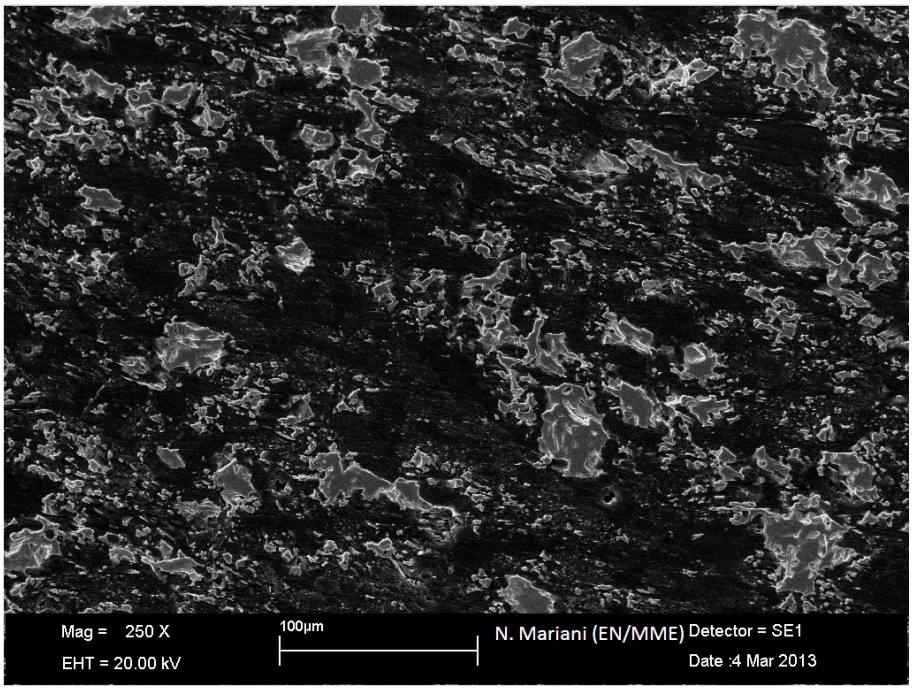


**Figure 10.17:** SE image at intermediate magnification of MoGRCF-4Bis plate (transversal cross section) sintered at $2200^oC$ with the $30\%_V$ of short fibers and the $30\%_V$ of blended long fibers. The $Mo_2C$ phase is more regularly dispersed and have smaller dimensions than in the other 4 plates.

In order to verify if the thermal properties follow the same behaviour (as expected in graphitic materials because of the electron transfer only mechanisms already discussed) also the thermal conductivity has been evaluated both in the central part and in the periphery. In order to do that the thermal test bench sample (80 mm long, see Paragraph 6.5.1) has been instrumented at four different positions to divide the thermal path in three zones along the sample, two peripheral and one central, and by evaluating the thermal conductivity in each zone by 6.5.

The results are summarized in Table 10.3.

The plots in Figure 10.18 suggest that Mo squeezed in some way out from the plate centre and accumulates at approximately 30 mm from the plate centre, this effect is due to the local melting of the $Mo_2C$ phase during the process as shown in following SEM analysis made in both locations (Figures 10.19, 10.20, 10.21 and 10.22).

**Table 10.3:** Comparison of Plate N.10 with plates N.3 and N.4Bis. * indicates the values in the plate centre and in the plate periphery (always lower).

| **Plate Id.** | **Short CF** | **Long CF** | $\rho$ | $\sigma$ | $k$ | $R_{Fl}$ |
|---|---|---|---|---|---|---|
| Unit | $\%_V$ | $\%_V$ | $[g/cm^3]$ | $[MS/m]$ | $[W/mK]$ | $[MPa]$ |
| $N.3$ | 20 | 20 | 3.65 | 0.98-0.5* | 315 | 53 |
| $N.4-Bis$ | 30 | 30 Blended | 3.73 | 0.42 | 205 | 77.5 |
| $N.10$ | 30 | 30 Blended | 3.69 | 1.03-0.5* | 420-330* | 74.5 |

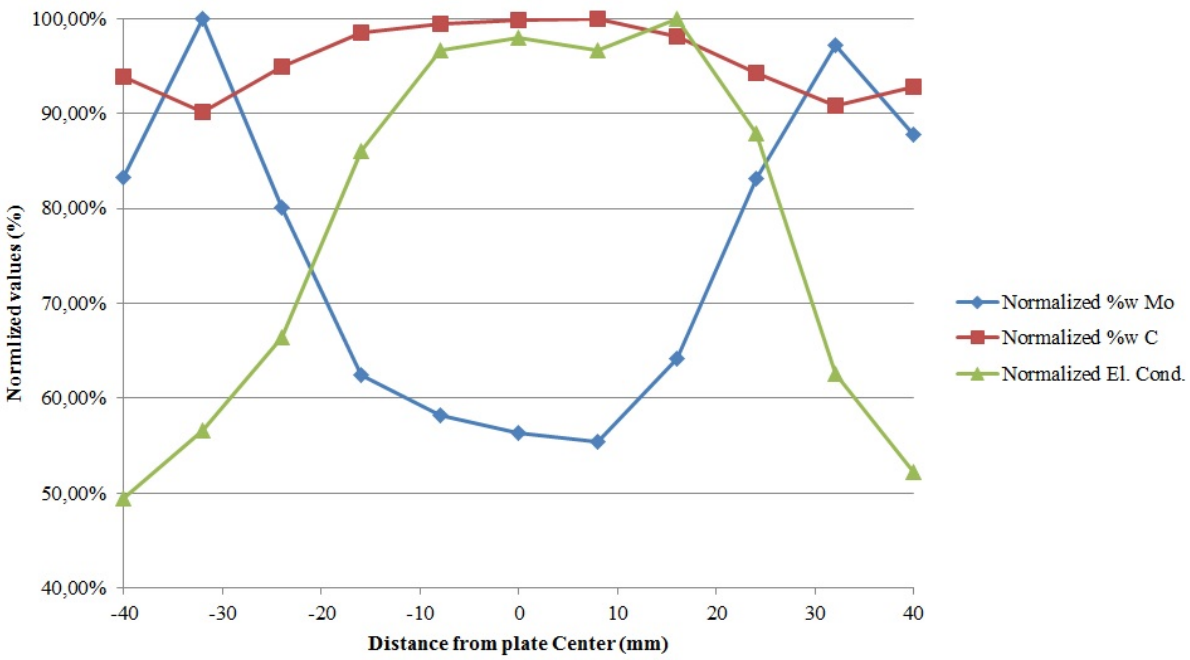


**Figure 10.18:** Normalized chemical composition (by EDS) and electrical conductivity (by Sigmatest) on Plate N.10 along radial direction.

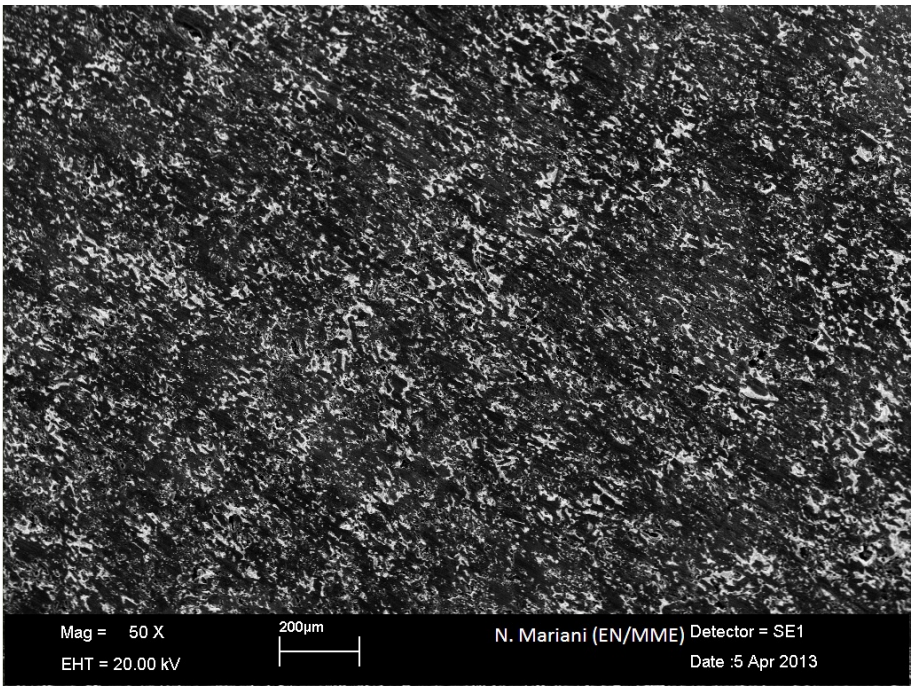


**Figure 10.19:** SE image at low magnification of MoGRCF-10 plate (transversal cross section) in the central area. The $Mo_2C$ phase forms a fine dispersion of homogeneously distributed small grains embedded into the graphitic matrix. The local amount of Mo can be estimated around the 55% of the peripheral concentration.

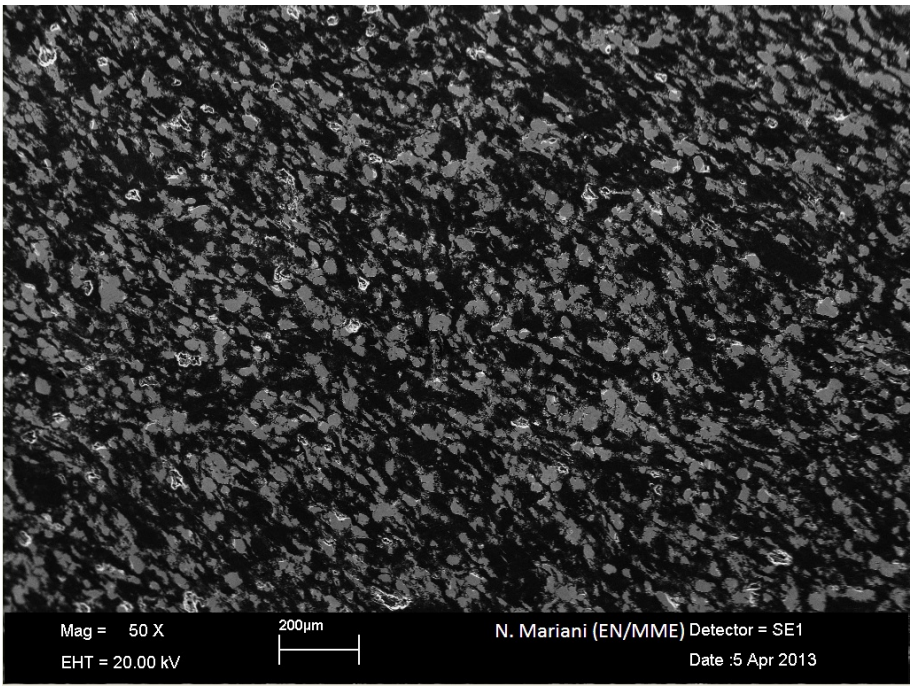


**Figure 10.20:** SE image at low magnification of MoGRCF-10 plate (transversal cross section) in the peripheral area. The $Mo_2C$ phase remains solid giving a microstructure very similar to previous plates with large coalesced $Mo_2C$ grains. There are also many macro cavities that reduce the final density of the Plate.

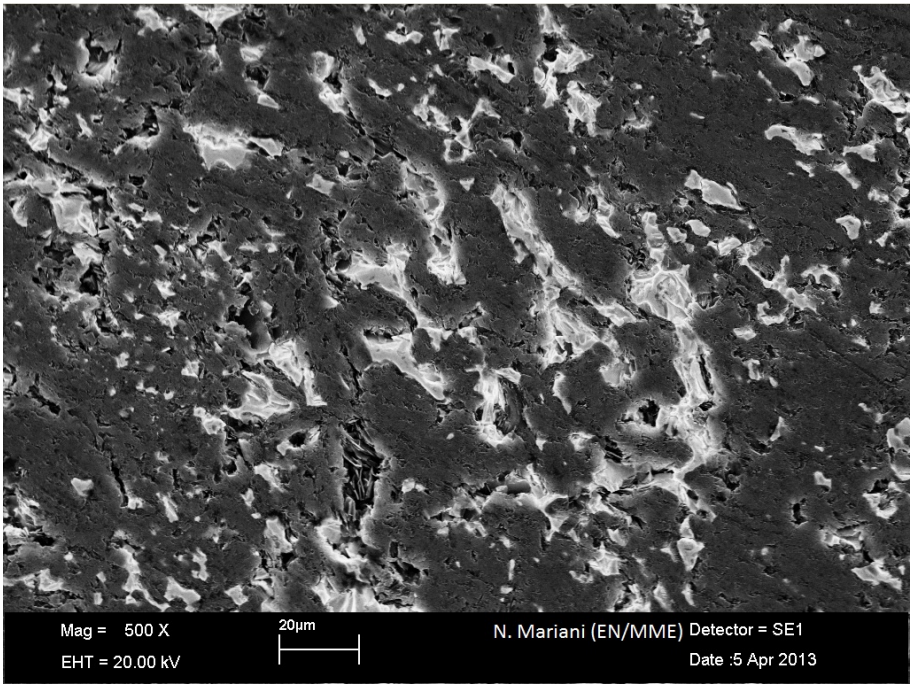


**Figure 10.21:** SE image at intermediate magnification of MoGRCF-10 plate (transversal cross section) in the central area. The small $Mo_2C$ grains have melted and squeezed in between the CF and the graphite phase, filling well the interstitials. However they also tend to contract during solidification leaving a small gap at the interface with graphite.

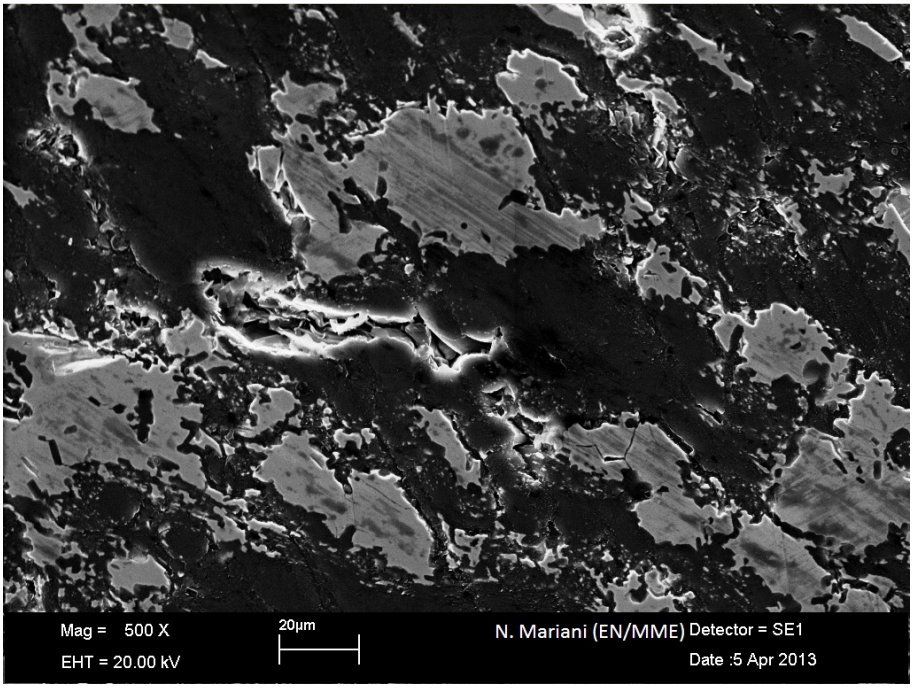


**Figure 10.22:** SE image at intermediate magnification of MoGRCF-10 plate (transversal cross section) in the peripheral area. The situation is analogous to previous non melted plates (large $Mo_2C$ grains and macro cavities) with the difference of the local increase in Mo content.

#### 10.3.2.2 Conclusions on Liquid Phase MoGRCF

The results so far proved without doubt that the internal temperature distribution was largely non homogeneous with a difference between the pyrometer measurement ($2200^oC$) and the effective temperature in the plate centre ($>2505^oC$) that overcome $300^oC$. The origin of such very high gradient have been identified in the radial heat transfer from the graphite mould external surface, that increases non-linearly with the temperature becoming non negligible above $2000^oC$, as all other previous plates were practically homogeneous. Another secondary effect is due to the powder electrical conductivity during the sintering process that gives different heat generations profiles for different compositions, as seen in the comparison between the first 5 plates (10.2).

**Table 10.4:** CERN Characterization of LPS MoGRCF. L indicates a measurement along the longitudinal direction while T along the transversal one. Note: since $Mo_2C$ flown out of the mould the final density cannot be compared to the predicted one and no compaction rate has been calculated. However the plate microstructures confirm visually a very good compaction of the material.* indicates the values along the two principal directions, longitudinal and transversal.

| **Plate Id.** | **Short CF** | **Long CF** | $\rho$ | $\sigma$ | $k$ | $R_{Fl}$ |
|---|---|---|---|---|---|---|
| Unit | $\%_V$ | $\%_V$ | $[g/cm^3]$ | $[MS/m]$ | $[W/mK]$ | $[MPa]$ |
| 10/10 | 20 | 20 Blended | 2,78 | 0.95-0.45* | 720-380* | 73 |

Once blocked the composition to the values identified for plate N.10, the furnace have been equipped with an additional insulating sarcophagus in order to control the radial heat losses without composition effects: the lower radial flux allowed to increase the nominal temperature in the pyrometer measuring point up to $2560^oC$ while minimizing the radial temperature gradient and allowing the complete melting of $Mo_2C$ all over the plate.

The resulting plate (id. Plate N.10/10) characterization results are reported in Table 10.4: the final density is lower than the nominal value because there have been an overflow of liquid $Mo_2C$ during the process due to the hydrostatic pressure of the molten phase. The EDS estimation of the effective composition also confirms that practically half of the total Mo content flow out of the material and remained attached to the graphite moulds. The $Mo_2C$ content remains in forms of elongated small grains that follow the shape of the CF and of the graphite grains (see Figure 10.24).

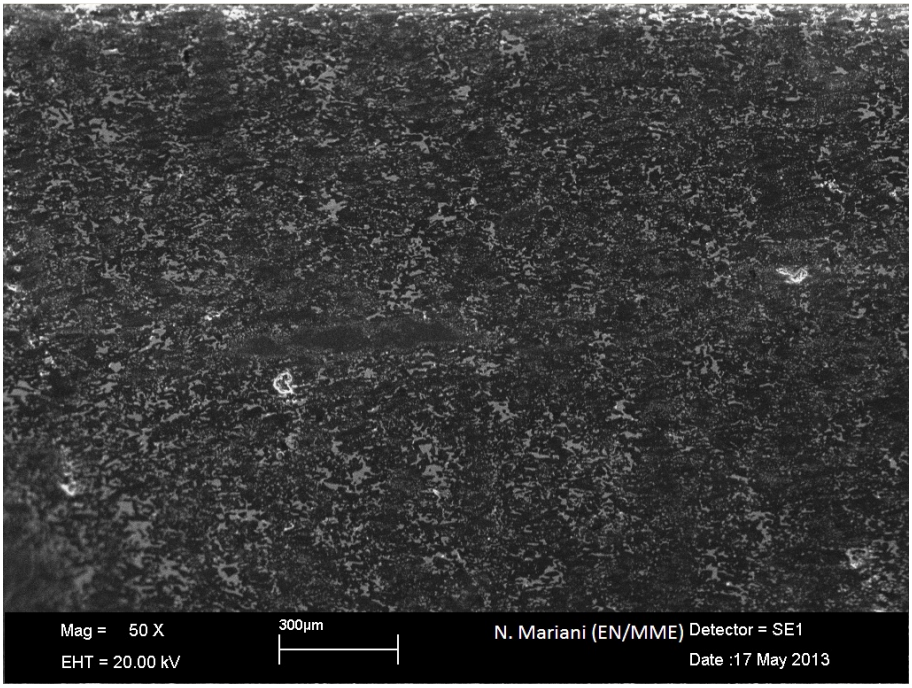


**Figure 10.23:** SE image at low magnification of MoGRCF-10/10 plate (transversal cross section). General aspect of the material, similar to the microstructure in Figure 10.19. The main difference is the presence of few macro cavities that were absent in the molten area of plate N.10.

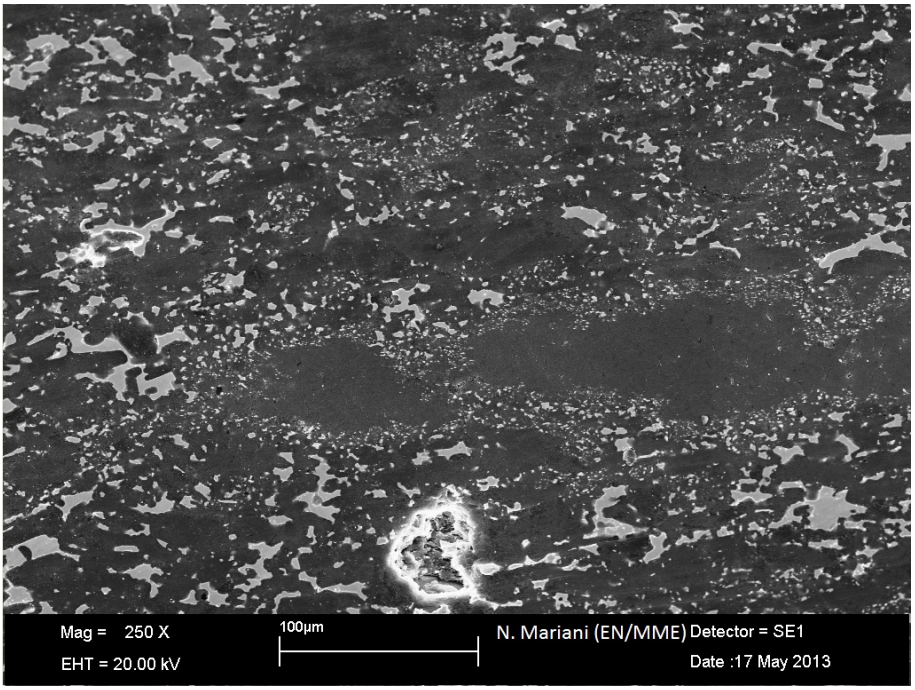


**Figure 10.24:** SE image at low magnification of MoGRCF-10/10 plate (transversal cross section). Presence of few (and small) long fibers aggregates, macrocavities and molten $Mo_2C$ grains.

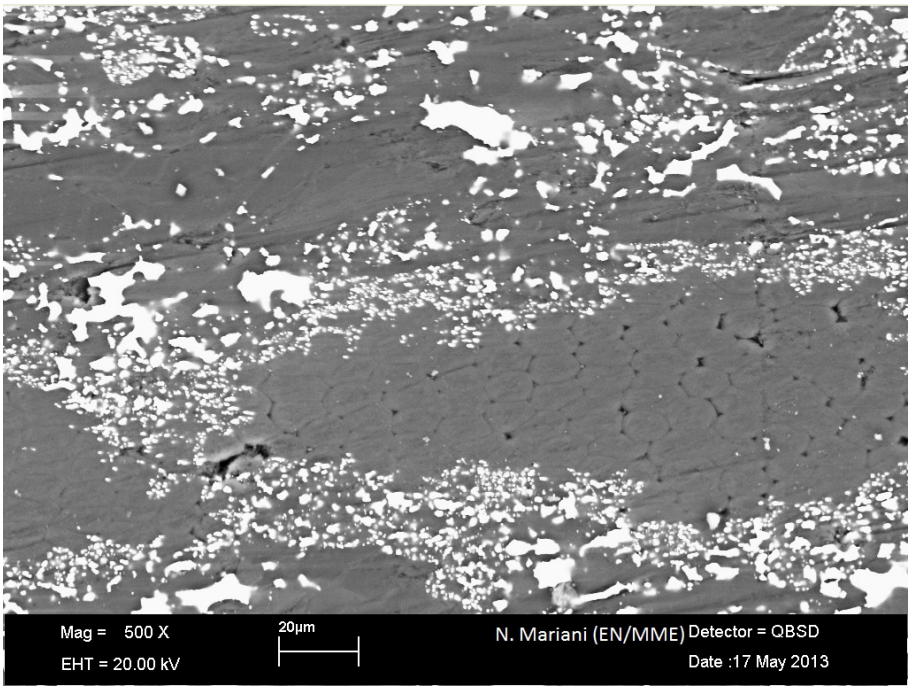


**Figure 10.25:** QBSD image at intermediate magnification of MoGRCF-10/10 plate (transversal cross section). The QBSD technique has been used to mark the slight differences in graphite phase compaction: it allows to see the partial sintering of long fibers inside the aggregate and to distinguish between graphite and CF inside the matrix (upper area).

However, the plate is perfectly homogeneous in terms of microstructures, local EDS composition and electrical conductivity so we can assume that the temperature gradient has been minimized and has no longer visible effects on the material final homogeneity.

The most spectacular result is the obtained thermal conductivity of above 700 $W/mK$, value that has to be compared with the expected thermal conductivity evaluated by the Kapitza model as for MoGR (see 9.5.1) along the plate longitudinal direction, which is $\approx 720W/mK$ (and $\approx 280W/mK$ in the transversal direction). It means that $MoGRCF - 10/10$ plate shows an effective thermal conductivity which is $\approx 97\%$ of the theoretical one, proving the effectiveness of the production process and of the chosen composition.

There is still an uncertainty in the measurement made with CERN's thermal test bench due to the lack of suitable references for such very good conductors, but the measurement has been repeated more times with different thermal probes giving re-

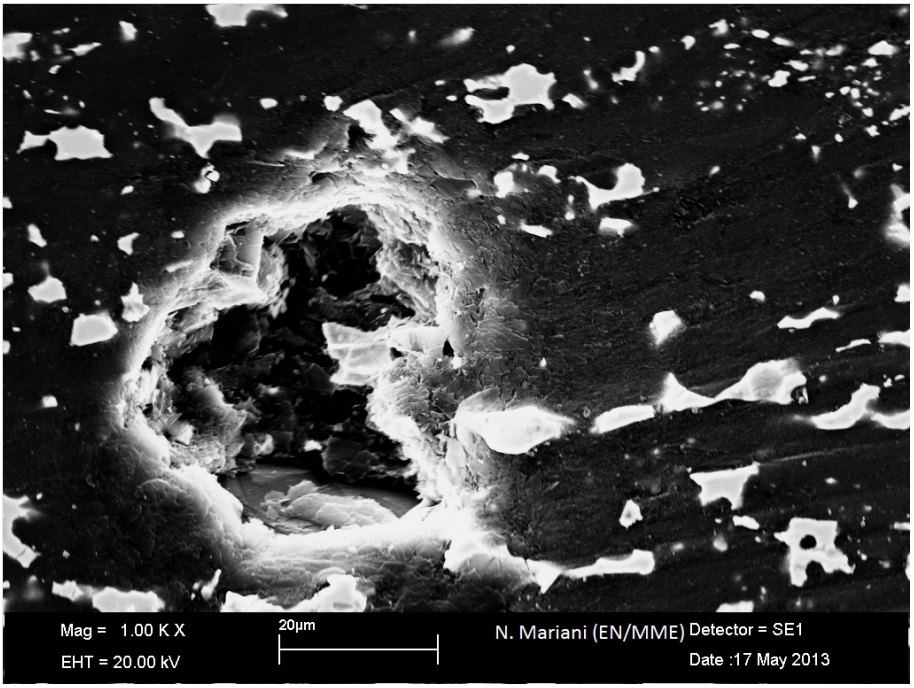


**Figure 10.26:** SE image at high magnification of MoGRCF-10/10 plate (transversal cross section). Particular on the macro cavity: the cavity has not been filled by liquid $Mo_2C$ during the LPS and was too large to disappear by diffusion. The surrounding volume appears instead fully dense with recrystallized graphite grains.

producible results. A second source of error is the reduced temperature interval inside the sample that reflects in higher dispersion of the final values. For all these reasons a more precise laser flash measurement will be performed on the massive final plates to validate the material thermal conductivity with standardized measurements.

## 10.4 Conclusions on MoGRCF

The *R&D* program on MoGRCF concluded with the identification of a suitable composition and production cycle to obtain a material having outstanding thermal and physical properties. The material final properties are as usual compared with the other materials of interest in Table 10.5 in order to appreciate the evolution of the FoM of the materials developed during the present study. As made for CFC (see Paragraph 4.1.1 and 4.3) the value of $k$ is a ROM average between the three directions, while the values of CTE, Poisson's ratio and ultimate strength have been obtained using the approach described in Paragraph 9.5.1.

**Table 10.5:** Final properties and FoM for MoGRCF compared to MoCuCD, CuCD and MoGR. Values with * are estimations based on the considerations reported in 9.5.1.

| Material | Unit | CFC | MoCuCD | CuCD | MoGR | MoGRCF |
|---|---|---|---|---|---|---|
| Density | $[g/cm^3]$ | 1.65 | 6.9 | 5.4 | 5.3 | 2.78 |
| Atomic Number (Z) | $[-]$ | 6 | 17.4 | 11.4 | 15.9 | 13.7 |
| Melting Temperature | $[^oC]$ | 3650 | 1083 | 1083 | 2505 | 2505 |
| Thermal Conductivity | $[W/mK]$ | 168 | 155 | 490 | 135 | 487 |
| CTE | $[10^{-6}K^{-1}]$ | 1.88 | 7 | 7.8 | 7.59* | 2.61* |
| Specific Heat | $[J/kGK]$ | 780 | 360 | 420 | 261.1* | 568.5* |
| Young's Modulus | $[GPa]$ | 53 | 260 | 220 | 179.25* | 51.76* |
| Tensile Strength | $[MPa]$ | 87 | 140 | 70 | 95.7 | 50 |
| Poisson's Ratio | $[-]$ | 0.16 | 0.3 | 0.22 | 0.19* | 0.17* |
| Electrical Conductivity | $[MS/m]$ | 0.14 | 10 | 12.6 | 1 | 1 |
| Radiation Length $\chi_0$ | $[cm]$ | 12.25 | 2.82 | 4.78 | 4.99 | 8.13 |
| SSNI | $[kWm^2/kg]$ | 54.1 | 3.2 | 11.6 | 3.4 | 67.2 |
| TSNI | $[kJ/kg]$ | 570.8 | 19.4 | 13.4 | 14.9 | 174.3 |

The main advantages of the newly introduced MoGRCF materials are:

- Exceptional thermal properties along the planar direction, resulting in an optimal balance of stationary and transient thermal stability. Properties along the transversal directions are anyway in the order of the 50% of the respective values in longitudinal direction.
- Tailored density of 2.78 $g/cm^3$ that lead to an intermediate radiation length between CFC and CuCD, allowing for a smooth but effective beam cleaning.
- High stability at high temperature: MoGRCF is made only by very stable refractory phases (recrystallized graphite and $Mo_2C$) that will not melt until $2500^oC$.
- Shock wave dumping: the low Young's Modulus and the high graphite content assure a good wave dumping effect that will allow for a smooth shock wave dissipation.
- Electrically conductive in both directions, allowing a good charge evacuation and reducing the overall Collimators Impedance.

The newly introduced composite is now being produced in thicker plates at BrevettiBizz to verify the reproducibility of the results obtained on the thin test plates.

# 11

# High Energy Beam Impacts on Materials

The present Chapter includes the numerical simulations of direct high energy proton beam impacts on materials and the experimental activities carried out to validate the proposed models. The activities entailed the understanding of very fast dynamic phenomena, the development of experimental apparatus for the data acquisition and the results analysis.

The chapter is therefore so structured:

- Numerical modelling of thermally induced dynamic phenomena
- Description of experimental activities inside the HiRadMat facility at CERN
- Experimental results
- Discussion on the post irradiation damage on all tested materials

## 11.1 Introduction to Thermally Induced Dynamic Phenomena

As stated in Paragraph 3.3 it is paramount to assess the responses to potentially destructive events such as highly energetic proton beam impacts on the materials presently used, or being developed for future use, in LHC Collimators (and of course in other BID devices like targets, dumps, absorbers, spoilers, windows etc.).

The approach followed to study the problem is to first derive numerical methods capable to predict the entire dynamic phenomena generated in matter when it is impacted by beams made of highly energetic particles (phase transitions, density changes, generation and propagation of shock waves, explosions and fragment projections) and then verify the proposed numerical methods with an ad hoc experiment (id. HRMT-14) carried out inside the HiRadMat facility at CERN during 2012 (106), (107).

### 11.1.1 Shock waves

The rapid interaction of highly energetic particle beams with matter induces a dynamic responses in the impacted structure which nature, intensity and time scale depend on several parameters, mainly deposited energy and energy density, interaction duration, physical and mechanical properties of the impacted material. The phenomena is governed by the blocked thermal expansion of the impacted material's core by the cold surrounding material that provokes a pressure spike with the formation of travelling stress waves inside the material (108), (22). When the deposited energy density is high enough to provoke strains and stresses overcoming the critical threshold for the specific material, a shock wave is formed propagating at a velocity higher than $C_0$ (sound speed in standard condition), potentially leading to severe damages in the affected component. A shock wave can also be reflected at the free surfaces or at the interfaces with other components, leading to the shock wave propagation or reflection. In the second case the wave will pass from compressive to tensile and can lead to failures due to hydrostatic spallation.

## 11.2 Numerical Modelling

When dealing with changes of phase and significant changes of density, one has to resort to a new class of wave propagation codes, known as hydrocodes. These are highly non-linear finite element tools, using explicit time integration schemes, developed to study very fast and intense loadings on materials and structures (109). Hydrocodes take their name from the original assumption of pure fluid-like behaviour of the impacted solids, which is typically acceptable when achieved stresses greatly exceed the flow strength of the material and the stress tensor can be reduced to its hydrostatic component only;

nowadays the deviatoric behaviour (responsible for material strength) is also taken into account; however the original name is still widely used.

Hydrocodes usually rely on complex material constitutive models encompassing a very large range of densities and temperatures, which, unlike implicit FEM codes, may include large changes of density and phase transitions. Strength and failure models are also more complicated as they have to account for the effects of strain rate, temperature, changes of density etc as shown in following Paragraphs.

### 11.2.1 Importation of Energy Deposition maps

The input for numerical simulations is the map of the thermal load generated by the beam impact on the component. The deposited energy can be calculated through a Monte-Carlo particle transport code and depends proportionally to the density and the atomic number of the impacted material as already discussed in Paragraph 3.3.3: the higher the density, the higher the stopping power of the target and the energy deposited by the beam. Simulations described in this paper are performed with Autodyn (110), while energy deposition 3D maps are calculated with FLUKA (111) (112).

FLUKA raw output is a tabular $3D$ map of the internal energy density as a function of the number of incoming particles $p$ (unit $[GeV/p * cm^3]$): since Autodyn requires values in $[J/Kg]$ it is necessary to scale the FLUKA results by the chosen number of incoming protons and by the density of each element. In addition the FLUKA elements are usually not coincident with the Autodyn elements so the FLUKA map has to be applied to the mesh of Autodyn by apposite algorithms of mesh interpolation.

The conversion is made by a Fortran subroutine integrated in Autodyn, which has been developed at CERN in past years to conveniently import FLUKA maps in hydrocodes (113) for studying beam impacts on Uranium targets; the subroutine can deposit the energy both continuously during all the impact or divided into bunches with imposed bunch spacing. It is worth noting that in this case the time step has to be kept smaller than the bunch duration to appreciate the effect of the stepped deposition leading to very long calculation times. The assigned internal energy is then treated by Autodyn as explained in following Paragraphs.

### 11.2.2 Constitutive Models

### 11.2.3 Equations of state

The Equation Of State (EOS) is a constitutive relation between the state variables of a material; usually it expresses the pressure (or the internal energy) as a function of two independent variables such as density and temperature. Most widely adopted EOS for wave propagation in solids are Shock, Tillotson (114) and MieGrneisen: these formulations involve complex theoretical models based on the band theory and combine them with shock compression experimental data. However, analytical modelling can describe only a single region of the EOS (115), excluding the description of phase transitions. Tabular EOS overcome this problem, integrating different analytical formulations to describe the behaviour of different phases and the related phase transitions (116).

The EOS used in this work is the tabular SESAME N.3550 (117) shown in Figures 11.1 and 11.2 (in two distinct Matlab plots for pressure and internal energy); it has been devised for pure tungsten, for which experimental Hugoniot data are close to those of W-Ni-Cu heavy alloys (118).

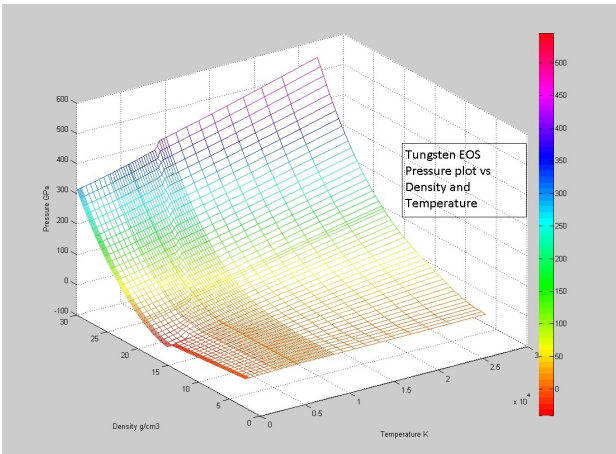


**Figure 11.1:** Equation of State SESAME 3550 for pure tungsten: plot of Pressure as a function of density and temperature.

#### 11.2.3.1 Strength Model

The strength model simulates the deviatoric behaviour of the material and has to take into account the phenomena occurring in the matter during the beam impact, such as

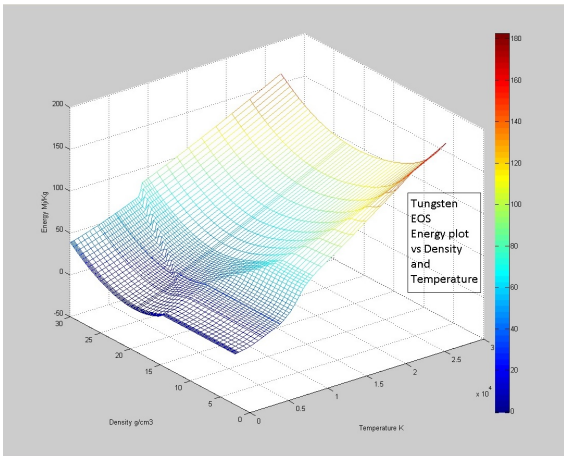


**Figure 11.2:** Equation of State SESAME 3550 for pure tungsten: plot of internal energy as a function of density and temperature.

the melting of the impacted volume (loss of material strength), the variations in elastic and plastic behaviour in the thermally altered zone and the hardening due to high strain rates in order to evaluate the propagation speed, the intensity and the damping during the travel inside the sample and obtain the wave intensity on the free surface. A widely adopted model that considers the above mentioned effects is the Johnson-Cook (JC) model (119), whose parameters can be obtained through a set of experimental tests, which include Hopkinson Bars, Taylor cylinders, tensile and compression tests at different temperatures. The JC model expresses the flow stress as:

$$\sigma_y = (A + B\epsilon_{pl}^n) + \left(1 + C * ln\frac{\dot{\epsilon_{pl}}}{\dot{\epsilon_0}}\right) * \left(1 - \left(\frac{T - T_m}{T_m - T_r}\right)\right) \tag{11.1}$$

where A is the J-C elastic limit $[MPa]$, B $[MPa]$ and n $[-]$ are the work hardening parameters, C $[MPa]$ express the strain-rate sensitivity and m $[-]$ describes the thermal softening with respect to the reference temperature $T_r$ $[K]$.

The Inermet180 parameters used for hydrodynamic simulations are reported in Table 11.1; such values are based on the experimental results on W-Fe-Ni alloys and were slightly modified to fit Inermet180 mechanical properties.

The JC Model is not suitable for the composite materials of interest because of their intrinsic fragility discussed in Paragraph 5.3.2: the statistical distribution of defects can be taken into account only relying on statistical empirical models like the Johnson-Holmquist model (120). The main disadvantage with respect to semi analytical models

**Table 11.1:** Johnson Cook Model parameters used for Inermet180 simulations.

| **Equation of State** | **Strength Model** | | **Failure Model** | |
|---|---|---|---|---|
| Tabular | Johnson Cook | | Hydrostatic Minimum Pressure | |
| SESAME 3550 | Shear Modulus | $140GPa$ | Pmin | $2.7GPa$ |
| | A | $715MPa$ | Fracture Energy | $515J/m^2$ |
| | B | $177MPa$ | | |
| | n | 0.12 | | |
| | C | 0.016 | | |
| | m | 1.00 | | |
| | $T_m$ | 1616 K | | |
| | Ref. Strain rate | $1s^{-1}$ | | |

like JC is that a large number of experimental tests is required to obtain reliable parameters, and it has not been possible to prepare suitable models for the 3 studied composites.

#### 11.2.3.2 Failure model

This model contains the set of conditions which lead to the bulk failure of the material; its choice heavily depends on the physical fracture mechanism. In case of particle beams impacting close to a free surface, the compressive shockwave immediately reflects back and turns into a tensile wave in the adjacent volume, causing the bulk failure of external crust and the projection of melted material (121). This mechanism could be reproduced in Autodyn through the Minimum Hydrostatic Pressure model (Pmin); the model also implements the energy necessary for crack formation, calculated on the basis of the material fracture toughness. Reference values have been obtained experimentally with laser-induced spallation tests on polycrystalline tungsten (122).

### 11.2.4 Numerical Methods

#### 11.2.4.1 Lagrangian method

Impacted components can often be modeled with a lagrangian mesh: even when high deformations or material spallation occur, it is possible to overcome the limitations of the lagrangian method by, for example, implementing the erosion of elements at

given thresholds of stress, temperature or deformation. This approach was therefore adopted to simulate the response of type 1 samples impacted at medium energy during the test in the HiRadMat facility. When importing the thermal load in Autodyn, a subroutine interpolates the energy deposition map calculated by FLUKA and assigns the corresponding energy density to the Autodyn elements: ideally, no interpolation artifacts are generated throughout the process if the two meshes are identical. On the other hand, in order to decrease the simulation time, the mesh in Autodyn is often coarser and is refined only around the impact point, i.e. in the volume containing the most loaded elements. The impinging proton pulse is constituted by trains of bunches spaced by 25 ns, while the impact duration of each bunch is 1 ns. The energy distribution deposited by one bunch, calculated with FLUKA, is therefore uploaded in Autodyn every 25 ns: this means that the time step of the simulation should be lower than 1 ns in order to correctly reproduce the impact phenomenon. The time step can be increased after the end of the beam impact up to 10 ns for numerical stability.

#### 11.2.4.2 Smoothed-particle hydrodynamics

The above mentioned lagrangian method is no longer adequate when the main goal of the study is to model the material fragments ejected after high-energy impacts and the residual damage on structures and components. In such case, one has to adopt a different approach, such as the smoothed-particle hydrodynamics (SPH) technique. In this computational method, the material is modelled by discrete elements (particles) with a spatial distance of interaction (smoothing length) over which their properties are weighted by a kernel function. This method was used for the simulation of high energy deposition on HiRadMat type 2 samples which will be object of the present thesis work; since the SPH algorithm requires high computational time, only the inner volume of the specimen was modelled with SPH particles, while all the other regions were meshed with lagrangian elements to save computational time.

## 11.3 Experimental Activity

The performed tests entailed the controlled impact of intense proton pulses on specimens made of seven materials of interest for LHC Collimators already discussed in the present thesis work and reported below:

- Metallic materials
  - Inermet180 Tungsten Heavy Alloy (see Paragraph 4.1.3)
  - Molybdenum (see Paragraph 4.1.5)
  - Glidcop (see Paragraph 4.1.4
- Composites
  - CuCD (see Paragraph 7)
  - MoCuCD (see Paragraph 8)
  - MoGR and MoGRCF (see Paragraphs 9 and 10)

Two different specimen shapes were chosen for each material (Figure 11.3):

- Cylindrical disks (type 1) for medium intensity tests, to measure axially symmetric shockwaves;
- Cylinders with a half-moon cross section (type 2) for high intensity tests, allowing extreme surface phenomena (melting, material explosion, debris projections etc.) to be visualized and optically acquired.

The specimens were arranged into the sample holder tank maintained under vacuum shown in Figure 11.4, (106).

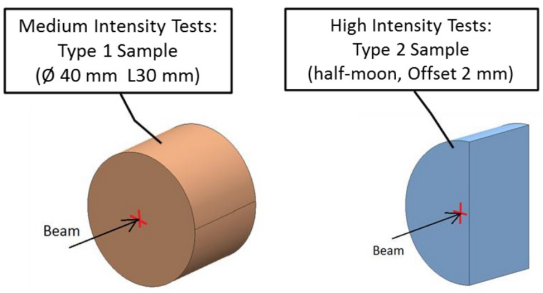


**Figure 11.3:** Material specimen shapes for tests at medium and high intensity.

The effects of thermally induced shock waves on the materials were acquired via high speed acquisition system including strain gauges, laser Doppler vibrometer and high speed camera. Information of beam induced damages on materials were also collected by the observation through a lateral view port.

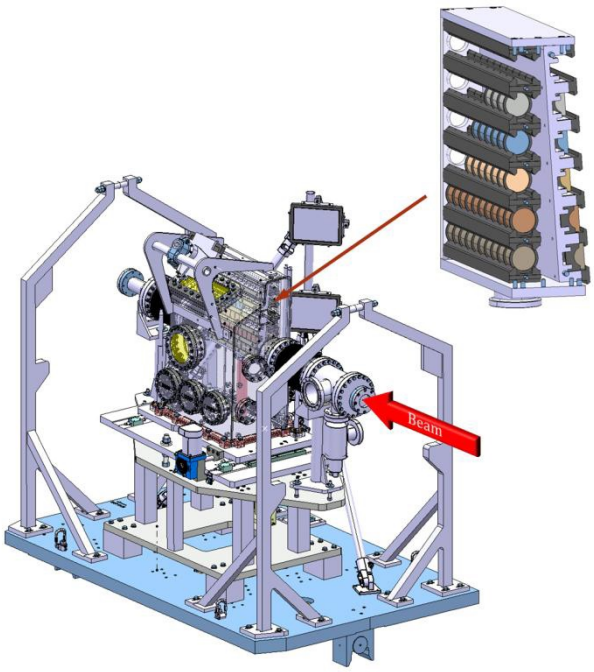


**Figure 11.4:** General assembly of the HRMT14 test-bench. Red arrow represents the beam.

The results have then been compared to the numerical analysis, when available: in fact, the material models which are required to perform the numerical simulations, at the extreme conditions, as to temperature, pressure and density, induced by such impacts, are hardly available in scientific literature; besides, most of the existing information is often classified as it is drawn from military research mainly related to nuclear weaponry. Finally, very little data can be found for advanced ceramics and compounds, in particular the lack of materials constitutive models for Mo, $Mo_2C$, graphite and diamond hamper the realization of numerical simulations on such materials.

However, the post irradiation analysis presented in Paragraph 11.4 of impacted samples offers the opportunity to compare the strength of the different materials in view of the materials choice for future LHC Collimators.

Table 11.2 reports the characteristic values of the impacting beam during tests on Inermet180 in the HiRadMat facility. Numerical simulations adopted the same parameters, except for the beam transverse dimension which was set to 2.5 $x$ 2.5 $mm^2$.

**Table 11.2:** Beam parameters for tests performed on Inermet180 during HRMT-14 experiment.

| Parameter | Medium intensity test | High intensity test |
|---|---|---|
| Proton energy | $440GeV$ | $440GeV$ |
| Number of bunches | 24 | 72 |
| Pulse intensity | $2.7 * 10^{12}$ protons | $9.05x10^{12}$ protons |
| Energy on the most loaded specimen | $8.35kJ$ | $25.1kJ$ |
| Theoretical impact point | Centre | 2 mm from flat surface |
| Beam transverse dimension | $1.4\ x\ 2mm^2$ | $1.9\ x\ 1.9mm^2$ |

### 11.3.1 Medium intensity impacts

Strain gauges measured axial and hoop strains on the external surface of type 1 samples, while the laser Doppler vibrometer acquired the radial velocity. Acquired raw data were then compared to the results of numerical simulations (Figure 11.5). A strong electromagnetic noise induced by the particle beam perturbed the strain gauge measurements during the first few microseconds after the impact, concealing the first deformation peak. However, this effect was limited to the beam impact duration, allowing to capture the remainder of the phenomenon. Measured and simulated signals are in good accordance during the first three reflections of the shock wave; afterwards, the modifications in the material bulk induced by the shock wave lead to an overestimation of the wave speed. Random spikes in the signal of gauges and LDV will be treated during more accurate signal processing.

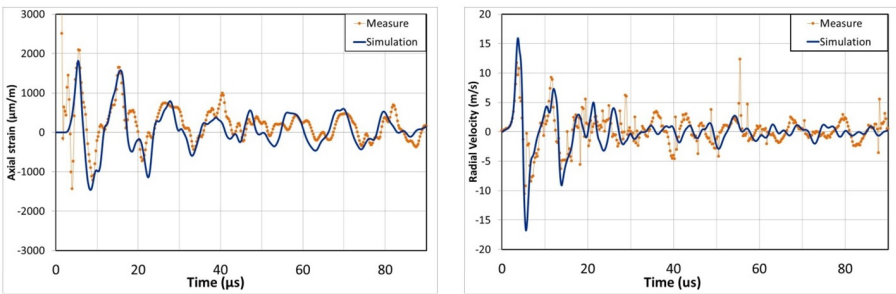


**Figure 11.5:** Left: Axial strain measured with strain gauge at r = 20 mm, L = 15 mm and numerically simulated. Right: Radial velocity measured with LDV at r = 20 mm, L = 15 mm and numerically simulated.

### 11.3.2 High intensity impacts

The developed high-speed camera system allowed for the first time, to the best of authors knowledge, to record images of the impact of a proton beam on solid targets and of the effects induced.

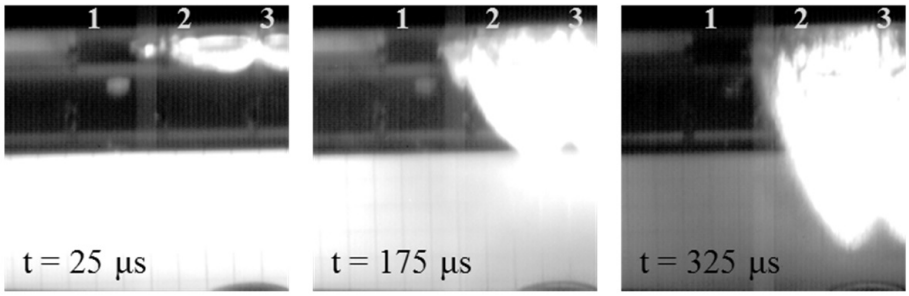


**Figure 11.6:** High-speed video camera images of the ejected particle cloud: the beam is coming from the left while the cloud is moving downwards; three Inermet180 samples are partially visible (numbered 1 to 3).

As shown in Figure 11.6, a large quantity of hot material was ejected at high velocity from the two most loaded Inermet180 type 2 samples, generating the large cavities shown in the post irradiation analysis. Concerning the SPH simulation results, ejected material front shape and calculated absolute velocity (ABS VEL in Figure 11.7) are both consistent with the high-speed camera measurements,even considering the differences in beam size between real and simulated scenarios. The velocity of the fragment front has been estimated by measuring the displacement between two successive frames and is about $275m/s$, well matching the calculated velocity of $316m/s$ (difference is about 15%).

### 11.3.3 Post Irradiation Damage

The prediction of the post irradiation damage based on hydrodynamic simulations cannot rely only on the simple erosion of failed elements, since the entire phenomena of material ejection and hole formation lasts several milliseconds that are (with actual algorithms and computers) impossible to simulate in a reasonable amount of time. In addition the hydrodynamic code cannot take into account the solidification of molten elements (once the SPH correlation is broken the code cannot re create the bonding).

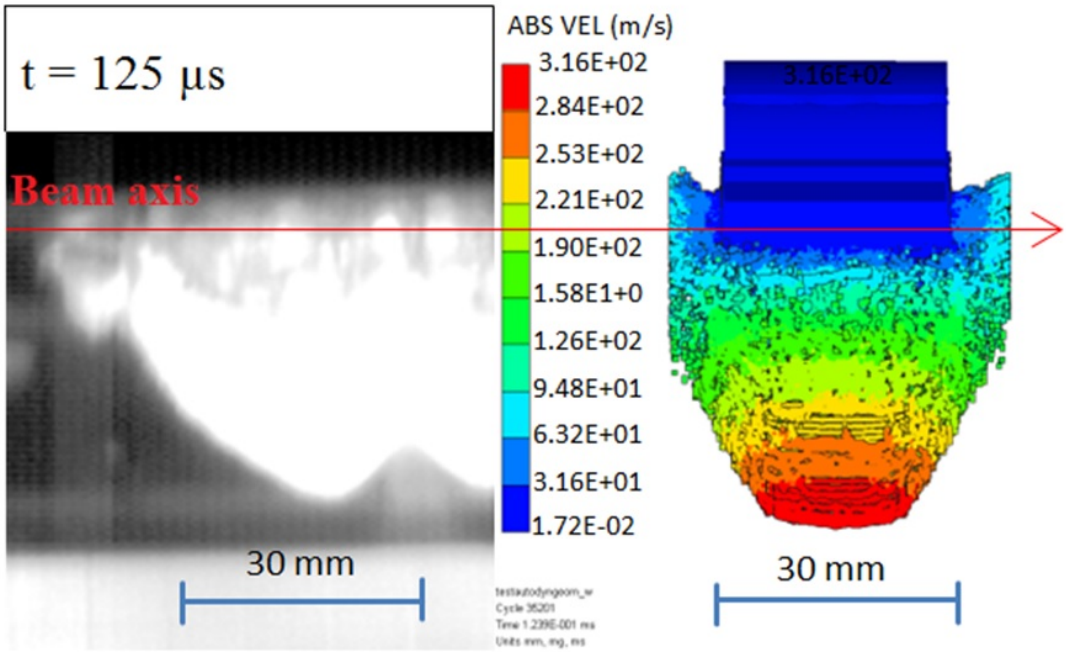


**Figure 11.7:** Comparison between simulation (SPH) and acquired image.

Finally, the erosion criterion must take into account the effects of the material internal structure, especially for composites materials where the reinforcement phase has usually a much higher $T_M$ than the matrix and therefore there will be a two stage phase change inside the composite. Note that from this point of view Inermet180 can be assimilated to a MMC since the Tungsten and Cu-Ni phase are completely separated and have different $T_M$ ($3400^oC$ vs. $\approx 1400^oC$ as shown in Figure 4.3.

As an example in Figure 11.8 is reported the effect of imposing the erosion to the elements where the Cu-Ni phase melted ($T > 1400^oC$) for Inermet180: the residual cavity has a maximum diameter of $\approx 9.2mm$ in good agreement with the experimental result ($\approx 10.5mm$) shown in Figure 11.11.

The performed work on Inermet180 showed how the implemented numerical tools are able to predict the effects of intense beam impacts on solid targets if proper constitutive models are available, pushing forward to obtain similar models for all materials of interest, including ceramics and composites.

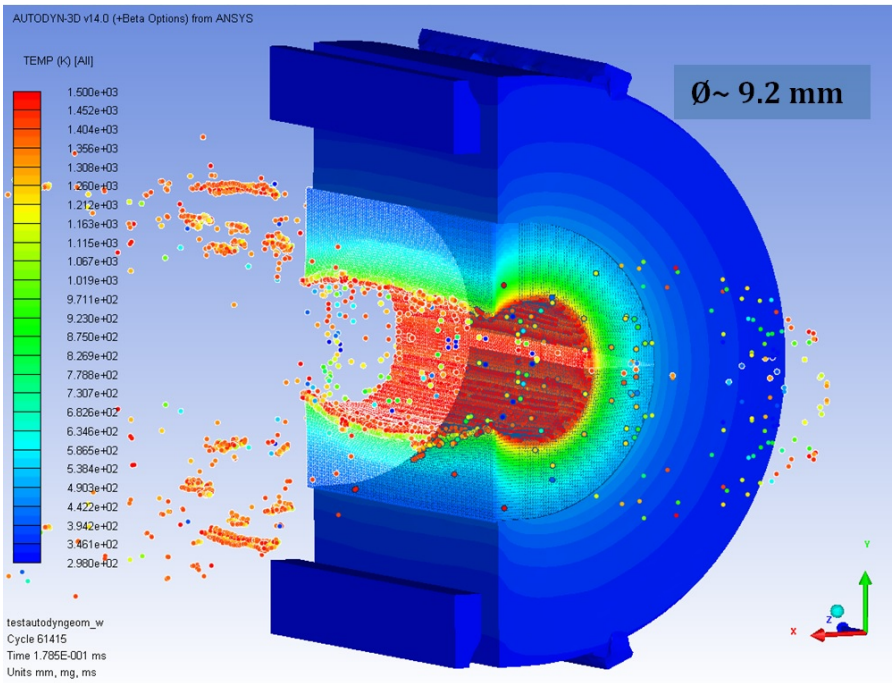


**Figure 11.8:** Autodyn simulation of the High Intensity beam impact on Inermet180: residual damage estimation by imposing the erosion criterion.

## 11.4 Post Impact Residual Damage

### 11.4.1 Energy Deposition on Materials

The energy deposition maps of all the HRMT-14 impacts have been recently updated by A. Manousos and V. Vlachoudis (123): the calculations are based on the method described in 11.2.1 and have been performed taking into account the effective beam sizes and final intensities had during the experiment.

The final sample disposition for the High intensity shot is reported in Figure 11.9: the total number of samples have been priorly evaluated to completely stop the incoming beam, at least for denser metals.

The last array for MoGR and MoGRCF consists in a mix of three different grades available in 2012: all materials have sintered in solid state, the references are listed below.

- $MoGR - 24C$, Sintered at $1700^oC$, Density 5.4 $g/cm^3$, see Paragraph 9.5 for properties;

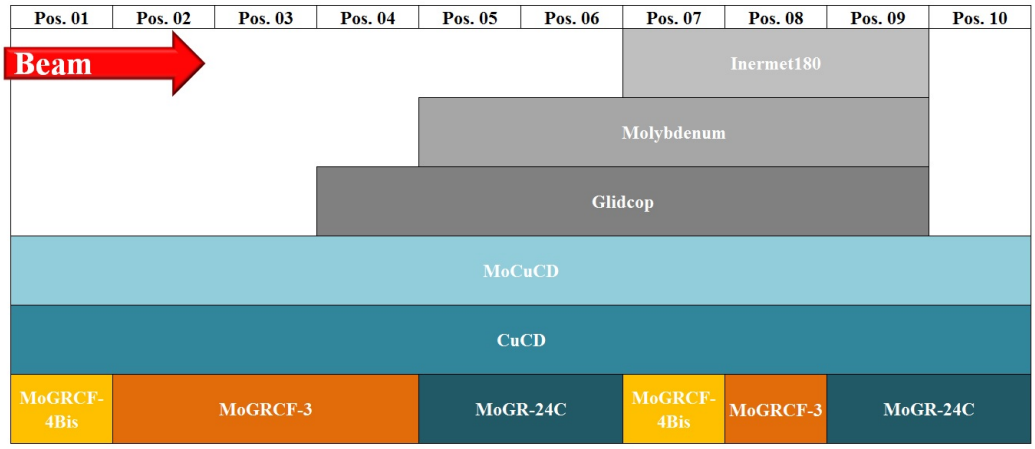


**Figure 11.9:** High Intensity shots samples location for all the different materials.

- $MoGRCF-3$ and $MoGRCF-4Bis$, Sintered at $2200^oC$, Density $\approx 3.8\ g/cm^3$, see Paragraph 10.3.1 for properties.

The summary of the High Intensity shots for all materials is reported in Table 11.3: the centred shots consists in 72 bunches of $\approx 1.15 * 10^{11}$ protons for metals and of 144 bunches at the same Intensity for composites. At the end of all foreseen tests due to absence of visible damage on Mo a second High Intensity shot (H5 o) have been performed with a vertical offset of 10 mm and double the intensity, allowing to produce extended damage on Mo samples too.

In the following sections the Post Impact Damage for each shot will be presented and discussed in separate Paragraphs.

### 11.4.2 Inermet180

The final aspect of the Inemert180 sample array after the H6 shot is reported in Figure 11.11: the exposed fracture surface appears nubby and there are no signs of plastic deformation, indicating a brittle failure with projection of independent small particles; the particles can also be seen on the white plate on the bottom of Figure 11.11. There is also a slightly visible sign of external colour variation in the Zone Thermally Altered (ZTA) due to the superficial oxidation at high temperature. This confirms the presence of some oxygen in the tank due to the low vacuum level.

**Table 11.3:** Summary of the High Intensity shots parameters. Each shot is identified by H + material number + impact location (c, center or o, offset 10mm), for each shot its reported the total number of impacting bunches (impacting in the same location and spaced in time by 25 ns), the total number of impacting protons (Total intensity), the maximum Energy Density Peak and the Total Energy deposited along the entire raw.

| **Shot Id.** | **Material** | **Bunch N.** N. of Bunch | **Tot. Int.** N. of $p^+$ | **Max En. Dens.** $[KJ/cm^3/pulse]$ | **Tot. En.** $[KJ/pulse]$ |
|---|---|---|---|---|---|
| H1 c | MoGRCF | 144 | $1.95 * 10^{13}$ | 5.1 | 10 |
| H2 c | CuCD | 144 | $1.95 * 10^{13}$ | 4.9 | 9.9 |
| H3 c | MoCuCD | 144 | $1.96 * 10^{13}$ | 8 | 15.5 |
| H4 c | Glidcop | 72 | $8.71 * 10^{12}$ | 7 | 9.5 |
| H4 o | Glidcop | 72 | $8.71 * 10^{12}$ | 7 | 9.5 |
| H5 c | Mo | 72 | $9.05 * 10^{12}$ | 8 | 11.8 |
| H6 c | In.180 | 72 | $9.05 * 10^{12}$ | 17.5 | 25.2 |
| H5 o | Mo | 144 | $1.95 * 10^{13}$ | 26 | 24.2 |

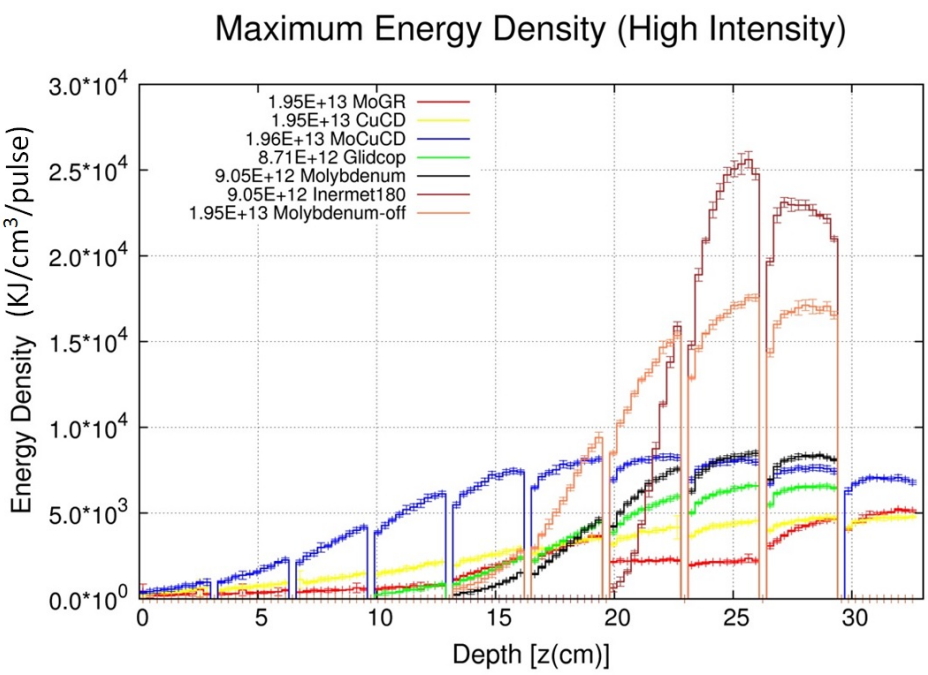


**Figure 11.10:** Energy Deposition profile for all the HRMT-14 materials arrays. Values have been normalized to the entire pulse (of 72 or 144 bunches). Note that the MoGRCF Array is composed by three different grades as reported in Figure 11.9.

This interpretation is consistent with the discussion reported in previous Paragraph 11.3.3 about the failure model imposed to Inermet180: the fracture appears when the Cu-Ni matrix (that embeds the W particles as shown in Figure 4.2) melts leaving the W grains practically free to move under the pressure gradient generated during the Beam Impact.

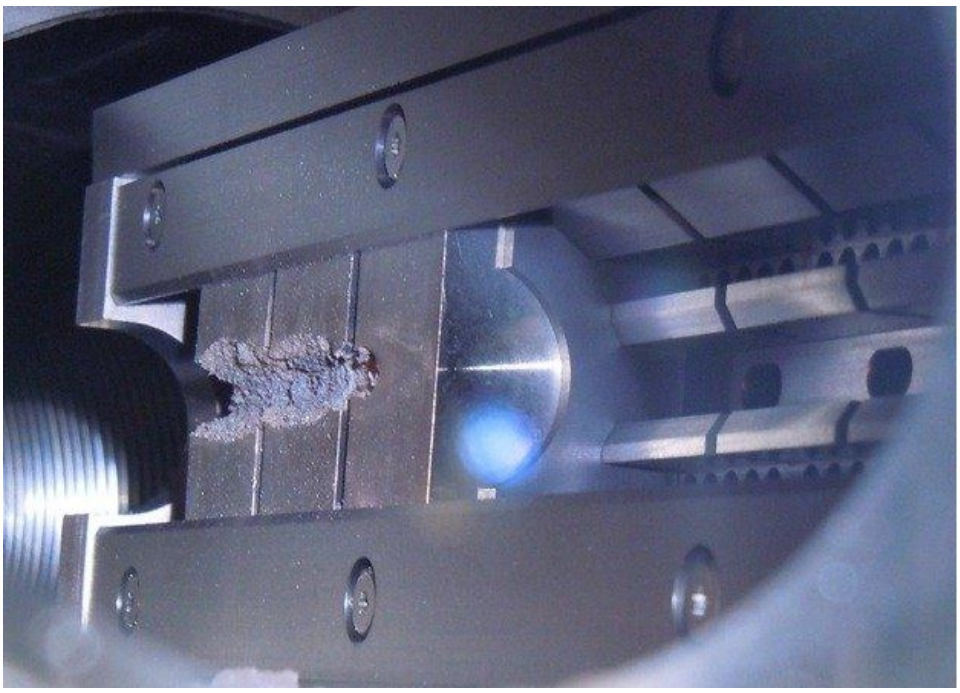

**Figure 11.11:** Inermet180 H6 c impact damage observation from lateral view port.

Comparing the energy density profile of Figure 11.10 with the damage extent in Figure 11.11 it is also possible to roughly estimate the energy density threshold that starts the material ejection as the energy density corresponding to the position of the failure start (en. density threshold $\approx 10KJ/cm^3/pulse$).

### 11.4.3 Molybdenum

As already anticipated the first shot at High Intensity (H5 c, 72 bunches in the centre of the samples) on Mo did not provoke the material failure: a deeper analysis however indicates the formation of a longitudinal crack in sample Pos. 6, that is not completely understood due to the lower values of deposited energy density in the cracked sample

with respect to the following ones (energy density in sample pos.6 $\approx 5KJ/cm^3/pulse$, in sample pos. 7 $\approx 8KJ/cm^3/pulse$).

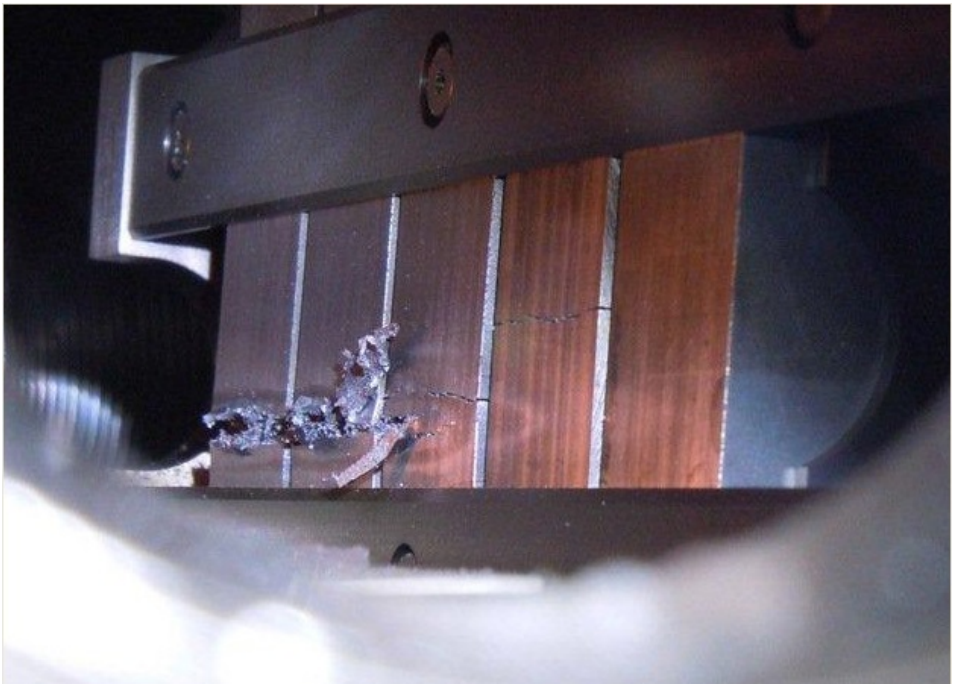

**Figure 11.12:** Molybdenum H5 c (top) and H5 o (bottom) impacts damage observation from lateral view port.

The second shot (H5 o, 144 bunches impacting 10 mm below the centre of the samples) on the other hand was able to provoke extended damage on the material with projection of big, hot fragments of Mo: the aspect of the failure is also completely different from the previous one on inermet180 due to the presence of conspicuous plastic deformation of Mo samples external solid crust. in addition there is the formation of a crack following the upper part of the ZTA.

The energy density threshold in this case can be identified in $\approx 13KJ/cm^3/pulse$, $\approx 30\%$ higher than in Inermet180.

This difference can be explained by comparing few features of Mo and Inermet180:

- the absence of low melting phases in Mo increases the energy density threshold the material can withstand before failure (more energy is needed to provoke phase variation in the material);

- the superior plasticity of Mo allows for a higher energy consumption during the failure propagation (the energy absorbed during the deformation is the integral all over the plastic deformation) that results in lower final internal pressure.

### 11.4.4 Glidcop

Glidcop exhibits a completely different behaviour with respect to Mo and Inmermet180: looking at the post impact damage in Figure 11.13 we can see the longitudinal plastic deformation leaved by the samples expansion during the impact and a slight colour variation in the ZTA, but there is no cavity formed as in previous cases.

**Figure 11.13:** Glidcop H4 c (top) and H4 o (bottom) impact damage observation from lateral view port.

This situation is due to the the melting of only an internal cylindrical portion of the Glidcop samples taking place all over the sample length: the internal pressure provokes the flow out of melted material from the lateral surfaces of the samples instead of the front surface like in Inermet180 or Mo.

This effect has been verified by the video camera observations made during the two impacts: due to the the low quality of the pictures they will not be reported here,

however the moving fragments were visible and followed a $45^o$ trajectory with respect to the samples axis.

In this way the internal pressure is evacuated by the ejection of the liquid Cu from the sides and is no more able to provoke a radial crater, but is leaving instead a slightly deformed surface.

For Glidcop the energy density threshold has been evaluated considering the position of the first visible plastic deformation, giving $\approx 4KJ/cm^3/pulse$; the value is considerably lower than in Inermet180 but it corresponds to a less catastrophic damage extension.

For that reason it might be possible (in the case of impacts depositing a similar Energy Density) to take advantage of the LHC Collimators jaw vertical movement capability (thanks to the so-called 5th axis) to expose to the beam a fresh portion of the jaw surface after the first impact without replacing the collimator.

### 11.4.5 MoCuCD

MoCuCD exhibits a failure very similar to the Inermet180, like shown in Figure 11.14, with an estimated energy density threshold of $\approx$ 7 $KJ/cm^3/pulse$.

As in Inermet180 the fracture appears nubby and without plastic deformation or colour variations and is made by the detachment of solid, hard particles from the material bulk. In the case of MoCuCD the diamond and Mo phases remain solid while Cu melts (see microstructures in Figure 8.15 and 8.18), breaking the bounds between adjacent Mo particles and diamonds (made by brittle $Mo_2C$ interlayer) that are afterwards free to move and being ejected by the action of the internal pressure.

On top of that, MoCuCD's density and especially the atomic number are significantly higher than the other composites leading to higher stopping power and sharp energy deposition profiles (lower radiation length), but without a proportional increase in the melting temperature and in the TSNI parameter, as shown in table 10.5.

### 11.4.6 CuCD

CuCD survived to the High Intensity beam impact without any visible plastic deformation or damage, as shown in Figure 11.15.

The only external sign of the beam passage is the oxidation around the ZTA that follows very well the energy deposition profile calculated by FLUKA. However, the

**Figure 11.14:** MoCuCD H3 c impact damage observation from lateral view port.

**Figure 11.15:** CuCD H2 c impact damage observation from lateral view port.

material internal structure must have been damaged by the shock wave passage reducing the optimal heat transfer of the material, further microstructural analysis of impacted samples will help to verify the presence of internal micro-cracks and/or detachments of the Copper matrix.

In that case the maximum Energy Density deposited on the most loaded sample was $\approx 5KJ/cm^3/pulse$ and was not able to provoke damage, therefore the threshold energy density can be defined as $> 5KJ/cm^3/pulse$.

### 11.4.7 MoGRCF and MoGR

In the array of MoGR and MoGRCF the energy density profile is non regular due to the disposition of heavy MoGR and light MoGRCF samples along the array, as reported in Figure 11.10 and Figure 11.9. In particular there is a first slight increase for the first 4 MoGRCF samples (approximately half of the energy density deposited in CuCD), followed by the rapid increase during the passage across the first two heavy MoGR samples. Afterwards the energy density reduces significantly in the following two light MoGRCF samples (here the energy is mainly due to secondaries shower) and increases back for the last two heavy MoGR samples.

This situation lead to an energy density peak in MoGR and MoGRCF of $\approx 5.1\ KJ/cm^3/pulse$(Pos. 10) and $\approx 2\ KJ/cm^3/pulse$ (Pos. 7) respectively.

Concerning the damage on MoGR (see Figure 11.16) the sample in Pos. 6 does not show any damage or colour variation, while in Pos. 9 there is a longitudinal crack like in Molybdenum sample (Figure 11.12 and finally the sample in Pos. 10 exploded leaving the usual nubby crater. For MoGR the threshold can be considered around $\approx 4 - 4.5\ KJ/cm^3/pulse$.

Finally, MoGRCF did not show any visible sign of deformation or colour variation after the energy deposition, but it must be kept in mind that the maximum energy density deposited on MoGRCF is significantly lower than any other tested material thanks to the very low density of such material.

For that reason MoGRCF can be considered more similar to CFC than to CuCD or MoGR: it has a very good TSNI but at the same time more beam-jaw interaction (i.e. increase jaw length or total collimator number) is required to obtain the same cleaning efficiency.

**Figure 11.16:** MoGR H1 c impact damage observation from lateral view port.

**Figure 11.17:** MoGRCF H1 c Impact Damage Observation from lateral view port.

## 11.5 Conclusions on Beam Impact Resistance of Collimator Materials

The robustness of LHC Collimators materials has been studied, by analytical and numerical means, and experimentally verified participating to a complex and comprehensive experiment that has been carried out at CERN during 2012.

The experiment aimed at the characterization, mostly in real time, of six different materials of interest, including three new composites developed during the present thesis work, impacted by 440 GeV intense proton pulses.

The design of the test set-up required innovative solutions in terms of lighting, support stabilization, radiation resistance and noise control. The test was a success under any point of view: all experiment systems (DAQ, electronics, and mechanics) worked properly in spite of the very harsh environment and of the technological challenges allowing the collection of valuable data.

The high-speed camera and flash systems then allowed for the first time to the best of authors knowledge to record images of the impact of a hadron beam on solid targets and of the effects this induced on materials. Preliminary measurements on Glidcop and Inermet180 specimens very well match results of advanced numerical simulations proposed in this Chapter, confirming the reliability of the simulation methods and supplying promising indications on the validity of constitutive models used for these materials.

A very large amount of data is still to be treated to help deriving constitutive models for the less known materials, namely for the novel composite material which were tested for the first time during the experiment. The provided preliminary post impact damage evaluations will be completed by the final campaign, implying the dismantling of the Materials Sample Holder and the destructive testing of irradiated samples. For obvious safety reasons the tank opening must be performed inside a special Class C laboratory that has still to be identified.

Finally, the experimental results allowed to compare in an ordered way the different materials of interest giving a more detailed view of the final behaviour inside the LHC accelerator.

# 12

# Conclusions

This Chapter collects the most important scientific contributions and results obtained during the PhD and summarizes the conclusions of this work.

## 12.1 Research Context

Recent advances in high-energy particle physics require particle accelerators to reach unprecedented energies. In particular, the Large Hadron Collider (LHC) at the European Organization for Nuclear Research (CERN, Meyrin, CH) stands out for its incredible quantity of energy stored inside the beams, which allows to explore a completely new field of High Energy Physics (HEP): however, a tiny fraction of this potentially destructive energy is sufficient to cause catastrophic damages to sensitive components and materials leading to machine stop, with high costs in terms of time and resources (see Chapter 3). Therefore, the study of new advanced materials for Beam Intercepting Devices (BID) is having strong interest in the particle accelerator community. The study of available solutions, reported in Chapter 4, pointed out that conventional materials do not fulfil the two main requirements of LHC Collimators: reliable and efficient beam cleaning as well as high robustness in accidental scenarios.

This thesis aimed to fill the technological gap developing novel advanced composites for BID.

The most important result is a novel composite (MoGRCF) having exceptional thermal and physical properties combined with suitable mechanical strength. This

novel material is very appealing in view of Hi-Lumi LHC Collimators as well as future challenging BID.

## 12.2 Scientific Contributions and Results

This section collects a brief summary of the most important results achieved during the PhD. The first part includes the materials developed as well as the principal innovations proposed in the composites production, while the second part regards the evaluation of the beam impact resistance of BID materials.

- Molybdenum - Copper - Diamond (MoCuCD): diamond-reinforced MMC for thermal management applications. MoCuCD is the final result of more than one year of research made to identify the correct RHP production cycle parameters, raw materials and compositions for the material production. The work included a large study on Cu coated diamonds and on the possible solutions to reduce diamond graphitization during production. The obtained material exhibits an optimal combination of thermal and mechanical properties as confirmed by the characterization reported in Chapter 8. However, its relatively high density for a BID material is limiting its resistance in the case of high energy beam impacts.

- Molybdenum Carbide - Graphite (MoGR): graphite-reinforced CMC for high temperature thermal management applications. Always produced by RHP of selected powders its production relies on a solid state reaction without the use of low melting phases to infiltrate the interstitials (as Cu in MoCuCD). This allows for a superior thermal stability at high temperature and a melting temperature above $2500oC$, although the other thermal and mechanical properties are not as good as previous MoCuCD. The most significant contributions given during the work are the innovations in production technology of advanced refractory carbides - graphite composites, such as the developed solid state reaction-based production process and the introduction of Palladium sub micrometric powder as sintering activator for refractory materials.

- Molybdenum Carbide - Graphite - Carbon Fibers (MoGRCF): Carbon Fibers (CF)-reinforced CMC for BID. MoGRCF, produced by Liquid Phase Sintering of selected and treated powders, can be considered as the final result of the PhD

and represents an important milestone in the research of advanced CMC for BID applications. The material shows in fact exceptional thermal and physical properties combined with very low density and adequate mechanical properties. This result has been possible thanks to its very high CF content (up to $40\%_V$), which is the highest value obtained for CF-reinforced CMC in the best of our knowledge. The main contributions given during the thesis are the identification of suitable compositions and powder treatments that, combined with the Liquid Phase Sintering (LPS) process at very high temperatures, allowed to achieve a thermal conductivity in excess of 700 W/mK. MoGRCF has been identified as the most suitable material for Hi-Lumi LHC Collimators and more in general for application where low density, high thermal and electrical conductivity and high thermal stability are required.

- Verification of BID materials robustness against beam impacts. This part of the work includes the FEM modelling of the beam impacts, the development, inside a team, of an ad-hoc experiment to test the different materials and the evaluation of their damage threshold. More in details, the FEM simulations have been performed relying on the hydrodynamic code Autodyn using Smooth Particle Hydrodynamics (SPH) elements, multi-phase equations of state and complex strength and failure materials models. The proposed simulations allow for the prediction of the shock wave (and the following explosion) provoked during the beam impact and of the residual damage on conventional materials. However, for the composites of interest this models are unavailable leading to the need of apposite experiments. The experiment, called HRMT-14, has been carried out inside the HiRadMat facility at CERN: it consisted in the controlled impact of the highly energetic SPS beam onto instrumented materials samples with the real time acquisition of key parameters such as samples face strain, radial velocity and temperature. On top of that the samples explosion has been recorded using a high speed video camera, placed 40 m away from the impact to avoid radiation induced damage. The main contributions during this part were the samples design through FEM simulations and the preparation of the video camera acquisition setup, including the development of a synchronized and radiation resistant lighting system for the video acquisition. The experiment has been a success from all

points of view, allowing for the first time in the best of our knowledge to observe in real time the materials explosion due to beam impacts. In addition, the data collected during the impacts were in very good agreement with the numerical simulations results, confirming the validity of the proposed methods. Finally, the post irradiation damage observation allowed to benchmark the conventional and newly introduced materials: the two most promising materials are CuCD and MoGRCF, which survived the high intensity beam impacts without visible signs of damage.

As a final remark, the very good results achieved with the R&D on novel Mo-based composites allowed for the creation of a spin-off R&D program on Alumium - Graphite composites, which is currently ongoing with the aim to produce a thermal management material for low temperatures applications.

## 12.3 Future Outlook

The work performed lays the foundations for a a large number of valuable research topics, providing also a useful set of tools for the development and the testing of BID materials.

A brief list of future activities is reported below.

- Production and characterization of large MoGRCF plates with dimensions suitable for LHC Collimators jaws. The dimensional increase brings additional challenges to the plates production, that must be carefully controlled. The material industrialization will then allow to introduce MoGRCF to other applications.

- Development of metallic coatings for MoGRCF to improve its superficial electrical conductivity and reduce the high frequency RF Impedance to values similar to CuCD. The coatings must be as thin as possible to avoid local energy deposition while providing good bonding and electrical continuity with the MoGRCF matrix.

- Continuation of the study of the radiation induced degradation of aforementioned materials in partner institutes (NRC-Kurchatov Institute, BNL) together with the corresponding LHC life time.

- Preparation of a new HiRadMat experiment taking advantage from the large experience maturated with $HRMT - 14$: in particular there is the need to increase the energy density deposited on composites in order to observe the damage threshold, to upgrade the video camera acquisition system to obtain better pictures, to create a protective system for the window, and finally to reduce the beam perturbation on the in situ acquisition system (strain gauges).

# References


[1] Various. **HL-LHC: High Luminosity Large Hadron Collider Project**. xiv, 7

[2] A. Ryazanov. **"Measurement of the thermophysical properties of material candidates for LHC collimator jaws." Presentation at the Collimation Working Group Meeting N. 155 of 18/02/2013 at CERN.** xvii, xxv, 78, 79, 82

[3] **Asbury Graphite Webpage**. xix, 117

[4] J. Goma and M. Oberlin. **Graphitization of thin carbon films**. *Thin Solid Films*, **65**(2):221 – 232, 1980. xx, 139

[5] J D Buckley and D D Edie. *Carbon-Carbon Materials and Composites, 1st Edition.* 1993. xxi, 140

[6] Alessandro Dallocchio, G Belingardi, T Kurtyka, and A Bertarelli. *Study of Thermo-Mechanical Effects Induced in Solids by High Energy Particle Beams: Analytical and Numerical Methods.* PhD thesis, Turin Polytechnic, Turin, 2008. Presented on 26 May 2008. xxv, 18, 24

[7] G. A. Izquierdo. **Measurement of the thermophysical properties of material candidates for LHC collimator jaws**. xxv, 23, 24, 25

[8] Various. **EuCARD WP8 Home page**. 3

[9] Oliver Sim Brning, Paul Collier, P Lebrun, Stephen Myers, Ranko Ostojic, John Poole, and Paul Proudlock. *LHC Design Report.* CERN, Geneva, 2004. 6

[10] R W Assmann, O Aberle, G Bellodi, A Bertarelli, C Bracco, H Braun, M Brugger, S Calatroni, R Chamizo, Alessandro Dallocchio, B Dehning, A Ferrari, P Gander, A Grudiev, E B Holzer, J B Jeanneret, J M Jimnez, M Jonker, Y Kadi, K Kershaw0, J Lendaro, Jacques Lettry, R Losito, M Magistris, A Masi, M Mayer, E Mtral, R Perret, C Rathjen, S Redaelli, G Robert-Dmolaize, S Roesler, F Ruggiero, M Santana, P Sievers, M Sobczak, A Tsoulou, V Vlachoudis, T Weiler, I S Baishev, and I Kurochkin. **The final collimation system for the LHC**. In *LHC-PROJECT-Report-919.*, page 4 p, Jul 2006. revised version submitted on 2006-09-15 14:36:59. 7

[11] Various. **ATLAS Collaboration website**. 9

[12] Various. **ALICE Collaboration website**. 9

[13] Various. **CMS Project website**. 9

[14] Various. **LHCb Collaboration website**. 9

[15] Various. **TOTEM Collaboration website**. 9

[16] Various. **LHCf Collaboration website**. 9

[17] J B Jeanneret, D Leroy, L R Oberli, and T Trenkler. **Quench levels and transient beam losses in LHC magnets**. Technical Report LHC-Project-Report-44. CERN-LHC-Project-Report-44, CERN, Geneva, May 1996. 11

[18] Various. **LHC Collimation Project Website**. 11

[19] Assmann. **Collimation for the LHC High Intensity Beams**. In *HB2010 Proceedings, Morschach, Switzerland*, page 13 p, Jan 2011. 12

[20] Assmann. **Beam Halo on the LHC TCDQ Diluter System and Thermal Load on the Downstream Superconducting Magnets**. In *EPAC 2006 Proceedings, Edinburgh, Scotland*, pages 547–549, 2006. 12

[21] R W Assmann, B Goddard, Eugne B Vossenberg, and E Weisse. **The consequences of abnormal beam dump actions on the LHC collimation system**. Technical Report LHC-PROJECT-NOTE-293, CERN, Geneva, May 2002. 14

[22] A Bertarelli, V Boccone, F Carra, F Cerutti, A Dallocchio, N Mariani, L Peroni, and M Scapin. **Limits for Beam Induced Damage: Reckless or too Cautious?** (EuCARD-CON-2011-068), 2011. 14, 167

[23] M Cauchi, R Assmann, A Bertarelli, R Bruce, F Carra, A Dallocchio, D Deboy, N Mariani, A Rossi, L Lari, P Mollicone, and N Sammut. **Preliminary assessment of beam impact consequences on LHC Collimators**. (CERN-ATS-2011-132):3 p, Sep 2011. 14

[24] F. Goldenbaum D. Filges. *Handbook of Spallation research. Theory, Experiments and Applications.* WILEY-VCH, 2009. 15

[25] Various. **FLUKA website**. 15

[26] Assmann et Al. **Designing and building a collimation system for the high-intensity LHC beam**. In *PAC2003 Proceedings, Portland, Oregon, US*, pages 45–47, May 2003. 16

[27] Bertarelli. **Presentation: Phase II Collimators at CERN: design status and proposals**. 19

[28] P Sievers. **Appropriate Materials for LHC Collimators**. 2003. 22

[29] **EDMS reports of Flexural tests performed at CERN Mechanical Laboratory on CFC**. 23

[30] **SGL Carbon GmbH Webpage**. 25

[31] P Morgan. *Carbon Fibers and Their Composites.* 2005. 25, 115, 135, 146

[32] Various. **Plansee Tungsten heavy Alloys webpage**. 25, 29

[33] C.W. Corti. **Sintering Aids in Powder Metallurgy: The role of the platinum metals in the activated sintering of refractory metals**. 1986. 26

[34] J. T. Smith. **Diffusion Mechanism for the Nickel-Activated Sintering of Molybdenum**. 1965. 26

[35] SCM Metals Products Inc. **Glidcop Material Datasheet**. 26

[36] Various. *ASM Specialty Handbook, Copper and Copper Alloys.* 28, 86, 89

[37] A Bertarelli, A Dallocchio, L Gentini, N Mariani, R Perret, and M A Timmins. **Mechanical Engineering and Design of the LHC Phase II Collimators**. (EuCARD-CON-2010-020. CERN-ATS-2010-148):3 p, Apr 2010. 28

[38] A Bertarelli, G Arnau Izquierdo, F Carra, A Dallocchio, M Gil Costa, and N Mariani. **Research and development of novel advanced materials for next-generation collimators**. (CERN-ATS-2011-224):4 p, Nov 2011. 29, 30

[39] William D Callister Jr. *Scienza e Ingegneria dei Materiali una Introduzione.* EdiSES, Napoli, IT, 2002. 34

[40] P. J. Whiters T.W. Clyne. *An Introduction to Metal Matrix Composites.* Cambridge Solid State Science Series, Cambridge, UK, 1993. 35

[41] Shu-bin REN Xuan-hui QU; Lin ZHANG; Mao WU. **Review of metal matrix composites with high thermal conductivity for thermal management applications**. 2011. 35

[42] M. Ganor J. Pelleg. **The influence of third element on the interface reactions in metal-matrix composites (MMC): Al-grphite system**. 2000. 36

[43] Karl Ulrich Kainer. *Basics of Metal Matrix Composites*, pages 1–54. Wiley-VCH Verlag GmbH & Co. KGaA, 2006. 37

[44] L. Weber and R. Tavangar. **On the influence of active element content on the thermal conductivity and thermal expansion of CuX (X = Cr, B) diamond composites**. *Scripta Materialia*, (57):988–991, 2007. 38, 45, 65

[45] Leone Corradi Dell'Acqua. *Meccanica delle Strutture. Le teorie strutturali e il metodo degli elementi finiti.* MacGraw-Hill Libri Italia srl, 1992. 38

[46] N. Mariani. *Caratterizzazione Elastica di Film Nanometrici Multistrato Mediante Scattering Brillouin di Superficie.* PhD thesis, Milan's Polytechnic, Department of Nuclear engineering Enrico Fermi, Milan, 2007. Presented on 21 December 2007. 40, 41

[47] L. Vergani. *Meccanica dei materiali.* Collana di istruzione scientifica: Serie di ingegneria meccanica. McGraw-Hill Companies, 2006. 43

[48] M.L. Scott. *Proceedings: Metal matrix composites and physical properties*. Number v. 3 in Eleventh International Conference on Composite Materials. Australian Composite Structures Society, 1997. 43

[49] T.J. Holmquist G.R. Johnson. **An improved computational constitutive model for brittle materials**. *High Pressure Science and Technology*, (309):981–984, 1993. 43

[50] G. McIntosh. **The Johnson-Holmquist Ceramic Model as used in LS-Dyna2D**. Technical Report DREV-TM-9822, Research and Development Branch Department of National Defence Canada., Defence Research Etablishment Valcartier, Canada, Dec 1998. 43

[51] H. Morigami K. Yoshida. **Thermal properties of diamond/copper composite material**. 2004. 44, 45

[52] JC Maxwell. *A treatise on electricity and magnetism*. Oxford University Press, Vol. 1 3rd ed., 1904. 45

[53] Johnson LF Hasselmann DPH. **Effective thermal conductivity of composites with interfacial thermal barrier resistance**. 1987. 45

[54] T Schubert L Ciupinsky W Zielinsky A Michalsky T Weissgaerber and B Kieback. **Interfacial characterization of Cu/diamond composites prepared by powder metallurgy for heat sink applications**. 2007. 45

[55] Ce-Wen Nan, R. Birringer, David R. Clarke, and H. Gleiter. **Effective thermal conductivity of particulate composites with interfacial thermal resistance**. *Journal of Applied Physics*, **81**(10):6692–6699, 1997. 45, 46

[56] P S Turner. **Thermal-Expansion Stresses in Reinforced plastics**. *Part of the Journal of the National Bureau of Standards*, **37**:239–250, 1946. 46

[57] E H Kerner. **The Elastic and thermo-elastic Properties of Composite Media**. *Proceedings of Physical Society LXIX*, (8):808–813, 1956. 46

[58] C.L. Hsieh and W.H. Tuan. **Thermal Expansion Behaviour of a model ceramic-metal composite**. *Materials Science and Engineering A 460-461*, pages 453–458, 2007. 46

[59] Various. **Brevetti Bizz srl Home page**. 48, 84

[60] Foerster. **Sigmatest 2.069 by Foerster webpage**. 49

[61] ASTM International. **ASTM C 1161 02c "Standard Test Method for Flexural Strength of Advanced Ceramics at Ambient Temperature"**. 55

[62] B. Snaith, S.D. Probert, and P.W. O'Callaghan. **Thermal resistances of pressed contacts**. *Applied Energy*, **22**(1):31 – 84, 1986. 58

[63] V V Rao, K Bapurao, J Nagaraju, and M V Krishna Murthy. **Instrumentation to measure thermal contact resistance**. *Measurement Science and Technology*, **15**(1):275, 2004. 58

[64] A. Noranzik. **Thermal Conductivity Measurements of Graphite Samples**. 2009. 58

[65] H.G. Moser C.A. Heusch and A. Kholodenko. **Direct measurements of the thermal conductivity of various pyrolytic graphite samples (PG,TPG) used as thermal dissipation agents in detector applications**. *Nuclear instruments and Methods in Physics Research A*, **480**:463–469, 2002. 58

[66] Netzsch. **Netzsch Laser Flash Technique informative website**. 62

[67] Netzsch. **Netzsch Laser Flash LFA 427 website**. 62

[68] Netzsch. **Netzsch Dilatometer website**. 63

[69] Netzsch. **Netzsch DSC website**. 63

[70] Katsuhito Yoshida and Hideaki Morigami. **Thermal properties of diamond/copper composite material**. *Microelectronics Reliability*, **44**(2):303 – 308, 2004. 65

[71] Q. Sun and O.T. Inal. **Fabrication and characterization of diamond/copper composites for thermal management substrate applications**. *Materials Science and Engineering: B*, **41**(2):261 – 266, 1996. 65

[72] W.Z. Shao, V.V. Ivanov, L. Zhen, Y.S. Cui, and Y. Wang. **A study on graphitization of diamond in copperdiamond composite materials**. *Materials Letters*, **58**(12):146 – 149, 2004. 65

[73] O. Beffort, S. Vaucher, and F.A. Khalid. **On the thermal and chemical stability of diamond during processing of Al/diamond composites by liquid metal infiltration (squeeze casting)**. *Diamond and Related Materials*, **13**(10):1834 – 1843, 2004. 65

[74] J. Field. *The properties of natural and synthetic diamonds.* J Field, 1992. 66, 69

[75] W. Erlich, E.I.; Dan Hausel. **Diamond Deposits.** *Society for Mining, Metallurgy, and Exploration*, pages 74–78, 2005. 66

[76] F.P. Bundy. **Pressure-Temperature Phase Diagram of Elemental Carbons**. *Physica A*, pages 156 – 169, 1898. 69

[77] J M Zazula. **On Graphite Transformations at High Temperature and Pressure Induced By Absorption of the LHC Beam**. Technical Report LHC-Project-Note-78, CERN, Geneva, Jan 1997. 69

[78] J. Qian, C. Pantea, J. Huang, T.W. Zerda, and Y. Zhao. **Graphitization of diamond powders of different sizes at high pressurehigh temperature**. *Carbon*, **42**(1213):2691 – 2697, 2004. 69

[79] D.V. Fedoseev S.P. Vnukuv V.L. Bukhovets B.A. Anikin. **Surface Graphitization of Diamond at elevated Temperatures**. *Surface and Coatings Technology*, (28), 1986. 69

[80] S. Redaelli on behalf of the Collimation Project and HL-LHC-WP5. **LHC Collimation Status and Upgrade Strategy**. Presented at LARP CM18/HiLumi LHC Meeting, May 7-9 2012 at Fermilab, Batavia, 2012. 72

[81] N. Mariani. **LHC Phase II Collimator Material Design: Copper Diamond Composite. Visit to AIT: Austrian Institute of Technology**. 73

[82] S. Redaelli (CERN) A. Bertarelli (CERN), N. Simos (BNL). **Materials for HL-LHC Collimators: R&D, Tests and Irradiation Studies**. 78

[83] N. Mariani. **Collection of available documents on the Irradiation Tests to be performed at BNL (Brookhaven National Laboratory, US) on Collimator Materials. Materials under testing: Molybdenum, Glidcop, CuCD, MoGR.** 78

[84] R.B. Matthews and G.M. Jenkins. **The high temperature interaction between molybdenum and graphite**. *Journal of Materials Science*, **10**(11):1976–1990, 1975. 83, 120

[85] N. Mariani. **Molybdenum Diamond Composite (MoCD) Development Summary**. 84

[86] Various. *ASM Specialty Handbook, Powder Metal Technologies and Applications.* 85

[87] Various. *ASM Specialty Handbook, Heat-Resistant Materials.* 85

[88] J.H. Adair P. Chillar, D.Agrawal. **Sintering of molybdenum metal powder using microwave energy**. *Powder Metallurgy*, **51**(2), 2008. 86

[89] Guorong Hu, Yexiang Liu, Jianhong Yang, Kaihua Yang, Fenglin Tang, and Jihong Jin. **Electroless plating composite coatings of Ni-Ti-Re on the surface of diamond**. *Journal of Central South University of Technology*, **6**(1):13–15, 1999. 89

[90] G.A. Rubin Y. Harada. **Fabrication and Characterization of Metal Carbide-Graphite Composites**. *IITRI, 68th Annual Meeting of the American Ceramic Society*, 1966. 114

[91] D. John and G.M. Jenkins. **Hot-working and strengthening in metal carbide-graphite composites**. *Journal of Materials Science*, **21**(8):2941–2958, 1986. 115

[92] H O Pierson. *HANDBOOK OF CARBON, GRAPHITE, DIAMOND AND FULLERENES: Properties, Processing and Applications.* 1993. 117, 135

[93] **Phase Diagram of Molybdenum - Carbon system calculated with MTDATA Phase Diagram Software from the National Physical Laboratory, Teddington, Middlesex, UK**. 119

[94] H.O. Pierson. *Handbook of Refractory Carbides & Nitrides: Properties, Characteristics, Processing and Apps.* Elsevier Science, 1996. 119

[95] C.W. Corti. **Sintering Aids in Powder Metallurgy the role of platinum metals in the activated sintering of refractory metals**. *Platinum Metals rev.*, **30**(4):184–195, 1986. 121, 122

[96] V.V. Panichkina, V.V. Skorokhod, and A.F. Khrienko. **Activated sintering of tungsten and molybdenum powders**. *Soviet Powder Metallurgy and Metal Ceramics*, **6**(7):558–560, 1967. 121

# REFERENCES


[97] K.S Hwang and H.S Huang. **Identification of the segregation layer and its effects on the activated sintering and ductility of Ni-doped molybdenum**. *Acta Materialia*, **51**(13):3915 – 3926, 2003. 121

[98] Various. *ASM Specialty Handbook, Alloy Phase Diagrams*. 121, 122

[99] T Matsumoto. **Mesophase pitch and its carbon fibers**. *Pure & Applied Chemistry*, **57**(11):1553–1562, 1985. 137

[100] **Nippon Fiber Corporation webpage**. 137

[101] **Cytec ThermalGraph DKD Carbon Fiber Producer Datasheet**. 137

[102] J.D. Brooks and G.H. Taylor. **The formation of graphitizing carbons from the liquid phase**. *Carbon*, **3**(2):185 – 193, 1965. 139

[103] L.S. Singer. **The mesophase and high modulus carbon fibers from pitch**. *Carbon*, **16**(6):409 – 415, 1978. 141

[104] J L White M W Roberts, J M Thomas and J. E. Zimmer. *Disclination structures in carbonaceous mesophase and graphite*. 1976. 141

[105] R. M. German. *Liquid Phase Sintering*. Plenum press, New York and London, 1985. 151

[106] A Bertarelli, E Berthome, V Boccone, F Carra, F Cerutti, N Charitonidis, C Charrondiere, A Dallocchio, P Fernandez Carmona, P Francon, L Gentini, M Guinchard, A Masi, S D Marques dos Santos, P Moyret, L Peroni, S Redaelli, and M Scapin. **An Experiment to Test Advanced Materials Impacted by Intense Proton Pulses at CERN HiRadMat Facility**. Jan 2013. Preprint. 167, 173

[107] A. Bertarelli, F. Carra, F. Ceruttiand A. Dallocchioand M. Garlaschand M. Guinchardand N. Marianiand S. D. Marques dos Santosand L. Peroniand M. Scapin, and V. Boccone. **Behaviour of advanced materials impacted by high energy particle beams**. *Journal of Physics: Conference series*, **451**, 2013. 167

[108] Alessandro Bertarelli, Oliver Aberle, Ralph Wolfgang Assmann, Alessandro Dallocchio, Tadeusz Kurtyka, Matteo Magistris, Mario Santana-Leitner, and Manfred Mayer. **Permanent Deformation of the LHC Collimator Jaws Induced by Shock Beam Impact: an Analytical and Numerical Interpretation**. page 3 p, 2006. 167

[109] J.A. Zukas. *Introduction to hydrocodes*. Elsevier, 2004. 167

[110] Ansys Inc. *ANSYS Autodyn User Manual, Release 13.0*. 2010. 168

[111] Giuseppe Battistoni, F Cerutti, A Fass, A Ferrari, S Muraroi, J Ranft, S Roesler, and P R Sala. **The FLUKA code: Description and benchmarking**. *AIP Conf. Proc.*, **896**(SLAC-REPRINT-2007-184):31–49. 19 p, 2007. 168

[112] A Ferrari, Paola R Sala, A Fass, and Johannes Ranft. *FLUKA: A multi-particle transport code (program version 2005)*. CERN, Geneva, 2005. 168

[113] H. Richter, E. Noah, H. Aiginger, and K. Poljanc. **Simulation of target response due to uranium ion beam impact**. *The European Physical Journal A*, **42**(3):301–306, 2009. 168

[114] J. H. Tillotson. **Metallic Equations of State for Hypervelocity Impact. Report No. GA-3216, July 18 (General Atomic, San Diego, California, 1962)**. 169

[115] I V Lomonosov V E. **Equations of State of Matter at High Energy Densities**. *The Open Plasma Physiscs Journal*, pages 122–130, 2010. 169

[116] Various. **SESAME: the Los Alamos National laboratory Equations Of State database**. 169

[117] G I Kerley. **Equations of state for Be, Ni, W and Au**, 2003. 169

[118] Various. **Compendium of Shock Wave Data**, 1977. 169

[119] W. H. Cook G. R. Johnson. **A Constitutive Model and Data for Metals Subjected to Large Strains, High Strain Rates and High Temperatures**. In *Proc. 7th Int. Symp. on Ballistics*, 1983. 170

[120] G. R. Johnson and T. J. Holmquist. **An Improved Computational Constitutive Model for Brittle Materials**. *High Pressure Science and Technology*, **2**:981–985, 1993. 170

[121] D E Grady. **The spall strength of condensed matter**. *Journal of Mech. Phys. Solids*, **36**(3):535–584, 1988. 171

[122] J Wang L Hu, P Miller. **High strain-rate spallation and fracture of tungsten by laser-induced stress waves**. *Material Science and Engineering A*, **504**:73–80, 2009. 171

[123] A. Manousos and V. Vlachoudis. **Energy Deposition Results in: HRMT14 Samples & TCSx**. Presented at the Working Group on Advanced Materials for Collimators AdColMat - 3rd Meeting 25.11.2013, 2013. 178

# Glossary

**AIT** Austrian Institute of Technology

**ASTM** American Society for Testing and Materials

**AgCD** Silver - Diamond

**AlCD** Aluminium - Diamond

**BNL** Brookhaven National Laboratories

**BPMs** Beam Position Monitors

**CERN** European Organization for Nuclear Research

**CF** Carbon Fibers

**CFC** Carbon Fiber Carbon composite

**CMC** Ceramic Matrix Composites

**CTE** Coefficient of Thermal Expansion

**CuCD** Copper - Diamond

**CucCD** Copper coated Diamonds

**DAQ** Data Acquisition System

**DSC** Differential Scanning Calorimetry

**EBSD** Electron Back Scatter Diffraction

**EDS** Energy Dispersion Spectroscopy

**EOS** Equation of State

**EPFL** cole Polytechnique Fdrale de Lausanne

**EuCARD** European Coordination for Accelerator Research & Development

**FE** Finite Elements

**GSI** Helmholtz Centre for Heavy Ion Research

**Hi-Lumi** High Luminosity LHC Upgrade

**HiRadMat** High Radiation to Materials

**INOX** Stainless Steel

**JC** Johnson-Cook Strength Model

**LDV** Laser Doppler vibrometer

**LHC** Large Hadron Collider

**LS1** LHC Long Shutdown 1

**MMC** Metal Matrix Composites

**MoCuCD** Molybdenum - Copper - Diamond

**MoCucCD** MoCuCD with CucCD

**MoGR** Molybdenum Carbide - Graphite

**MoGRCF** Molybdenum Carbide - Graphite - Carbon Fibers

**NRC** National Research Center

**OF** Oxygen Free

**OM** Optical Microscopy

**PAN** Polyacrylonitrile

**PMC** Polymer Matrix Composites

**QBSD** Quadrants Back Scattered (Electrons) Detector

**RF** Radio Frequency

**RHP** Rapid Hot Pressing

**ROM** Rule Of Mixture

**RT** Room Temperature, 25 $^{o}C$

**R&D** Research and Development

**SE** Secondary Electron (Detector)

**SEM** Scanning Electrons Microscope

**SPH** Smooth Particle Hydrodynamics

**SPS** Super Proton Synchrotron

**SSNI** Steady State Stability Normalized Index

**TCP** Primary LHC Collimator

# GLOSSARY

| | |
|---|---|
| **TCS** | Secondary LHC Collimator |
| **TCSM** | Hi-Lumi Secondary LHC Collimator |
| **TCT** | Tertiary LHC Collimator |
| **TCTP** | Tertiary LHC Collimator with Beam Position Monitors (BPMs) |
| **TSNI** | Transient Shock Normalized Index |
| **UHV** | Ultra High Vacuum |
| **US-LARP** | United States LHC Accelerator Research Program |
| **ZTA** | Zone Thermally Altered |
| $A$ | Area, $[m^2]$ |
| $A$ | Elastic Limit in JC model, [MPa] |
| $B$ | Work hardening constant in JC model, $[MPa]$ |
| $C$ | Strain rate sensitivity constant in JC model, [MPa] |
| $C_{ii}$ | Elastic Constants, [GPa] |
| $E$ | Young's Modulus, [GPa] |
| $F$ | Force, [N] |
| $G$ | Shear Modulus, [GPa] |
| $K$ | Bulk Modulus, [GPa] |
| $L$ | Support Span, [mm] |
| $P_{min}$ | Minimum Hydrostatic Pressure, $[GPa]$ |
| $Q$ | Heat Flux, [W] |
| $R$ | Ultimate Tensile Strength, [MPa] |
| $R_{Fl}$ | Ultimate Flexural Strength, [MPa] |
| $T_m$ | Melting Temperature, $[^oC]$ |
| $T_{HT}$ | Thermal Treatment Temperature, $[^oC]$ |
| $Z$ | Atomic Number, $[-]$ |
| $\%_V$ | Volume Percentage, [%] |
| $\%_w$ | Weight Percentage, [%] |
| $\alpha$ | Coefficient of Thermal Expansion, $[10^{-6}K--1]$ |
| $\alpha_k$ | Kapitza radius, $[\mu m]$ |
| $\chi_0$ | radiation Length, [cm] |
| $\delta_z$ | Vertical displacement, [mm] |
| $\dot{\epsilon}$ | Strain rate, $[s^{-1}]$ |
| $\epsilon$ | Real deformation, $[-]$ |
| $\lambda$ | Wavelenght, [m] |
| $\nu$ | Poisson's Ratio, $[-]$ |
| $\rho$ | Density, $[g/cm^3]$ |
| $\sigma$ | Electrical Conductivity, [MS/m] |
| $\sigma_{Fl}$ | Maximum Tensile and Compressive Flexural Stress ,[MPa] |
| $\theta$ | Angle of incoming X-Rays, [rad] |
| $c_p$ | Specific Heat, [J/KgK] |
| $d$ | Distance between adjacent crystallographic planes, [m] |
| $dpa$ | Displacements per atom, $[-]$ |
| $f_V$ | Volume Fraction, $[-]$ |
| $f_w$ | Weight Fraction, $[-]$ |
| $h$ | Height, [mm] |
| $h_c$ | Thermal Conductance, $[W/m^2K]$ |
| $k$ | Thermal Conductivity, [W/mK] |
| $m$ | Mass, [g] |
| $n$ | Work hardening exponent in JC model, $[-]$ |
| $w$ | Width, [mm] |
| $Atm$ | Atmosphere, pressure |
| $Hz$ | Hertz, frequency |
| $J$ | Joule, energy |
| $K$ | Kelvin, temperature |
| $N$ | Newton, force |
| $Pa$ | Pascal, pressure |

| | |
|---|---|
| $Sv$ | Sievert |
| $T$ | Tesla, magnetic field |
| $W$ | Watt, power |
| $^oC$ | Centrigrads, temperature |
| $bar$ | Bar, pressure |
| $eV$ | Electron Volt, energy |
| $g$ | Gram, mass |
| $h$ | Hour, time |
| $m$ | Meter, lenght |
| $mol$ | Number of moles |
| $rad$ | Radians, angle |
| $s$ | Second, time |
| $Ag$ | Silver |
| $Al$ | Aluminium |
| $Al_2O_3$ | Aluminium Oxide |
| $Ar$ | Argon |
| $Au$ | Gold |
| $C$ | Carbon |
| $Co$ | Cobalt |
| $Cu$ | Copper |
| $Fe$ | Iron |
| $H_2$ | Hydrogen |
| $Mo$ | Molybdenum |
| $Mo_2C$ | Molybdenum Carbide |
| $N_2$ | Nitrogen |
| $Nb$ | Niobium |
| $Ni$ | Nickel |
| $Pd$ | Palladium |
| $Pt$ | Platinum |
| $Rh$ | Ruthenium |
| $SiC$ | Silicon Carbide |
| $Ti$ | Titanium |
| $W$ | Tungsten |